NORTHWESTERN UNIVERSITY

Early Detection of Cancer Metastasis at a Synthetic Pre-Metastatic Niche Using Inverse Spectroscopic Optical Coherence Tomography

A DISSERTATION

SUBMITTED TO THE GRADUATE SCHOOL

IN PARTIAL FULFILLMENT OF THE REQUIREMENTS

for the degree

DOCTOR OF PHILOSOPHY

Field of Chemical Engineering

By

Graham L. C. Spicer

EVANSTON, ILLINOIS

June 2019

Abstract

Early detection of cancer metastasis at a synthetic pre-metastatic niche using inverse spectroscopic optical coherence tomography

Graham L. C. Spicer

Cancer progression is a complex process, leading to metastatic spread of primary tumor cells that colonize distant vital organs and mortality if not stopped. Since clinical strategies to stem this progression are still being developed, it is of great importance to detect this end stage metastatic spread as early as possible when the burden of the disease is still manageable by currently available treatments. The pre-metastatic niche describes a local tissue microenvironment where changes in chemokine signaling and immune cell recruitment allow for homing to and metastatic colonization of a specific organ site. An emerging approach to detect metastasis at its earliest stages is through the use of an implanted biomaterial scaffold to mimic this pre-metastatic niche and recruit circulating metastatic cells, lessening metastatic burden in organs and allowing for minimally invasive detection at a subcutaneous location. Using inverse spectroscopic optical coherence tomography (ISOCT), a novel optical spectral tomographic imaging technique, changes in nanoscale structure of the scaffold site in mice have been measured and correlated with presence of metastatic disease. This dissertation describes the development of ISOCT for early detection of metastasis via measurement of the scaffold *in vivo* and elucidates the milieu of cancer-associated restructuring effects detected with this technique. Laboratory models of carcinogenesis determined ISOCT sensitivity to both extracellular matrix crosslinking and its subsequent effect on proliferative and structural phenotype of cancer cells. A dual-bandwidth ISOCT benchtop instrument and an ISOCT probe housed in a hypodermic needle were developed to address the

challenge of imaging and measurement of a scaffold through the skin. Studies of scaffold structure determined increased cancer-associated fibrosis, dysregulated angiogenesis, and differences in scaffold-resident cell population and structure to be the prevailing changes in scaffold structure that allow for potential metastasis screening with ISOCT. Separate development and application of partial wave spectroscopic microscopy for gold nanoparticle imaging, tracking, and spectral analysis allowed for spectral classification of gold nanoparticles based on cellular internalization, with potential for future application to enhancing ISOCT contrast. Development of ISOCT measurement techniques and processing algorithms enabled novel application to imaging and measurement of optical, ultrastructural, and chemical properties in living corals.

Acknowledgements

I would like to thank my advisors, Vadim Backman and Lonnie Shea, for their mentorship, guidance, and support throughout my graduate education. Their guidance when needed and environment of independence allowed me to learn so many valuable skills during my time as a student and to grow as a researcher. Their wealth of knowledge and deep insight into the fields of biophotonics and tissue engineering, respectively, were of tremendous help to me in pursuing the many interdisciplinary projects that kept my research so varied and fulfilling – every step of the way I was learning new techniques and research areas, and these experiences will serve me well in future research endeavors. These kinds of cross-disciplinary investigations are a testament to the thriving research environment at Northwestern, and remind me why I chose to pursue my graduate studies here.

I thank my collaborators and committee members for their expertise that always reassured me I would have additional resources to reach out to whenever needed. The exciting projects investigating atherosclerotic plaques and wound healing with the Ameer lab, developing techniques for intrinsic contrast superresolution microscopy with the Zhang and Sun labs, and the incredible experiences studying coral physiology with the Marcelino and Kühl labs were truly enriching and I am thankful for the opportunity to have contributed to these projects.

A big thank you goes to all of the members of the Backman and Shea labs that helped me out along the way. Ji Yi, Samira Azarin, and Andrew Radosevich for their valuable mentorship when I was just getting started with research here at Northwestern, The-Quyen Nguyen, Sebastian Thompson, and Dr. Miao for their senior advice and company during many night shifts in the Silverman dungeon, Scott Young, Xiang Zhou, and Ron Ellis who worked so hard and always had interesting ideas to contribute, and all of my fellow PhD students in the Backman Lab who I have had the pleasure to work alongside and bounce ideas off of – working with Jimmy Winkelmann

and Aya Eid on ISOCT, Wenli Wu, Adam Eshein, Greta Wodarcyk, Luay Almassalha, Yolanda Stypula-Cyrus (and Greg for ice fishing). And David Vanderway for all of his help with cell culture, enjoyable humor in lab, and can-do attitude during endless shrimp at Red Lobster.

I also thank all of the members old and new at the Shea lab and specifically Team tumor – Grace Bushnell for her knowledgeable advice and passion for research, Liam Casey for his canny and unmatchable humor and delivery, Kevin Hughes for surrogate applicancy and making me laugh at work, and everyone who has taught me so much, Daniel Margul, Sophia Orbach, Pridvi Kandagatla, Matt Hall, Aaron Morris, Rohit Maramraju, Dom Smith, Yining Zhang, Joe Decker, and last but not least Eiji Saito for all of his advice and support in planning my next steps.

I also would like to acknowledge my friends Matt Kweon, Hyojun Lee, Sophia Liu, David Chen, and everyone else who always made for the best birthday celebrations whenever we could get together. My friends Julian Rucker and Brandon Perticone for always being down to play catch and my lifting partner Will Bothfeld for all of the enjoyable and much needed time off at the gym and on the beach with Finn. And to the whole Northwestern Cycling Team and the greater Chicago cycling community that helped me to discover and truly enjoy the sport of cycling and all it had to offer. Finally, I would like to thank my family for everything else.

Abbreviations and Notation

2D	Two-dimensional
3D	Three-dimensional
cDNA	Complementary deoxyribonucleic acid
CTC	Circulating tumor cell
ECM	Extracellular matrix
EDTA	Ethylenediaminetetraacetic acid
ESEM	Environmental scanning electron microscopy
FFPE	Formalin-fixed paraffin-embedded
FWHM	Full width at half-maximum
HBSS	Hank's balanced salt solution
HUVEC	Human umbilical vein endothelial cell
IACUC	Institutional Animal Care and Use Committee
ISOCT	Inverse spectroscopic optical coherence tomography
LEBS	Low-coherence enhanced backscattering spectroscopy
LOX	Lysyl oxidase
LOXL4	Lysyl oxidase homolog 4
MMP	Matrix metalloproteinase
NBF	Neutral-buffered formalin
OCT	Optical coherence tomography
OCT (histology)	Optimal cutting temperature [embedding medium]
ORJ	Optical rotary joint
PBS	Phosphate buffered saline
PCL	Polycaprolactone
PIGF	Placental growth factor
PWS	Partial-wave spectroscopic [microscopy]
RMS	Root mean-square [of backscattering spectral intensity in PWS]
RNA	Ribonucleic acid
ROI	Region of interest
RT-qPCR	Quantitative reverse transcription polymerase chain reaction
SEM	Scanning electron microscopy
SEM (statistics)	Standard error of the mean
STFT	Short-time Fourier transform
STORM	Stochastic optical reconstruction microscopy
VEGF	Vascular endothelial growth factor
g	Scattering anisotropy
α	Albedo
μ_t	Total attenuation coefficient
μ_a	Absorption coefficient
μ_s	Scattering coefficient
μ_b	Backscattering coefficient
D	Whittle-Matérn correlation function shape parameter
L_c	Whittle-Matérn correlation function characteristic length
$p(\theta)$	Scattering phase function
k	Wavenumber
λ	Wavelength

Table of Contents

Abstract 3

Acknowledgements 5

Abbreviations and Notation 7

Table of Contents 8

List of Figures 13

Chapter 1: Introduction to the Dissertation 20

1.1. Opening 21

1.2. Contents 21

Chapter 2: Metastasis detection at a synthetic pre-metastatic niche 25

2.1. Abstract 26

2.2. Introduction 27

2.3. The pre-metastatic niche 29

2.4. Metastasis magnet - the synthetic pre-metastatic niche 32

2.5. Optical coherence tomography 35

2.6. Inverse spectroscopic optical coherence tomography 39

2.7. ISOCT applications 44

2.8. Conclusions 46

Chapter 3: Detection of Extracellular Matrix Modification in Cancer Models with Inverse Spectroscopic Optical Coherence Tomography 48

3.1. Abstract 49

3.2. Introduction 50

3.3. Materials and methods 53

3.3.1. Lysyl Oxidase Treated Collagen Gels 53

3.3.2. STORM Imaging and Analysis 53
3.3.3. Cell Culture 54
3.3.4. WST-1 Proliferation Assay 54
3.3.5. ISOCT Study of Cellular Phenotype 54
3.3.6. Confocal Imaging of HT-29 Colonies on Collagen 56
3.4. Results 56
3.4.1 Ultrastructural study of crosslinked collagen gel 56
3.4.2. Measuring progression of crosslinking with ISOCT 58
3.4.3. Cancer cell phenotype induced by ECM 59
3.4.4. Measuring structural phenotype of cancer cells with ISOCT 60
3.5. Discussion 63
3.6. Supplementary Figures 67
Chapter 4: Development of Inverse Spectroscopic Optical Coherence Tomography for *in situ* imaging of a subcutaneous scaffold implant 69
4.1. Abstract 70
4.2. Introduction 71
4.3. Results 73
4.3.1. Dual band ISOCT instrument 73
4.3.2. Measurement of subcutaneous scaffold with dual band OCT 74
4.3.3. Development of ISOCT needle probe 78
4.4. Discussion 87
4.5. Supplementary figure 89
Chapter 5: Identification of structural changes at a synthetic pre-metastatic niche for label-free screening of early metastasis 90

5.1. Abstract 91

5.2. Introduction 92

5.3. Materials and Methods 94

5.3.1. PCL microsphere preparation 94

5.3.2. Scaffold fabrication 94

5.3.3. Scaffold implantation 94

5.3.4. Tumor inoculation 95

5.3.5. Scaffold retrieval survival surgery 96

5.3.6. Scaffold-derived cell suspensions for ISOCT imaging 97

5.3.7. ISOCT imaging and processing of scaffold-derived cell suspensions 97

5.3.8. ISOCT imaging of fixed scaffolds 98

5.3.9. Hydroxyproline assay 99

5.3.10. Gene expression assay 99

5.3.11. Scaffold histological processing for cryosectioning 100

5.3.12. Histological staining 101

5.3.13. Statistical analysis 101

5.4. Results 102

5.4.1. ISOCT detects metastasis-associated scaffold restructuring 102

5.4.2. Collagen deposition at scaffold increased in tumor-bearing mice . . . 103

5.4.3. Dysregulated angiogenesis in scaffold is associated with metastasis . . . 106

5.4.4. Cells isolated from scaffold show increased *D* 108

5.4.5. Degree of scaffold degradation does not affect *D* 109

5.4.6. ECM-related gene expression at the scaffold 111

5.5. Discussion 114

5.6. Supplementary Figures 122

Chapter 6: Label free localization of nanoparticles in live cancer cells using spectroscopic microscopy 128

6.1. Abstract 129

6.2. Introduction 130

6.3. Materials and Methods 132

6.3.1. Live-cell PWS Instrument 132

6.3.2. AOTF PWS Instrument 132

6.3.3. Cell Culture and Nanoparticle Treatment 133

6.3.4. Data Analysis and Imaging process 133

6.3.5. Temporal dynamic imaging and analysis 134

6.3.6. Preparation of glass slides 134

6.3.7. ESEM Imaging 135

6.4. Results 136

6.4.1. PWS sensitivity to GNPs 136

6.4.2. PWS Instrumentation 138

6.4.3. PWS Analysis 139

6.4.4. PWS measurement of nuclear structural response to GNPs 141

6.4.5. Principal Component Analysis 144

6.5. Discussion 149

6.6. Supplementary Figures 152

Chapter 7: Measuring light scattering and absorption properties of coral tissue and skeleton with Inverse Spectroscopic Optical Coherence Tomography (ISOCT) 154

7.1. Abstract 155

7.2. Introduction 156
7.3. Materials and methods 160
7.3.1. ISOCT instrument 160
7.3.2. OCT system resolution 161
7.3.3. Live coral imaging 162
7.3.4. Light scattering model for ISOCT signal analysis 162
7.3.5. ISOCT signal analysis 166
7.3.6. Validation of μ_t measurement 167
7.3.7. Analysis of microvariability of D 168
7.4. Results 169
7.4.1. ISOCT analysis 169
7.4.2. Mapping properties and chlorophyll *a* surface density 171
7.5. Discussion 179
7.6. Supplementary Figures 185
7.7. Supplementary video captions 185
Chapter 8: Conclusions and Future Directions 186
8.1. Summary 187
8.2. Future directions 188
8.2.1. Elucidate mechanisms of ECM-induced cellular restructuring 188
8.2.2. Further development of ISOCT imaging for scaffold screening 189
8.2.3. Building a clinically-relevant model of detection 192
8.2.4. Extension to other applications of ISOCT 195
References 201
Vita 217

List of Figures

Figure 2.1. ISOCT measurements of PCL scaffolds in mice. (A) Mean *D* values from scaffolds from healthy (N = 14 scaffolds) and tumor-bearing (N = 16 scaffolds) mice ($p < 0.05$, error bars denote s.e.m.). Three-dimensional renderings of scaffolds from (B) healthy and (C) tumor-bearing mice; gray scale image represents OCT intensity and color map overlay represents ISOCT *D* values (scale bar = 200 μm). Adaptation of figure presented in reference[1].

Figure 2.2. Schematic of spectral domain optical coherence tomography. Abbreviations used: BS – beam splitter, M – mirror, GV –galvanometer scanning mirrors, OB – objective, DG – diffraction grating, CCD – charge coupled device array.

Figure 3.1. ISOCT and STORM quantify increases in *D* from collagen crosslinking. STORM images of (A) Control and (B) LOXL4-treated collagen gel samples (scale bar length is 10 μm). (C) *D* values computed from Whittle-Matérn fit of STORM image autocorrelation functions (*$p < 0.01$, N = 4 per bar). (D) *D* values measured with ISOCT from gels prepared in the same manner as those used for STORM imaging (*$p < 0.0001$, N = 30 per bar).

Figure 3.2. ISOCT monitors collagen crosslinking progression. Results of time course experiment designed to measure ultrastructural changes in collagen gel with ISOCT as the gel solidifies and crosslinks. ISOCT non-invasively probes the bulk gel to measure change in *D* compared to initial measurement at 20 minutes (*$p< 0.001$ comparing 20 and 90 minute time points, N = 6 per bar).

Figure 3.3. Cancer cells proliferate more on crosslinked collagen. Results of WST-1 Assay performed on HT-29 and SW620 cell lines cultured on collagen gels to detect proliferative phenotype shift (*$p < 0.001$, N = 24 per bar).

Figure 3.4. Cancer cell *D* increases when cultured on crosslinked collagen. OCT *en face* projection images of HT-29 colonies cultured on top of (A) untreated and (B) LOXL4-treated collagen gels. Scale bar length = 250 μm. (C) Confluency of HT-29 colonies was greater when cultured on collagen gel crosslinked with LOXL4 (*$p < 0.05$, N = 3 per bar). (D) ISOCT *D* values measured from cell colonies of lines HT-29 and SW620 *in situ* on *in vitro* collagen gel (*$p < 0.05$, N = 3 per bar). Cell layers segmented manually to ensure measurement signal taken from cells without interference from collagen.

Figure 3.5. ISOCT provides complementary information to confocal imaging. (A) Confocal fluorescence cross section of live HT-29 cell colonies cultured on collagen gel, nuclei shown in green and collagen shown in red. Scale bar length = 50 μm. (B) Example OCT B-scan of HT-29 colony cultured on top surface of collagen gel. Image brightness is scaled by OCT intensity and color is scaled by ISOCT parameter, *D*. The bright layer near the top of the frame is the HT-29 colony, with the substrate collagen underneath showing as a fainter homogeneous media. Scale bar length = 250 μm.

Figure 3.6. Segmentation of cells from collagen substrate in OCT scans. Example OCT B-scans of HT29 segmentation from collagen substrate. In this B-scan, the top boundary of the 3D

ROI is shown by the red line and the bottom boundary is shown by the green line. In combination with manual lateral segmentation to select cellular colonies in the transverse plane, this segmentation is fairly effective at isolating signal from cells. Scale bar length = 250 μm.

Figure 3.7. Example autocorrelation function fitting from STORM images. (A) Control and (B) LOXL4 treated collagen gel image autocorrelation functions are fitted to the Whittle-Matérn model to determine *D* from STORM measurements.

Figure 4.1. Dual-bandwidth ISOCT instrument used for experiments. Schematic of the apparatus; abbreviations: LP - linear polarizer, PBB - partial beam block, PC – polarization controller, BS – beamsplitter, DM – dichroic mirror, ND – neutral density filter, DC – dispersion compensation plates, IR SLD – infrared superluminescent diode, CMOS – CMOS spectrometer camera.

Figure 4.2. Example Dual-band OCT images of mouse dorsal skin. Side-by-side simultaneously acquired visible (left panel) and infrared (right panel) OCT B-scans clearly demonstrate enhanced resolution in visible compared to enhanced penetration in IR which enables visualization of skeletal muscle through dermis and subcutaneous fat layers. EP: epidermis, DE: dermis, HF: hair follicle, AD: adipose tissue, SM: skeletal muscle. Scale bar length = 0.5 mm.

Figure 4.3. Example Dual-band OCT B-scans of subcutaneous scaffold *in vivo*. Visible (left panels) and infrared (right panels) images of scaffold under mouse skin demonstrating ability of IR channel to reach scaffold in top row. Bottom row: Visualization of scaffold through skin is inconsistent due to morphological variability of fibrous encapsulation and fibrous strata overlying scaffold.

Figure 4.4. Coarse schematic of OCT needle probe apparatus. Two modules under novel development presented here include the optical rotary joint and distal probe optics housed in a hypodermic needle.

Figure 4.5. Visible band optical rotary joint designed and built for ISOCT needle probe. (A) Schematic of rotary joint design, incorporating two visible collimators on kinematic mounts and two mirrors to allow for precise alignment of collimated beam into rotating collimator. (B) Photograph of completed benchtop rotary joint.

Figure 4.6. Schematic of distal needle probe optical assembly.

Figure 4.7. Fusion steps to create distal needle probe optical assembly. (A) Flat-cleaved single mode (SM) fiber and 50 nm gold-coated flat-cleaved end of coreless or multimode fiber. (B) Fusion splice of SM to coreless fiber. (C) Cleaving distal end of coreless fiber to precise length for ball lens formation. (D) Create ball lens with arc fusion splicer program.

Figure 4.8. Example far field spot pattern from fused ball lens (unpolished) in forward-viewing direction. (A) Example image of spot pattern resultant from a length of coreless fiber that is too long, causing multiple propagation modes and chromatic interference fringes in the far-field spot. (B) Example image of spot pattern resultant from asymmetric ball lens formed from poor

centering in splicer. (C) Example image of acceptable far-field symmetric Gaussian-profile spot pattern resultant from appropriate coreless fiber length and symmetric ball lens fusion.

Figure 4.9. Sequence of polishing steps to create side-viewing ball lens. (A) Unpolished ball lens fixed inside hypodermic needle with cyanoacrylate glue. (B-D) Coarse polishing of ball down to angled surface with diameter approaching that of ball (ball diameter ~250 microns). (E-F) Fine polishing of angle surface to optical-quality finish.

Figure 4.10. Characterization of distal optics assembly. (A) Photograph of angle-polished 250 micrometer diameter ball lens. (B) Validation of side-viewing far-field Gaussian spot profile. (C) Measurement of ball lens side view focal length, measured here to be 1.5 mm. (D) Simple scanning set-up to image paper barcode target. (E) photograph of illuminated probe optics demonstrating diffuse reflection from internal reference interface.

Figure 4.11. Infrared OCT channel produces >twofold increase in penetration depth in skin. Dual band OCT B-scans of depilated mouse ear in (A) visible 520 nm-centered window and (B) IR 1300 nm-centered window (scale bar length 100 micrometers). Penetration depth calculated by depth at which signal decays to 5% of maximum intensity, shown in (C) and (D) for visible and IR bands, respectively. Calculated penetration limits were 240 microns in visible and 570 microns in IR. Figure adapted with permission from reference[2].

Figure 5.1. ISOCT detects changes in scaffold structure associated with cancer. (A) Flowchart for ISOCT animal experiment. (B) Average ISOCT *D* values of scaffolds from healthy (N = 71 regions) and tumor-bearing mice (N = 71 regions), (*$p < 0.01$).

Figure 5.2. Increased fibrosis is observed in scaffolds from tumor-bearing mice. Example histology images of Masson's trichrome-stained scaffold sections showing relatively (A) low and (B) high levels of collagen (blue staining) deposition in the scaffold. (C) Higher collagen deposition observed in scaffolds from tumor-bearing mice (N = 12 scaffolds) compared to healthy control (N = 11 scaffolds) 28 days after tumor inoculation/mock inoculation (*$p < 0.05$).

Figure 5.3. Hydroxyproline assay quantifies early fibrotic changes at the scaffold. Hydroxyproline content of scaffolds (weight % of scaffold dry mass) from healthy and tumor-bearing (Cancer) mice 0, 7, and 14 days post-tumor inoculation. N = 4 (Healthy) and N = 6 (Cancer) animals/scaffolds per bar.

Figure 5.4. Scaffold vasculature changes characterized with CD31+ IHC staining. (A) Example CD31+ IHC-stained (brown) scaffold section with hematoxylin staining nuclei (dark blue). (B-D) Vasculature metrics obtained from deep-learning segmentation of vessels from scaffold sections (*$p < 0.01$, **$p < 0.05$).

Figure 5.5. Results from ISOCT measurement of scaffold-derived cells resuspended in collagen gel. (A) Volume percentage of gel sample occupied by cells extracted from scaffold. (B) Average *D* value of 3D segmented cells in gel, measured with ISOCT (*$p < 0.05$).

Figure 5.6. Scaffold degradation does not lead to significant change in *D* measured with ISOCT. Representative ESEM micrograph of (A) untreated and (B) partially degraded scaffolds.

(C) ISOCT-measured *D* from scaffolds as a function of degradation showed no significant change as scaffolds degrade.

Figure 5.7. Measurements of ECM-related gene expression at the scaffold in healthy and tumor-bearing (cancer) mice using RT-qPCR. (A) Gene expression heatmap showing $\log_2$(fold-change) of normalized gene expression in comparison to global expression from scaffolds in healthy animals for all genes measured (Col1a1, Col3a1, Col4a1, Fn1, Lox, TIMP-1, CTGF, MMP-2, MMP-9, LGALS3, VCAN) at days 0, 7, and 14 post-inoculation. (B-E) comparison of relative expression of COL1A1, COL3A1, COL4A1, and TIMP1, respectively, between scaffolds from healthy and tumor-bearing mice 0- and 14-days post-tumor inoculation (*$p < 0.005$, **$p < 0.05$).

Figure 5.8. Standard calibration curve for hydroxyproline assay. All measured absorbances at 555 nm from sample wells fell within this linear range of the calibration curve with R^2 of 0.999. Calibration equation used for hydroxyproline content: $Mass_{hydroxyproline}(micrograms) = (A_{555} - 0.0654)/0.04612$.

Figure 5.9. Representative OCT B-scans of subcutaneous PCL scaffolds in Balb/c mice from (A) visible (544-678 nm) and (B) infrared (1225-1375 nm) channels. Arrows in (A) point to epidermis, dermis, subcutaneous fat, and scaffold with increasing depth.

Figure 5.10. Processing of Masson's trichrome images to determine proportional collagen coverage. (A) Original RGB image of scaffold with manually segmented region of interest. (B) Gray scale image of (A). (C) Masked (A) based on intensity threshold applied to (B). (D) Masked from RGB image where blue value above threshold and red value below threshold. Proportional collagen coverage calculated as nonzero area of (D) divided by nonzero area of (C).

Figure 5.11. Collagen distribution in scaffold is concentrated at the peripheral fibrous capsule. (A) Masson's trichrome stain of scaffold section through center of scaffold, showing collagen deposition (blue) heavily on margins of scaffold. (B) Picrosirius red staining with cross-polarization microscopy of an adjacent slice of the scaffold shown in (A), demonstrating highly birefringent fibrous encapsulation of scaffold.

Figure 5.12. Deep-learning based segmentation of vessels from CD31+ IHC stained sections. (A) Original microscopy image of CD31+ IHC stain (brown) with hematoxylin staining for nuclei (blue). (B) Segmentation confidence map output from trained convolutional neural network scaled from 0 (black) to 1 (white) where 1 represents full certainty that the region is a vessel. (C) Resultant binary ROI mask from adaptive thresholding of confidence map in (B). (D) Binary mask after morphological closure of segmented regions in (C). (E) Final binary vessel mask achieved from removing small objects and subsequent morphological closure of segmented structures.

Figure 5.13. Live-cell PWS quantifies change in endothelial nuclear structure associated with VEGF. (A) Example map of RMS values from live HUVECs. (B) Mean RMS values from HUVEC nuclei show increase in RMS associated with VEGF treatment ($p < 0.001$).

Figure 5.14. Autocorrelation analysis of ESEM-images of scaffolds independently measures *D*. (A) ESEM micrograph of scaffold surface showing surface structure. (B) Example autocorrelation function of ESEM image along with corresponding fit from Whittle-Matérn function. (C) Average *D* values calculated from autocorrelation analysis of scaffold ESEM micrographs reveal no significant difference between fresh and degraded scaffolds.

Figure 6.1. PWS microscopy images GNP clusters. (A) BFRI interference image (B) ESEM image of the same view of aggregated GNPs deposited on glass slide (scale bar = 5 μm). (C) Normalized scattering spectra from GNP clusters labeled 1, 2, and 3 measured with PWS. (D) Magnification of the GNP cluster 2 where a proximal salt crystal is also observed (scale bar = 0.45 μm). In this figure, it can be appreciated how PWS is capable of differentiating between GNPs and salt crystals.

Figure 6.2. Schematic of Live-cell PWS instrument used for imaging experiments. Light emitted from an LED source is focused in the cell sample, after which scattered and reflected signal interferes and is spectrally resolved by a tunable filter before acquisition (LED: light emitting diode, LCTF: liquid crystal tunable filter, CMOS: complementary metal-oxide-semiconductor).

Figure 6.3. Spectral analysis enhances GNP contrast in microscopy image. Images of GNPs incubated with HeLa cells derived from (A) BFRI and (B) PWS RMS parameter. Contrast of GNPs compared with surrounding field is enhanced in RMS map compared to BFRI (C). PWS RMS map typically plotted in color scaled to magnitude of RMS value used to quantify cellular structure (D).

Figure 6.4. GNPs induce changes in nuclear structure and temporal dynamics. Live-cell PWS kymograph (x axis cross-sectional position across cell nucleus and y-axis time) shows temporal dynamics of chromatin structure in HeLa cells incubated (A) without and (B) with GNPs. Variance of normalized RMS along the temporal dimension confirms fewer dynamic changes in cells incubated with GNPs. Scale bar length = 5 μm. (C) RMS from live HeLa nuclei (n=252 control, n=214 GNP treated) measured with live-cell PWS quantifies nuclear structure, showing HeLa cells incubated with GNPs have a small but significant decrease in nuclear RMS. (D) Temporal variance of nuclear RMS in Hela cells in media +- GNPs indicates a significantly decreased nuclear motion associated with GNP treatment (*$p < 0.001$, **$p < 0.01$).

Figure 6.5. GNP spectral shift is associated with internalization. Averaged scattering spectra from GNPs inside and outside live HeLa cells, along with mean spectra from GNP-free regions of cell and glass slide. We observe a distinct shift in the spectral scattering peak when comparing internalized GNPs to those remaining outside of cells. This distinct shift is present due to interaction between GNPs and cytoplasmic protein and GNR aggregation.

Figure 6.6. Principal component analysis characterizes GNP scattering spectra. Principal component spectra for the first 3 principal components of GNP scattering spectra (A). GNP scattering spectral signal explained well by the first 3 principal components, after which subsequent components each contribute less than 7% to the total spectral shape (B).

Figure 6.7. Image of HeLa cells incubated with GNPs (bright specks). GNPs color-coded by score of the first spectral principal component (PC 1).

Figure 6.8. 3D scatter plot of principal component scores (P_1, P_2, and P_3, respectively) for each GNP location. GNPs inside cells show tighter clustering of principal component scores than GNPs outside of cells.

Figure 6.9. Confirmation of structures in ESEM images. ESEM images of GNP cluster surrounded by salt crystals (A) before and (B) after electron beam bombardment confirms distinct composition of bright structures in the image. Salt crystals bombarded by the electron beam quickly disappear whereas GNPs remain on the glass slide.

Figure 6.10. UV-Vis absorption spectrum of stock GNP suspension used for these studies.

Figure 7.1. Changes in *D* affect light scattering behavior. (A) Shape of scattering phase function, $p(\theta)$, for D values ranging from 1-5. Simulated phase function incorporates correlation length l_c of 50 nm and wavelength of 600 nm in the absence of absorption. (B) Surface plot shows behavior of scattering coefficient with respect to changes in D and g in the Born approximation as characterized theoretically in a previously reported derivation[3].

Figure 7.2. Flowchart for ISOCT data processing. Processing starts with the acquisition of the OCT volume and detection of surfaces of tissue and skeleton. From a short-time Fourier transform, the spectral cube is generated and wavelength-dependent backscattering and attenuation coefficients are computed. Fractal dimension D is fit from μ_b, and the μ_s spectral shape and scaling factors for μ_a and μ_s are also fit. Finally, the wavelength-dependent (g) is computed from the albedo (α) and D.

Figure 7.3. Example rendering of ISOCT data from *Merulina ampliata*. Photograph of live coral measured shown on left, with box demarcating region scanned. 3-D volumetric rendering of OCT scan volume shown on right, with traditional OCT image intensity shown in grayscale with 3-D overlay of local D value in color. Rendering box is 2.56x2.56x1.5 mm.

Figure 7.4. Top-down projection maps of optical and structural properties. Photographs of *Merulina ampliata* (A1) and *Diploastrea heliopora* (A2) with box demarcating region scanned with ISOCT. *En face* projection maps of total attenuation coefficient μ_t (B1, B2), chlorophyll *a* concentration (C1, C2), and D value (D1, D2) for *Merulina* and *Diploastrea*, respectively. Maps B1, C1, and D1 are 2.56 x 2.56 mm; maps B2, C2, and D2 are 1.85 x 1.85 mm.

Figure 7.5. Quantifying scattering anisotropy in coral. Histograms of scattering anisotropy g from tissue and skeleton of *Merulina ampliata* and *Diploastrea heliopora*. Projection map of g from tissue layer of *Merulina ampliata* (right).

Figure 7.6. Optical and structural property maps from coral skeletons. *En face* projection maps of μ_t, Chlorophyll A density, and D for visible skeletal ridges from *Merulina ampliata* (top row) and *Diploastrea heliopora* (bottom row).

Figure 7.7. Histograms of *D* values from tissue and skeletal compartments of *Merulina ampliata* and *Diploastrea heliopora*. Frequency plotted reflects likelihood of a 5 x 5 μm pixel having a given D value.

Figure 7.8. Spatial microvariability of *D* in coral far exceeds the noise floor. 2D maps of *D* from (A) 80 nm polystyrene beads suspension and (B) *Merulina ampliata* tissue. (C) Spatial variance comparison between *D* value maps from a homogenous sample of 80 nm polystyrene beads and *Merulina ampliata* tissue. (D) Histogram of *D* values from maps in (A) and (B).

Figure 7.9. Spatial resolution of OCT system. Quantification of spatial resolution of visible OCT system used in lateral (A) and axial (B) directions.

Figure 7.10. Validation of total attenuation coefficient measurement. Experimental (red series) comparison with Mie theory (blue line) for samples of 200 nm polystyrene spheres of varying concentrations (0.1-1.0 wt%).

Figure 7.11. *Diploastrea heliopora* imaged with dual-band ISOCT. (A) Photograph of live coral with 2.8x2.8 mm OCT scan region demarcated by salmon box. OCT B-scans show depth section through tissue layer down to underlying skeleton. Complementary strengths of high spatial resolution of visible channel (B) and penetration depth of infrared channel (C) shown in side-by-side B-scans taken from cross-section shown by green line in (A).

Chapter 1:

Introduction to the Dissertation

1.1. Opening

Despite significant advances in clinical treatments and biological understanding of cancer since the inception of the National Cancer Act of 1971, cancer remains the second leading cause of death in the United States and worldwide, with metastatic spread of the disease responsible for over 90% of cancer-related deaths. Detection of cancer metastasis at its earliest stages is important for ensuring effective treatment while disease burden is low, but in practice there are currently no accepted techniques for early staging of metastasis before it has taken root in vital organs. The research presented in this dissertation advances a transformative approach to early metastasis detection that marries the fields of cancer biology, biomaterials, and biophotonics, with particular focus on the development and application of novel optical imaging technologies to catch metastasis at its earliest stage.

1.2. Contents

Chapter 1 introduces the dissertation with an overview of the research fields contained within. A brief description is given of the motivation and background of the main project covered, metastasis detection at a synthetic pre-metastatic niche.

Chapter 2 summarizes the current state of the art for the several research fields involved in the main motivation for the dissertation and provides the intellectual framework for the research presented in following chapters 3-5. An overview of the current clinical standard of care for breast cancer screening after treatment and a description of the leading techniques for cancer staging from blood samples is followed by a review of the idea of a pre-metastatic niche that is required for successful metastasis to take hold in a distant organ. Then, a brief review of biomaterial-based strategies for the creation of a simulant pre-metastatic niche is given along with results showing that this approach, paired with a new optical imaging modality, inverse spectroscopic optical

coherence tomography (ISOCT) can be used for detection of metastatic cancer. The chapter finishes with a description and background of optical coherence tomography (OCT) and ISOCT, with a brief review of current and future applications of this technique.

Chapter 3 presents the results of a study implementing the central technique employed and developed through the dissertation, ISOCT for the study of cellular-extracellular matrix interactions in cell-line models of primary and metastatic colon cancer. The central goals of this study were determination of ISOCT sensitivity to enzymatic crosslinking of a collagen proteins, which was validated with imaging analysis from superresolution microscopy. This study further explores how a crosslinked extracellular matrix effects both the proliferative phenotype and averaged nanoscale structure of cancer cells growing within. This chapter establishes ISOCT to be sensitive to both extracellular (collagen crosslinking) and intracellular structural modification in cell line models of cancer progression.

Chapter 4 provides an overview of the instrumentation approaches developed to extend ISOCT imaging to non-invasive imaging of a scaffold that is implanted beneath the skin. Development of a dual-bandwidth OCT system is described along with conclusions regarding its applicability for scaffold imaging *in vivo*. Design and fabrication of a novel ISOCT imaging probe encased in a hypodermic needle for transcutaneous scaffold imaging is presented. This chapter shows how the inherent resolution-penetration trade-off present in OCT imaging can be addressed by implementing a dual-band scheme and introduces a novel visible-bandwidth OCT needle probe.

Chapter 5 explores the potential structural modifications occurring at the scaffold that are uniquely associated with metastatic cancer. The goal of this study was to elucidate the primary remodeling effects that lead to previously and currently observed increases in scaffold mass fractal dimension that are associated with metastatic disease. *In vitro* modeling of ISOCT sensitivity to scaffold degradation found that degree of degradation does not affect the measured fractal

dimension, which was validated with nanoscale surface texture analysis by scanning electron microscopy. However, this study does show an increase in scaffold collagen deposition associated with progression of metastatic disease, as well as increases in blood vessel size, CD31+ staining area, and scaffold-derived cell volume and fractal dimension that are associated with metastasis in this mouse model. This study presents findings suggesting that a combination of mass-density restructuring at the subcellular and extracellular levels in the scaffold accompany systemic metastasis through differentially-regulated mechanisms that are under continued investigation.

Chapter 6 reports a study that is separate from previous chapters, which demonstrates the use of a sister technique of ISOCT, partial wave spectroscopic (PWS) microscopy, for the spectra analysis of gold nanoparticles in live cancer cells. PWS has been demonstrated for the measurement of subcellular macromolecular distribution, in particular the fractal dimension of chromatin in the nucleus of cells, which in this study provides an enhanced contrast mechanism for gold nanoparticles in cells and is used to track the effect of nanoparticles on cellular chromatin structure and dynamics. A novel development of analysis of hyperspectral scattering signature from gold nanoparticles incorporating a principle components approach is presented and shown to indicate differences in scattering spectra based on internalization of nanoparticles by cells.

Chapter 7 describes the development and implementation of a novel ISOCT analysis for the imaging characterization of optical, structural, and chemical properties of living corals. This novel application of optical coherence tomography provides important insight an independent measurement of a comprehensive suite of parameters that govern light transport and harvest by the symbiotic algae that reside within coral and provide photosynthetic energy to the host coral animal. The novel analysis algorithms and approach developed for this application will be of further use in a more comprehensive study of conserved coral physiology and mechanisms of light harvest developed through evolution, and for other potential applications in biomedical imaging.

Chapter 8 concludes the dissertation and discusses prospective directions for the work presented.

Chapter 2:

Metastasis detection at a synthetic pre-metastatic niche

2.1. Abstract

Cancer is the second leading cause of death in the US, with metastasis accounting for over 90% of mortality in cancer patients. The importance of early detection of metastasis in ensuring favorable patient outcome has led to the development of "liquid biopsy" strategies for cancer screening from blood. Another strategy exploits the concept of the pre-metastatic niche to concentrate circulating tumor cells at a biomaterial implant that can be studied for mechanistic insights into metastasis biology or imaging-based screening to confirm presence of circulating metastasis. Optical coherence tomography is a 3D light-based imaging modality that has been used for the detection of metastasis by measurement of these biomaterial implants in mouse models of metastatic cancer. In this chapter, we will provide a broad review of the clinical relevance of cancer metastasis screening, the emerging picture of the pre-metastatic niche in cancer biology and how biomaterial implants have been used to mimic the niche *in vivo*, and describe the principles and applications of optical coherence tomography imaging with focus on a recent extension of the technique that permits the statistical measurement of the nanoscale structural character of tissue.

2.2. Introduction

Tremendous increases in government-sponsored cancer research brought on by President Nixon's "War on Cancer" and the passage of the National Cancer Act of 1971 have allowed for impressive advances in our understanding of cancer biology and available treatments, but cancer remains today the second most common cause of death in the United States[4]. The spread of cancer cells from a primary tumor to colonize distant tissues, referred to as metastasis or stage IV cancer, is a constant concern for affected patients and rightly so. The ultimate cause of death in 90% of solid tumor cancers is due to metastasis that is resistant to currently available therapies[5]. Therefore great motivation exists to understand the mechanistic progression of cancer from a primary tumor to stage IV metastatic disease so that therapeutic strategies may be developed to stop this deadly process. It is commonly accepted amongst clinicians that as metastatic disease becomes more advanced, resulting in more and larger tumors that colonize vital organs, patient prognosis is greatly diminished. If the disease can be caught early, in many cases, available treatment will lead to better outcomes.

Breast cancer is currently the second leading cause of cancer deaths in women, and the most common cancer diagnosed in women[4,6]. Current screening guidelines for breast cancer recommend yearly mammograms for women between the ages of 45 and 54, with additional MRI screening recommended for particular susceptible patients[7]. These screening strategies are effective at detecting cancers while still at an early stage; between 5 and 10% of newly diagnosed breast cancers are metastatic[8]. To accurately stage breast cancer progression after treatment of the primary neoplasm, axillary sentinel node biopsies are taken to detect whether tumor cells have spread past the primary site. However, while this is an effective test to determine treatment options, up to 30% patients with node-negative biopsies will have recurrence of the cancer past primary tumor removal surgery[8]. The current standard of care does not recommend routine imaging scans

for evaluation of metastatic disease in the asymptomatic population after primary tumor resection[9]. Clinical studies evaluating the use of routine chest x-ray, bone scan, and liver echography, following primary tumor resection found no significant increase in patient survival when compared to routine physical examination without the use of these imaging techniques for metastatic tumor detection[10–14]. Therefore the added risks and expense of full-body imaging with conventional clinically available modalities preclude the use of intensive non-specific imaging for breast cancer metastasis detection and staging in the general population of primary cancer survivors[15]. Although more recently introduced multimodal imaging techniques for breast cancer surveillance such as digital breast tomosynthesis and near-infrared spectroscopy may improve outcomes, they are still investigational and not suitable for detection of disseminated metastasis throughout the body[16–18].

In general, metastatic disease is not detected until distal tumors have already formed and grown to an anatomically significant size, leading to symptomatic response or large enough to be detected with CT, PET, or MRI scans (~ 5 mm) during elective surveillance imaging. By this point, the metastatic cancer has typically reached a point where it is difficult to treat due to advanced progression and unmanageable burden of disease. In addition, CT and MRI scans are expensive, time-consuming, and in the case of CT, expose the patient to possibly harmful ionizing radiation. Therefore, there is considered to be an unmet clinical need for novel strategies to detect metastatic progression at its earliest stages when treatment has the greatest chances of success, resulting in a substantial impact in medicine and human health.

Much research effort is currently devoted to this problem, with many approaches focusing on testing patient blood samples i.e. "liquid biopsy" for presence of circulating tumor cells (CTCs) or cancer-secreted exosomes that may provide diagnostic information[19–26]. Development of clinically feasible technologies to screen bodily fluids for CTCs, however, is not without major challenges. In addition to the specificity required for CTC separation from the abundance of

erythrocytes and leukocytes in blood, the precise risks presented by different populations of CTCs are not fully understood, especially considering longstanding observations of a high degree of metastatic heterogeneity among disseminated tumor cells[27,28]. In a study tracking CTC potential for metastatic colonization, less than 0.1% of CTCs were able to establish a distal lesion[29]. Furthermore, the sparseness of CTCs in all but the most advanced stages of cancer (on the order of ~1 cell per mL of blood[24]) require sampling of large amounts of blood to ensure CTCs, if present, will be sampled and detected; the metric of CTC number density may be indicative of late-stage treatment efficacy but not useful for early staging of metastatic progression[24,26]. Therefore, while CTC capture techniques for early staging of metastatic cancer could provide valuable information about CTC populations and cancer staging, feasibility constraints of this approach encourage the development of alternative strategies for early metastatic detection and development of prognostic markers. Similar development of a liquid biopsies for analysis of tumor-derived exosomes and circulating tumor DNA have the potential to provide life-saving molecular information of patient-specific cancer phenotypes and drug resistances, but inherent heterogeneity in exosome populations[30] and unknown mutations in circulating tumor DNA and difficulty in interpreting relevant biomarkers from detected DNA limit their current potential to improve patient survival. Nevertheless, there remains definite clinical need for similarly non-invasive translatable techniques for early staging of metastasis with the potential to extend patient survival and improve quality of life.

2.3. The pre-metastatic niche

Cancer metastasis from a primary solid tumor follows a predictable sequence: proliferation and neovascularization in a primary tumor, epithelial-mesenchymal transition of tumor cells, invasion of the basement membrane enabling intravasation in to the (lymphatic or hematogenous)

circulatory system, survival in circulation, metastatic homing to amenable sites, extravasation across the basement membrane, and colonization of a distal metastatic site[31–34]. When this colonization is successful, cellular proliferation and angiogenesis lead to growth of metastases to a size where they are clinically detectable. The homing step in this sequence is far from random, as first reported by Stephen Paget in his seminal seed and soil hypothesis[35]. Paget described how individual cancer cells circulating throughout the body could each form a distant metastasis, so long as they would "fall on congenial soil". While at the time Paget discounted the scientific opinion that the primary tumor has a "seminal influence" upon distant metastatic sites, recent work has shown bone marrow-derived hematopoietic progenitor cells (HPCs) recruited by the primary tumor-derived secreted factors (TDSFs) to be a main player in the pre-metastatic conditioning that creates the fertile soil for metastatic homing[36,37]. This conditioning results in the formation of a pre-metastatic niche, study of which has potential to prevent niche formation and subsequent metastatic homing and colonization[38].

The significance of the concept of a pre-metastatic niche has been more widely appreciated in the field of cancer biology in recent years[39]. The secretion of exosomes, or nano-scale extracellular vesicles capable of delivering molecular cargo including signaling molecules, proteins, lipids, and genetic material, microvesicles, and recently recognized large oncosomes from the primary tumor is implicated in a wide range of processes responsible for homing to and preparation of the pre-metastatic niche[39–41]. Inter-organ migration of natural killer (NK) cells was shown to affect reconditioning of the host organ microenvironment before arrival of metastases, facilitating regulation of anti-metastatic potential by elimination of fibrinogen at the pre-metastatic site and pro-metastatic potential mediated by NK secretion of interferon-gamma[42]. HPCs are recruited from bone marrow by a host of TSDFs including vascular endothelial growth factor (VEGF), placental growth factor (PIGF), and inflammatory chemokines[36,43]. In a mouse model of

colorectal cancer, tissue inhibitor of metalloproteinase 1 (TIMP-1) was found to increase liver susceptibility to metastases; systemic upregulation of TIMP-1 had the effect of increasing expression of stromal cell-derived factor 1 (SDF1) in the liver which recruited neutrophils, thereby tuning and creating a pre-metastatic niche in the liver[44]. This effect and subsequent hepatic metastasis was abrogated by inhibition of neutrophil recruitment, implicating this cell population in creating the pre-metastatic niche in this mouse model[44]. In a separate mouse model of spontaneous metastatic pancreatic cancer, primary tumor-derived exosomes carrying macrophage migration inhibitory factor that arrived at the liver stimulated transforming growth factor beta and fibronectin production in resident Kupffer cells, a specialized hepatic macrophage[45]. The enhanced fibrotic microenvironment at this had the effect of recruiting bone marrow-derived macrophages which further effected the local microenvironment into a suitable pre-metastatic niche[45]. Primary-tumor secreted factors from a metastatic lung cancer line were found to activate macrophages by way of toll-like receptors, leading to an inflammatory microenvironment and production of tumor necrosis factor alpha and interleukin 6[46]. Specifically, the ECM proteoglycan versican was uniquely identified in activation of macrophages in the pre-metastatic niche by activating toll-like receptor complexes and tumor necrosis factor alpha secretion, a step required for metastatic growth in this model[46]. While inflammatory processes at the primary tumor are well-understood to potentiate the spread of metastasis, the novel identification of these and other inflammatory mediators such as S100A8 and S100A9 in the pre-metastatic niche[47] are of direct interest for strategies to prevent or recapitulate niche formation.

The TDSF lysyl oxidase (LOX), an enzyme responsible for crosslinking collagen and elastin in the extracellular matrix (ECM), accumulates at the pre-metastatic niche along with fibronectin, leading to crosslinking and remodeling of the niche microenvironment that aids in metastatic extravasation[48,49]. Lysyl oxidase expression has been implicated as a key mediator of

not only BDMC recruitment to the niche, but also as a highly expressed protein in the pre-metastatic niche, along with fibronectin[50,49]. After metastatic cells have arrived at the niche, TDSFs such as VEGF and PIGF recruit endothelial progenitor cells to the new micrometastases, and further stimulate angiogenesis through endocrine stimulation. The resultant angiogenesis in nascent metastatic foci allows for growth of the these micrometastases to sizes greater than the diffusion-limited radius (~1 mm), allowing for progression to lethal macrometastases in the host organ[36,51]. A well-established effect of VEGF signaling in endothelial cells is an increase in intracellular calcium concentration, which has been shown to increase chromatin condensation in the nucleus of HeLa cells[52,53]. Other effects of mechanotransduction along the ECM-chromatin axis are hypothesized to influence nuclear and cytoskeletal structure in tumor cells[54]. Together, these processes serve to create a distinct local tissue microenvironment in a potential host organ with distinct structural features at the extracellular, vascular, and subcellular levels.

2.4. Metastasis magnet - the synthetic pre-metastatic niche

Based on the observation that a pre-metastatic niche must form in an organ to allow for metastatic colonization and progression, an emerging approach to mimic the pre-metastatic niche is being developed which uses a biomaterial implant to attract and capture circulating metastatic cells that could otherwise develop into metastases in a vital organ, for potential applications in basic metastasis research or clinical theranostics. A variety of biomaterials have been employed for this purpose, such as biocompatible degradable polymers poly(lactide-co-glycolide) (PLG), poly(ε-caprolactone) (PCL), Poly-L-lactic acid (PLA), polyurethane, and polyallylamine, or other natural materials such as bone grafts, silk, purified collagen gel, or decellularized ECM from host organs[55]. When fabricated into porous scaffolds, these materials integrate into the host tissues in the body through adhesion, neovascularization, and gradual incorporation and degradation through

natural processes. After implantation, the intrinsic foreign body response takes effect to varying degrees dependent upon the implantation site, material, form, and potential delivery of factors to facilitate biocompatibility[56,57]. Furthermore, these implanted scaffolds present an opportunity to create pre-defined sites in the body that are specifically engineered to recapitulate the secreted factors and microenvironment of a native pre-metastatic niche through bioactive modifications or controlled delivery of chemokines and other factors[55,58,59]. Coating of scaffolds with ECM proteins fibronectin and collagen IV increased tumor cell accumulation in the scaffold, indicating effective functionalization of polymer surfaces may better re-capitulate a native niche in the body[59]. Proteomics screening of differentially-expressed proteins in native metastatic sites identified myeloperoxidase as a potential contributing factor to metastatic colonization which was confirmed by increased CTC recruitment at scaffolds coated with myeloperoxidase[59]. Therefore, the functional engineering of scaffold mimics of the pre-metastatic niche provides an exciting avenue for mechanistic investigation of metastasis and practical implementation for CTC capture and detection strategies.

However, the prevailing intrinsic foreign body response to bare PLG and PCL implants has been shown to create a synthetic pre-metastatic niche in the body that successfully attracts CTCs from the primary tumor in the absence of any surface modification[1,60]; these attracted cells were also shown to mirror populations of disseminated tumor cells in a native lung metastatic niche[61]. The ability of synthetic pre-metastatic niche scaffolds to concentrate circulating tumor cells has also enabled a variety of *in vitro* spheroid assay, chemotherapeutic response, and other mechanistic studies that previously were infeasible due to natural sparsity of this rare cell population in circulation[62–64]. In particular, the development of a composite approach harnessing the CTC capture capability of scaffold mimics and genome sequencing with personalized *in vitro* drug testing is an exciting frontier in precision medicine approaches to cancer treatment.

Scaffolds have also been used as mimics of the pre-metastatic niche in mouse models of breast cancer. When implanted in the peritoneal fat pad, a porous PLG scaffold was shown to reduce burden of metastatic lung tumors in immunodeficient mice injected with 231BR human metastatic breast carcinoma cells in the mammary fat pad[60]. Furthermore, significant recruitment of metastatic cells to the scaffold occurred despite the fact that 231BR cells do not normally metastasize to the peritoneal fat pat. These results indicate the scaffold implant decreases metastatic burden in the mouse by removing metastatic cells from circulation and preventing their proliferation in the lung[60].

In addition to lessening metastatic spread, the scaffold has shown promise as a sentinel site for early detection of metastasis. Label-free imaging with inverse spectroscopic optical coherence tomography (ISOCT), an emerging nanoscale-sensitive optical measurement technique discussed in section 2.6, showed a significantly higher value of ISOCT structural parameter *D* from scaffolds in tumor-bearing mice when compared with control animals[17]. Recruitment of metastatic cells to the scaffold was significant regardless of whether the scaffold was implanted in the peritoneal fat or the dorsal subcutaneous space[60]. This result indicates the scaffold can be implanted subcutaneously to allow for minimally invasive ISOCT measurement of the scaffold to monitor for metastatic progression in the clinic.

To facilitate translation of this scaffold technology to the clinical setting, PCL scaffolds with a slower rate of degradation *in vivo* were developed to allow for longer periods of scaffold monitoring after implantation[1]. In a follow-up study where these PCL scaffolds were implanted subcutaneously in BALB/c mice, the scaffold implant site was allowed to heal for 28 days, after which a subset of mice were inoculated with 231BR cells to induce metastatic breast cancer. After an additional 5 days, mice were sacrificed, and scaffolds were exposed by making an incision in the dorsal skin to allow for ISOCT measurement. In this study, we observed a significantly higher

D value from PCL scaffolds in tumor-bearing mice compared to the healthy control group, as is shown in figure 1[1]. These studies suggest ISOCT as a promising technique for measuring changes in the scaffold associated with metastatic disease.

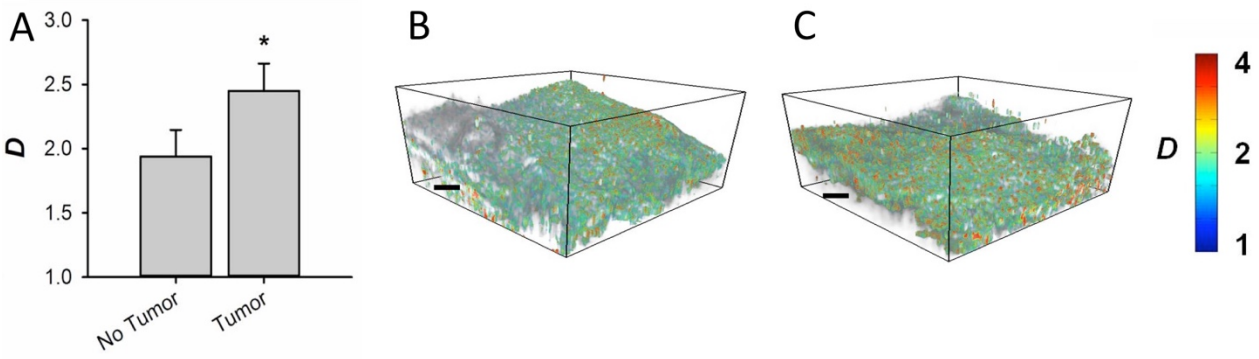

Figure 2.1. ISOCT measurements of PCL scaffolds in mice. (A) Mean *D* values from scaffolds from healthy (N = 14 scaffolds) and tumor-bearing (N = 16 scaffolds) mice ($p < 0.05$, error bars denote s.e.m.). Three-dimensional renderings of scaffolds from (B) healthy and (C) tumor-bearing mice; gray scale image represents OCT intensity and color map overlay represents ISOCT *D* values (scale bar = 200 μm). Adaptation of figure presented in reference[1].

2.5. Optical coherence tomography

Widely considered to be an optical analog of ultrasound imaging, Optical Coherence Tomography (OCT) is a 3D tomographic optical imaging technique first developed by the Fujimoto Lab at MIT in 1991[65]. OCT utilizes the interference of low-coherence illumination between a sample and reference beam to produce tomographic slices representative of the sample's spatial backscattering intensity profile with typical resolution on the order of several micrometers and imaging depth on the order of a millimeter. By imaging the backscattering nature of various

thick tissues, OCT provides important structural information that is complementary to other biomedical imaging techniques such as ultrasound, x-ray, histology (wide field microscopy), and video endoscopy. In particular, OCT has found great utility in the field of ophthalmology, where the transparency of the vitreous humor allows for direct imaging of the layered structure of the retina allowing for diagnosis of various conditions such as macular degeneration, glaucoma, diabetic retinopathy, among others[66]. It is this unparalleled imaging performance that, despite its recent invention, has enabled OCT to be rapidly implemented in the clinic where it is currently a screening standard of care in the United States for most retinal conditions. OCT has also been implemented for clinical use in the fields of cardiology, dentistry, oncology, gastroenterology, and dermatology; with current rapid advances in the development and implementation of OCT into an expanding field of biomedical applications, today can be thought of as the "epoch of OCT"[67].

While OCT originally utilized scanning of the reference arm position to sweep through different depths in the sample, known as spatial domain OCT, Spectral Domain OCT (SD-OCT), also known as Fourier Domain OCT (FD-OCT) has come into prominence due to its enhanced speed of imaging (no reference arm scanning is necessary) and higher sensitivity[68]. Two main configurations of OCT operating in Fourier Domain are currently in use: those using a broadband light source for sample illumination and a spectrometer for full spectral acquisition at a single time point (SD-OCT) and those using a fast switching "swept-source" laser which probes the sample with narrow bandwidth highly coherent light that temporally oscillates its central wavelength and collects signal at a photodiode (SS-OCT). Current advances in swept-source laser technology have increased the adoption of SS-OCT due to its potential for faster imaging and higher imaging depth[69]. This imaging depth, also referred to as sensitivity roll-off in FD-OCT, is governed by the spectral resolution of interference spectrum acquisition technique. For spectrometer-based SD-OCT, this spectral resolution depends on the camera pixel size, grating performance, constraints

of optical focusing on the array, and interpixel cross-talk[70]. For SS-OCT, this spectral resolution is governed by the spectral line width of the swept source and the clocking frequency of the photodetector which is not a limiting parameter.

In spectrometer-based SD-OCT, henceforth simply referred to as OCT, the interference spectrum resulting from the coherent interference of backward reflected illumination from sample and reference arms is sent to a spectrometer for acquisition. A simple schematic of this is shown in figure 2.

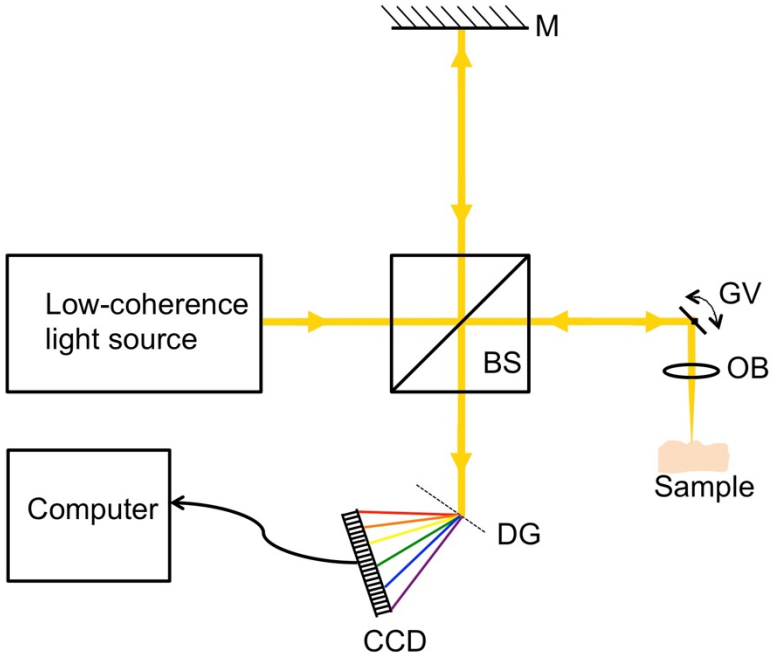

Figure 2.2. Schematic of spectral domain optical coherence tomography. Abbreviations used: BS – beam splitter, M – mirror, GV –galvanometer scanning mirrors, OB – objective, DG – diffraction grating, CCD – charge coupled device array.

In OCT, imaging resolution in the transverse dimension is limited by the Abbe diffraction limit, stemming from the numerical aperture of the objective used to focus the incident sample

beam. This transverse spatial resolution limit, Y, for incoherent illumination is shown in equation 1,

$$Y \sim 0.61 \cdot \frac{\lambda_o}{NA} \tag{1}$$

where λ_o is the wavelength of illumination and NA is the numerical aperture of the focusing lens[71,72]. In the axial direction, OCT resolution is dictated by the bandwidth of coherent light probing the sample and detectable by the spectrometer. This axial resolution limit is given by the round-trip coherence length of the light source, l_c, in equation 2,

$$l_c = \frac{2ln2}{\pi} \cdot \frac{\bar{\lambda}^2}{\Delta\lambda} \tag{2}$$

where $\bar{\lambda}$ is the mean wavelength and $\Delta\lambda$ is the spectral bandwidth, assuming a Gaussian spectral shape[73]. As the bandwidth is increased, the axial resolution of the OCT is improved, approaching the shortest wavelength of illumination as the bandwidth becomes very large. The axial and transverse resolutions achievable by OCT are independent, allowing for tuning of the OCT system for specific study of either thin or thick samples with an inherent trade-off for each due to instrumental constraints.

These constraints include light source spectral shape and stability, optic transmission efficiency, and spectrometer bandwidth and spectral resolution constraints. For instance, due to chromatic dispersion through glass, the objective used to focus sample illumination will have different focal lengths depending on wavelength, resulting in a longer path length to the focal point for longer wavelengths. In addition, antireflective coatings for optics are typically rated for a specified wavelength range that does not typically encompass both visible and NIR wavelengths. Therefore, the resolution of traditional OCT is limited to the micron scale in the transverse (lateral) and axial dimensions.

While these resolution considerations limit the imaging capability of OCT to microscale structures that can be readily observed in traditional histology with bright field microscopy, the spectral signals acquired from an OCT scan can be analyzed to extract information regarding the nanoscale structure of tissue. This post-processing analysis of raw OCT spectra which reveals statistical information regarding nanoscale tissue structure, referred to as inverse spectroscopic OCT (ISOCT), will be discussed in the following section 2.6.

2.6. Inverse spectroscopic optical coherence tomography

In the fields of physics and optics, the direct scattering problem describes the determination of a resultant distribution of radiation after it has scattered from a scattering object with known characteristics. When this problem is inverted, known as the inverse scattering problem, the distribution of scattered radiation from the object is known but characteristics of the object are unknown. In practice, while simulation and solution of the direct scattering problem can be fairly straight forward for a range of scattering systems, addressing the inverse scattering problem to fully characterize a scattering object based on its scattering signal is generally a more involved process. This is especially true when the scattering system is biological tissue, which is a complex and heterogeneous scattering system with varying scattering characteristics that are highly dependent upon tissue type and length scale of interest. Inverse spectroscopic OCT aims to address the inverse scattering problem in tissue by applying a mathematical model of tissue structure and a physical scattering approximation to spectroscopic OCT data in order to solve the inverse scattering problem, thereby measuring the nanoscale structure of tissue.

When tissue is assumed to be a spatially continuous random refractive index distribution, it is convenient to quantify such a distribution by its spatial autocorrelation function (ACF). For a bulk medium, statistically averaged structural properties are completely characterized by the ACF.

The ACF can be modeled using the Whittle-Matérn functional family to parameterize spatial distribution characteristics. This model incorporates three parameters that quantify tissue structure: the deterministic factor, D, the refractive index correlation length, l_c, and a scaling factor, A_n, which represents the variance of RI fluctuations within the media. While the physical meaning of l_c can be appreciated as the largest length scale to which the statistical mass density distribution is still correlated, the precise physical meaning of D depends upon its value. When $0 < D < 3$, D represents a mass fractal dimension, thus quantifying the extent to which the density distribution fills a given volume. For instance, an object in space that completely fills the volume it occupies would correspond to a fractal dimension of 3; as fractal dimension decreases the fraction of space filled by the mass density distribution will also decrease[74]. When $D = 3$, the resultant light scattering phase function of the medium is equivalent to the Henyey-Greenstein phase function. When $3 < D < 4$, the RI correlation function reflects a stretched exponential shape, when $D = 4$, the correlation function is an exponential function, and as D get higher, approaching infinity, the correlation function shape approaches a Gaussian distribution[3].

For any given refractive index correlation function, the optical properties of the medium can be more readily deduced if one considers that incident illumination upon the sample solely undergoes single scattering events. This limit is also known as the first-order Born Approximation, which applies when a media is weakly scattering and/or the characteristic length scale of the media is much smaller than the wavelength of light[71,74]. When this approximation is valid, the power spectral density, $\Phi(k)$, is equal to the Fourier transform of the tissue autocorrelation function, $B_n(r)$,

$$\Phi(k) = \mathcal{F}\{B_n(r)\} = \frac{A_n {l_c}^2 \Gamma(m)(1+k^2 {l_c}^2)^{-m}}{\pi^{3/2}\left|\Gamma(m-\frac{3}{2})\right|} \tag{3}$$

where *m* represents the quantity *D/2* in three-dimensional Euclidean space, and Γ represents the complex gamma function. The differential scattering cross section per unit volume, $\sigma(\theta, \phi)$, can be expressed in terms of this power spectral density from equation (3),

$$\sigma(\theta, \phi) = 2\pi k^4(1 - \sin^2(\theta)\, cos^2(\phi))\Phi(2k\, sin(\theta/2)) \quad (4)$$

where ϕ represents the polarization orientation of the incident illumination[3]. From this scattering cross section, the optical properties μ_s, μ_b, and g can be calculated, representing the scattering coefficient, backscattering coefficient, and scattering anisotropy, respectively. To compute μ_s, the scattering cross section σ is integrated over all scattering angles θ; μ_b is computed by evaluating $\sigma(\theta, \phi)$ in the backward scattering direction, when θ is equal to π radians. Finally, the scattering anisotropy g is used to describe the propensity for forward scattering and is computed by taking the average value of the cosine of the scattering angle, $\langle cos\theta \rangle$. Thus, by assuming a tissue satisfies the first-order Born Approximation, we can directly relate the optical properties of the tissue to functional parameters incorporated in the Whittle-Matérn functional model of the sample's refractive index correlation function. This connection enables quantification of structural features described by Whittle-Matérn parameters from the measurement of tissue optical properties.

Because OCT only measures scattering in the backward direction, we will consider the form of μ_b, an optical property proportional to the square of the OCT intensity, I^2,

$$I^2 = r{I_o}^2 \frac{\mu_b}{4\pi} L \cdot e^{-2zn\mu_s} \quad (5)$$

where *r* is the reference arm reflectance coefficient, I_o is the incident light intensity, *L* is the temporal coherence length of the incident light, and *n* is the mean refractive index of the tissue. It is important to note that equation (5) applies when the sample does not have appreciable absorbance in the OCT spectral range. Equation (5) also assumes a plane wave approximation which is appropriate due to the low numerical aperture typical of objective lenses used with OCT.

Evaluating $\sigma(\theta, \phi)$ in the backward scattering direction from equations (3) and (4), we yield an expression for the backscatter coefficient,

$$\mu_b = 8\sqrt{\pi}A_n k^4 {l_c}^3 (1 + 4k^2 {l_c}^2)^{-D/2} \cdot \Gamma(D/2) \quad (6)$$

While this expression is unwieldy for use in determining ultrastructural properties from μ_b, it can be simplified with the assumption that $kl_c > 1$, which is commonly satisfied in biological tissue, leading to the following simplified expression for μ_b,

$$\mu_b = 2^{3-D}\sqrt{\pi}A_n k^{4-D} {l_c}^{3-D} \cdot \Gamma(D/2) \quad (7)$$

Equation (6) clearly shows a power law dependence of the backscatter coefficient on the Whittle-Matérn deterministic factor, D. Because OCT intensity is proportional to the square root of μ_b, its proportionality to D can be written as follows,

$$I(k) \propto k^{2-\frac{D}{2}} \quad (8)$$

The proportionality described in equation (8) can be used to determine D from OCT signal, provided that the OCT intensity is given as a function of k, in other words, spectrally resolved. In order to accomplish this spectral resolution of OCT signal, ISOCT has been developed.

ISOCT is an emerging technique that performs spectral resampling of raw OCT spectra in order to produce independent, wavelength-dependent OCT images. This technique utilizes the short-time Fourier transform (STFT) to transform raw spectral domain OCT spectra into four-dimensional images by reporting the backscattering spectral intensity distribution at each voxel[75]. This spectral information can then be analyzed to obtain a complete set of scattering optical properties from biological tissue[76]. Because axial OCT resolution is dictated in part by wavelength, as shown in equation (2), the STFT narrows the spectral bandwidth with a Gaussian spectral resampling window, effectively decreasing axial resolution for each center wavelength. However,

what is gained is a spectrally resolved OCT image for multiple center wavelengths within the spectral bandwidth captured by the spectrometer.

Thus, ISOCT resampling techniques can be used to obtain spectrally resolved OCT intensity profiles, enabling spectral fitting of the OCT intensity using equation (8) to measure D at each OCT resolution voxel. If we assume the scattering coefficient μ_s to be independent of depth in a homogeneous sample, the Beer's Law decay in OCT signal due to scattering, represented by the exponential term in equation (5), can be fit along depth in the OCT scan to determine μ_s. The ratio of μ_b and μ_s, termed the reflection albedo, α, can be described by the following expression in the regime where $kl_c > 1$,

$$\alpha \approx \frac{\Gamma(D/2)}{\Gamma(D/2-1)} \cdot (2kl_c)^{2-D} \tag{9}$$

After D is known and μ_s is calculated for the media, reflection albedo can be computed and l_c can be similarly deduced from equation (9). Therefore, ISOCT enables the quantification of D and l_c at every OCT resolution-limited voxel. Because these parameters are intrinsic to the Whittle-Matérn model, their ability to describe the structure of the tissue is not necessarily confined to length scales set by the traditional resolution limits of OCT shown in equations (1) and (2).

Numerical simulation of random media measured with ISOCT to determine D has shown that for an illumination band between 650 and 800 nm, D is only sensitive to perturbations in the refractive index distribution when these perturbations occur at length scales between 35 and 450 nm. Experiments using ISOCT to scan polystyrene bead phantoms were performed to validate this finding, and corroborated the lower length scale sensitivity of ISOCT, showing a significant change in D when 40 nm diameter beads were removed from a phantom having a mixture of sizes. These experiments also showed that changes in D resulting from sphere removal persisted up to sphere sizes of around 2 μm[75]. Thus, while D values from tissues scanned with ISOCT can only

be localized within a voxel with size limited by OCT resolution, *D* computed from the resampled OCT gives information about structural changes at length scales well below the resolution limit of even the most powerful optical imaging techniques.

2.7. ISOCT applications

In recent studies, *D* has been used extensively as a biomarker for carcinogenesis at the earliest stages of disease. ISOCT study of *ex vivo* rectal biopsies from patients with colorectal cancers of varying advancement found a steady increase in *D* correlated with disease progression[77]. Furthermore, the 3D resolution of ISOCT enabled the segmentation of colonic epithelial crypts from the surrounding lamina propria, allowing detailed measurement of the differing ultrastructural properties of these distinct tissue compartments[77]. The depth resolution of both μ_b and *D* allowed for selection of the most characteristic regions of tissue to indicate the relative progression of CRC between patient groups. For all regions, however, in CRC progression, μ_b was lower and *D* was higher in patients with advanced adenomas. Further study of duodenal biopsies with ISOCT revealed a similar trend between normal healthy tissues and those associated with pancreatic field effect carcinogenesis, a predisposition to neoplastic development[77]. This study likewise identified *D* as being an elevated biomarker in response to presence of pancreatic adenocarcinoma, indicating that increase in *D* could be a general trait indicative of carcinogenesis.

It has been postulated that these relative changes in optical and ultrastructural properties are from modification in certain intra- and extra- cellular components of tissue. Specifically, nuclear chromatin condensation was investigated as a contributing factor to the difference in ISOCT signal. A study using ISOCT to study nuclear chromatin compaction confirmed that as chromatin compaction is relaxed by HDAC inhibitors, *D* correspondingly decreased[78]. It is therefore likely that the strong scattering signature of the cell's nucleus in conjunction with

dysregulation of chromatin condensation associated with carcinogenesis is a contributing factor to the difference in ISOCT signal between healthy and diseased tissues seen previously[77,79]. Because highly scattering collagen, specifically collagen type I, is the most abundant fibrous protein in the stroma, restructuring of the extracellular collagen network in carcinogenesis is also of great interest for optical screening methods to detect carcinogenesis of several organs. Prior study of collagen networks in oral cancer biopsies with confocal imaging and FDTD simulation of scattering found a significant decrease in scattering from neoplastic stroma, an effect similarly observed in ISOCT study of colorectal and pancreatic cancers, as well as with light scattering spectroscopy measurements of oral cancers[77,80,81].

Other potential applications of ISOCT lie outside the field of cancer biology and detection, such as its potential use for characterization of differences in collagen structure and crosslinking indicative of risk or diagnosis in various diseases[82]. One such potential application is in intracoronary OCT, where imaging of atherosclerotic plaque composition and fibrous cap morphology may provide insight into the risks of plaque rupture and inform treatment regimen[83–86]. The complementary ultrastructure measurement provided by ISOCT may be of value in this application for evaluation of fibrous cap crosslinking and integrity in future clinical studies. Other fibrotic mechanisms involved in wound healing have also been recently explored with ISOCT, which provided valuable imaging information of both ultrastructure and microvasculature remodeling as granulation tissue was gradually replaced with a fibrotic scar in a mouse skin wound model[2]. A distinct field of intense recent interest for application of OCT and novel ISOCT analysis is marine biology and coral ecology, where the micro-resolution 3D spatial rendering of OCT provides valuable insight into living coral anatomy and physology[87]. Extension of ISOCT to corals allows for new measurements of absorbing pigment density and light scattering properties in the

full living coral, allowing for unprecedented insight into the true mechanisms governing light transport and harvest that are essential for coral survival in the wild[88].

2.8. Conclusions

The goal of this chapter was to provide an overview of the main themes presented within the dissertation; namely, the pairing of novel optical imaging technology with transformative bioengineering approaches to address the current unmet clinical need for a robust clinical screening paradigm for early detection of metastatic relapse. The chapter started with an introduction outlining the motivation for development of new techniques designed to detect when a patient relapses into stage IV metastatic cancer as early as possible, with a brief recap of the current clinical standard of care and the leading "liquid biopsy" approach to this problem. Then a discussion of underlying biology behind cancer metastasis was presented, with an explanation of the theory and principles underlying the emerging idea of the "pre-metastatic niche" and the complex interplay between immune cells, primary tumor, and stromal cell populations that permits metastatic colonization in host organs. Specific attention is given to the structural aspects of pre-metastatic remodeling, with an overview of the required and upregulated structure-related proteins that have been implicated in the development of a native pre-metastatic niche. Biomaterial scaffold implants were then reviewed, and a summary of prior work studying their ability to recapitulate a native pre-metastatic niche *in vivo* was presented. Our recent work[1] using a recently-developed biomedical imaging technique, ISOCT, to discriminate between healthy mice and mice with metastasis by measurement of scaffold structure was shown, with following thoughts about the extension of this prior study into a more detailed analysis of scaffold restructuring and technological development that are presented in chapters 4 and 5 of the dissertation. Finally, a review of the history and theoretical background of optical coherence tomography was presented,

transitioning in to the rationale behind the development of inverse spectroscopic OCT for characterization of tissue nanoscale structure. A didactic review of scattering theory and tissue-modeling approximations underlying the ISOCT technique was given, with the following sections discussing the structural sensitivity of ISOCT and potential applications of this technique for disease screening and marine biology. Together, this chapter provided a broad review of the current state of the art in various disciplines covered in this thesis, chiefly of the pre-metastatic niche in cancer biology, scaffold implants in biomaterials and tissue engineering, and optical coherence tomography in biomedical imaging.

Chapter 3:

Detection of Extracellular Matrix Modification in Cancer Models with Inverse Spectroscopic Optical Coherence Tomography

Authors: Graham Spicer, Samira Azarin, Ji Yi, Scott Young, Ronald Ellis, Greta Bauer, Lonnie Shea, and Vadim Backman

3.1. Abstract

In cancer biology, there has been a recent effort to understand tumor formation in the context of the tissue microenvironment. In particular, recent progress has explored the mechanisms behind how changes in the cell-extracellular matrix ensemble influence progression of the disease. The extensive use of *in vitro* tissue culture models in simulant matrix has proven effective at studying such interactions, but modalities for non-invasively quantifying aspects of these systems are scant. We present the novel application of an imaging technique, Inverse Spectroscopic Optical Coherence Tomography, for the non-destructive measurement of *in vitro* biological samples during matrix remodeling. Our findings indicate that the nanoscale-sensitive mass density correlation shape factor D of cancer cells increases in response to a more crosslinked matrix. We present a facile technique for the non-invasive, quantitative study of the micro- and nano-scale structure of the extracellular matrix and its host cells.

3.2. Introduction

Colon cancer is the third-most prevalent cause of new cancer cases and cancer-related deaths in the U.S., with an estimated 93,090 new cases expected to be diagnosed in 2015[4]. While screening methods have improved detection of colon cancer, many of the mechanisms governing disease progression remain poorly understood. Interactions between cells and the extracellular matrix (ECM) have been implicated in promotion of tumor growth and progression in many types of cancer[89–97]. In particular, matrix crosslinking has been shown to facilitate invasion and migration of tumor cells [98,99]. Collagen is a major constituent of the extracellular matrix in both normal colon tissue and colorectal tumors [100]. In the tumor microenvironment studies using second harmonic generation microscopy (SHG) have shown transformation of collagen structure in tumors compared to healthy tissue, with ECM in tumors displaying a higher orientation of collagen fibers and thicker fiber bundles indicative of crosslinking[101–103]. Collagen crosslinking in the tumor microenvironment is believed to be catalyzed by the enzyme lysyl oxidase (LOX), which oxidizes lysine residues from collagen and elastin to form reactive semialdehydes[104]. LOX upregulation is associated with proliferation, invasion, and metastasis of breast cancer cells[48,105,106]. Colon tumor tissues exhibit higher levels of LOX expression than normal colon tissue, with even greater increase in LOX expression for metastatic tumor tissues[107]. Another study using PCR found that upregulation of LOX, LOXL2, and LOXL4 was found in colorectal adenomas with absence of lymphovascular invasion, indicating oxygen tension dependent expression of these enzymes[108]. This suggests that LOXL2 and LOXL4 also contribute to the progression of CRC. In addition, LOX-mediated collagen crosslinking increases matrix stiffness to increase proliferation and invasiveness of colon cancer cells *in vitro* and *in vivo*[109]. Proliferation studies of early stage colorectal adenocarcinoma line SW480 and metastatic colorectal

adenocarcinoma line SW620 cultured on 3D collagen matrices found increased cellular proliferation with LOX treatment to both SW480 and SW620 lines[107].

Current techniques used to study the interplay between cells and matrix include migration assays to measure cellular motility through the ECM, proliferation assays to measure cellular proliferation and metabolic activity[48,105–110]. In addition, biochemical and genetic analyses have been used extensively to quantify differential gene expression and cell signaling. To complement these functional and biochemical studies, histology and microscopy techniques have been used for qualitative and pseudo-quantitative analysis of antigen localization and structural morphology of tissue and in-vitro models[95,105,107–109,111]. Furthermore, the development of superresolution microscopy has enabled the direct visualization of nanoscale structures in and outside the cell, including actin, tubulin, mitochondria, and many ECM proteins. These recent advances have enabled much new insight into cellular structure at the nanoscale, leading to a better understanding of these complex systems and how their morphologic and chemical signaling leads to cancer progression. However, superresolution microscopy techniques have very limited working distances and require introduction of molecular probes to label structures of interest, complicating sample preparation. The introduction of a technique sensitive to nanoscale changes such as superresolution microscopy with the capability to image a wide variety of unlabeled biological systems will be of great utility in further structural study of the complex interplay between cells and the ECM in cancer biology.

Inverse Spectroscopic Optical Coherence Tomography (ISOCT) is an emerging technique utilizing spectral domain OCT signal resampling to determine the backscatter intensity spectra at every voxel in a three-dimensional OCT scan[76]. From this spectral information, ultrastructural parameters can be extracted to quantitatively characterize the sample. Specifically, by assuming tissue to be a continuous random medium, a mass density correlation parameter, D, can be obtained

from the relation, $\mu_b \propto k^{4-D}$, where μ_b is the backscattering coefficient, which is proportional to the squared OCT intensity, and *k* is the wavenumber, for each 3D OCT resolution voxel measuring 8x8x4 μm. Physically, when *D* is less than 3, it represents a mass fractal dimension characteristic of the voxel being sampled. In previous studies with ISOCT, the length scale sensitivity of *D* has been established theoretically and experimentally to structures between 35 and 450 nm in size[75]. Measurement of *ex vivo* biopsies from patients with colorectal and pancreatic cancers showed ISOCT is sensitive to ultrastructural changes induced by field carcinogenesis, manifesting in higher *D* values measured from patients with cancer [77]. The fact that tissues associated with field carcinogenesis appear histologically normal is in agreement with the ISOCT observation that the associated structural modifications occur below the optical diffraction limit. Although they cannot be imaged by conventional microscopy, these alterations are still detectable with ISOCT[112]. While ISOCT is as limited as traditional OCT with regards to spatial resolution, its ability to detect structural changes at the nanoscale from spectral fitting lends it for non-invasive study of dynamic phenomena in biological systems that occur at length scales below the diffraction limit. The penetration depth and working distance of ISOCT, on the order of 1-2 millimeters, far surpasses the working distance of traditional optical microscopes. This enables rapid facile imaging of thick 3D cell cultures quickly with minimal sample preparation.

Here, we demonstrate ISOCT as a valuable tool for the study of cell-ECM interactions in the context of a simple *in vitro* model. We show the sensitivity of ISOCT to enzymatic collagen crosslinking, as well as present it as a technique to study the structural phenotype of cells, as reflected by the response of colon cancer cells to a crosslinked collagen substrate. The increased proliferative phenotype adopted by colon cancer cells on a crosslinked collagen substrate is shown here to correlate with an increase in *D* measured from live cell colonies on collagen. Thus, the proliferative phenotype shift is accompanied by a nanoscale structural phenotype shift of cells in

this model of cancer progression, a finding that will push forward the development of optical screening strategies and testing of therapeutics to stem cancer progression.

3.3. Materials and methods

3.3.1. Lysyl Oxidase Treated Collagen Gels

Solutions of collagen were prepared by mixing rat-tail collagen I (BD Biosciences) with sterile dH_2O water, 10X PBS (Sigma, 1:10 dilution), and 1 M NaOH (Sigma, 1:100 dilution) on ice. For all LOXL4 treated gels, LOXL4 (Sigma) was added to the freshly mixed collagen I solution to reach a final LOXL4 concentration of 350 ng/mL prior to collagen gelation.

3.3.2. STORM Imaging and Analysis

For STORM imaging, collagen gel structures were labeled with Alexa Fluor 647 dye (Thermo Fisher) by directly mixing 1 aliquot of dye with 250 μL of freshly prepared 2.5 mg/mL collagen solution. After incubation for 1 hour for gelation, dye was leached from gels by adding 1X PBS to gels, replacing every 24 hours for 3 days. Imaging was performed on a Nikon STochastic Optical Reconstruction Microscope at the Northwestern Feinberg School of Medicine Nikon Imaging Center. Two-dimensional depth-sectioned STORM images were acquired from a depth within the collagen gel sample, away from the glass coverslip, with a lateral resolution of 50 nm. The spatial autocorrelation function, $B_n(r)$, of each STORM image was taken to be representative of the collagen fiber network mass density distribution, due to the absence of other scattering species within the sample. This function, $B_n(r)$, was fit to the Whittle-Matérn family of correlation function, whereby the fit parameter D was taken as a representative quantification of collagen mass density at the nanoscale resolution of STORM.

3.3.3. Cell Culture

Human colon cancer lines HT-29 (primary tumor) and SW620 (metastatic site) were cultured in McCoy's 5A (Thermo Fisher, Carlsbad, CA) and Dulbecco's Modified Eagle media (Sigma, St. Louis, MO), respectively, substituted with 10% fetal bovine serum. Cells were grown in a 5% CO2 environment at 37°C and split upon reaching 80% confluency.

3.3.4. WST-1 Proliferation Assay

To quantify cellular proliferation as a marker of phenotype induced by matrix crosslinking, HT-29 and SW620 human colon cancer cell lines were split and seeded on top of collagen gels prepared as described above. 50 μL of the collagen solution having LOXL4 concentrations of either 0 or 350 ng/mL was added to each well of a 96 well plate. The collagen-coated wells were incubated for 1 hour at 37 °C to allow for gelation, then 150 μL of split cells in media was added to each well. After 2 days incubation, media was replaced with fresh media containing WST-1 (4-[3-(4-iodophenyl)-2-(4-nitrophenyl)-2H-5-tetrazolio]-1, 3-benzene disulfonate) reagent (Sigma, St. Louis, MO). After 30 min incubation at 37 °C with WST-1, the absorbance of the plate was read at 440 nm in a Synergy H1 Multi-Mode plate reader at the Northwestern Recombinant Protein Production Core. After measurement, the plate was incubated for an additional 15 minutes before additional measurement. Cell proliferation is directly related to the difference in absorbance between the second measurement, taken at 45 minutes, and the first measurement, taken at 30 minutes.

3.3.5. ISOCT Study of Cellular Phenotype

For ISOCT study of cellular phenotype dependence on ECM structure, collagen gels were made in an 8-well chamber slide (Thermo Fisher Scientific) with 1.6 mg/mL collagen

concentration. Gels were incubated at 37 ℃ for 24 hours prior to seeding cells on the surface of the gel. After seeding, cells were incubated for 6 days prior to imaging with ISOCT in chamber slides.

ISOCT imaging was conducted on an instrumental setup described in references[76,77]. Briefly, the instrument consisted of a traditional spectral domain OCT system utilizing a supercontinuum laser source (NKT Photonics) for illumination and a spectrometer with spectral coverage from 650 to 820 nm over a 2048 pixel CMOS camera. OCT scans of 256 x 256 A-lines were acquired at 2560 Hz over a 2 x 2 mm scan area, giving a B-scan rate of 10 frames per second. The axial and lateral resolutions of the system were approximately 1.5 μm and 10 μm, respectively, with an effective NA of 0.04. ISOCT data collected from cell samples was normalized using an aqueous suspension of 80 nm polystyrene spheres as a Rayleigh scattering reference medium with backscattering coefficient μ_b proportional to k^4. 3D spatially resolved mass-density correlation functional factor, D, was calculated from this relation with a voxel edge length of 4 μm axially and 8 μm laterally, using 7 separate spectral resampling windows in a wavelength range from 674 to 754 nm.

To perform 3D segmentation of cells from their collagen substrate, regions of interest (ROIs) were manually drawn on *en face* projections of the 3D OCT spatial intensity maps generated by each OCT scan. These ROIs were used to select areas of the collagen substrate covered by cellular colonies. OCT B-scans of cell layers on collagen were surveyed to determine a characteristic thickness of these layers. An edge detection algorithm was used to find the height of the top surface of the cell layer. Taking into account a pixel buffer below the detected edge to the bright cell layer for both cell lines, 3D ROIs were generated by extruding the manually segmented lateral ROI along the z-dimension between 2-15 pixels and 2-10 pixels for HT-29 and SW620 cell lines, respectively, corresponding to the characteristic thicknesses of 56 μm and 36

μm for these lines determined from the survey of OCT B-scans. An example OCT B-scan of an HT29 cell layer on top of collagen with corresponding upper and lower pixel bounds is shown in Supplementary figure 3.6. Mean *D* values for cellular colonies in each scan were computed as the arithmetic mean of all *D* values for voxels within the 3D ROI.

3.3.6. Confocal Imaging of HT-29 Colonies on Collagen

For confocal imaging of live HT-29 colonies and their interaction with their collagen substrate, 100 μL of collagen solution (1.6 mg/mL) was used to coat the coverslip of a 35 mm glass bottom culture dish. Collagen was allowed to gel for 24 hours at 37 ºC prior to seeding the gel with split HT-29 cells in media. After allowing cells to culture for 2 days, 10 μg/mL Hoechst dye was added to cell media, after which cells were incubated for 2 hours to ensure thorough nuclear staining. For confocal imaging, media was removed and cells were rinsed and covered with 1X PBS. Confocal fluorescence microscopy was performed on an upright Leica TCS SP5 laser scanning confocal microscope system, with a 20X water immersion objective imaging through PBS covering cells from the top. Confocal reflectance images were acquired simultaneously using 488, 496, and 514 nm lasers, in conjunction with a 405 nm laser for Hoescht fluorescence excitation.

3.4. Results

3.4.1 Ultrastructural study of crosslinked collagen gel

In order to image the structural effects of LOXL4-induced crosslinking of collagen, Stochastic Optical Reconstruction Microscopy (STORM), with a transverse resolution of 40 nm, was used to image collagen gels, untreated and treated with 350 ng/mL of LOXL4, a concentration reflective of LOX expression in rat connective tissues[113]. Representative images of collagen gels from each

group are shown in figure 3.1(a) control and 3.1(b) LOXL4 treated. In the gel treated with LOXL4, crosslinking manifests in thicker fibrous structures throughout the gel, and sporadic bundles of thick fiber bundles. To quantify this characteristic clumping of the collagen fiber network from STORM images, the autocorrelation function of the full image was computed and fit to the Whittle-Matérn model of autocorrelation functions. Examples of Whittle-Matérn fit of the image autocorrelation for control and crosslinked collagen samples are presented in Supplementary figure 3.7. The fit parameter *D*, corresponding to the shape of the optical backscattering spectrum, was averaged from 4 independent images of collagen gels in each group. Average *D* values from STORM images are presented in figure 3.1(c).

ISOCT was used to measure gels prepared identically to those imaged with STORM. ISOCT spectral signal was averaged from a manually selected region of interest from the *en face* projection of each OCT scan, and the mean *D* value for the scan was calculated from the fit of this averaged intensity spectrum. Results were taken as the mean of 30 independent scans of collagen gel from each group, shown in figure 3.1(d). ISOCT detected a similar increase in *D* when comparing LOXL4 treated gels to the untreated control gel group. While the value of *D* determined by STORM compared to ISOCT differs when comparing groups, this could be attributable to the different measurement techniques introducing differing systematic errors to this measurement. Since ISOCT has been rigorously validated to establish the accuracy of *D* values measured from polystyrene bead phantoms, we believe this difference to arise due to the labeling accuracy of STORM images, which reflect the distribution of fluorescent dye molecules and not necessarily all collagen structures which scatter light[75,76]. Furthermore, the isotropy of a collagen gel network lends itself to quantification of *D* from ISOCT signal, regardless of illumination direction. This isotropy allows for direct comparison of ultrastructural parameters measured in the transverse sample plane by STORM with measurements taken in the axial dimension with ISOCT.

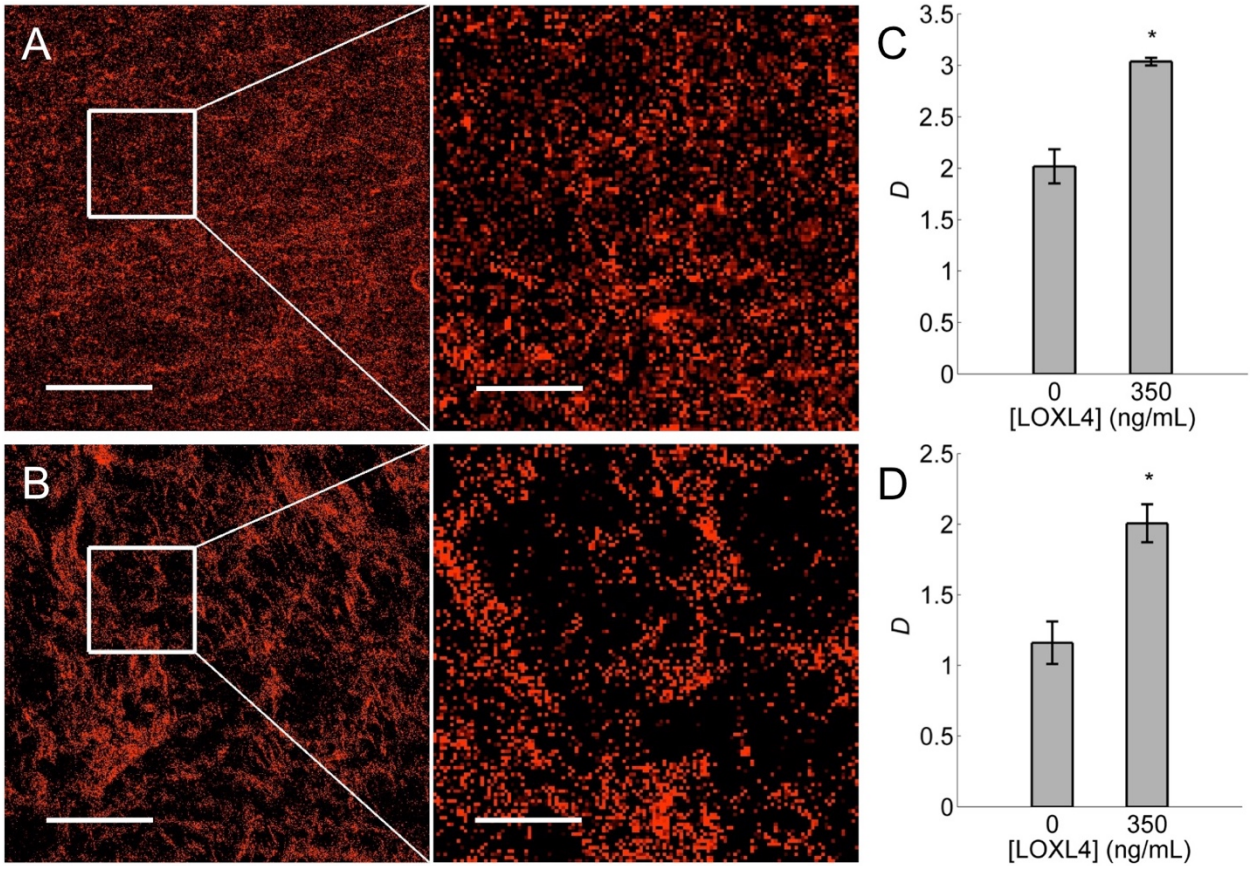

Figure 3.1. ISOCT and STORM quantify increases in *D* from collagen crosslinking. STORM images of (A) Control and (B) LOXL4-treated collagen gel samples (scale bar length is 10 μm). (C) *D* values computed from Whittle-Matérn fit of STORM image autocorrelation functions (*$p < 0.01$, N = 4 per bar). (D) *D* values measured with ISOCT from gels prepared in the same manner as those used for STORM imaging (*$p < 0.0001$, N = 30 per bar).

3.4.2. Measuring progression of crosslinking with ISOCT

Further study of the crosslinking of collagen gel as a time course experiment was conducted to demonstrate how the *D* value of collagen gel changes as the collagen changes from a transparent

liquid solution to the weakly scattering gels used in these studies. This gelation is induced by the mixing of sodium hydroxide with the collagen solution to lower the pH, enabling hydroxylation and covalent crosslinking of tropocollagen molecules into a collagen microfibril network. As this reaction proceeds, an increase in *D* is expected as fibers aggregate into larger bundles with a higher spatial autocorrelation. Results from this time course experiment are presented in figure 3.2.

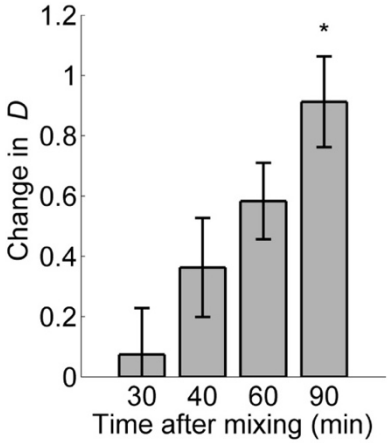

Figure 3.2. ISOCT monitors collagen crosslinking progression. Results of time course experiment designed to measure ultrastructural changes in collagen gel with ISOCT as the gel solidifies and crosslinks. ISOCT non-invasively probes the bulk gel to measure change in *D* compared to initial measurement at 20 minutes (*$p < 0.001$ comparing 20 and 90 minute time points, N = 6 per bar).

3.4.3. Cancer cell phenotype induced by ECM

To study the effect of enzymatic matrix crosslinking on cellular phenotype in cancer, human colon cancer lines HT-29 (primary tumor) and SW620 (metastatic site) were used to model this interaction. Cells were seeded on top of hydrated collagen gels prepared similarly to those

used for STORM study, with the omission of Alexa 647 dye. After culturing the cells on the collagen gel substrates for two days, a WST-1 assay was performed on the cells to quantify the degree of proliferation during the two-day culture period. The assay revealed significant increase ($p < 0.001$) in proliferation of both HT-29 and SW620 cells when cultured on collagen crosslinked with LOXL4, compared to control as shown in figure 3.3.

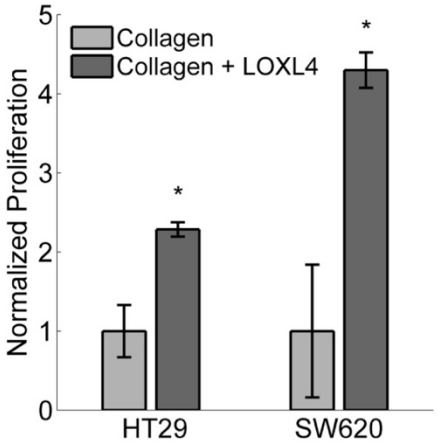

Figure 3.3. Cancer cells proliferate more on crosslinked collagen. Results of WST-1 Assay performed on HT-29 and SW620 cell lines cultured on collagen gels to detect proliferative phenotype shift (*$p < 0.001$, N = 24 per bar).

3.4.4. Measuring structural phenotype of cancer cells with ISOCT

ISOCT was used to measure the same cell-ECM model system used for WST assay study. Normal culture media was removed from cell beds cultured on collagen in an 8-well chamber slide, and cell beds were quickly scanned with ISOCT. The results of this study of structural cellular phenotype are presented in figure 3.4, representing data taken from a single experimental run (sample size n=3). Two additional runs of the experiment verified these results with similar trends

being shown for all trials. We observe a significant ($p<0.05$) effect of LOXL4-conditioned collagen substrate on the *D* value of cells when compared to the control collagen without LOXL4 induced crosslinking. This is indicative that matrix crosslinking has a positive effect on the *D* value and respective phenotype of HT-29 cells growing on a collagen substrate.

The 3D imaging ability of OCT enable the visualization of individual colonies of HT-29 cells growing on the collagen. This capability was used to determine cellular confluency of HT-29 colonies within the transverse 2 mm square scan area taken for ISOCT analysis. Manual segmentation of these colonies from the *en face* projection of the 3D OCT image cube yielded a significantly higher confluency of HT-29 colonies when grown on collagen treated with LOXL4 compared to the control collagen gel. This corroborates the finding that these cells proliferate more when cultured on the more crosslinked collagen substrate. To better visualize the cellular and collagen morphology with high resolution, confocal fluorescence microscopy was used with Hoechst dye to label cell nuclei. A superimposed confocal fluorescence image of the Hoechst channel with confocal reflectance microscopy to show collagen structure underlying live HT-29 colonies on collagen is presented in figure 3.5(a). In addition, an animation of a rotating confocal scan of this system is presented in Supplementary video 1. For comparison with ISOCT as a quantitative imaging technique, an ISOCT B-Scan of a highly confluent cell bed, color-coded by *D* value, is shown in figure 3.5(b).

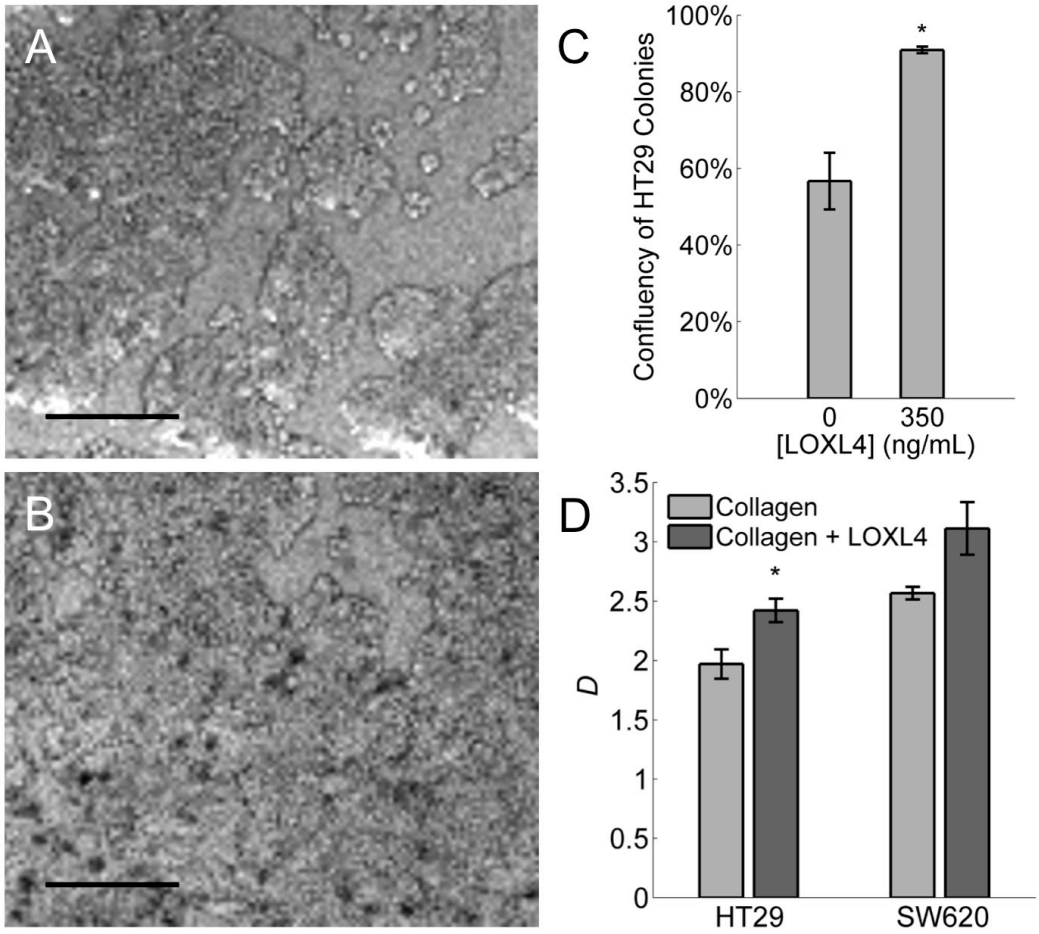

Figure 3.4. Cancer cell *D* increases when cultured on crosslinked collagen. OCT *en face* projection images of HT-29 colonies cultured on top of (A) untreated and (B) LOXL4-treated collagen gels. Scale bar length = 250 μm. (C) Confluency of HT-29 colonies was greater when cultured on collagen gel crosslinked with LOXL4 (*$p < 0.05$, N = 3 per bar). (D) ISOCT *D* values measured from cell colonies of lines HT-29 and SW620 *in situ* on *in vitro* collagen gel (*$p < 0.05$, N = 3 per bar). Cell layers segmented manually to ensure measurement signal taken from cells without interference from collagen.

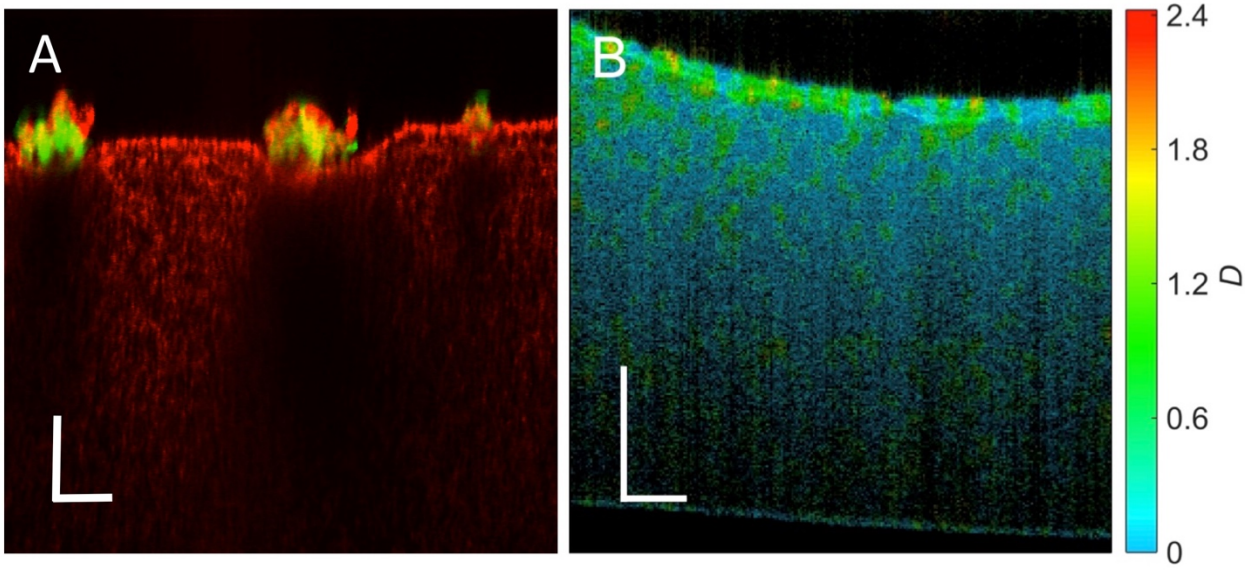

Figure 3.5. ISOCT provides complementary information to confocal imaging. (A) Confocal fluorescence cross section of live HT-29 cell colonies cultured on collagen gel, nuclei shown in green and collagen shown in red. Scale bar length = 50 μm. (B) Example OCT B-scan of HT-29 colony cultured on top surface of collagen gel. Image brightness is scaled by OCT intensity and color is scaled by ISOCT parameter, *D*. The bright layer near the top of the frame is the HT-29 colony, with the substrate collagen underneath showing as a fainter homogeneous media. Scale bar length = 250 μm.

3.5. Discussion

We present here a study of enzymatic collagen crosslinking with ISOCT to show how this prevalent effect in carcinogenesis manifests in changes in nanostructure and ISOCT signal. The effects of lysyl oxidase (LOX)-catalyzed crosslinking of collagen have been well described by matrix stiffness and SHG measurements on tissues and *in vitro* models[99,101,114]. We extend this study to the nanoscale, using STORM microscopy to resolve previously unobserved nanoscale

structure of a hydrated collagen network and its response to LOXL4-mediated crosslinking. By calculating the correlation function shape parameter *D* from STORM images, we were able to parameterize the extent of crosslinking of collagen gels quantitatively. For *D* values between 0 and 3, *D* represents the mass fractal dimension of the sampled medium, a quantitative value reflective of the relative clumping of its statistical mass density. With increased crosslinking of collagen fibrils, *D* from the fibrous collagen network will increase. ISOCT measurement of the same collagen gel system revealed a similar effect size of LOXL4 crosslinking of the collagen gel when compared to the difference in *D* values between groups measured from STORM images. After confirming the sensitivity of ISOCT to collagen crosslinking, we demonstrated its applicability to longitudinal study of increasing *D* in a crosslinking collagen gel. While this is a simple model, it is a novel extension of ISOCT, demonstrating for the first time non-invasive nanoscale-sensitive study of structural modification of unlabeled hydrated collagen. This will lead to further study of animal models to study how collagen modifications occur in the earliest stages of carcinogenesis, as well as utilizing the 3D resolution of ISOCT to localize regions of ECM modification in tissue to optimize site-specific cancer screening with ISOCT.

We extended this model of collagen crosslinking in cancer to study how the crosslinked matrix affects cellular phenotype. When two commonly used colon cancer cell lines, HT-29 and SW620, were cultured on these collagen gel substrates, cells on the more crosslinked substrate showed a markedly higher proliferation and confluency, a shift in phenotype in line with previous behavioral studies such as migration and proliferation assays, as well as *in vivo* tumor models[107]. The results obtained here show the multimodality of ISOCT, with regards to its ability to resolve cellular localization and confluency in a live culture and demonstrate its potential for further study of more advanced 3D cell culture models.

To study the nanoscale differences in cells cultured on collagen gels, we quantified the cellular nanostructure and organization (*D*) using ISOCT. We demonstrated ISOCT to be a facile non-invasive technology for the study of structural phenotype of cells to complement the established imaging capabilities of traditional OCT. ISOCT is sensitive to changes in cellular structure leading to an increased *D* value when cells are cultured on a more crosslinked matrix. Based on previous studies that determined the length scale sensitivity of *D* to be between 35 and 450 nm, the higher *D* associated with cells on a stiffer matrix likely arise due to changes in nuclear chromatin structure but may also be attributable to changes in the cytoskeleton, cellular organelles, or membrane structures[75].

Previously, a study from our lab has identified dysregulated condensation of nuclear chromatin to be a diagnostic marker in the identification of early colon field carcinogenesis[115]. Furthermore, these chromatin alterations via histone acetylation were detected by ISOCT[116]. Therefore, due to the relatively large scattering signature from the cell nucleus, the higher *D* measured from cells on crosslinked collagen could be attributable to such changes in the nuclear chromatin. Further studies are being pursued to determine dominant structural effects underlying the change in *D* in these models, and will better explain the biological meaning of ISOCT signal, establishing ISOCT as an unparalleled technique in studying cellular nanostructure due to its superior depth of field and imaging speed when compared with superresolution microscopy.

Moreover, it has been well established that cells growing on a stiffer substrate adapt to this environment through mechanotransduction pathways, resulting in an altered cytoskeleton and cellular shape. While the HT-29 and SW620 cell lines studied here do not typically have a large cellular space outside of the nucleus, the higher elastic modulus of crosslinked collagen would likely have an effect on the cytoskeleton and glycoprotein adherence to the gel. Cytoskeletal disruption in isolated rat colonocytes has been shown to have a profound influence on optical

scattering spectra derived ultrastructural parameters, indicating the possibility of a similar effect from cytoskeletal modification in this cell model[117].

In conclusion, in this study we have used ISOCT to measure the nanoscale sensitive mass density correlation parameter *D* from living cell cultures. ISOCT is also presented as a tool to monitor an evolving system of collagen crosslinking, tracking the increase in *D* from a collagen gel as collagen molecules and microfibrils covalently crosslink during gelation. This capability of ISOCT to non-invasively probe living and evolving systems for 3D spatially resolved sub-diffractional nanoscale structural information is novel in the field of biomedical optics, and introduces a technique to address the tantalizing scientific puzzle of nanoscale dynamics in a native biological system. By harnessing the complementary information obtained from the 3D imaging of traditional OCT and the nanoscale-sensitive structural measurements of ISOCT, we anticipate this technique to be of great utility in further study of cell-ECM interactions and cancer screening. Future work will elucidate specific mechanisms of ECM modification in cancer, using ISOCT to probe subtle nanoscale changes in structure *in vitro* and *in vivo*.

3.6. Supplementary Figures

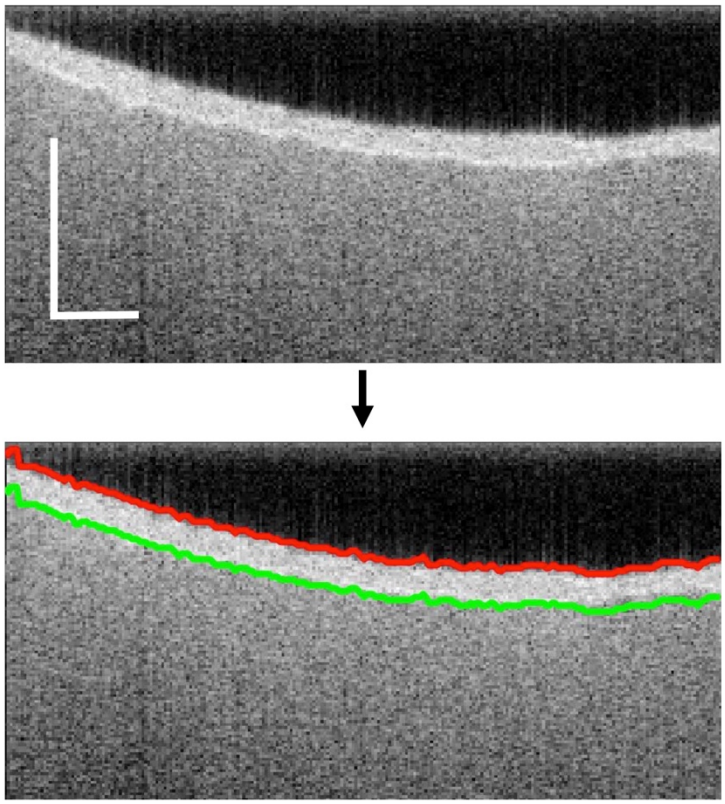

Figure 3.6. Segmentation of cells from collagen substrate in OCT scans. Example OCT B-scans of HT29 segmentation from collagen substrate. In this B-scan, the top boundary of the 3D ROI is shown by the red line and the bottom boundary is shown by the green line. In combination with manual lateral segmentation to select cellular colonies in the transverse plane, this segmentation is fairly effective at isolating signal from cells. Scale bar length = 250 μm.

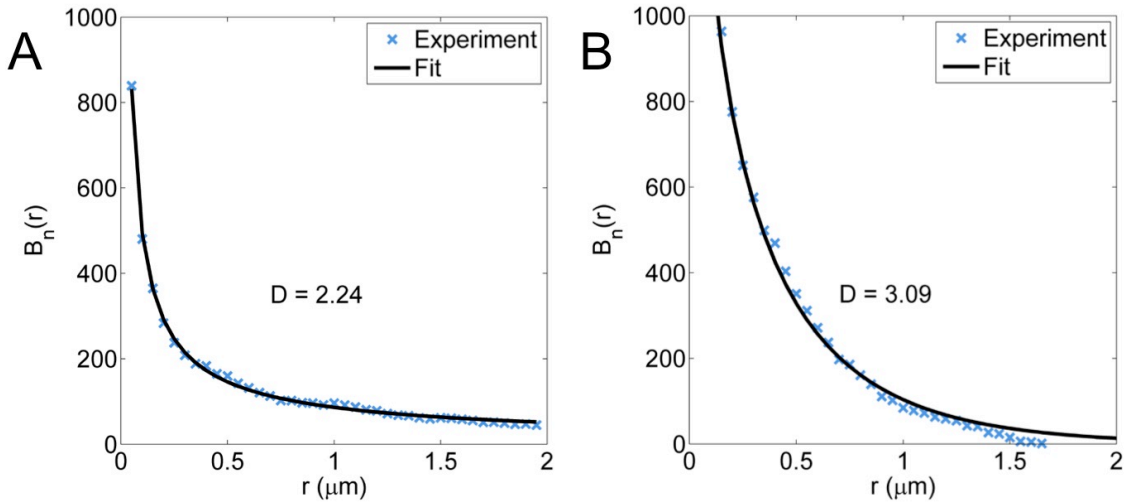

Figure 3.7. Example autocorrelation function fitting from STORM images. (A) Control and (B) LOXL4 treated collagen gel image autocorrelation functions are fitted to the Whittle-Matérn model to determine *D* from STORM measurements.

Chapter 4:

Development of Inverse Spectroscopic Optical Coherence Tomography for *in situ* imaging of a subcutaneous scaffold implant

Authors: Graham Spicer, Jimmy Winkelmann, Aya Eid, Ji Yi, Vadim Backman

Acknowledgements to Irawati Kandela and Fraser Aird of the Northwestern Developmental Therapeutics Core for animal model assistance.

4.1. Abstract

Current approaches for subcutaneous imaging with inverse spectroscopic optical coherence tomography (ISOCT) for detection of ultrastructure in a scaffold implant have been restricted to imaging the exposed scaffold after incision through the skin at a terminal time point. This is due to the intrinsic limitations of penetration depth of visible and near-infrared OCT, which typically limit imaging depth to less than a millimeter in highly turbid tissues. While other biomedical imaging modalities such as ultrasound imaging or photoacoustic tomography have the potential to improve upon this imaging depth, they utilize different contrast mechanisms that do not possess the same nanoscale structural sensitivity of ISOCT that may prove useful for early metastasis screening at the scaffold implant. To address this penetration depth limitation of ISOCT, in this chapter we present work conducted to develop dual-bandwidth ISOCT which incorporated a novel co-focal infrared imaging channel allowing for a ~twofold increase in imaging penetration through mouse skin and work conducted to develop a novel ISOCT needle probe for direct trans-cutaneous imaging of the scaffold *in vivo*. Together, these developments address a trade-off commonly encountered in biomedical optics between resolution and penetration, and advance the capability of ISOCT for imaging access to deeply situated tissues in the body.

4.2. Introduction

While biomaterial scaffold mimics of the pre-metastatic niche have shown great promise for early screening applications of stage IV cancer in metastatic breast cancer mouse models, their potential clinical applicability remains limited due to a current lack of non-invasive imaging and detection modalities that can characterize their structure *in situ* with high sensitivity. Previously, all animal studies utilizing optical based screening techniques for this application such as inverse spectroscopic optical coherence tomography (ISOCT) have either exposed through dissection or removed the scaffold from the subcutaneous space for direct imaging of scaffold structure[1,60]. While this information has been of value for proof of concept of the use of fractal dimension *D* as a biomarker indicating presence of metastasis, there is an unmet need for ISOCT or similar modalities that can be used for longitudinal minimally-invasive monitoring.

Current investigations into the use of high frequency spectrally-resolved ultrasound are promising but still experimental[118] and are limited in spatial resolution, and while other non-imaging approaches such as gene expression profiling from scaffold biopsies or explants provide very sensitive monitoring of disease, they may prove to be too invasive for widespread clinical use[119]. Therefore, there remains a need for sensitive, minimally-invasive, high-resolution imaging strategies for subcutaneous scaffold monitoring *in vivo*.

To address this need, one potential avenue is extension of ISOCT imaging into the infrared (IR) where optical scattering is less strong, leading to enhanced imaging penetration depth in tissue. Traditionally, spectral domain OCT imaging depth is limited by scattering in turbid media and by a characteristic signal intensity roll-off away from the zero-frequency point, which is directly related to the spectral resolution of the spectrometer[120]. Previous investigation into dual bandwidth OCT centered at 1300 and 1600 nm found enhanced OCT imaging depth at 1600 nm for samples with low water content[121]. A dual-band OCT scheme operating with bands centered at

415 and 808 nm applied for ophthalmic imaging showed different imaging appearances between these bands but suffered from low image quality due to narrow bandwidth and low resultant resolution at 415 nm[122]. More recently, a dual visible (566 nm) and IR (841 nm) OCT system was developed to provide complementary hemoglobin absorption-based spectral information for blood oxygenation measurement and robust anatomical information provided by the IR channel. Here, we devised a scheme to provide simultaneous co-focal scanning and acquisition of OCT signal from visible (600 nm) and IR (1300 nm) channels with a novel dual-bandwidth benchtop OCT system[2].

An alternative approach to address the limited penetration depth of OCT is adaptation of sample arm optics to fit inside a small probe, such as a catheter for intracoronary imaging or hypodermic needle for potential imaging of deeper structures in the body[65,123–125]. Typical designs for these OCT needle probes utilize a gradient index (GRIN) fiber-based lens for focusing the sample beam[126–129]. For spectroscopic OCT, this arrangement is typically unsuitable because it introduces a degree of chromatic aberration due to the dispersive effects of the GRIN lens, resulting in poor fidelity of different windows used in the short-time Fourier transform analysis utilized for spectral fitting of OCT signal. Several designs have been recently introduced to allow for achromatic performance of small diameter OCT probes, including the use of diffractive lens technology to compensate GRIN chromatic aberration[130,131], and custom-fabricated achromatic ball lenses with tuned optical properties based on ball diameter and mean refractive index[132–134]. These latter designs operated in the near-IR range, centered at 800 nm; we sought to develop a similar custom ball-lens based needle probe with rotational scanning and novel operation in the visible (~600 nm) for robust ISOCT analysis and potential for hemoglobin concentration and oxygenation measurement. This novel visible-band needle probe would be of potential clinical

applicability for direct subcutaneous measurement of the scaffold for minimally invasive monitoring *in situ*.

4.3. Results

4.3.1. Dual band ISOCT instrument

The first consideration in design of an OCT instrument is often the light source to be used. In spectral domain OCT, high spatial coherence, high source stability and intensity, and low temporal coherence (directly related to the central wavelength and bandwidth of the source) are desirable to optimize image quality and resolution. A popular choice for OCT sources in the visible range are supercontinuum lasers, which provide high intensity broadband illumination with high spatial coherence. An NKT Photonics SuperK Extreme source was used for visible band illumination and a separate superluminescent diode (Thorlabs SLD1325) was used for IR band illumination due to its lower form factor, lower cost (~$5,800 vs ~$50,000), and higher stability compared to the IR illumination provided by the NKT supercontinuum source. Visible band illumination provided by the supercontinuum laser had a high intensity spike in the middle of the wavelength range, so a spectral flattening scheme was developed to allow for higher dynamic range over the entire analysis bandwidth from ~510 to ~700 nm. To achieve this spectral flattening, the collimated beam of visible light from the laser source was sent to two equilateral F2 glass prisms to spatially separate the spectrum, after which the center portion was attenuated with a crescent-shaped spatial beam block. A mirror reflected the spatially-filtered spectrum back through the prisms, slightly offset in the vertical plane to allow the back-propagated beam to be directed to a fiber port collimator via a pickoff mirror. Visible and IR beams were combined in the sample arm at a dichroic mirror, which also separated the backscattered signal for downstream interference and collection at respective visible (custom homebuilt, Basler spL 4096, 140 kHz) and IR

(Wasatch Cobra 1235-1385) spectrometers. A schematic of this dual band OCT benchtop instrument is shown in Figure 4.1.

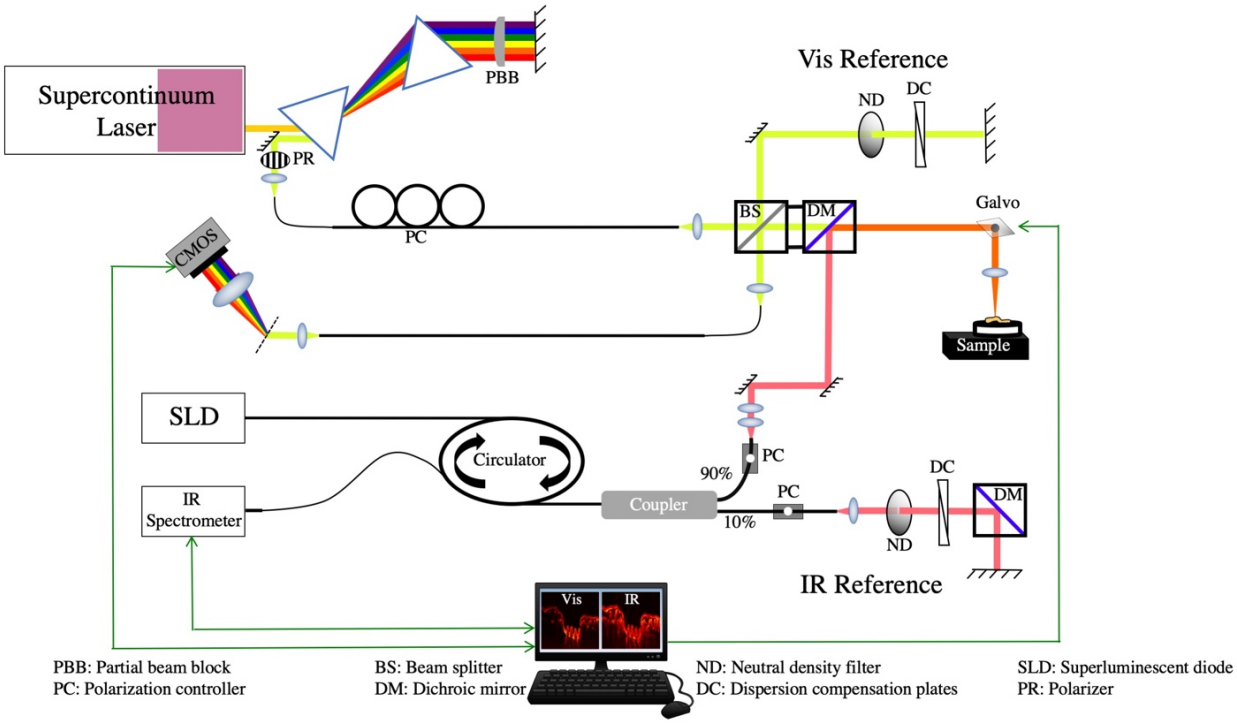

Figure 4.1. Dual-bandwidth ISOCT instrument used for experiments. Schematic of the apparatus; abbreviations: LP - linear polarizer, PBB - partial beam block, PC – polarization controller, BS – beamsplitter, DM – dichroic mirror, ND – neutral density filter, DC – dispersion compensation plates, IR SLD – infrared superluminescent diode, CMOS – CMOS spectrometer camera.

4.3.2. Measurement of mouse skin and subcutaneous scaffold *in situ* with dual band OCT

To test the ability of our dual band OCT system to image through the skin, we imaged skin on the upper back of a Balb/c mouse. Skin was shaved and thoroughly depilated with Nair, then

clamped with a magnet in a custom-fabricated skin imaging window to minimize movement during OCT imaging. Example OCT B-scan images of normal skin on the upper back of a mouse from visible and IR channels are shown in Figure 4.2. The trade-off between spatial resolution and depth penetration can be clearly observed in these scans, where clearly defined epidermis (stratum corneum) and dermis layers are visible in the visible channel with underlying skeletal muscle/fascia being barely visible. However, the enhanced penetration of the IR channel allows clear imaging of hair follicles throughout the thickness of the dermis, and clear imaging through the subcutaneous fat and deeper, in principle allowing for the imaging of a scaffold implanted in this space. Further characterization of the relative penetration depth of these channels in the skin of a mouse ear is shown in Supplementary figure 4.11, which indicates a >2 fold increase in penetration depth in the IR compared to the visible channel.

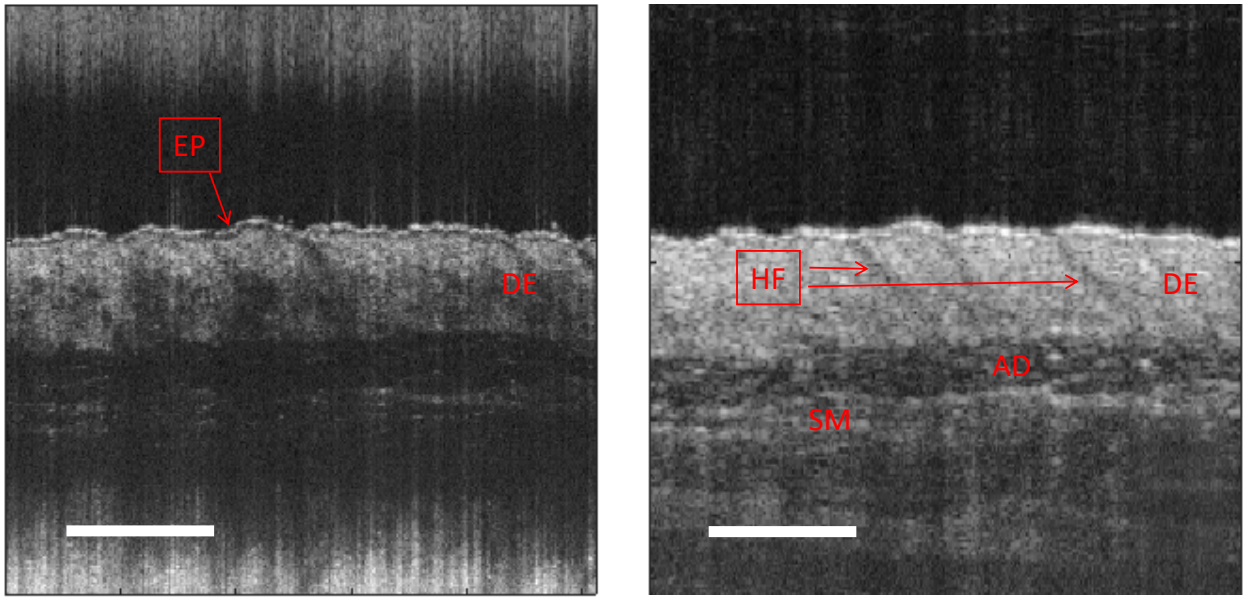

Figure 4.2. Example Dual-band OCT images of mouse dorsal skin. Side-by-side simultaneously acquired visible (left panel) and infrared (right panel) OCT B-scans clearly demonstrate enhanced resolution in visible compared to enhanced penetration in IR which enables

visualization of skeletal muscle through dermis and subcutaneous fat layers. EP: epidermis, DE: dermis, HF: hair follicle, AD: adipose tissue, SM: skeletal muscle. Scale bar length = 0.5 mm.

To test this potential capability of dual band OCT to image the scaffold through the skin, we conducted an animal study described in sections 5.3.1 - 5.3.4, a model consistent with previous work using ISOCT for sensing metastasis through scaffold measurement[1]. After allowing the scaffold implantation site to heal for 4 weeks, mice were inoculated with either 4T1 cancer cells or PBS control vehicle in the mammary fat pad. Scaffolds were imaged through the skin with dual band OCT 2 days before this inoculation procedure, 2 days after, then once per week until the tumor endpoint was met 4 weeks after inoculation. This monitoring procedure is considered to be a somewhat condensed timeline of a human clinical application, yet mirrors the potential application of longitudinal monitoring of the scaffold for indications of metastatic progression. Initially, the scaffold was clearly visible through the skin in most of the experimental mice, an example B-scan being shown in the top panels of Figure 4.3. However, we observed increased local swelling in the scaffold site at subsequent measurement timepoints, which increased tissue thickness over the scaffold and lead to the scaffold not being visible in OCT B-scans. Furthermore, intrinsic variability in the anatomic situation of the scaffold created large variability in image interpretation and analysis. As an example, the bottom panels of Figure 4.3 show how fibrous membrane layers, potentially associated with fibrous encapsulation of the scaffold in the chronic foreign body response, occlude view of the main bulk volume of the scaffold and confuse interpretation of OCT images through the skin.

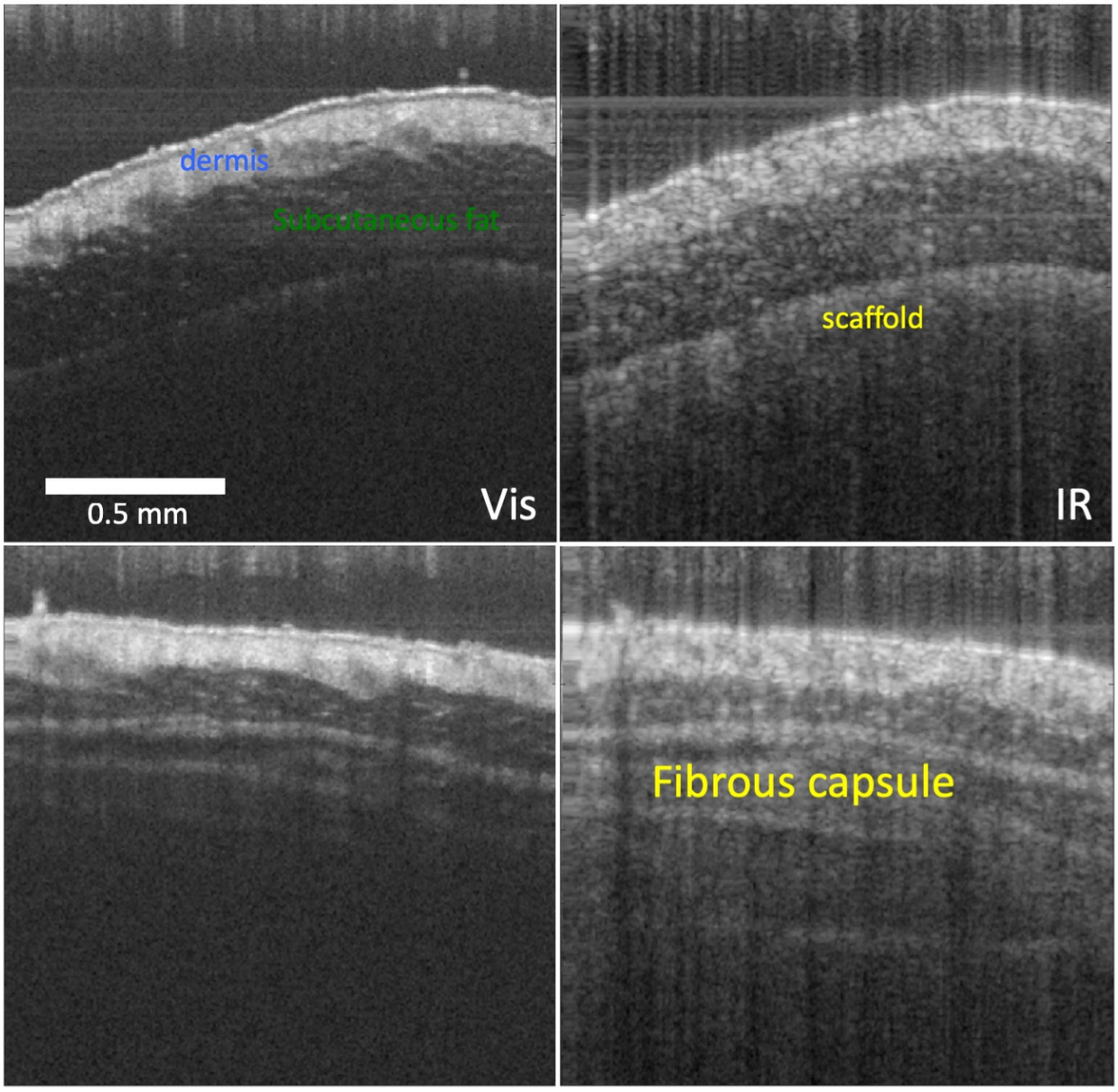

Figure 4.3. Example Dual-band OCT B-scans of subcutaneous scaffold *in vivo*. Visible (left panels) and infrared (right panels) images of scaffold under mouse skin demonstrating ability of IR channel to reach scaffold in top row. Bottom row: Visualization of scaffold through skin is inconsistent due to morphological variability of fibrous encapsulation and fibrous strata overlying scaffold.

Due to the inherent variability of depth of scaffold implantation, skin thickness in different regions of the body, observed variability in fibrous strata covering and encapsulation around the scaffold, and the fact that skin in humans is much thicker than that of a mouse, we conclude that OCT imaging approaches for imaging the scaffold through the skin are infeasible for the reliable measurement of scaffold structure. While the extension of visible OCT to the IR band demonstrated here provides a substantially enhanced penetration and is of use for providing complementary morphological and potentially spectral information for certain applications, imaging of the scaffold *in situ* requires a different approach.

4.3.3. Development of ISOCT needle probe for transcutaneous scaffold imaging

An alternative implementation of ISOCT imaging of scaffold structure incorporates recently developed micro-optical fabrication and assembly techniques in order to miniaturize the sample arm focusing and rotational scanning optics into a needle probe unit that can be inserted directly into the scaffold site through the skin for minimally-invasive direct imaging measurement of scaffold structure. Design of this ISOCT needle probe incorporates several novel advances in OCT needle probe technology, which as of yet have not been demonstrated in the visible regime due to several technical limitations addressed here. In this section we describe in detail the current design of this ISOCT needle probe and processes developed for its fabrication. A schematic of the vis-ISOCT needle probe system is presented in Figure 4.4.

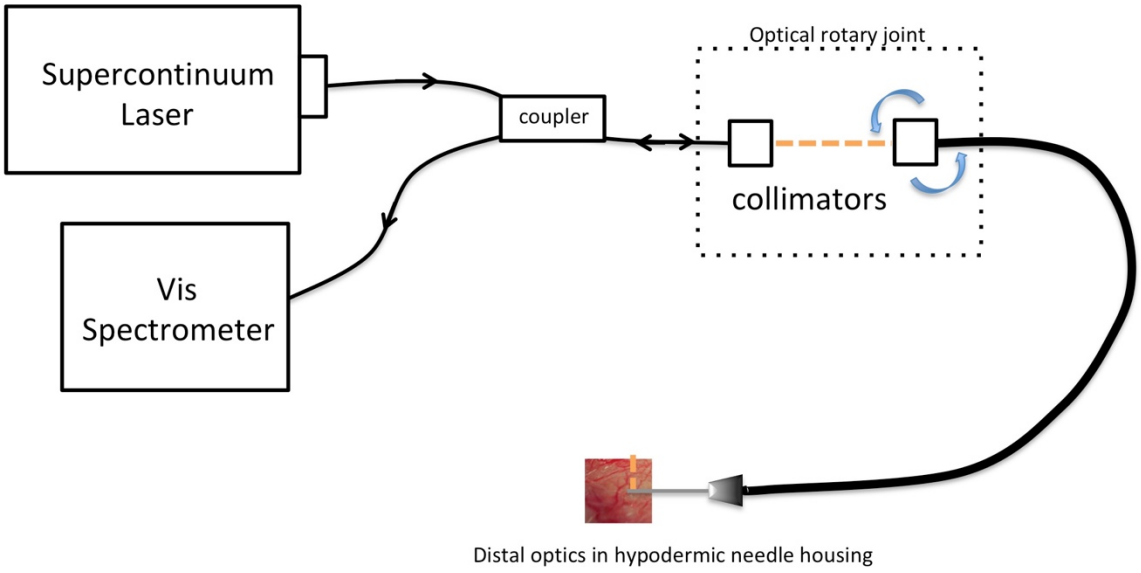

Figure 4.4. Coarse schematic of OCT needle probe apparatus. Two modules under novel development presented here include the optical rotary joint and distal probe optics housed in a hypodermic needle.

This OCT probe uses in-probe interferometry to achieve the OCT interferogram that is collected by the visible spectrometer after the fiber coupler. The system throughput is multiplied by the square of the transfer function across the visible optical rotary joint (ORJ), which was custom-built for this system using a novel design due to the current unavailability of ORJs in the visible. A much higher alignment and rotational stability is required for this when compared to more commonly available IR-operating ORJs due to the larger operational bandwidth and smaller mode field diameter for single mode fiber collimation. A schematic of the visible optical rotary joint and photo of the completed module are shown in Figure 4.5.

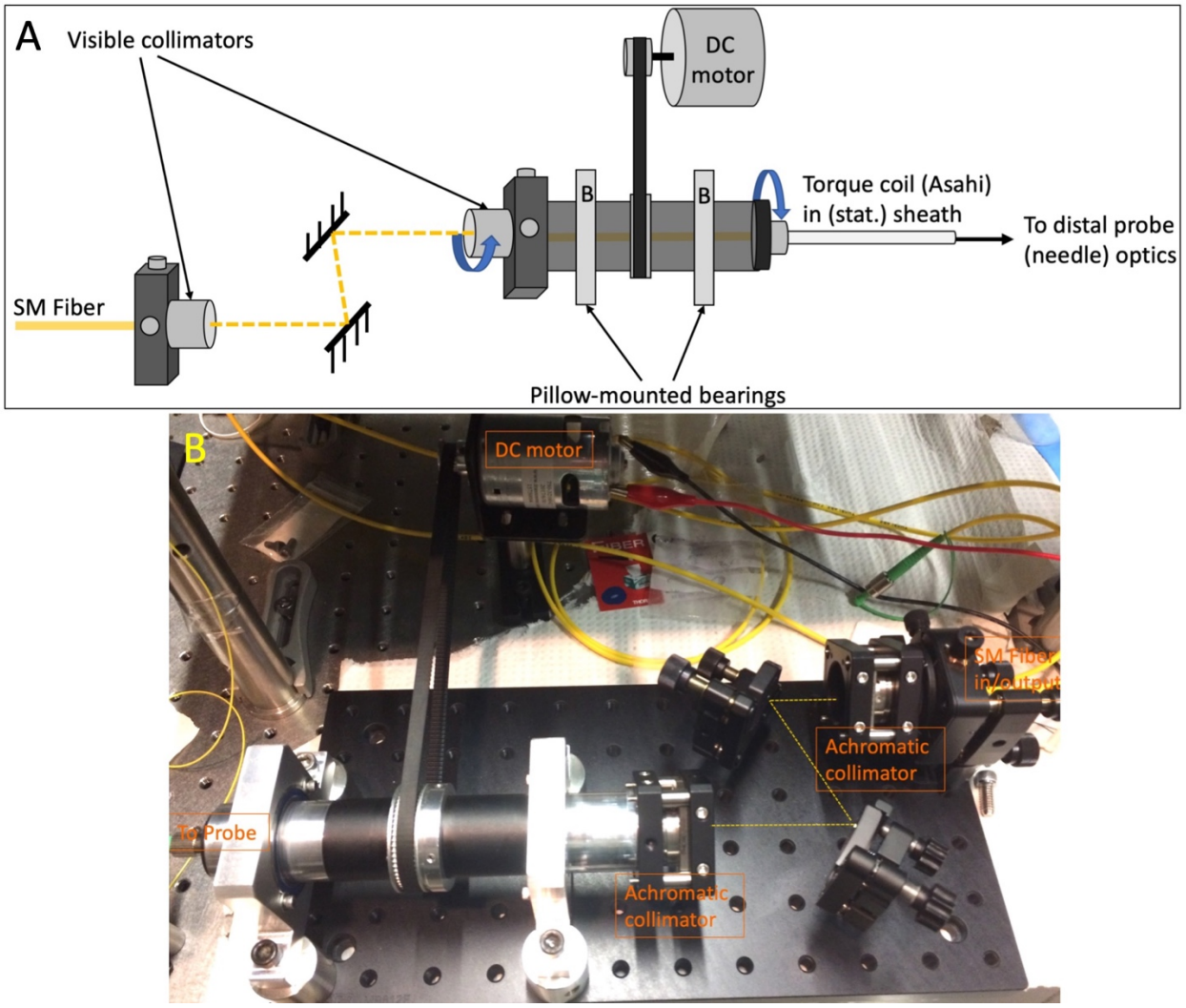

Figure 4.5. Visible band optical rotary joint designed and built for ISOCT needle probe. (A) Schematic of rotary joint design, incorporating two visible collimators on kinematic mounts and two mirrors to allow for precise alignment of collimated beam into rotating collimator. (B) Photograph of completed benchtop rotary joint.

The ORJ uses a DC motor powered by DC power supply (right of frame) to tune the analog rotation rate of the drive shaft by manually adjusting voltage. To align the optical rotary joint, the distal "to probe" fiber (the left of frame) was removed to allow light to come directly out of the

end of the rotating shaft, illuminating a diffuse spot on a target card. Angle control of 5-axis mount holding the fixed achromatic collimator and the two 2-axis mounted mirrors allows the beam to be walked into the center of the rotating collimator. Subsequent adjustment of the X-Y set screws on the rotating collimator centers the collimator coaxially with the drive shaft to minimize the rotation angle-dependent transmission intensity of the ORJ. Iteration of these adjustments should fully allow for maximal throughput and rotational stability of the ORJ transfer function, provided that the mount into which the rotating collimator is screwed is fixed squarely on the cage rods. This is necessary to ensure the rotation axis of the drive shaft and the optical axis of the rotating collimator are parallel.

The second main module newly developed for this system is the distal probe optics used for sample illumination, collection, and in-probe signal interference. A schematic of this optical assembly is shown in Figure 4.6.

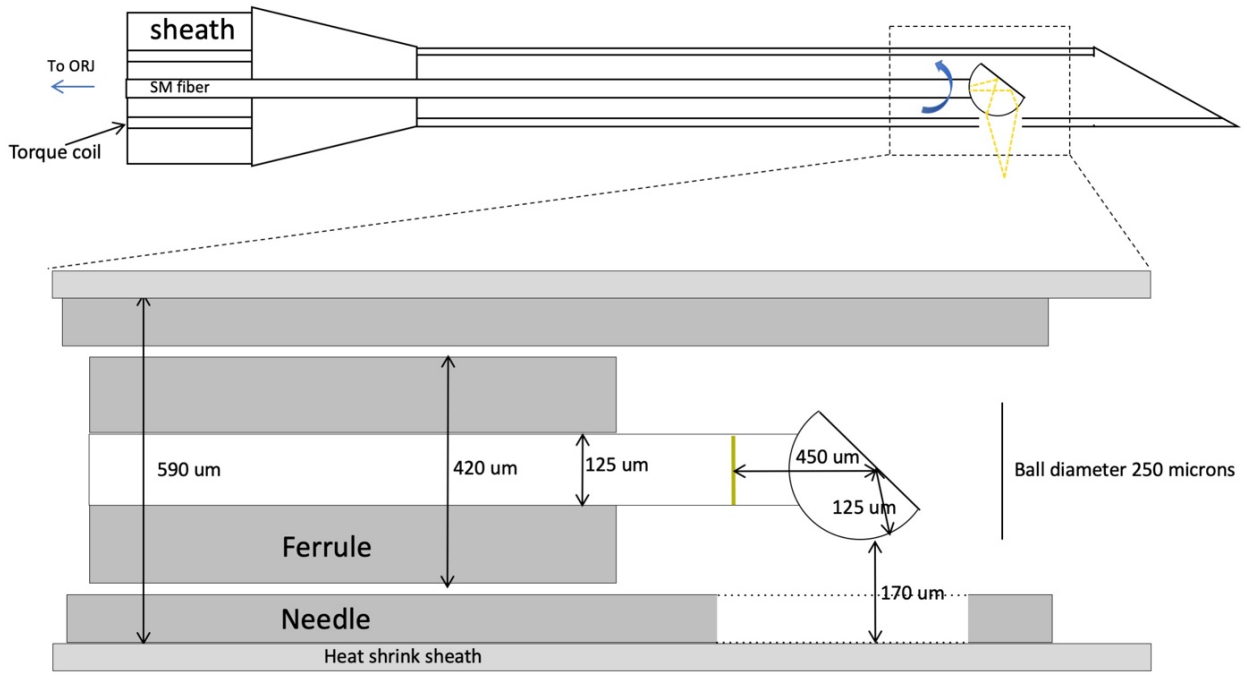

Figure 4.6. Schematic of distal needle probe optical assembly.

The distal probe optics use a design similar to that presented in a previous publication[134]. This design incorporates a single mode fiber pigtail, connected directly to the fiber port on the distal end of the rotating drive shaft, which is spliced to a predetermined length of coreless fiber that is fused to make a ball lens for focusing on sample target. Angle-polishing the ball lens at an angle of 53° allows for total internal reflection from the angle polished surface and a side viewing optical path that provides radial scanning through a tri-spoke window in the hypodermic needle housing. Reference arm signal is achieved by gold coating the interface between coreless and single-mode fibers before splicing them together. Probe rotation is sustained by seating the single-mode fiber firmly inside a torque coil (Asahi Intecc) and running the torque coil-SM fiber unit through a stationary sheath that is fixed to the stationary needle housing with an internal mating sleeve. The steps for fabricating this distal optic assembly are summarized in Figure 4.7.

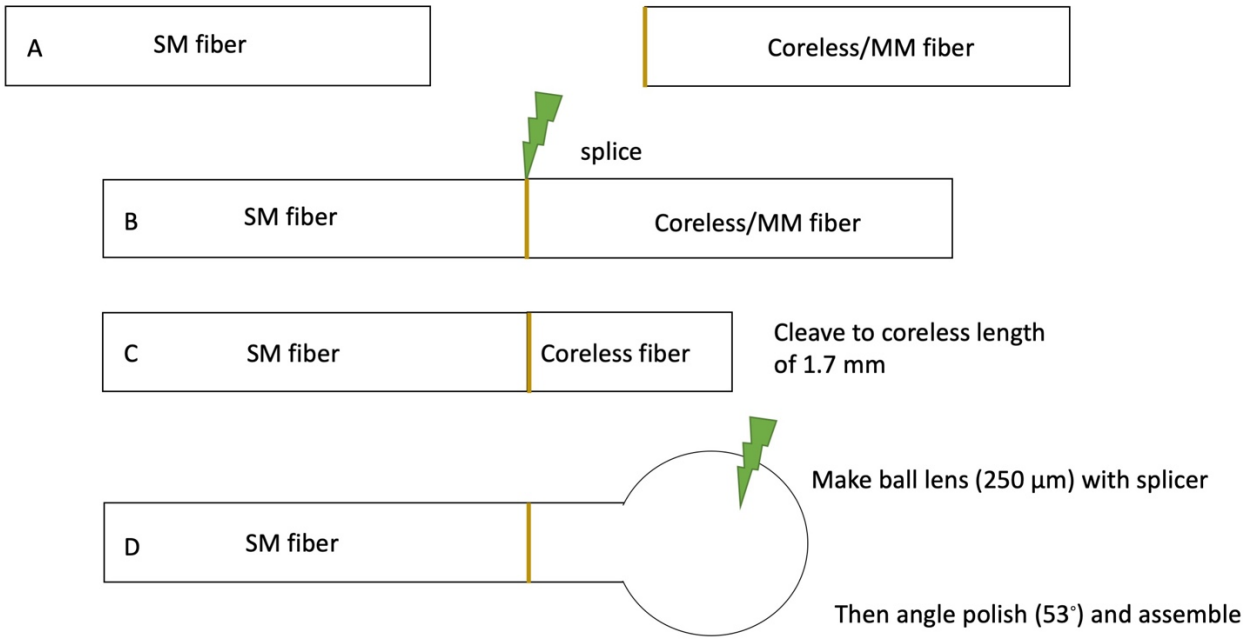

Figure 4.7. Fusion steps to create distal needle probe optical assembly. (A) Flat-cleaved single mode (SM) fiber and 50 nm gold-coated flat-cleaved end of coreless or multimode fiber. (B) Fusion splice of SM to coreless fiber. (C) Cleaving distal end of coreless fiber to precise length for ball lens formation. (D) Create ball lens with arc fusion splicer program.

A summary of the fabrication steps shown in Figure 4.7 follows. A section of coreless fiber (Thorlabs) greater than 5 inches in length is cut from a stock spool and approximately 2 cm of one of the ends of the fiber is stripped of casing, and stripped end is cleaned with alcohol. Then, the stripped fiber end is mounted in the fiber cleaver carefully so that the margin of stripped casing is positioned at approximately 11.4 mm on the ruling scale. Accuracy in this measurement within 0.1 mm is important because after fusion to the single mode fiber the coreless fiber will be cleaved at exactly 10.0 mm to yield a 1.4 mm section of coreless fiber fused on the end of the single mode fiber. The coreless length of 1.4 mm was arrived at by trial and error and needs to be adjusted depending on the size of the ball lens made (here the diameter is 250 micrometers).

To make the internal reference arm interface, the stripped and cleaved coreless fibers are bundled with all ends together for gold sputter coating. Sputter coating was done at the Northwestern NUANCE Center in a Denton Desk IV sputter coater using a gold target; fibers were oriented so that cleaved faces faced upward towards target (face angle horizontal) and were mounted by taping to the sample mount. Gold coating thickness was set at 50 nm in the sputter coater program and fiber ends were coated. Next, the coated coreless fiber is spliced to the flat-cleaved single mode fiber pigtail using an auto-aligning fiber splicer. For this step, it was determined that the plasma arc splicer used (Ericsson FSU 995 PM) destructively ablates the gold coating during the arc fusion procedure, so a CO_2 laser-based splicer (Fujikura AFL LZM 100)

was determined to be essential for this splicing step. For this process, fabrication was contracted to a custom optics company (LaseOptics) with the requisite instrumentation.

Next, the spliced fiber is mounted in a fiber cleaver and the coreless fiber housing margin is lined up at the 10.0 mm mark on cleaver, after which the fiber is cleaved to leave 1.4 mm of coreless fiber on the end of the pigtail. The plasma arc splicer is then used with a pre-set program determined through experimentation to melt the distal coreless fiber end into a spherical ball lens with a diameter of 250 micrometers.

To check the spot profile output of the completed ball lens assembly, a paper target is placed in the far field ~12 inches from the end of the ball lens and the light propagation pattern is observed to determine whether the ball lens assembly is suitable. Example images of common errors and an acceptable spot pattern resulting from this iterative process are shown in Figure 4.8.

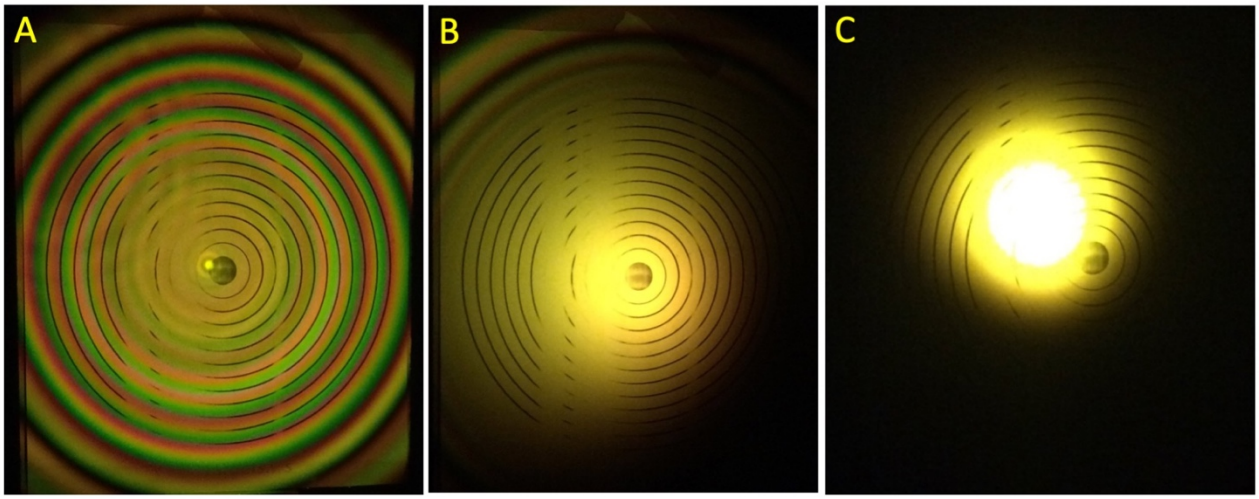

Figure 4.8. Example far field spot pattern from fused ball lens (unpolished) in forward-viewing direction. (A) Example image of spot pattern resultant from a length of coreless fiber that is too long, causing multiple propagation modes and chromatic interference fringes in the far-field spot. (B) Example image of spot pattern resultant from asymmetric ball lens formed from poor

centering in splicer. (C) Example image of acceptable far-field symmetric Gaussian-profile spot pattern resultant from appropriate coreless fiber length and symmetric ball lens fusion.

The completed ball lens is then angle-polished by gluing the ball lens inside a hypodermic needle, mounting the needle/fiber inside a custom 53° angle-polish fiber mount, and polishing on an orbital fiber polisher with a sequence of polishing pads having 3 micrometer to 0.3 micrometer coarseness, then finishing the polishing process with a finishing pad until surface is optically smooth. This sequence of polishing steps is depicted in Figure 4.9 which shows the angle-polished ball lens surface at each step. After polishing, the needle/fiber is soaked in acetone to dissolve the glue and the needle is removed.

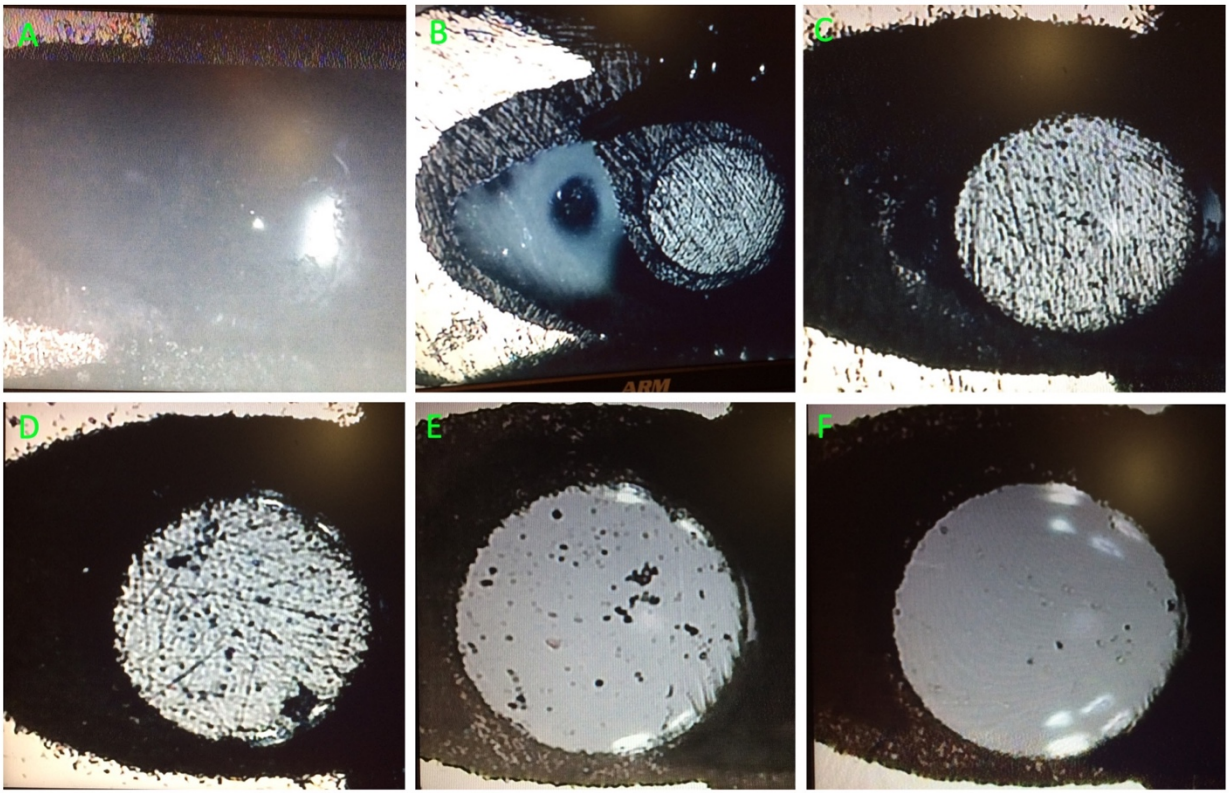

Figure 4.9. Sequence of polishing steps to create side-viewing ball lens. (A) Unpolished ball lens fixed inside hypodermic needle with cyanoacrylate glue. (B-D) Coarse polishing of ball down to angled surface with diameter approaching that of ball (ball diameter ~250 microns). (E-F) Fine polishing of angle surface to optical-quality finish.

The completed angle-polished ball lens assembly is then inspected for optical spot profile output, focal length, and imaging performance. These steps are shown in Figure 4.10. Depending on output, the ball lens is either re-polished in the case of cut-off beam profile or a new assembly is fabricated in the case of issues with focal length (which should be between 1 and 2 mm) or far-field spot profile.

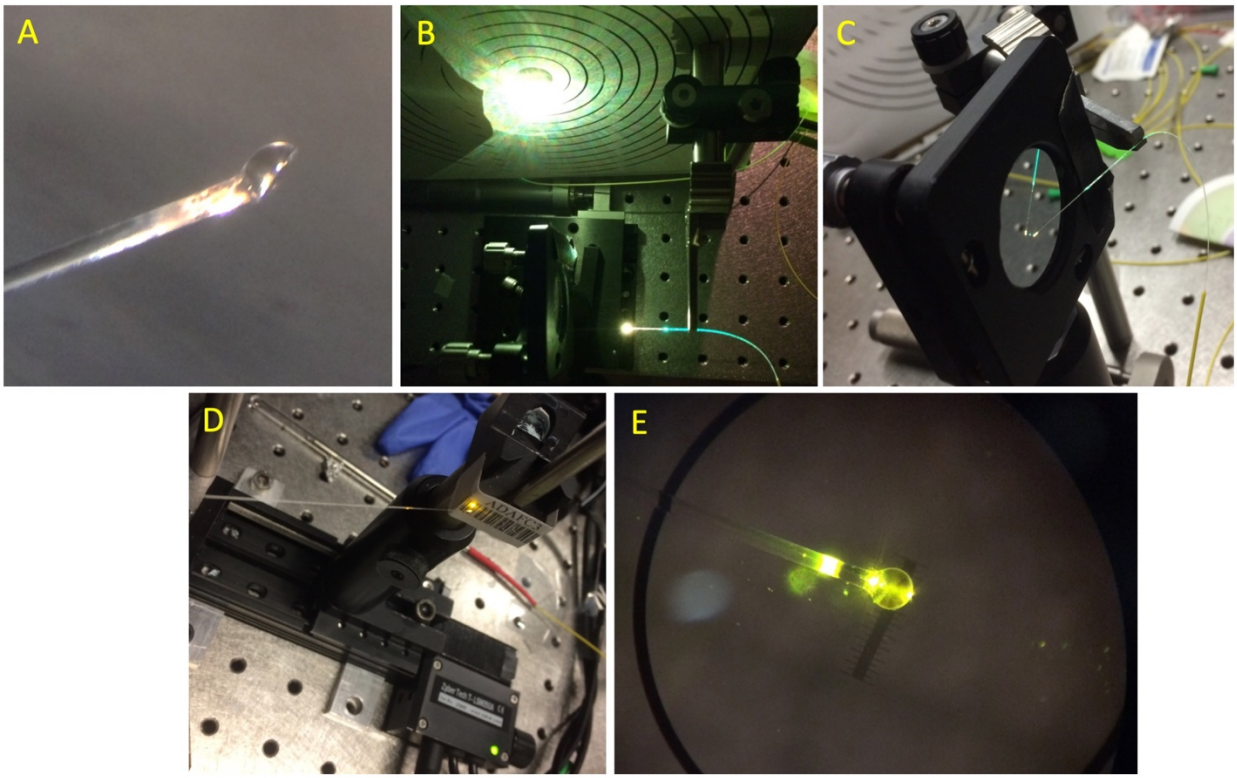

Figure 4.10. Characterization of distal optics assembly. (A) Photograph of angle-polished 250 micrometer diameter ball lens. (B) Validation of side-viewing far-field Gaussian spot profile. (C) Measurement of ball lens side view focal length, measured here to be 1.5 mm. (D) Simple scanning set-up to image paper barcode target. (E) photograph of illuminated probe optics demonstrating diffuse reflection from internal reference interface.

While current development of this probe for imaging performance is still in progress due to inadequate back-reflected signal from the internal gold reference interface which is currently being addressed by a custom optics company as is discussed above, current characterization of this probe indicates this process to be effective at fabrication of an adequately achromatic OCT needle probe. The distal probe optics are threaded through a 24.5 Gauge hypodermic needle with side-cut windows and the single mode fiber is routed through a torque coil (Asahi Intecc) for robust transmission of scanning rotation to the probe. This torque coil is connected directly to the spinning lens tube of the ORJ and rotates inside of a stationary sheath that connects directly to the stationary needle hub in a completed prototype of the visible OCT needle probe system. A video demonstrating the operation of this prototype system with radial beam scanning inside a translucent styrofoam sample is shown in Supplementary video 2.

4.4. Discussion

Here we present the design and construction of two instrumentation approaches for the extension of ISOCT imaging to the measurement of a subcutaneous scaffold implant *in situ*. We demonstrate the performance a of dual visible-IR bandwidth OCT system for the imaging of mouse skin and subcutaneous scaffold implants. While the two-channel OCT imaging developed here produced useful complementary images addressing the common trade-off in OCT imaging

between imaging resolution and penetration, we observed that a large inherent anatomical variability of scaffold location and depth underneath the skin rendered this approach infeasible for potential future clinical use in humans.

The subsequent development of a novel OCT needle probe operating in the visible range was also described. We present the fabrication and characterization of two main modules of this OCT needle-probe system: (1) a custom visible-bandwidth ORJ incorporating visible collimators and a stable high-precision bearing mounted lens tube rotational shaft and (2) a distal hypodermic needle-enclosed optical assembly incorporating an angle-polished side-viewing ball lens with common path in-probe interferometry at an internal reference interface. While this probe system is currently under development and not yet capable of producing reliable images due to a current challenge encountered in the fabrication of the internal reference surface, we foresee its continued development as an important step towards extending high-resolution visible OCT capable of spectroscopic analysis to a wide range of biomedical applications currently limited by imaging penetration depth.

4.5. Supplementary figure

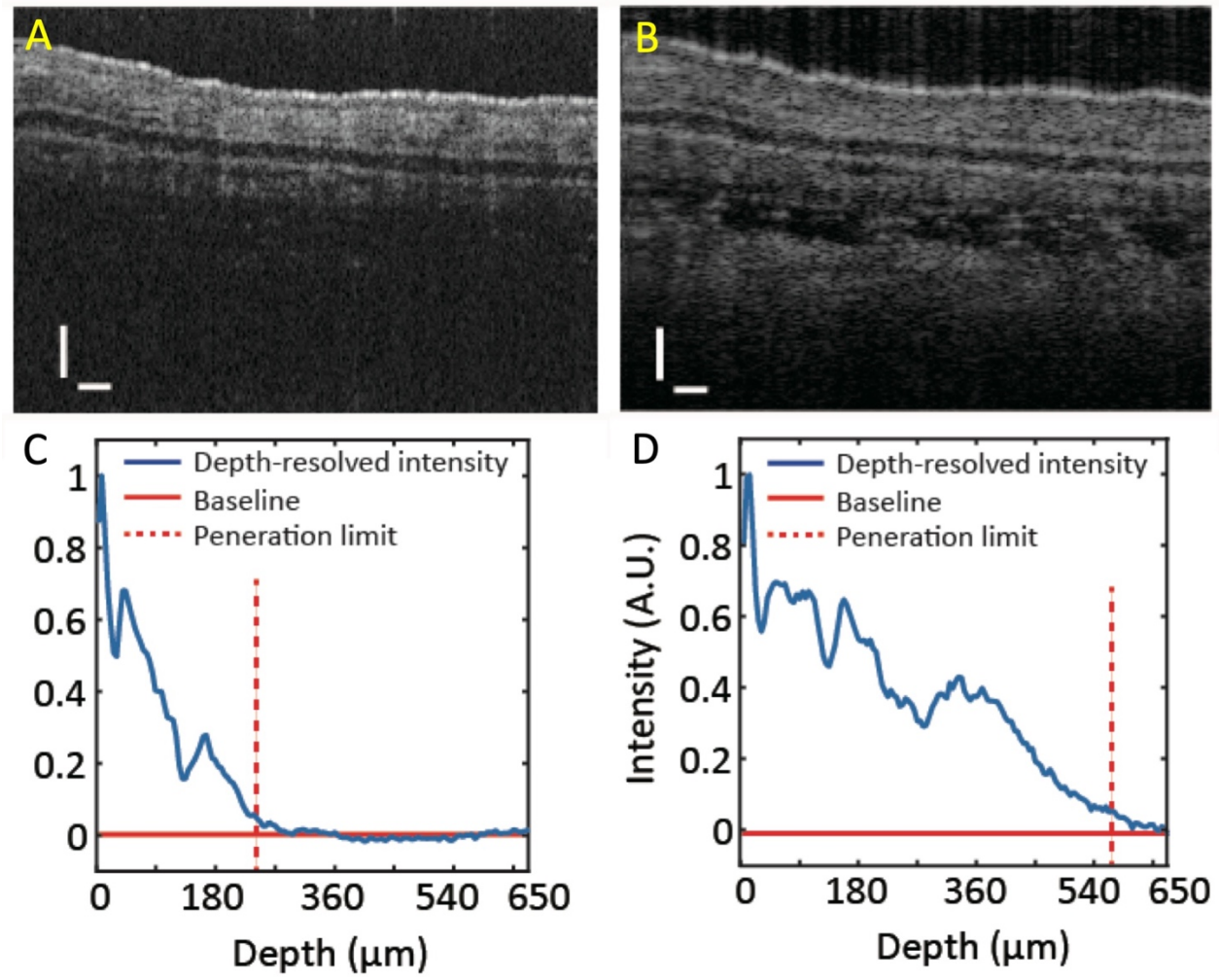

Figure 4.11. Infrared OCT channel produces >twofold increase in penetration depth in skin. Dual band OCT B-scans of depilated mouse ear in (A) visible 520 nm-centered window and (B) IR 1300 nm-centered window (scale bar length 100 micrometers). Penetration depth calculated by depth at which signal decays to 5% of maximum intensity, shown in (C) and (D) for visible and IR bands, respectively. Calculated penetration limits were 240 microns in visible and 570 microns in IR. Figure adapted with permission from reference[2].

Chapter 5:

Identification of structural changes at a synthetic pre-metastatic niche for label-free screening of early metastasis

Authors: Graham Spicer, Grace Bushnell, Aya Eid, Jimmy Winkelmann, Ronald Ellis, Sophia Orbach, Ji Yi, Vadim Backman, and Lonnie Shea

Acknowledgements to Xiang Zhou for assistance with python implementation of neural network

5.1. Abstract

An emerging strategy for the early detection of metastasis is through the implantation of a biomaterial implant that attracts extant circulating tumor cells to a defined, easily-monitored site in the body. Minimally-invasive optical imaging modalities that have been used to image the scaffold for this screening rely on measurements of averaged physical properties of statistical distribution of tissue density to discern the presence of cancer in mice. Physiologic structural changes associated with presence of cancer metastasis at the scaffold leading to this detection capability remain poorly understood. Here we present a comprehensive study to determine the sensitivity of our imaging technique to several leading mechanisms of tissue and scaffold restructuring at this synthetic "pre-metastatic niche". We further validate previous measurement of elevate tissue fractal dimension *D* at the scaffold in the case of advanced disease and perform a quantitative analysis of scaffold histology, collagen content, and gene expression to determine potential metastasis-associated remodeling at the niche. We find cancer-associated differences in fibrosis and angiogenesis at the scaffold explain in part the increase in *D* previously observed in scaffolds from diseased mice, augmenting our understanding of stromal remodeling in the synthetic pre-metastatic niche and suggesting other potential biomarkers for future imaging study of the scaffold for early detection of metastasis.

5.2. Introduction

Metastasis, the spread of cancer cells from the primary tumor to distant tissues, is responsible for over 90% of cancer-related deaths[5]. There is great need for tools to detect metastasis at its earliest stages, when the disease is most manageable by current therapeutics. Currently used techniques for diagnosis of metastasis include computerized tomography scans and magnetic resonance imaging, which can only stage the cancer once metastatic tumors reach a detectable size, typically on the order of several millimeters. Furthermore, circulating tumor cell (CTC) capture techniques for metastatic diagnosis suffer from low sensitivity due to sparseness of CTCs in the body, and more novel strategies incorporating a larger suite of secreted factors and circulating cell-free tumor DNA, termed "liquid biopsies", are still experimental and suffer from limited sensitivity and specificity[135,136]. A potentially transformative approach to early metastasis detection is the use of biomaterial scaffolds to attract and pull CTCs from circulation, concentrating them at a predetermined site in the body for easy surveillance[55]. This strategy has shown promise in attracting tumor cells to both lower metastatic burden in typically colonized organs and in allowing for optical, ultrasonic, secreted factor, and gene expression characterization of the scaffold to correlate with cancer presence in mouse models of breast cancer[1,58–60,118,119].

The phenomenon underlying the recruitment of CTCs to the scaffold is considered to mirror the idea of the "pre-metastatic niche" at a synthetic site in the body[1]. The pre-metastatic niche describes a localized system at a specific tissue site where soluble factors and immune cell recruitment allow for metastatic homing and colonization[38,55]. During this conditioning of a native pre-metastatic niche in the body, in addition to homing factors which attract the cells to the specific site, other stromal remodeling influenced by tumor-shed exosomes containing secreted factors such as VEGF and lysyl oxidase (LOX) modify the extracellular matrix and vasculature in the niche to permit metastatic cell extravasation and growth at the nascent metastatic site[48,137–139].

While the ability of implanted biomaterial scaffolds to recapitulate a similar local immune environment and enabled metastatic homing similar to a native pre-metastatic niche has been characterized, it is still relatively unknown how metastasis-associated stromal reconditioning at the synthetic pre-metastatic niche might mirror a native niche[59,60]. Understanding of specific structural changes that accompany arrival of metastatic cells at the scaffold implant may allow for more informed sensitive screening strategies for metastasis via scaffold monitoring.

A particularly promising imaging technique for minimally invasive monitoring of the scaffold for metastasis-associated changes that would indicate presence of systemic metastasis is inverse spectroscopic optical coherence tomography (ISOCT), which provides 3D images of tissue structure and quantified nanoscale-sensitive mass fractal dimension, *D*, with spatial resolution on the order of several micrometers and penetration depth on the order of 1 millimeter. In studies of scaffold structure in an orthotopic model of metastatic breast cancer in mice, ISOCT was used to measure the *D* from exposed scaffolds, consistently showing a higher *D* value in tumor-bearing mice in comparison with healthy controls[1,60]. This lends *D* as a potential diagnostic parameter for ISOCT screening of metastasis at the scaffold site, but until now it has not been established what changes in tissue structure occur at the scaffold that are associated with the pre-metastatic niche.

In order to better inform screening for structural remodeling at the scaffold that is indicative of metastasis and development of a pre-metastatic niche, we investigated the contributing factors to the observed metastasis-associated increase in *D* at the scaffold. We present a histological evaluation of stromal changes at the scaffold and several *in vitro* models to understand the specific structural changes that are present and to measure the sensitivity of ISOCT to several remodeling processes hypothesized to occur at the scaffold and that explain measurable changes in *D*. Improved understanding of the salient changes in the stroma of the synthetic pre-metastatic niche will provide valuable information for scientific understanding of the niche *in vivo* and practical

information for future design of sensitive imaging modalities for the non-invasive detection of metastasis through scaffold measurement.

5.3. Materials and Methods

5.3.1. PCL microsphere preparation

PCL microspheres to be used for scaffold fabrication were prepared according to a procedure described in a previous publication[1]. Briefly, a 6% (w/w) solution of polycaprolactone dissolved in dichloromethane was emulsified in an aqueous 10% polyvinyl alcohol by homogenization at 10,000 rpm for 1 minute. Microspheres were centrifuged and washed in DI water, then lyophilized to prepare the powder used to make scaffolds.

5.3.2. Scaffold fabrication

For each cylindrical (2 mm thickness, 5 mm diameter) scaffold, 2.5 ± 0.1 mg of PCL microspheres and 75 ± 1.5 mg of NaCl (grain size between 250 and 425 micrometers) were mixed well and pressed in a steel die with a hydraulic press at 1500 psi for 45 seconds. The pressed polymer-salt discs were then heated at 60 ^{o}C for 5 minutes on each side on a hot plate to fuse the PCL particles. Then salt was leached from the discs in 3 changes of deionized water with gentle rocking. Scaffolds were sterilized by soaking in 70% ethanol, then rinsing in sterile water prior to drying and freezing at -80 ^{o}C where they were kept until implantation.

5.3.3. Scaffold implantation

ISOCT and histology studies: All animal studies were carried out according to approved IACUC protocols at Northwestern University and the University of Michigan. For scaffold implantation, 8-10 week old female Balb/c mice (The Jackson Laboratory) were initially

anesthetized and anaesthesia was maintained with isoflurane(2%, inhaled). Each mouse received topical eye ointment and subcutaneous injection of carprofen analgesic (5 mg/kg in lactated ringer's) and the mid-thoracic dorsal skin was shaved and cleaned with betadine swab followed by an isopropanol swab. Next, a ~5 mm long incision was made along the midline in the mid-thoracic dorsal skin on the upper back and blunt dissection of skin from underlying fascia with microscissors created a pocket where two scaffolds (one per side) were inserted as far from the midline as was safely possible. The incision was closed with two wound clips (Reflex 7 mm, Roboz Surgical Instrument Co.), which were applied with hemostatic forceps. Clips were removed within two weeks from initial implantation. Follow-up subcutaneous carprofen (5 mg/kg) analgesic was administered the day following the surgical procedure.

Gene expression, hydroxyproline assay, and early-timepoint histology studies: Scaffold implantation procedures for these studies were the same as above, with the exception that ten scaffolds were implanted per mouse instead of two. To achieve this, two separate ~5 mm long incisions were made along the midline on the upper and lower back of the mouse. Through the incision on the upper back (front), three scaffolds were implanted on the left side and two on the right side, with care taken to dissect a separate pocket for each scaffold to prevent scaffold stacking under the skin. Through the rear incision, three scaffolds were implanted on the left side and two on the right, with special care to place the right-side scaffolds as far forward as to avoid proximity to the mammary fat pat inoculation site.

5.3.4. Tumor inoculation

To induce an orthotopic model of metastatic breast cancer in the Balb/c mouse, we used a 4T1-luc2-tdTomato (Perkin Elmer) cell line that had been subcultured in RPMI 1640 medium. When cells reached a confluency of 80-90%, they were harvested for inoculation and resuspended

in PBS at a concentration of $4x10^7$ cells/mL to give a dosage of $2x10^6$ in a 50 microliter bolus. 28 days after scaffold implantation, the Balb/c mouse was anesthetized with isoflurane (2% inhaled) and the surgical site over the right mammary fat pad was shaved and cleaned with betadine then isopropanol swabs, after which a ~5 mm incision exposed the mammary fat pad. A total of $2x10^6$ 4T1 cells were injected into the fat pad and the surgical site was closed with monocryl sutures and surgical glue (Vetbond). For healthy control group animals, this injection consisted of 50 microliters of sterile 1X PBS. In gene expression studies, this procedure was performed in tandem with scaffold retrieval described below. Carprofen analgesic (5 mg/kg) was administered through subcutaneous injection prior to incision and 24 hours after surgery.

5.3.5. Scaffold retrieval survival surgery

Scaffolds were retrieved 0 (3 scaffolds), 7 (3 scaffolds), and 14 (4 scaffolds) days after tumor inoculation. On day 0 [after inoculation], this retrieval was performed in tandem with the inoculation procedure on the anesthetized mouse. Skin over the scaffolds was shaved and cleaned with betadine then isopropanol swabs, and a 5 mm incision was made immediately adjacent to the center scaffold in the group of 3. Microscissors were used to gently dissect the scaffold from the surrounding skin and fascia, and semken forceps were used to extract the scaffold from the subcutaneous space. The first scaffold extracted was placed in 4% neutral buffered formalin at room temperature for histology, and the next two were both plunge frozen in isopentane chilled on dry ice for later hydroxyproline and gene expression assays. Care was taken to gently dissect surrounding tissue and tease the fibrous capsule from the scaffold for samples intended for freezing and later quantitative assays. At day 14 the mouse was sacrificed before extraction and the final scaffold was placed in liberase digestion buffer for further processing for cell isolation and

resuspension. At both survival timepoints, carprofen analgesic (5 mg/kg) was administered through subcutaneous injection prior to incision and 24 hours after surgery.

5.3.6. Scaffold-derived cell suspensions for ISOCT imaging

For measurement of scaffold-derived cells with ISOCT, the final scaffold extracted at the terminal time point 14 days post-inoculation was removed and placed in 3 mL of Liberase TM (Sigma) in HBSS at a concentration of 0.2 Wunsch units/mL. The scaffold was minced finely with a scalpel then incubated in the liberase digestion buffer for 20 minutes at 37 ºC. Then the digested sample was placed on ice and 750 microliters of 0.5 M EDTA was added prior to straining, mashing, and rinsing through a 70 micron nylon cell strainer with addition of a buffer consisting of PBS, 0.5 wt% BSA, and 2 mM EDTA. The cell filtrate suspension was then centrifuged for 5 minutes at 500 xg and 4 ºC to pellet scaffold-derived cells. Supernatant was gently poured from this tube to leave a pellet and residual buffer with a volume of approximately 50 microliters. A 4 mg/mL collagen gel solution was separately prepared by combining rat tail collagen I (BD Biosciences) in a 0.1% (v/v) acetic acid solution with 1 N NaOH, 10X M199 medium, and DMEM in a proportion previously described to enhance gelation [140,141]. The cell pellet was gently resuspended in an equal volume of this collagen gel solution by pipette trituration careful to avoid introduction of bubbles but thorough enough to provide adequate dissociation and homogenization of cellular distribution through the gel. The 100 microliters of cell collagen suspension for each sample was added to a well of a 24 well plate and incubated at 37 ºC for 30 minutes for collagen gelation. Then the samples were placed on ice and transported to Evanston for ISOCT measurements.

5.3.7. ISOCT imaging and processing of scaffold-derived cell suspensions

The ISOCT instrument used for this study has been described previously[2]. A visible (540-680 nm) OCT bandwidth was used to scan cell suspensions in collagen gels to provide a full 2.5x2.5x2.5 mm scan volume of the sample. Six scans were collected from separate locations in each gel for later statistical analysis. Manual segmentation was applied to scan volumes of each gel to demarcate the top and bottom surfaces of each gel throughout the scan volume, and OCT *en face* images were manually segmented to remove lateral regions of high specular reflectivity. This 3D segmented OCT image volume was then filtered with a gaussian window having full width at half-maximum of 10 micrometers and processed with an intensity-based cell segmentation algorithm which selected volumetric regions with intensity higher than three times the median intensity value within the gel for individual cell cluster segmentation and structural measurement. Volumetric regions of interest smaller than 5 voxels (5x5x5 micron) in size were excluded from further analysis as a lower bound on realistic size of detected cells in the collagen gel. ISOCT analysis for quantification of mean cellular fractal dimension *D* was performed by exponential fitting the backscattering spectrum which was normalized by calibrated scans of a Rayleigh scattering phantom consisting of 80 nm polystyrene spheres (2 wt%) in water[1,54,75–78]. Mean *D* value from each scan was obtained by averaging all voxels that had been previously identified as cells by 3x global median threshold segmentation.

5.3.8. ISOCT imaging of fixed scaffolds

For study of scaffold structure at a late (28 days post-inoculation) timepoint, mice (6 healthy, 6 tumor-bearing) were sacrificed and scaffolds (2 per mouse) were retrieved and fixed in neutral buffered formalin at 4 ^{o}C for one week, allowing for leaching of erythrocytes from the scaffold and crosslinking of proteins. Next, 3 separate 2x2 mm regions on the fixed hydrated scaffolds were scanned with ISOCT for ultrastructure (*D*) quantification, calculated as the

exponential factor of backscattering spectral decay, $I^2(k) \propto k^{4-D}$, where I is OCT signal intensity and k is wavenumber. Scaffolds were then sent to the Northwestern University Mouse Histology and Phenotyping Laboratory (MHPL) for paraffin embedding, sectioning at 5 micrometer slice thickness, and staining with either Masson's trichrome stain or immunostaining with anti-CD-31 for vessel imaging.

5.3.9. Hydroxyproline assay

For hydroxyproline assay of scaffold collagen content, flash frozen scaffolds were weighed to obtain wet weight, then lyophilized for 48 hours and weighed to obtain scaffold dry mass. The scaffold samples were each homogenized at 15,000 rpm (IKA homogenizer) for ten seconds in 500 microliters of deionized water. The scaffold homogenate was added to 500 microliters of concentrated (12 M) hydrochloric acid in a pressure-tight glass vial with silicone seal and heated at 120 ^{o}C for three hours to hydrolyze the sample. 15 mg of activated charcoal was mixed into the scaffold hydrolysate and samples were centrifuged at 10,000 xg for 3 minutes. 10 and 20 microliters of supernatant from each sample were transferred to individual wells of a 96 well plate and dried in a 60 ^{o}C vacuum oven overnight. A hydroxyproline assay kit (Sigma-Aldrich MAK008) was used to create a standard curve from 0-2 micrograms of hydroxyproline standard per well and quantify hydroxyproline content of each scaffold sample by measuring well absorbance at 555 nm on a Synergy H1 plate reader. The standard curve used to convert well absorbance to hydroxyproline concentration is shown in Supplementary figure 5.8 with the corresponding equation used for hydroxyproline content calculation.

5.3.10. Gene expression assay

For gene expression assay of ECM-related genes at the scaffold, flash frozen scaffolds were each added to 800 microliters of Trizol reagent (Fisher) and homogenized at 15,000 rpm (IKA homogenizer) for approximately 15 seconds. Samples were centrifuged at 10,000 xg for 10 minutes at 4 ^{o}C and 700 microliters of supernatant was then transferred to a Zymo-Spin IIICG column (Zymo Research), with following steps for RNA purification performed according to supplied protocol with the RNA extraction kit used (Direct-zol RNA miniprep plus, Zymo Research). Isolated RNA from samples in nuclease free water was analyzed for RNA concentration and purity (A_{260} /A_{280}) using a Nanodrop UV/Vis spectrophotometer. Before cDNA synthesis, RNA was diluted to a concentration of 200 ng/microliter and a SuperScript VILO cDNA synthesis kit (Fisher) was used to create cDNA for all samples in preparation for qPCR amplification. qRT-PCR was performed on all samples using TaqMan Gene expression assays (Fisher) with FAM (6-carboxyfluorescein) dye for ECM-related genes selected due to the prevalence of their encoded proteins in the ECM or their identified cancer-associated activity reported in previous literature. Genes assayed were TIMP1, LGALS3, MMP2, MMP9, COL1A1, COL3A1, COL4A1, FN1, VCAN, LOX, and CTGF with housekeeper control genes GADPH, HMBS, TBP, UBC, and YWHAZ used for expression normalization. Expression normalization was performed according to a previously reported comparative threshold cycle (C_T) method with fold change expression referenced to the average of all control samples across all time points [142]. Reported values in heat map represent log-2 of the calculated fold change.

5.3.11. Scaffold histological processing for cryosectioning

Scaffolds were placed in freshly prepared 4% neutral buffered formalin directly after retrieval and soaked for 24 hours at 4 ^{o}C to allow complete fixation. Then scaffolds were soaked in 1X PBS for 1 hour, followed by soaking in 15% (w/v) sucrose in 1X PBS, then 30% sucrose in

1X PBS until the sample sank. After this, scaffolds were placed in OCT embedding medium (Fisher) supplemented with 30% (w/v) sucrose for 24 hours. Scaffolds were set in the base of small cryomolds with this 30% sucrose OCT medium covering a thin (~3 mm) layer on top, then quickly frozen in a liquid nitrogen-chilled isopentane bath and stored at -80 ^{o}C until they were sectioned at a 14 micron slice thickness in-plane with the scaffold face on a cryomicrotome.

5.3.12. Histological staining

For Masson's trichrome staining of cryosectioned scaffolds, a trichrome stain kit (Polysciences 25088) was used according to the provided protocol. For picrosirius red staining of collagen, a seminal protocol from literature was used as a starting point[143]. To prepare picrosirius solution, Direct Red 80 (Sigma, 365548) was dissolved in saturated aqueous picric acid at a concentration of 0.1% (w/v) . Slides were stained for 30 minutes at room temperature in picrosirius solution then rinsed in acidified water (0.1% w/v acetic acid) before mounting. All histology slides were mounted in Cytoseal 60 mounting medium (Thermo Richard-Allan Scientific). Histology example images of scaffold were acquired on an Olympus IX83 inverted microscope with a DP80 color camera at 10X magnification in either bright field mode for Masson's trichrome-stained slides or cross-polarization mode for picrosirius-stained slides. Images acquired for quantitative collagen area coverage were taken on a Leica DM IL microscope with a DMC2900 color camera through a 2.5x objective.

5.3.13. Statistical analysis

All data shown in charts are reported as mean ± standard error on the mean (SEM). Significance-determining p values were calculated by Student’s two-sided t-test with unequal variances, implemented in either Excel or Matlab.

5.4. Results

5.4.1. ISOCT detects metastasis-associated scaffold restructuring in advanced metastatic disease

In an orthotopic model of metastatic breast cancer in a mouse, poly(ε-caprolactone) (PCL) scaffolds were implanted bilaterally into the subcutaneous dorsal space of 14 BALB/c mice, with two scaffolds implanted per mouse. After allowing the implant site to heal for 5 weeks, 7 of the mice were inoculated with 4T1 mouse metastatic breast cancer cells in the mammary fat pad[1]. Skin covering the scaffold was shaved and depilated for transdermal ISOCT imaging of the scaffold in the live animals using a dual-band ISOCT apparatus with simultaneous visible (510-720 nm) and infrared (1225-1375) bandwidth imaging for complementary imaging resolution and penetration, respectively. Example OCT B-scans of the scaffold *in situ* in a live mouse are shown in Supplementary figure 5.9. Scaffolds were then excised and fixed in NBF, measured with ISOCT, and sent for histological processing. A schematic of this experimental design is shown in Figure 5.1(A). Measured *D* values from the scaffold were significantly higher in tumor-bearing mice compared to healthy controls, shown in Figure 5.1(B).

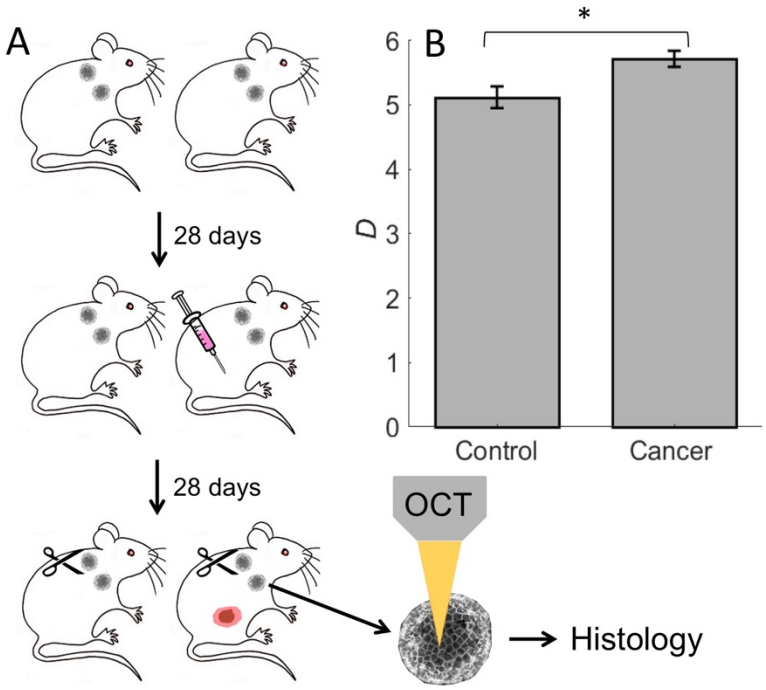

Figure 5.1. ISOCT detects changes in scaffold structure associated with cancer. (A) Flowchart for ISOCT animal experiment. (B) Average ISOCT *D* values of scaffolds from healthy (N = 71 regions) and tumor-bearing mice (N = 71 regions), (*$p < 0.01$).

5.4.2. Collagen deposition at the scaffold is increased in tumor-bearing mice

To investigate the hypothesis that differential collagen deposition associated with pre-metastatic remodeling of the scaffold microenvironment is a contributing factor to previously measured differences in scaffold *D* between healthy and tumor-bearing mice, we performed a histological analysis of collagen content in scaffolds measured in Figure 5.1(B). Formalin fixed-paraffin embedded 5 micron thick sections of these scaffolds were stained with Masson's trichrome, which stains collagen fibers blue, nuclei dark purple, and skeletal muscle, blood, and other structures red. Thus, blue collagen can be colorimetrically segmented from microscope images of these histology sections, an image processing sequence of which is shown in

Supplementary figure 5.9. Then, the proportional areal coverage of collagen in these sections was computed as a direct metric of collagen content and fibrosis at the scaffold. We observed a wide variability in the degree of this fibrosis in the scaffold, as evidenced by example images of scaffold sections with relatively low (Figure 5.2(A)) and relatively high (Figure 5.2(B)) collagen content. Overall, a significantly higher degree of scaffold fibrosis was observed in scaffolds from tumor-bearing mice when compared with healthy control (Figure 5.2(C)).

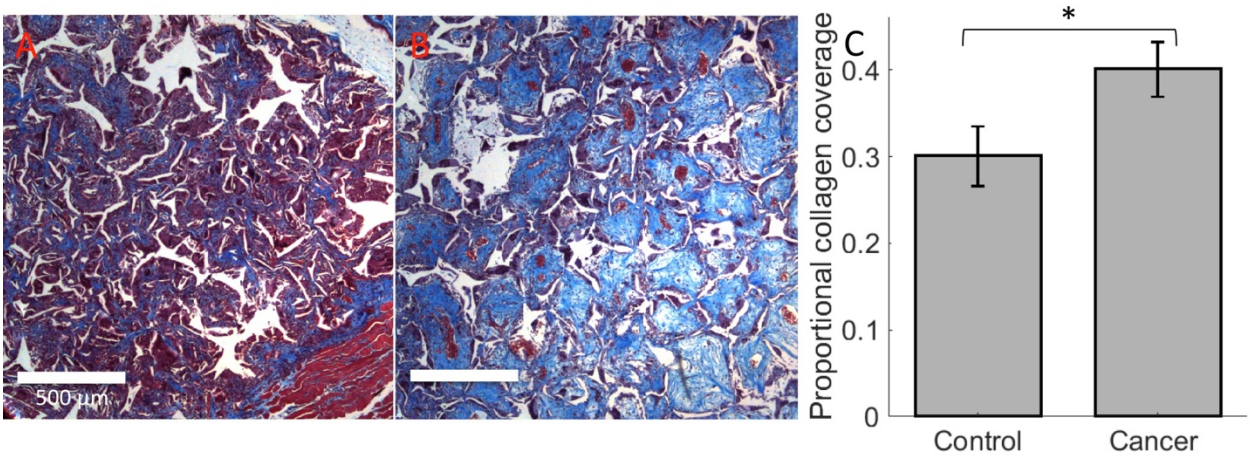

Figure 5.2. Increased fibrosis is observed in scaffolds from tumor-bearing mice. Example histology images of Masson's trichrome-stained scaffold sections showing relatively (A) low and (B) high levels of collagen (blue staining) deposition in the scaffold. (C) Higher collagen deposition observed in scaffolds from tumor-bearing mice (N = 12 scaffolds) compared to healthy control (N = 11 scaffolds) 28 days after tumor inoculation/mock inoculation (*$p < 0.05$).

In addition to study of scaffold structure at this late (28 days post-tumor inoculation) timepoint, we studied the early progression of differential changes in scaffold structure at 0, 7, and 14 days post-inoculation in the same model. A hydroxyproline assay was used to quantify hydroxyproline

content from scaffolds as a direct measure of collagen content at these early time points, results of which are shown in figure 5.3. While no significant differences in hydroxyproline content are observed between scaffolds from healthy and tumor-bearing groups, a one can discern relative trend of increasing hydroxyproline content with time in scaffolds from tumor-bearing mice in comparison to the healthy control for each time point.

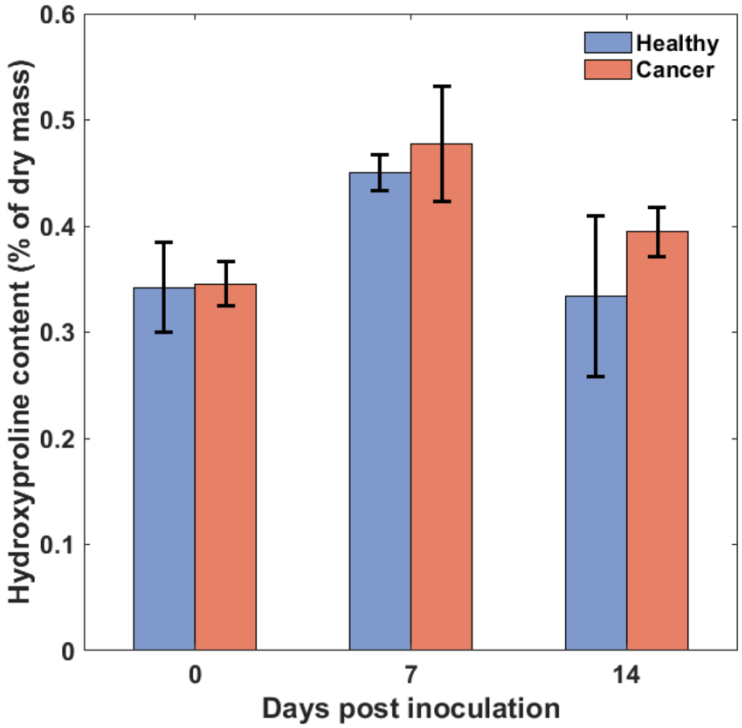

Figure 5.3. Hydroxyproline assay quantifies early fibrotic changes at the scaffold. Hydroxyproline content of scaffolds (weight % of scaffold dry mass) from healthy and tumor-bearing (Cancer) mice 0, 7, and 14 days post-tumor inoculation. N = 4 (Healthy) and N = 6 (Cancer) animals/scaffolds per bar.

A contributing effect to these measures of collagen content from the bulk scaffold is fibrous encapsulation of the scaffold, a typical effect observed in the foreign body response. Prior to any

tumor inoculation, this encapsulation can be well-observed in face-plane histological sections through the center of the scaffold taken 28 days after initial implantation, examples of which are shown in Supplementary figure 5.11, which clearly show intense blue staining from trichrome (figure 5.11(A)) and high birefringence from picrosirius red with polarization microscopy (figure 5.11(B)) at the edges of the scaffold.

5.4.3. Dysregulated angiogenesis in the scaffold is associated with metastasis

To investigate the hypothesis that neovascularization of the scaffold implant and associated angiogenic processes are differentially regulated due to the presence of system metastasis or a primary tumor, we used anti-CD31 immunohistochemical staining on scaffold sections to visualize vessel distribution in scaffolds measured in Figure 5.1(B). In these stained sections, an example of which is shown in Figure 5.4(A), dark blue/purple staining indicates cell nuclei, light blue indicates other tissue structures, and dark brown indicates presence of CD31 positive cells, which is a marker for endothelium. Thus, this marker can be used as a credible contrast agent for enhancing the appearance of vessel walls in histology slices. While a human can recognize these stained vessel walls with practice, a simple color, morphology, and/or intensity-based segmentation algorithm has difficulty with reliable segmentation of these features, especially considering the presence of non-specific staining artifacts prevalent in immunohistochemical staining. For these reasons, we trained and employed a convolutional neural network for segmentation of vasculature from these stained sections, followed by binarization of the output confidence mask and binary-shape based filtering for final refinement of the vessel segmentation mask. An example sequence of these image processing steps is shown in Supplementary figure 5.12. From these segmented vessel maps, we quantified average vessel area (Figure 5.4(B)), percentage of section area covered in CD31-positive cells (Figure 5.4(C)), and vessel density, calculated as number of vessel objects per square

millimeter in the histological section (Figure 5.4(D)). While this density of vessels did not show a significant difference between scaffolds from healthy control and tumor-bearing (cancer) mice, both the average area/diameter of vessels and the coverage of endothelial cells showed significantly higher levels in scaffolds from tumor-bearing mice, indicating differential angiogenic activity at the scaffold is a marker for metastatic cancer.

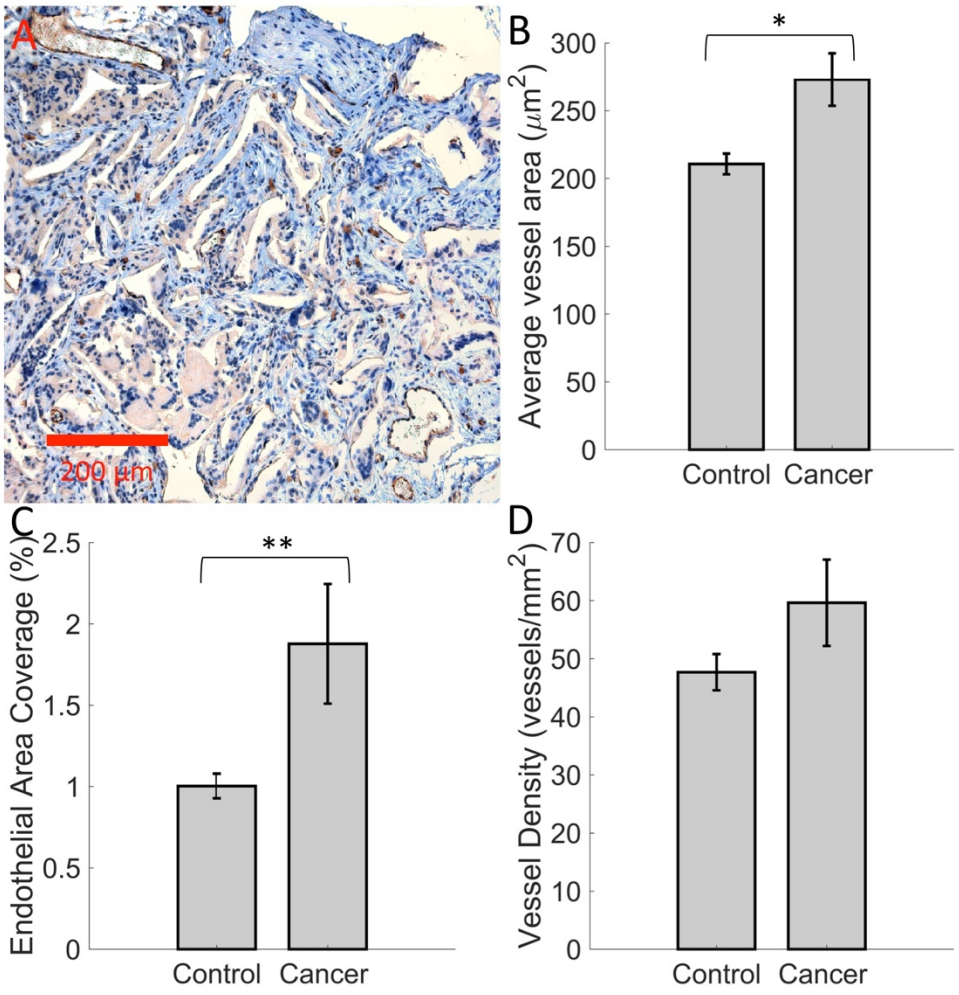

Figure 5.4. Scaffold vasculature changes characterized with CD31+ IHC staining. (A) Example CD31+ IHC-stained (brown) scaffold section with hematoxylin staining nuclei (dark

blue). (B-D) Vasculature metrics obtained from deep-learning segmentation of vessels from scaffold sections (*$p < 0.01$, **$p < 0.05$).

To understand how this effect might manifest in optical scattering measurements of tissue ultrastructure such as with ISOCT, we modeled angiogenesis *in vitro* using human umbilical vein endothelial cells (HUVECs). One hypothesis for the cause of differential angiogenesis at the scaffold is exosomal delivery of vascular endothelial growth factor (VEGF) or other potential angiogenic factors secreted by a hypoxic primary tumor. We modeled this by treatment of HUVECs with and without VEGF, then measured their nuclear structure with live-cell PWS microscopy to quantify the degree of chromatin compaction in the nucleus. In addition to displaying increased proliferation (not shown), HUVECs treated with VEGF showed a significant increase in nuclear RMS, a metric directly related to chromatin fractal dimension, *D*, which is shown in Supplementary figure 5.13.

5.4.4. Cells isolated from scaffold show increased fractal dimension *D* measured with ISOCT

To understand how different cell populations recruited to the scaffold affect the *D* values measured from the whole scaffold with ISOCT, we conducted a study to isolate cells from the scaffold and measure them directly in identical matrices with ISOCT. In an early-timepoint model of the study described in figure 5.1(A), mice were sacrificed 14 days after tumor inoculation and cells were isolated from extracted scaffolds, then re-suspended in collagen gel. Then, the cell suspensions were imaged with ISOCT, followed by segmentation of cells from their matrix and averaging of *D* values from segmented cells. The 3D imaging capability of OCT allowed for accurate segmentation of cells with a threshold algorithm, due to the cells being visible as highly scattering structures. Cells from scaffolds extracted from tumor-bearing mice filled a larger percentage of their gel volume (Figure 5.5(a)), indicating there were potentially more cells resident

in these scaffolds compared to those extracted from healthy mice. Furthermore, these cells showed a higher average *D* value (Figure 5.5(b)) compared to those from healthy mice, supporting the hypothesis that cellular structure could be a contributing factor to the previously observed difference in signal in measurements of *D* with ISOCT from the bulk scaffold.

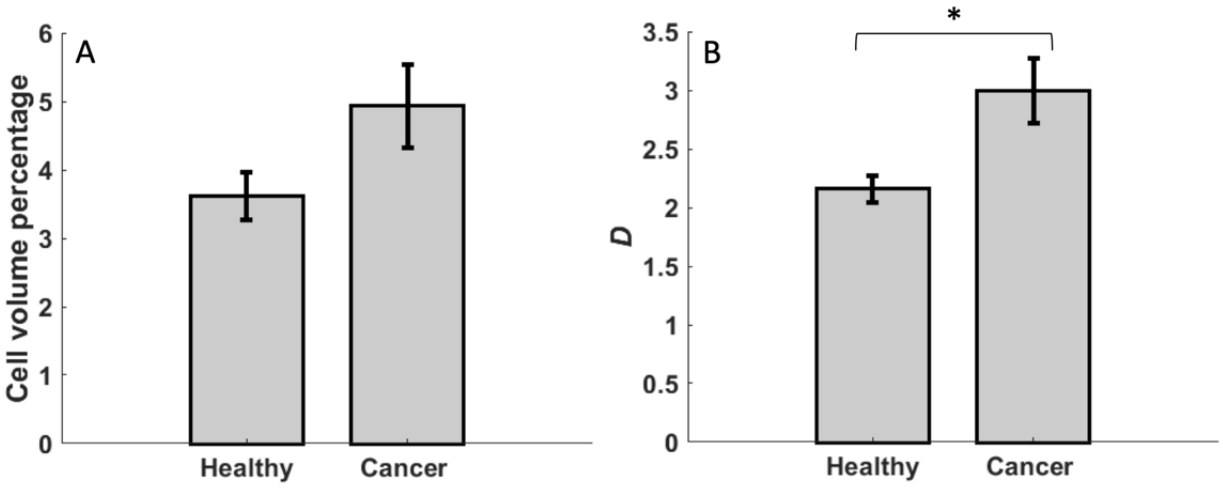

Figure 5.5. Results from ISOCT measurement of scaffold-derived cells resuspended in collagen gel. (A) Volume percentage of gel sample occupied by cells extracted from scaffold. (B) Average *D* value of 3D segmented cells in gel, measured with ISOCT (*$p < 0.05$).

5.4.5. Degree of scaffold degradation does not affect fractal dimension *D* measured with ISOCT

To study of the effect of scaffold degradation on ISOCT *D*, poly(lactide-co-glycolide) (PLG scaffolds) were immersed in deionized water and imaged with ISOCT for the preliminary timepoint. Sodium hydroxide was then added to the scaffolds to a concentration of 0.05 M in order to accelerate the degradation reaction. Scaffolds were subsequently imaged at several timepoints until disintegration in solution, mean *D* values for which are shown in figure 5.6(C).

Environmental scanning electron microscopy was used to image the nanoscale structure of scaffold topography during scaffold degradation, example images of which are shown in figure 5.6(A) (untreated) and figure 5.6(B) (partially-degraded) scaffolds. Furthermore, the nanoscale imaging capability of ESEM allowed for independent characterization of the nanoscale-sensitive mass fractal dimension measured with ISOCT. To do this, ESEM images were taken of the surfaces of new, partially-degraded, and fully-degraded PCL scaffolds and the image autocorrelation function was fit to the Whittle-Matern model to determine the fractal dimension *D* from the image. Similar to the findings with ISOCT shown in Figure 5.6, results from this technique shown in Supplementary figure 5.14 found no significant changes in scaffold fractal dimension with increased degradation, indicating that differential degradation of scaffolds would not contribute to a change in the ISOCT signal measured in previous metastasis studies.

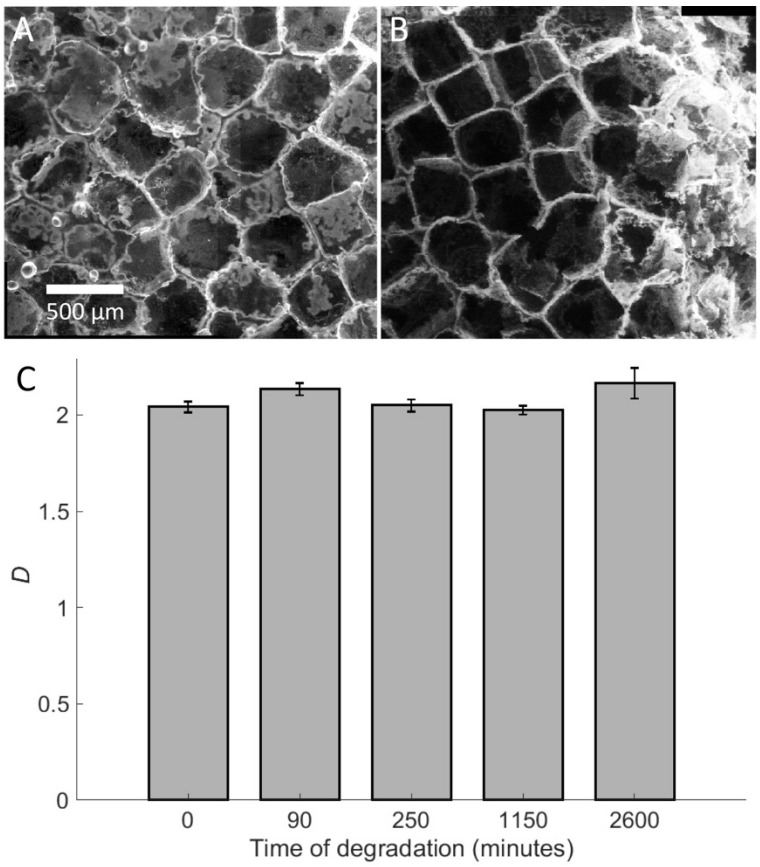

Figure 5.6. Scaffold degradation does not lead to significant change in *D* measured with ISOCT. Representative ESEM micrograph of (A) untreated and (B) partially degraded scaffolds. (C) ISOCT-measured *D* from scaffolds as a function of degradation showed no significant change as scaffolds degrade.

5.4.6. ECM-related gene expression at the scaffold characterized during early metastatic progression

To understand how gene expression might play a role in the early restructuring of the scaffold site in the case of metastasis, we performed reverse transcription-quantitative polymerase chain reaction (RT-qPCR) analysis to quantify relative levels of expression from a suite of ECM-related genes of interest in bulk scaffold samples from healthy and tumor-bearing mice 0, 7, and

14 days after tumor inoculation. A heatmap of the relative expression for these genes for all samples is shown in Figure 5.7(A). Bar plots showing changes in relative expression between groups for 3 collagens (COL1A1, COL3A1, and COL4A1) are shown in Figure 5.7(B-D), respectively. Interestingly, while structural and assay data suggests a potential increase in collagen protein expression even at these early time points, the RNA transcript levels reported here either do not show a difference or show a relative decrease for cancer scaffolds, in the case of collagen 3. A significant relative decrease in TIMP1 expression was observed between healthy and control mice, warranting further investigation as a potential gene of interest associated with structural remodeling of the pre-metastatic niche.

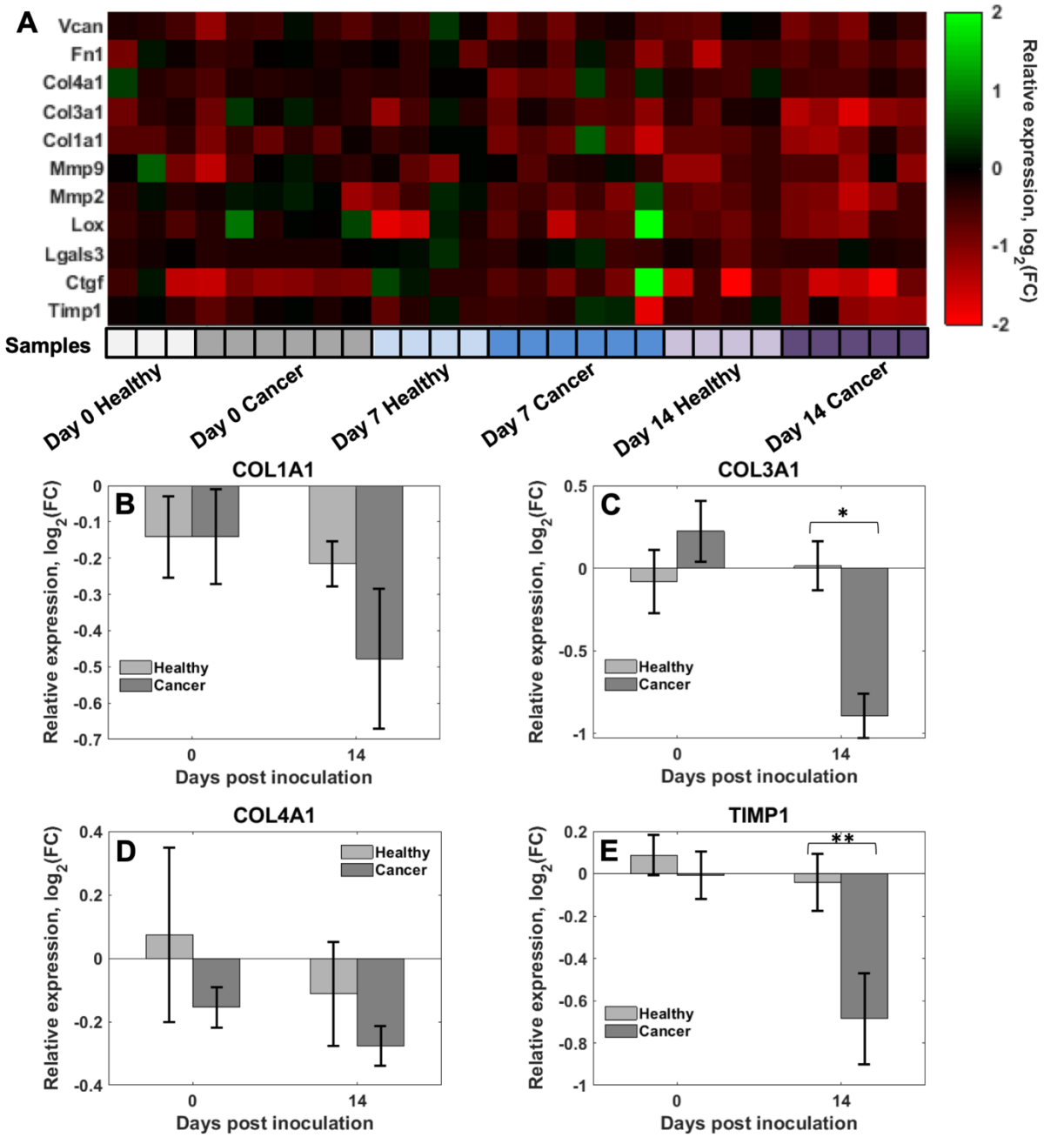

Figure 5.7. Measurements of ECM-related gene expression at the scaffold in healthy and tumor-bearing (cancer) mice using RT-qPCR. (A) Gene expression heatmap showing $\log_2$(fold-change) of normalized gene expression in comparison to global expression from scaffolds in healthy animals for all genes measured (Col1a1, Col3a1, Col4a1, Fn1, Lox, TIMP-1, CTGF,

MMP-2, MMP-9, LGALS3, VCAN) at days 0, 7, and 14 post-inoculation. (B-E) comparison of relative expression of COL1A1, COL3A1, COL4A1, and TIMP1, respectively, between scaffolds from healthy and tumor-bearing mice 0- and 14-days post-tumor inoculation (*$p < 0.005$, **$p < 0.05$).

5.5. Discussion

In this study, we used ISOCT imaging analysis to confirm previously reported findings that *D* measured from scaffolds in tumor-bearing mice is significantly higher than in scaffolds from healthy mice in this orthotopic model of metastatic breast cancer (4T1 cells) in immunocompetent Balb/c mice[1,60]. A distinction of this study is that this measurement was made at a much later time point than previously reported, 28 days post-inoculation compared to much earlier detection reported in earlier studies. Furthermore, scaffolds measured here were leached, which removed most of the blood which was previously suspected to contribute to elevated *D* values through uncompensated spectral absorption effects; however, the findings here show that other structural effects are contributing to true differences in elastic scattering signal from the scaffold. Collagen crosslinking and cancer cell structure (nuclear chromatin) have previously been suggested as possible causes for elevated *D* in the presence of carcinogenesis at the scaffold and other tissues used for pre-cancer detection through quantification of mass-fractal dimension [60,77,144–146]. However, direct and independent measurement of these changes for correlation with optical spectroscopic scattering techniques has thus far been scant.

Here we sought to directly test main hypotheses underlying the previously measured changes in scaffold *D* associated with presence of metastatic cancer in the mouse. These hypotheses included differences in collagen deposition and remodeling, angiogenesis, scaffold degradation, and bulk cellular structure associated with development and reconditioning of the

synthetic pre-metastatic niche. We tested these hypotheses by modeling these processes *in vitro* to determine ISOCT sensitivity to different sources of structural remodeling and by direct independent study of scaffold structure and constituent compartments with quantitative histological, chemical, and molecular biology techniques.

It has been established in prior work that ISOCT is sensitive to enzymatic crosslinking of collagen, which manifests in higher *D* values as degree of crosslinking increases [54,60]. In principle, while concentration of collagen in a pure hydrogel will not change the theoretical fractal dimension of its mass density distribution, in tissue collagens are synthesized, crosslinked, and deposited in a complex matrix including other ECM proteins and proteoglycans. Remodeling of the ECM is largely performed by resident fibroblasts and macrophages, which perform ECM deposition, degradation, and crosslinking through secretion of enzymes, proteins, and mechanical traction[94,147–150]. Therefore we anticipated a differential fibrosis response in the scaffold to display concomitant changes in collagen deposition and crosslinking, manifesting in both more collagen being deposited and changes in its potential orientation, fiber thickness, and fiber length, previous morphological metrics associated with crosslinking[102,151]. Histology of scaffolds retrieved 28 days after tumor inoculation revealed significantly higher collagen coverage in tumor-bearing animals compared to healthy controls (Figure 5.2), suggesting that differential fibrosis and ECM remodeling at the scaffold could be a contributing factor to differences in ISOCT signal, especially considering relatively high optical scattering from collagens in the visible[80,81,152,153]. Analysis of hydroxyproline content at earlier time points 0, 7, and 14 days post inoculation using a chemical assay showed no significant difference between groups (Figure 5.3), however a trend is observed that as time after inoculation progresses, a larger relative increase becomes apparent in hydroxyproline content of the scaffolds from tumor-bearing mice. Hydroxyproline constitutes approximately 13% of collagen mass and only about 1% of elastin mass, making it a good

estimator of collagen content in tissue[154]. The data presented here in Figure 5.5 indicate average scaffold hydroxyproline content on the order of 0.4% of scaffold dry mass, which translates collagen content on the order of 5% of dry mass. The fibrous encapsulation of scaffolds as a normal chronic stage of the foreign body response[56,57,155] certainly contributes to this metric, since although fibrous membrane structures were teased from the scaffolds during extraction, permeation and close adhesive encapsulation of the scaffold is well-observed from full face scaffold images shown in Supplementary figure 5.11.

Angiogenesis at a nascent metastatic site is required for further metastatic progression and growth of micrometastases[156]. In the development of the pre-metastatic niche, tumor derived secreted factors including angiogenic growth factors VEGF and PIGF circulate throughout the body, affecting tissues of the pre-metastatic organ[138]. Endothelial progenitor cells recruited to the pre-metastatic niche, along with endothelial cells, mediate angiogenesis at metastatic foci[50,157]. A well-established effect of VEGF signaling in endothelial cells is an increase in intracellular calcium concentration, which has been shown to increase chromatin condensation in the nucleus of HeLa cells[52,53]. We hypothesized that differential regulation of angiogenesis at the scaffold, a synthetic pre-metastatic site, could be a contributing effect to cancer-associated scaffold remodeling based on well-known observations of dysregulated angiogenesis at primary tumors and their secreted angiogenic factors, and more recent study of the role of VEGF in formation of the pre-metastatic niche and tumor-cell secreted exosomes containing VEGF[158–161]. To study angiogenesis at the scaffold, we used CD31 IHC staining to identify blood vessels in histology sections and employed a convolutional neural network for vessel segmentation from images of these sections [162]. We found that although changes in scaffold vessel density between healthy and tumor-bearing mice were non-significant, there was a significant increase in vessel area (mean vessel diameter) and area coverage of CD31+ endothelial cells in segmented IHC sections. This

finding is corroborated by recent flow cytometry data showing significantly higher populations of CD31+/CD45- endothelial cells in scaffolds from tumor-bearing mice in the same experimental model[118]. Implications of this increased and/or dysregulated angiogenesis at the scaffold include the possibility that leaky vasculature or enhanced permeability and retention may be a latent effect in scaffolds from tumor-bearing mice. This effect warrants further study for systemic delivery of therapeutics to the scaffold and more importantly for a more targeted investigation into blood supply and diffuse hemoglobin measurement in the scaffold for cancer detection. For this application, recently developed visible OCT algorithms that harness characteristic peaks in the hemoglobin absorption spectrum for angiography could provide additional diagnostic insight [163].

In addition to study of cancer-associated changes in stromal architecture in the scaffold, the structure of cells residing in the scaffold also has the potential to strongly affect diagnostic signal measured from the scaffold. While it is unlikely that the singular presence or absence of tumor cells strongly affect scaffold scattering signal due to their miniscule (<0.1%) proportion of all cells in the scaffold determined by flow cytometry [1], it is established that myeloid-derived cells recruited to the scaffold show distinct phenotype and populations in the presence of cancer[1,55,58,60]. Recent study using spectral ultrasound imaging determined that the structure of scaffold-derived cells can account for the cancer-associated difference in signal measured with the technique from the whole scaffold[118]. Furthermore, preliminary single cell RNA-sequencing analysis of cell populations at scaffolds (performed by and shared courtesy of Sophia Orbach, PhD in the Shea Lab) from healthy and tumor-bearing mice in the same model presented here (unpublished) suggest relatively decreased neutrophil populations and increased macrophage populations at scaffolds in tumor-bearing mice (49.9% of cells, compared to 38.1% in healthy group), the latter which are primarily responsible for the foreign body response but also play an important role in ECM degradation and remodeling. Furthermore, it has been reported that macrophages can be highly

reflective sources of OCT signal and visualized *in vivo* with high resolution OCT due to this additional scattering contrast, which may coincide with significant differences in measurable ultrastructure with ISOCT [124,164,165]. In this study we tested the hypothesis that ensemble structure of the cell population resident in the scaffold contributes to increased *D* in mice with cancer by isolating cells from the scaffold, resuspending them in identical volumes of the same collagen gel matrix, and measuring the cells with ISOCT. We measured a significantly higher *D* value in cells derived from cancer scaffolds compared to healthy control, and also observe a non-significant increase in the volume of these cells, indicating that there are more and/or larger cells in scaffolds from tumor-bearing mice. In addition, while endothelial cells do not make up a sizable proportion of cells in the scaffold (0.5% in healthy mice and 1.6% in tumor-bearing mice, determined from preliminary single cell RNA sequencing data), their stimulation with VEGF results in a significant increase in their nuclear chromatin packing, quantified by the fractal dimension-related parameter RMS using PWS microscopy shown in Supplementary figure 5.13. It is possible other stimulation of scaffold resident cells with other secreted factors similarly affects nuclear chromatin structure, leading to measured changes in ISOCT signal from the bulk cells, as has been previously reported through experimentation with histone deacetylase inhibition to influence chromatin structure[77,116].

In addition to potential changes in biological components of the scaffold, the underlying scaffold architecture was thought to also contribute to the scattering signal collected with ISOCT. Direct scanning of a bare scaffold produces a strong OCT image, and this can be attributed to the strong refractive index gradient between the PCL (n = 1.46) and water (n = 1.33) in the visible, however this is lessened after tissue ingrowth which is expected to reduce this mismatch to a value approaching that of inherent tissue heterogeneity. In the body, a PCL scaffold implant encounters a foreign body response, whereby initial recruitment and activation of innate immune cells initiate acute inflammation at the scaffold [166]. In the model used for this study, experimental groups were

only differentiated by tumor inoculation after this acute response had subsided and normalized to a chronic response 28 days after initial implantation, where activated macrophages and foreign body giant cells are main players in interaction with the biomaterial surfaces[56,166,167]. These cells are responsible in part for the biodegradation of PCL *in vivo*, whereby after a first initial step of random hydrolytic cleavage of ester groups throughout the bulk of the polymer which reduces PCL molecular weight, fragments of the partially degraded polymer are internalized by activated macrophages, fibroblasts, and foreign body giant cells and are fully degraded by intracellular and enzymatic mechanisms [167–170]. Due to the differential recruitment of myeloid lineage cells associated with the systemic metastasis in this model, we hypothesized that differential regulation of these processes could potentially contribute to a difference in scaffold degradation and ISOCT signal. To model this degradation *in vitro* for ISOCT and independent ESEM-based nanoscale imaging study, we accelerated the natural hydrolytic cleavage of the PCL polymer by lowering the ambient pH of the aqueous surrounding medium with 0.05 M sodium hydroxide. While enzymatic degradation can occur, the simplest and dominant mechanism of degradation *in vivo* is this hydrolytic cleavage step that is common to many polyester biopolymers including PLG, degradation of which was also quantified in this study but not reported here [171–174]. We observed no significant changes in D values of scaffolds in ISOCT scans regardless of the degree of degradation, and ESEM imaging autocorrelation analysis similarly characterized surface texture changes but no significant change in fractal dimension from the fitted Whittle-Matérn functional model [3] was observed, even up until complete collapse of the scaffold. Therefore, we conclude that scaffold degradation is not a significant contributor to the differential ISOCT signal previously observed between scaffolds in healthy and diseased mice.

While we observed here a degree of increased cancer-associated fibrosis in the scaffold in advanced cancer (Figure 5.2) and also potentially at earlier time points (Figure 5.3), this

information raises several questions regarding the biological cues and mechanisms underlying differences in stromal remodeling and fibrosis at the scaffold that could be potentially exploited for future screening strategies. To better understand the potential changes in these processes, we conducted a gene expression analysis of ECM-related genes to identify specific genes of interest and correlate with observed expression of collagen in histology. These genes of interest were selected due to their encoding for common ECM proteins and proteoglycans (COL1A1, COL1A1, COL1A1, FN1, VCAN), their role as enzymes or inhibitors responsible for ECM remodeling especially implicated in cancer and metastasis (MMP2, MMP9, LOX, TIMP1), or other related genes of particular interest in ECM-related processes associated with metastasis (LGALS3, CTGF)[46,49,50,105,175–186]. Here we performed RT-qPCR analysis of their relative expression at the scaffold in healthy and diseased mice 0, 7, and 14 days after tumor or mock tumor inoculation, shown in Figure 5.7. Interestingly, levels of collagen gene expression or expression of most genes surveyed did not display significant changes. However, the average relative expression for some genes decreased over time relative to the day 0 time point; included in these were COL3A1, which showed a significant decrease inexpression compared to healthy control 14 days post-inoculation. TIMP-1 also showed a significantly decreased expression compared to healthy control at this time point. While the levels of RNA transcripts for ECM proteins reported here do not reflect the observations of their final expression from histology, the significantly lower TIMP-1 expression in diseased scaffolds could suggest increased MMP activity in the scaffold due to its role as an inhibitor of these metalloproteinases. While the majority of gene expression studies at the scaffold have focused on diagnostically different genes of interest that are primarily associated with inflammatory responses at the scaffold, the analysis here presents some new insight into matrix-associated gene expression levels at the implant during early metastasis[119].

In conclusion, the study presented here provides novel insight into the specific metastasis-associated stromal changes occurring at a subcutaneous implant in a mouse model of metastatic breast cancer. We present a complementary *in vitro* study of modeled structural changes in the scaffold implant to better understand the dominant sources of previously and currently verified metastasis-associated differences in scaffold fractal dimension *D* measured with ISOCT. At a (28 days post-tumor inoculation) time point, we observe significant increases in *D*, scaffold collagen area, vessel size, and endothelial area. At earlier (7, 14 days) timepoints, we observe non-significant increases in collagen content and resident cell volume but significant changes in resident cell *D* (increased in diseased animals) and relative expression of COL3A1 and TIMP1 (decreased in diseased animals). We also conclude that the degree of scaffold degradation does not affect *D* measured with ISOCT. Together, these results indicate that measurable changes in scaffold structure arise from an increased fibrotic response and recruitment/activation of cells with higher fractal dimension that are both associated with systemic metastasis in a mouse model. Due to this ensemble of structural compartments leading to the changes in cancer-associated fractal dimension, it is likely that continued investigation and development of techniques to measure this bulk parameter with higher sensitivity will be of merit in imaging-based cancer screening from the scaffold. Furthermore, enhanced fibrosis of the scaffold and increased blood vessel size may prove as valuable complementary biomarkers to *D* in future iterations of optical coherence tomography modalities incorporating both quantitative birefringence and spectral contrast angiography capabilities[163,187].

5.6. Supplementary Figures

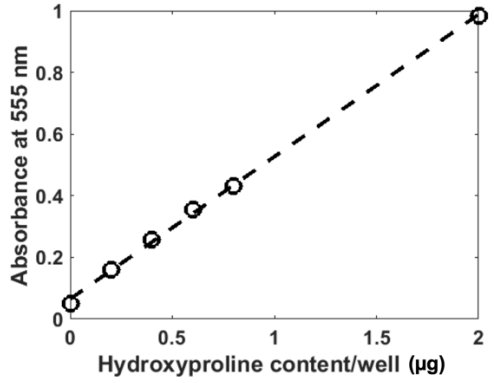

Figure 5.8. Standard calibration curve for hydroxyproline assay. All measured absorbances at 555 nm from sample wells fell within this linear range of the calibration curve with R^2 of 0.999. Calibration equation used for hydroxyproline content: $Mass_{hydroxyproline}(micrograms) = (A_{555} - 0.0654)/0.04612$.

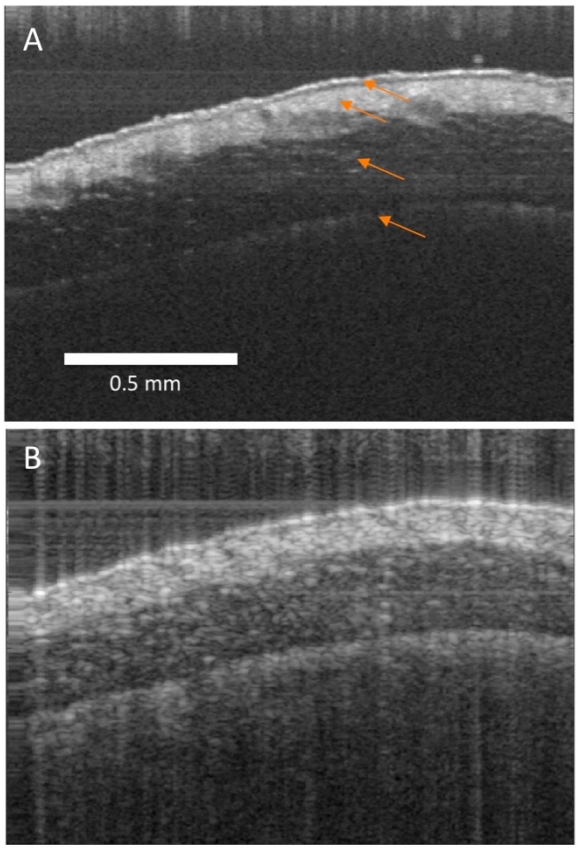

Figure 5.9. Representative OCT B-scans of subcutaneous PCL scaffolds in Balb/c mice from (A) visible (544-678 nm) and (B) infrared (1225-1375 nm) channels. Arrows in (A) point to epidermis, dermis, subcutaneous fat, and scaffold with increasing depth.

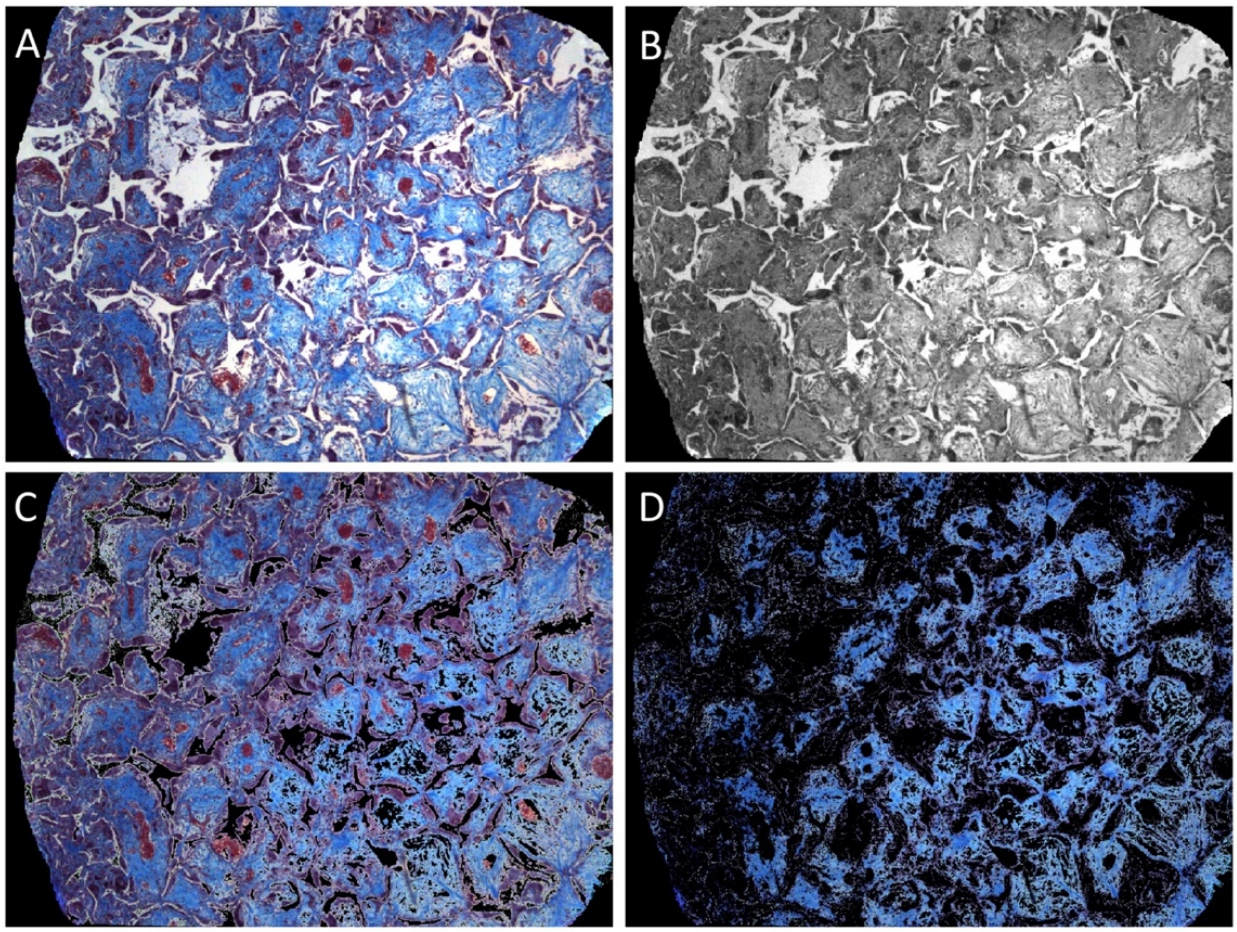

Figure 5.10. Processing of Masson's trichrome images to determine proportional collagen coverage. (A) Original RGB image of scaffold with manually segmented region of interest. (B) Gray scale image of (A). (C) Masked (A) based on intensity threshold applied to (B). (D) Masked from RGB image where blue value above threshold and red value below threshold. Proportional collagen coverage calculated as nonzero area of (D) divided by nonzero area of (C).

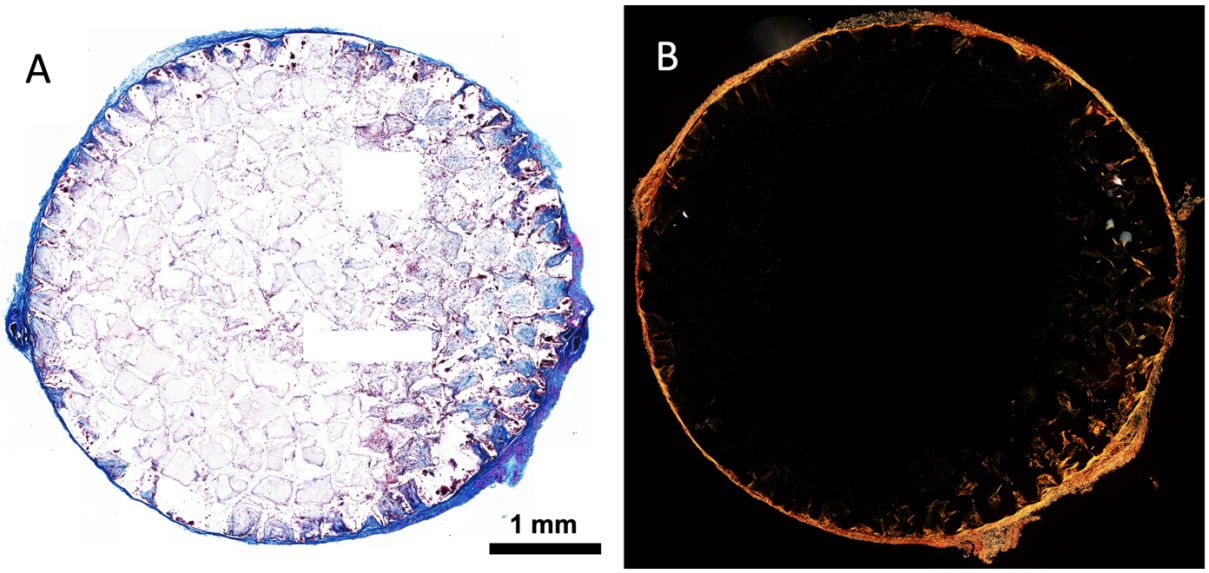

Figure 5.11. Collagen distribution in scaffold is concentrated at the peripheral fibrous capsule. (A) Masson's trichrome stain of scaffold section through center of scaffold, showing collagen deposition (blue) heavily on margins of scaffold. (B) Picrosirius red staining with cross-polarization microscopy of an adjacent slice of the scaffold shown in (A), demonstrating highly birefringent fibrous encapsulation of scaffold.

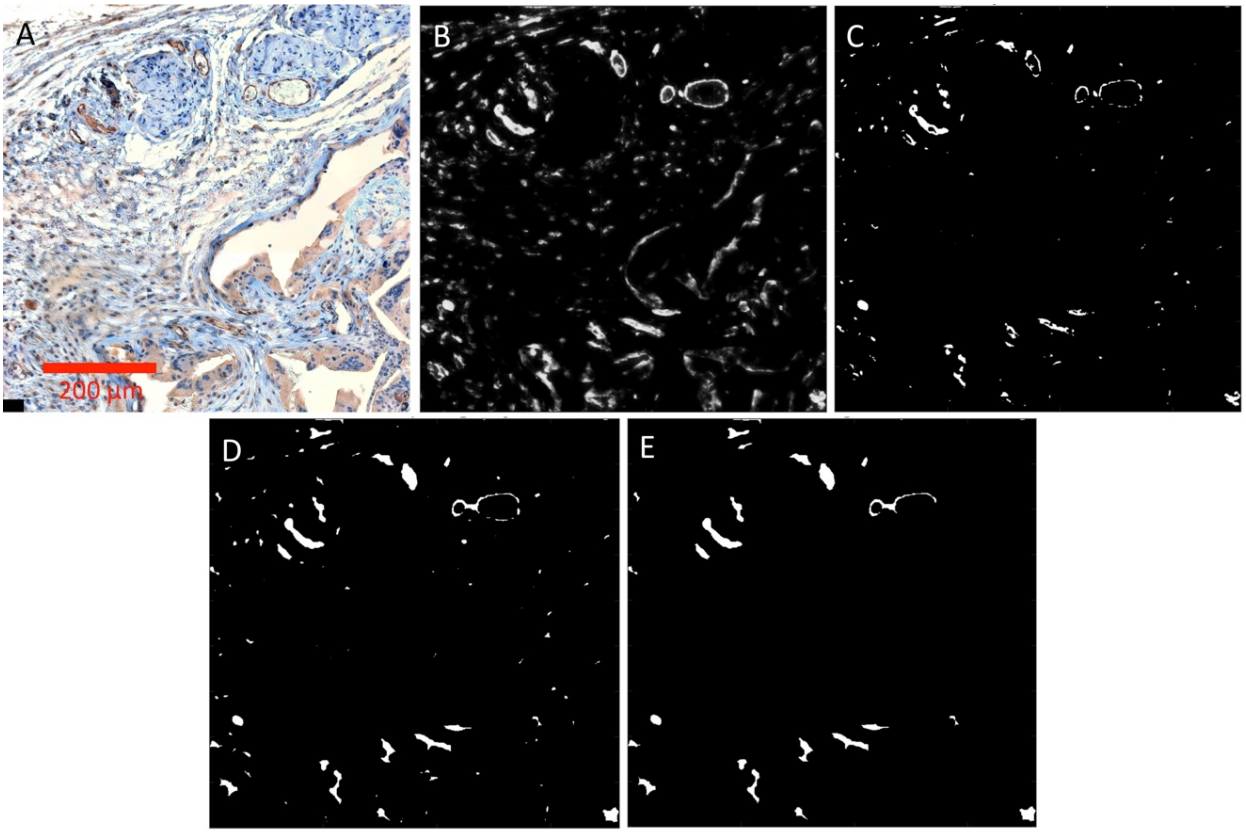

Figure 5.12. Deep-learning based segmentation of vessels from CD31+ IHC stained sections. (A) Original microscopy image of CD31+ IHC stain (brown) with hematoxylin staining for nuclei (blue). (B) Segmentation confidence map output from trained convolutional neural network scaled from 0 (black) to 1 (white) where 1 represents full certainty that the region is a vessel. (C) Resultant binary ROI mask from adaptive thresholding of confidence map in (B). (D) Binary mask after morphological closure of segmented regions in (C). (E) Final binary vessel mask achieved from removing small objects and subsequent morphological closure of segmented structures.

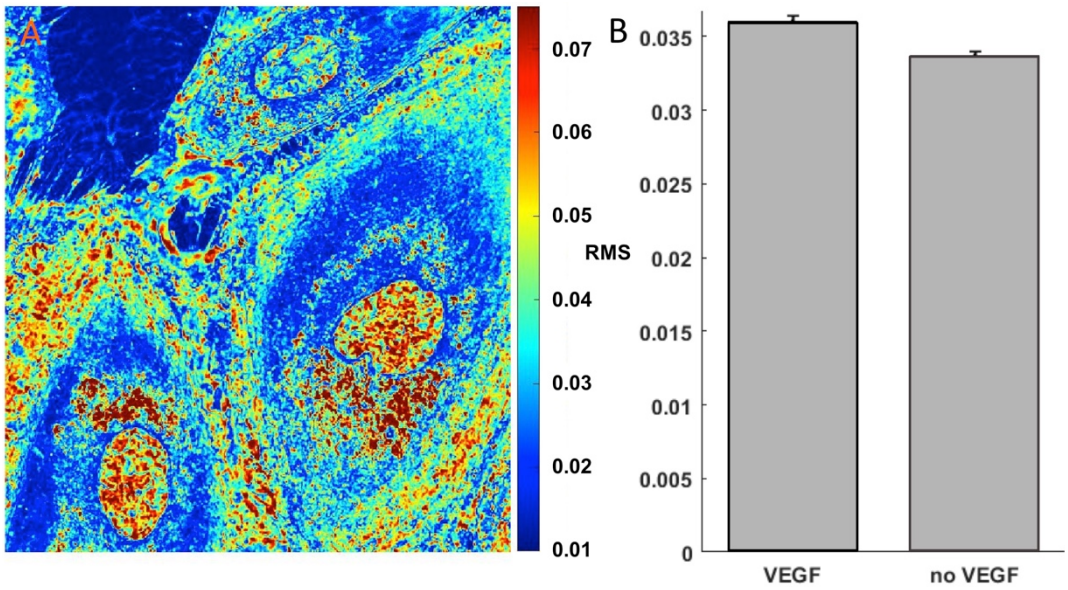

Figure 5.13. Live-cell PWS quantifies change in endothelial nuclear structure associated with VEGF. (A) Example map of RMS values from live HUVECs. (B) Mean RMS values from HUVEC nuclei show increase in RMS associated with VEGF treatment ($p < 0.001$).

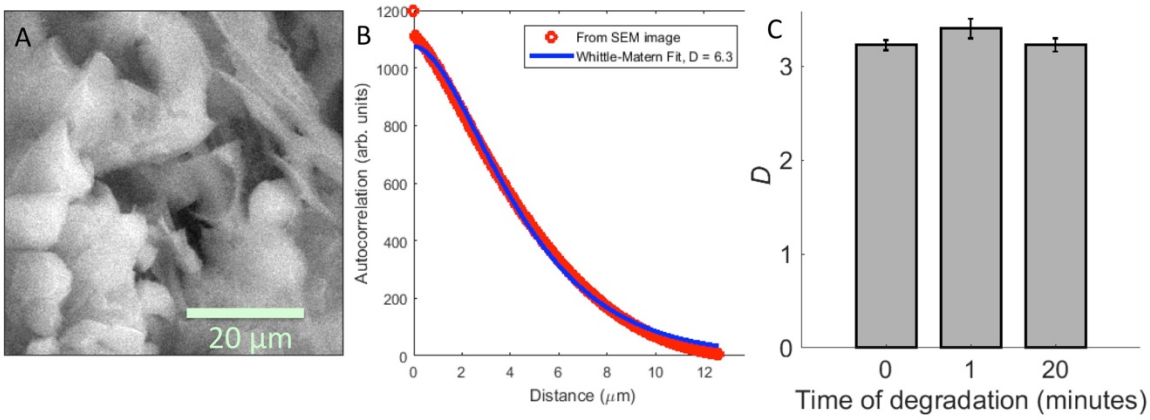

Figure 5.14. Autocorrelation analysis of ESEM-images of scaffolds independently measures *D*. (A) ESEM micrograph of scaffold surface showing surface structure. (B) Example autocorrelation function of ESEM image along with corresponding fit from Whittle-Matérn function. (C) Average *D* values calculated from autocorrelation analysis of scaffold ESEM micrographs reveal no significant difference between fresh and degraded scaffolds.

Chapter 6:

Label free localization of nanoparticles in live cancer cells using spectroscopic microscopy

Authors: Graham Spicer, Luay Almassalha, Ignacio Martinez, Ronald Ellis, John Chandler, Scott Gladstein, Di Zhang, The-Quyen Nguyen, Seth Feder, Hariharan Subramanian, Roberto de la Rica, Sebastian Thompson, and Vadim Backman

6.1. Abstract

Gold nanoparticles (GNPs) have become essential tools used in nanobiotechnology due to their tunable plasmonic properties and low toxicity in biological samples. Among the available approaches for imaging GNPs internalized by cells, hyperspectral techniques stand out due to their ability to simultaneously image and perform spectral analysis of GNPs. Here, we present a study utilizing a recently introduced hyperspectral imaging technique, live-cell PWS, for the imaging, tracking, and spectral analysis of GNPs in live cancer cells. Using principal components analysis, the extracellular or intracellular localization of the GNPs can be determined without the use of exogenous labels. This technique uses wide-field white light, assuring minimal toxicity and suitable signal-to-noise ratio for spectral and temporal resolution of backscattered signal from GNPs and local cellular structures. The application of live-cell PWS introduced here could make a great impact in nanomedicine and nanotechnology by giving new insights into GNP internalization and intracellular trafficking.

6.2. Introduction

In the last few decades, GNPs have become widely used in a variety of biological disciplines, such as cancer treatment and diagnostics[188,189], drug delivery[190], and plasmonic sensors[191], among others[192]. There are several benefits associated with the use of GNPs, including their photostability and low cellular toxicity. Furthermore, GNPs with different morphologies and sizes can easily be fabricated and functionalized with a variety of polymers and bioresponsive ligands[193,194]. This provides a flexible platform for imaging biological systems because the optical properties of the particles can be finely tuned based on the spectral needs of the experimental design. However, there are many unanswered questions about the interaction between GNPs and cells regarding GNP uptake, localization, and phototoxicity[195].

Techniques for tracking GNPs in cells, such as two-photon microscopy[196], dark-field microscopy[197], Optical Coherence Tomography[198], Magnetic Resonance Imaging[199], and many others[200] have been able to adequately image GNPs but present some limitations. Dark-field microscopy results in low phototoxicity for the cells and is based only on the light scattered by the GNPs. However, previous studies have shown that the signal from light scattered by the cell's organelles may combine with the characteristic spectrum of light scattered by the GNPs, thus obscuring the signal from the nanoparticles[201]. The other commonly used technique, two-photon microscopy, is based on the nonlinear excitation and resulting luminescence emission from GNPs irradiated with a pulsed laser. However, the use of a high-power laser leads to phototoxicity, making two-photon microscopy unsuitable for some applications. Other imaging techniques such as optical coherence tomography or photoacoustic imaging may be used for *in-vivo* imaging of GNPs in tissue by harnessing their characteristic absorption properties, but these techniques also lack the necessary spatial resolution to study intracellular localization of GNPs[202–204].

Recent studies using hyperspectral dark-field microscopy (HDM) offer a promising alternative for studying GNPs inside cells[201,205]. The main advantage of HDM is its ability to simultaneously image and obtain scattering spectra from GNPs. Together, this information allows for the spectral identification and differentiation of light scattered by the cell's organelles and by internalized GNPs. Hyperspectral reflected light microscopy (HRLM) has also been implemented to extend the capabilities and performance of hyperspectral microscopy for 3D localization and spectral identification of GNPs in fixed cells[14]. In this study, we present the application of a new HRLM method, termed live-cell partial-wave spectroscopic (PWS) microscopy, where the spectrally-resolved interference of scattered and reflected reference signal allows for the imaging, tracking, and spectral analysis of gold nanoparticles (GNPs) in live cancer cells. Light incident upon a GNP has a characteristic spectrally-dependent probability of absorption due to plasmonic resonance, along with a characteristic scattering signal from the GNP, which is affected by this absorption spectrum and the size of the particle. PWS measures the spectrally-resolved interference between light scattered from structures within a cell and a reference signal created by the Fresnel reflection between a glass coverslip and the cell. The capability of live-cell PWS for label-free study of native nanostructure of nuclear chromatin has been demonstrated previously[206]. Here, we apply this technique to also study the response of nuclear structure to treatment of live cancer cells with GNPs. This new hyperspectral reflected light microscopy technique can address current questions regarding the relationship between the aggregation of GNPs and their uptake by cells[207].

6.3. Materials and Methods

6.3.1. Live-cell PWS Instrument

The live-cell PWS instrument is described in a previous publication. Briefly, sample illumination is a low numerical aperture beam from a high power broad-spectrum LED source (Excelitas X-Cite 120 LED). During all imaging, cells are kept in a stage top incubation chamber kept at 37 C with 5% CO_2 atmosphere. For this imaging, cells are plated and grown in glass-bottom imaging dishes with an imaging window of number 0 glass coverslip. Scattered light from the sample is collected with a high numerical aperture oil-immersion objective (63x, NA = 1.4) and passed through a liquid crystal tunable filter (LCTF) that was programmed to sweep through a wavelength range from 500-700 nm in 1 nm increments for spectrally-resolved acquisition of the interference signal.

6.3.2. AOTF PWS Instrument

The HRLM instrument used in this experiment, consisted of an automated Epi-illumination widefield microscope with spectrally tunable illumination as described previously[208]. Broadband light from a Xenon lamp (66902,100W, Oriel Instruments, Stratford, Connecticut) was spectrally filtered by an AOTF (HSI-300, Gooch & Housego, Orlando, Florida). The spectrally filtered illumination light was then passed through an aperture stop to set the illumination numerical aperture (NA ~ 0.15) before illuminating the sample. Scattered light from the sample was collected using a high-NA objective lens (40X, NA = 0.6, LUCPlanFLN, Olympus, Center Valley, Pennsylvania). Images corresponding to each illumination wavelength, typically 500-700nm with 1 nm steps, were acquired using a high-speed CMOS camera (Hamamatsu, ORCA-Flash 2.8, Bridgewater, New Jersey). Raw data consisted of a hyperspectral image cube $I(x,y,\lambda)$ containing spectra at each pixel in the acquired image.

6.3.3. Cell Culture and Nanoparticle Treatment

HeLa cells were obtained from ATCC and were grown in Dulbecco's modified Eagle's medium supplemented with 10% Fetal Bovine Serum (FBS). Cells were maintained in a 37°C, 5% CO_2 humidified environment. Cells were trypsinized and plated on glass imaging dishes for imaging experiments after a two-day incubation. For incubation with GNPs, media was supplemented with 100 nm diameter methyl polymer functionalized gold nanoparticles (Nanopartz #C11-100-TM-50, Nanopartz Inc., Loveland, CO, USA)) at a concentration of 4E6 nanoparticles/mL, after which the cells were incubated for 24 hours prior to imaging. Immediately before imaging, the medium was replaced with fresh, GNP-free imaging medium through a triple-rinse procedure.

6.3.4. Data Analysis and Imaging process

Aggregated GNPs selectively reflect and scatter light at different wavelengths, creating a characteristic reflection spectrum at the far field. The locations of spectral peaks are determined by the size of the nanoparticles and other interfacial characteristics. To identify nanoparticles of various sizes, a spectral analysis can be useful. Since the locations of the peaks are unknown, images at a single wavelength will not identify all the nanoparticles. Here we propose using (root mean square) RMS as the indicator of nanoparticles. RMS is defined as the root mean square of the zero-mean intensities in the spectrum:

$$RMS = \sqrt{\frac{1}{N}\sum_{i=1}^{N}(I(\lambda_i) - \bar{I})^2}$$

Where N is the number of wavelengths, I denotes the spectrum of reflection normalized by the illumination intensity, $\bar{I}$ represents the mean intensity over the wavelength band. For each pixel of interest, RMS is large when a nanoparticle of any size is present and is small when there are no

nanoparticles. Although a cell without nanoparticles can also cause oscillations in backscattered spectra, the amplitude of these oscillations is much weaker than that obtained from nanoparticles[209]. Furthermore, sizes of nanoparticles (large/small) can be identified by the average reflectance. The bright field reflectance image is obtained by averaging all wavelengths from the reflected image between 500 and 700 nm. Bright Field Reflected Images (BFRI) are obtained by averaging the full interference image along wavelength in the range between 500 and 700 nm.

6.3.5. Temporal dynamic imaging and analysis

To image temporal dynamics of nuclear motion, HeLa cells were cultured and treated as described in section 6.3.3. Cell Culture and Nanoparticle Treatment. Then, a timecourse imaging protocol was implemented to measure the full 500-700 nm backscattering interference spectrum with 1 nm spectral resolution every 3 seconds in order to create a 250 frame, 12 minute long timecourse movie of cell structure quantified by RMS. To create temporal kymograph images of nucleus structural dynamics, an arbitrary arc was drawn across the nucleus for a spatial line profile of RMS which was plotted for every time point to create the kymograph. To quantify possible changes in temporal dynamics, the nuclei of all cells in each frame were segmented and average variance with respect to time was computed for each pixel in the nucleus. The calculated variances from all pixels in the nucleus were averaged together to calculate the mean temporal variance of RMS for each cell nucleus imaged.

6.3.6. Preparation of glass slides

For ESEM imaging with HRLM correlation experiments, glass slides were cleaned in piranha solution for 1 h. After rinsing with copious amounts of water, they were dried with nitrogen. The slides were then immersed in a 1% solution containing PDDA

(Poly(diallyldimethylammonium chloride)) for 30 mins, rinsed with water and dried with nitrogen. A drop of the nanoparticle solution was deposited on the slides for 5 minutes. The slides were then rinsed with water and dried with nitrogen.

6.3.7. ESEM Imaging

Spherical gold nanoparticles (GNPs) with 40 nm diameters were deposited onto glass microscope slides by suspending the particles at a concentration of 0.1 nM in an aqueous solution. In order to induce aggregation of particles, sodium chloride was introduced to the solution at a concentration of 10 mM. The solution was then pipetted onto the glass slide and allowed to air dry prior to imaging with PWS microscopy and ESEM.

For electron microscopy imaging of GNPs deposited on a glass substrate, a FEI Quanta 400 F ESEM was used in low vacuum mode. Locations of PWS images were co-localized with ESEM imaging of the same region using permanent marker to mark the surface of the glass slide in a distinctive manner for locative cross-registration.

Whereas salt crystals in the ESEM images of these slides appeared as bright cubic structures on the order of ~400 nm in the lateral dimension, these structures were not readily apparent in PWS microscopy images. However, aggregated clusters of GNPs, which appeared as light grey clusters in the SEM images, appear as bright spots in PWS micrographs (Fig 9A,B). This indicates a higher sensitivity of PWS microscopy to the GNP clusters compared to less reflective salt crystals. When aggregation of GNPs was not induced by the introduction of salt, the GNPs were not visible in PWS images, indicating the failure of PWS to detect the presence of singular GNPs.

6.4. Results

6.4.1. PWS sensitivity to GNPs

We first investigated the capability of partial-wave spectroscopic microscopy (PWS) to image GNPs on a glass slide in order to determine its sensitivity to GNPs particle aggregation. Since GNPs inside the cells will not be present as single GNPs due to the process of endocytosis or their interaction with cytosolic proteins, we focus our studies on aggregates of GNPs rather than single GNPs. Thus, the study was focused on characterize the signal of aggregated GNPs using PWS. In solution, aggregation of 40 nm spherical GNPs was induced by adding 10 mM NaCl, after which the particle suspension was deposited on a glass slide, rinsed and then allowed to dry, and a selected region was imaged with both PWS (AOTF instrument described elsewhere[208,210] and in Materials and Methods) and an environmental scanning electron microscope (ESEM). These co-registered images from both techniques are shown in figure 6.1.

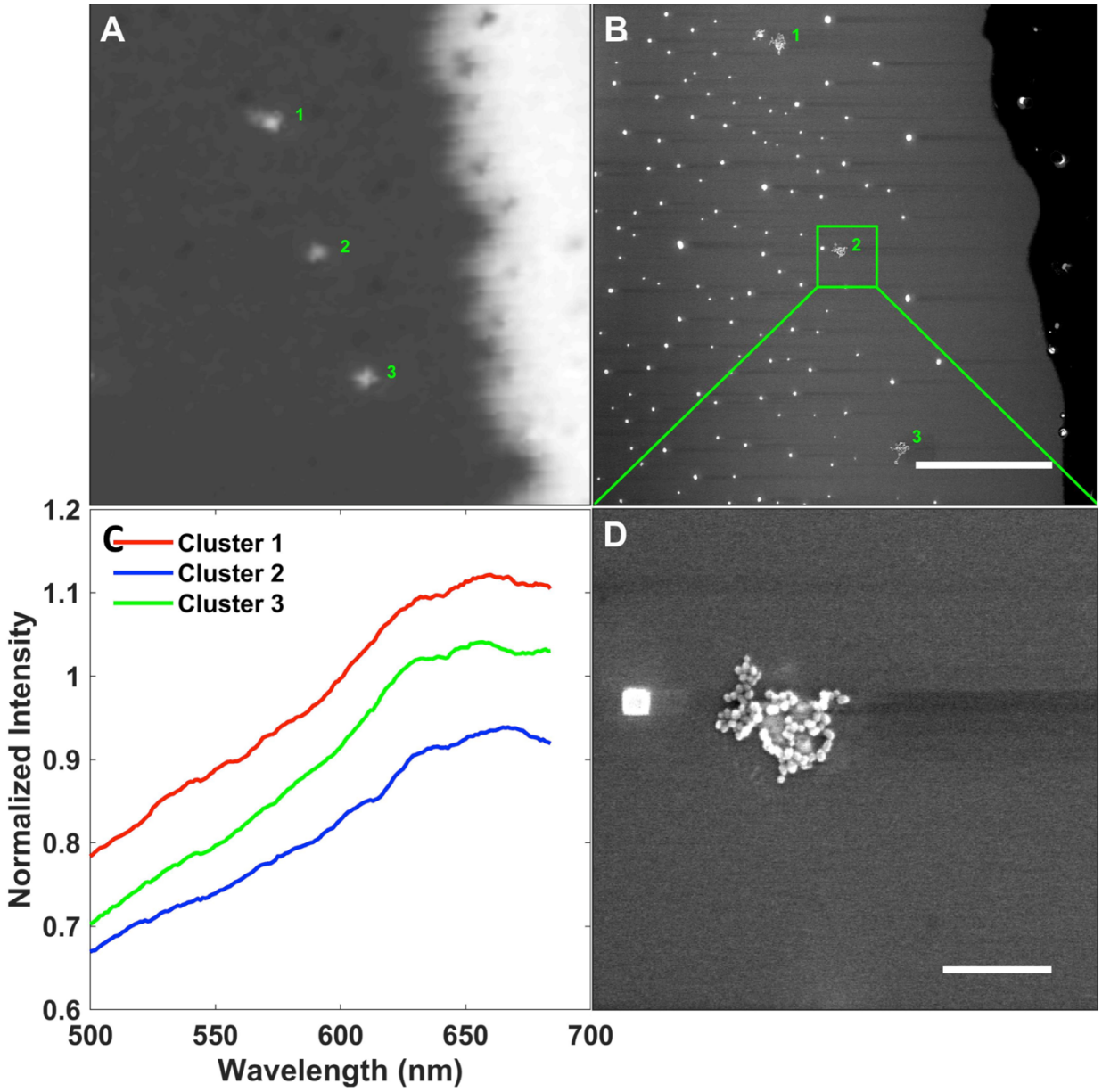

Figure 6.1. PWS microscopy images GNP clusters. (A) BFRI interference image (B) ESEM image of the same view of aggregated GNPs deposited on glass slide (scale bar = 5 μm). (C) Normalized scattering spectra from GNP clusters labeled 1, 2, and 3 measured with PWS. (D) Magnification of the GNP cluster 2 where a proximal salt crystal is also observed (scale bar = 0.45 μm). In this figure, it can be appreciated how PWS is capable of differentiating between GNPs and salt crystals.

From PWS imaging, the GNPs are readily observed as bright spots in the wavelength-summed interference image (BFRI), labeled as structures 1, 2, and 3 shown in Figure 6.1(A). The same structures are labeled in the ESEM image of the region shown in Figure 6.1(B) where it is evident that many other bright structures corresponding to salt crystals from the carrier solution are also visible in the ESEM but not PWS images. Difference in composition of these crystal structures and GNPs was confirmed through electron beam bombardment in the ESEM, shown in Supplementary figure 6.9. Furthermore, the expanded view of the region around GNP structure 2 shown in Figure 6.1(B) shows that in the desiccated sample, GNPs that are visible with PWS are in the form of aggregated clusters of many GNPs. Thus, for dried samples PWS is particularly sensitive to clusters of GNPs but not other, less scattering debris such as salt crystals.

6.4.2. PWS Instrumentation

For our studies of GNPs in live cells, measurements were obtained using the live-cell PWS optical set-up shown in Figure 6.2 and briefly described in 6.3.1 Materials and Methods Live-cell PWS Instrument.

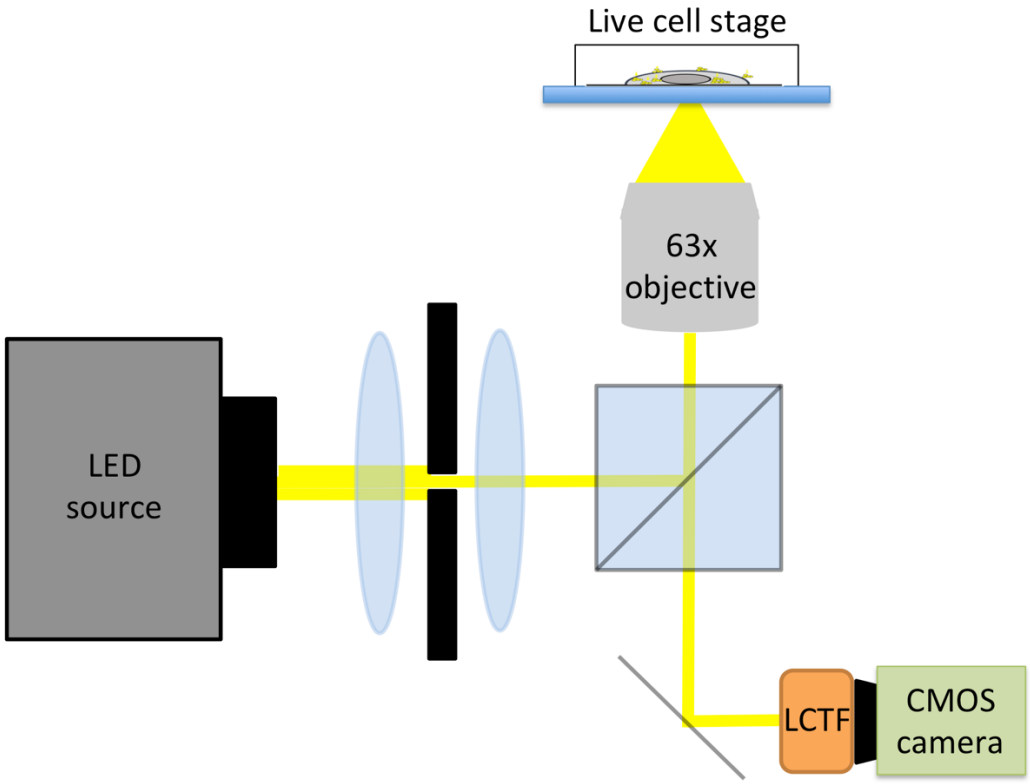

Figure 6.2. Schematic of Live-cell PWS instrument used for imaging experiments. Light emitted from an LED source is focused in the cell sample, after which scattered and reflected signal interferes and is spectrally resolved by a tunable filter before acquisition (LED: light emitting diode, LCTF: liquid crystal tunable filter, CMOS: complementary metal-oxide-semiconductor).

6.4.3. PWS Analysis

We applied PWS processing analysis to quantify cellular structural parameter RMS, which describes the fractal dimension of macromolecular organization in cellular compartments. In addition to quantifying this dimension, RMS also produces a highly enhanced signal contrast from GNPs in an image of the particles incubated in HeLa cells shown in Figure 6.3(B), when compared to the BFRI image, shown in Figure 6.3(A), with the quantified contrast of GNPs relative to

background shown in Figure 6.3(C). A quantitative colormap of RMS for this image is also shown in Figure 6.3(D).

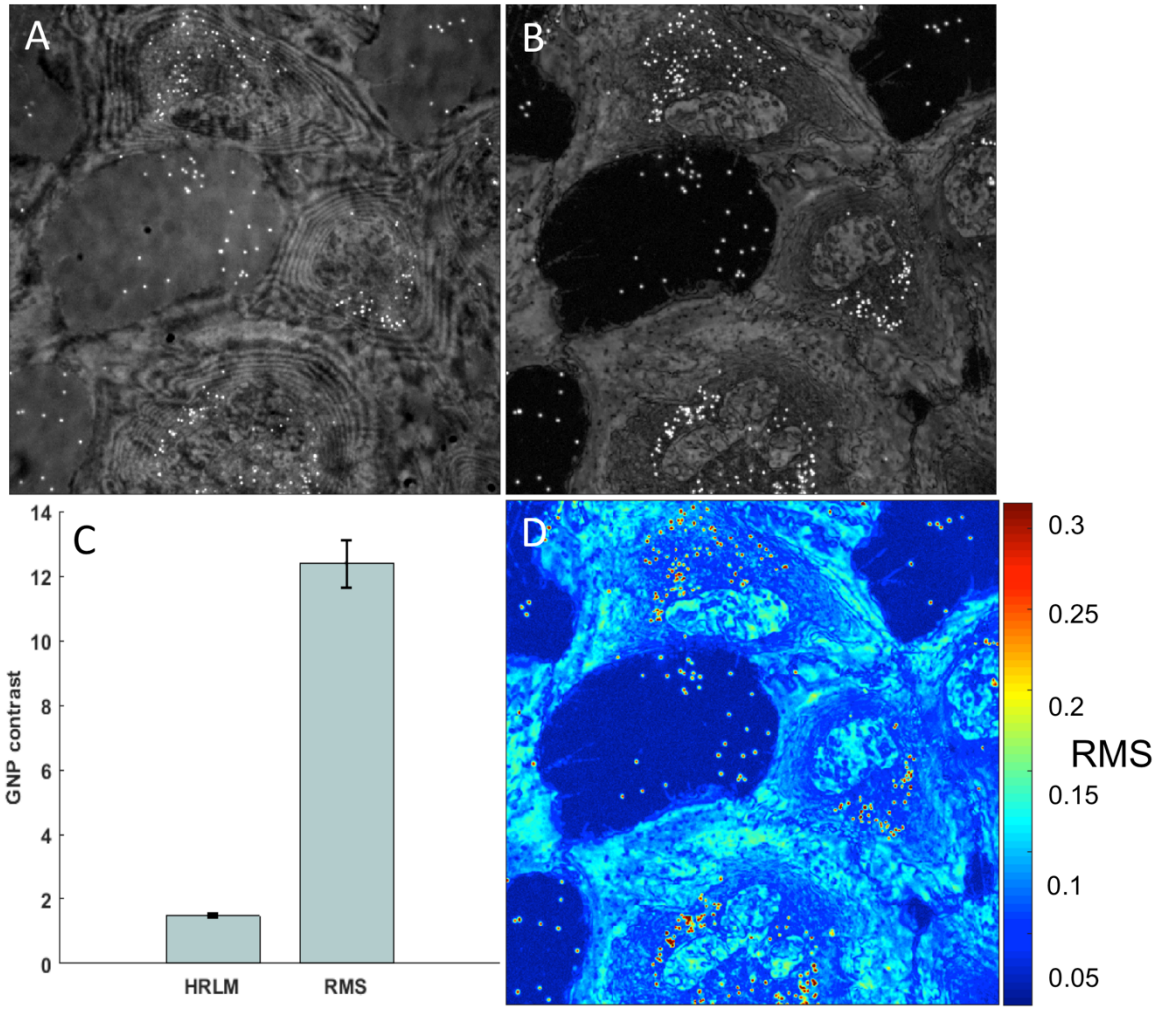

Figure 6.3. Spectral analysis enhances GNP contrast in microscopy image. Images of GNPs incubated with HeLa cells derived from (A) BFRI and (B) PWS RMS parameter. Contrast of GNPs compared with surrounding field is enhanced in RMS map compared to BFRI (C). PWS RMS map typically plotted in color scaled to magnitude of RMS value used to quantify cellular structure (D).

6.4.4. PWS measurement of nuclear structural response to GNPs

The ability of PWS to characterize cellular structure by quantifying local macromolecular distribution with RMS has been used for studies of nuclear chromatin topology and associated gene expression[211]. Here we measured cell nuclear RMS from HeLa cells incubated with and without GNPs as a control. Average nuclear RMS values from these groups are shown in Figure 6.4(B). When cells were incubated with GNPs, the mean nuclear RMS was significantly lower, a finding consistent with decompaction of nuclear chromatin[116,206,211].

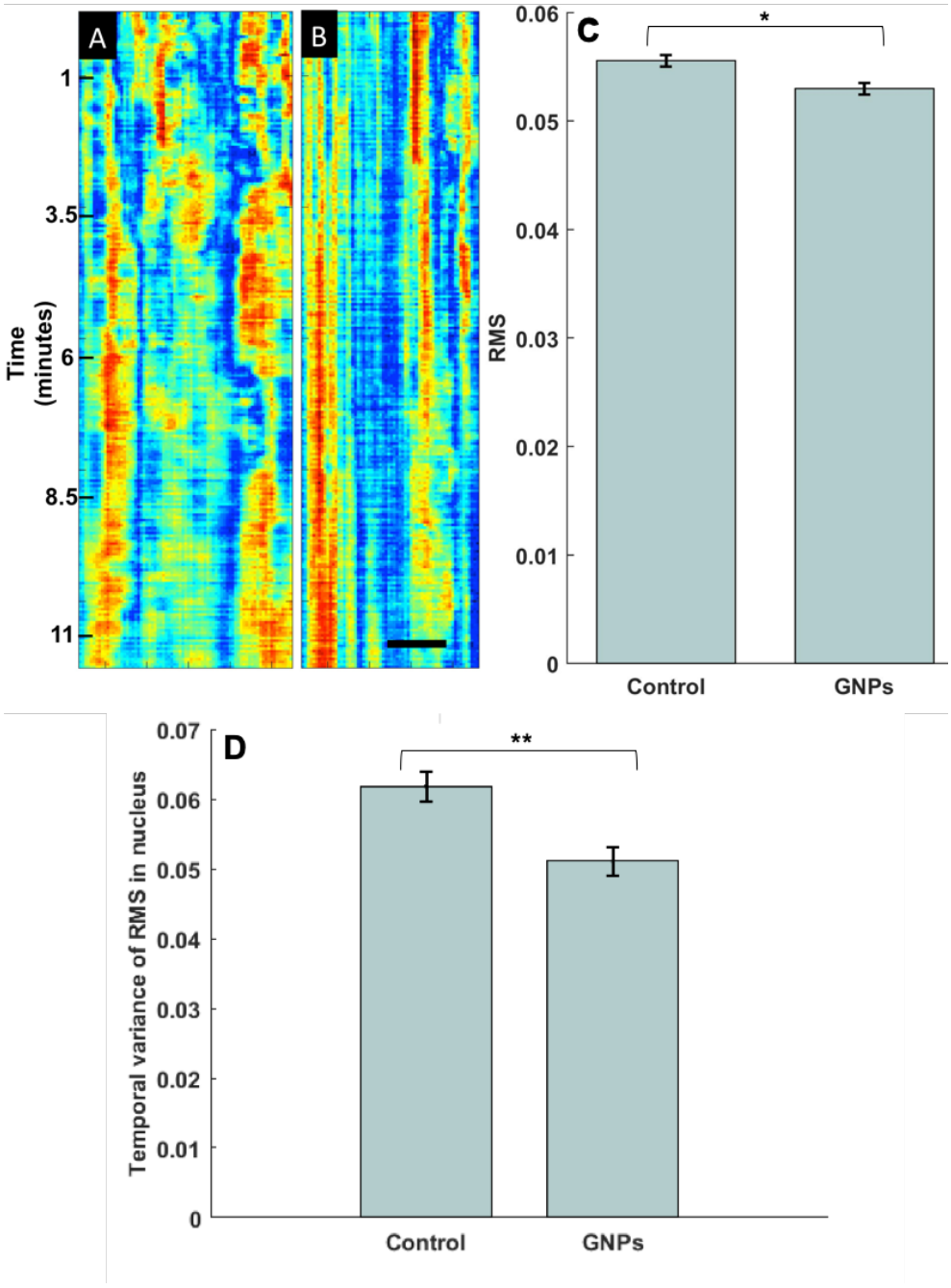

Figure 6.4. GNPs induce changes in nuclear structure and temporal dynamics. Live-cell PWS kymograph (x axis cross-sectional position across cell nucleus and y-axis time) shows temporal dynamics of chromatin structure in HeLa cells incubated (A) without and (B) with GNPs. Variance of normalized RMS along the temporal dimension confirms fewer dynamic changes in cells

incubated with GNPs. Scale bar length = 5 μm. (C) RMS from live HeLa nuclei (n=252 control, n=214 GNP treated) measured with live-cell PWS quantifies nuclear structure, showing HeLa cells incubated with GNPs have a small but significant decrease in nuclear RMS. (D) Temporal variance of nuclear RMS in Hela cells in media +- GNPs indicates a significantly decreased nuclear motion associated with GNP treatment (*$p < 0.001$, **$p < 0.01$).

In addition to an observed decrease in population-averaged nuclear RMS over the whole nucleus from GNP treatment, the temporal dynamics of nuclear RMS also appeared to slow with GNP treatment. An example kymograph, plotting a single line-section profile of nuclear RMS with respect to time, is shown in Figure 6.4. In this kymograph, the untreated example nucleus in Figure 6.4(A) shows dynamic changes in RMS across the line profile over a time domain of 12 minutes, while the GNP-treated example in Figure 6.4(B) shows much a more static nuclear structure, evident in the longer vertical striping in the kymograph.

With live-cell PWS we were able to directly observe GNP motion within the cell through the well-defined contrast provided in the RMS map. We demonstrate the applicability of this technique allowing the label-free intra- and extra-cellular discrimination of the GNPs and the study of intra- and inter-cellular transport of GNPs in Supplementary video 3, where potential intercellular trafficking of a GNP can be seen from the cell on the left to the cell on the right (momentarily moving out of the focal plane between observed locations in each cell).

6.4.5. Principal Component Analysis

To determine how cellular uptake of GNPs affects their visible scattering spectra, HeLa cells were cultured under standard conditions, then incubated with 100 nm diameter spherical GNPs (Nanopartz) at a concentration of $4x10^6$ particles/mL media for a period of 24 hours prior to imaging with live-cell PWS. From a single PWS image of a HeLa cell, cellular margins were manually segmented and a mask of GNP location was created using a threshold of image intensity. Averaged spectra from GNPs inside and outside of the HeLa cell, along with background intensity from cell and glass are shown in Figure 6.5. It was observed that internalized GNPs had a mean spectral scattering peak shifted up in wavelength compared to GNPs outside of the cell. The mean spectral absorption of the GNP suspension used to treat the cells was independently measured using a NanoDrop UV-Vis spectrophotometer. The absorption peak of the GNP treatment suspension was centered at approximately 580 nm, and is shown in Supplementary figure 6.10.

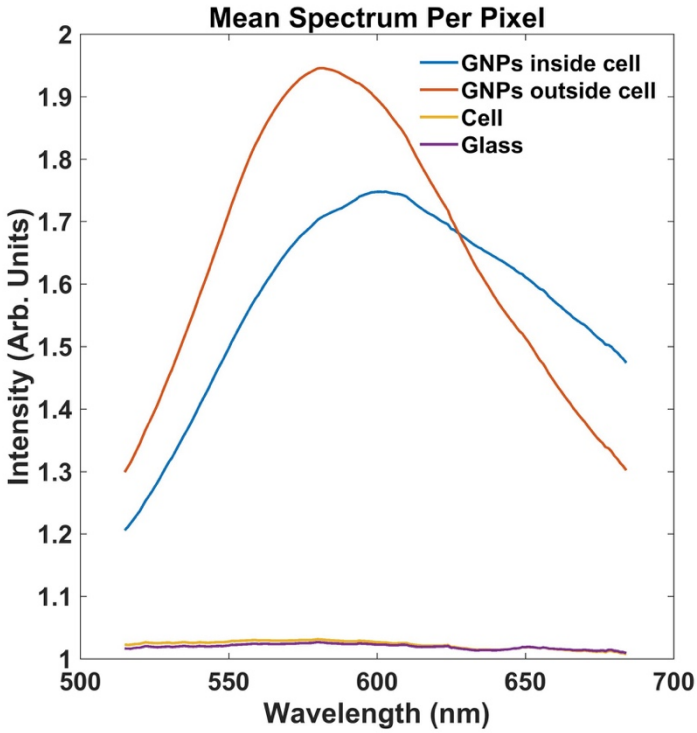

Figure 6.5. GNP spectral shift is associated with internalization. Averaged scattering spectra from GNPs inside and outside live HeLa cells, along with mean spectra from GNP-free regions of cell and glass slide. We observe a distinct shift in the spectral scattering peak when comparing internalized GNPs to those remaining outside of cells. This distinct shift is present due to interaction between GNPs and cytoplasmic protein and GNR aggregation.

To characterize the features of the GNP scattering spectra, we performed a K-means clustering analysis on individual spectra from each GNP location in the PWS image. This analysis decomposes the scattering spectrum into a sum of discrete principal component functions that describe the scattering spectra from all visible GNPs in our measurements. These principal component spectra are plotted in figure 6.6(A). When we plot the mean relative contribution of each principal component to the full scattering spectrum, we can see that the full spectrum can be fairly well-characterized by the first 3 principal components, with the first component accounting for approximately 43% of the full spectral behavior of GNPs, shown in figure 6.6(b).

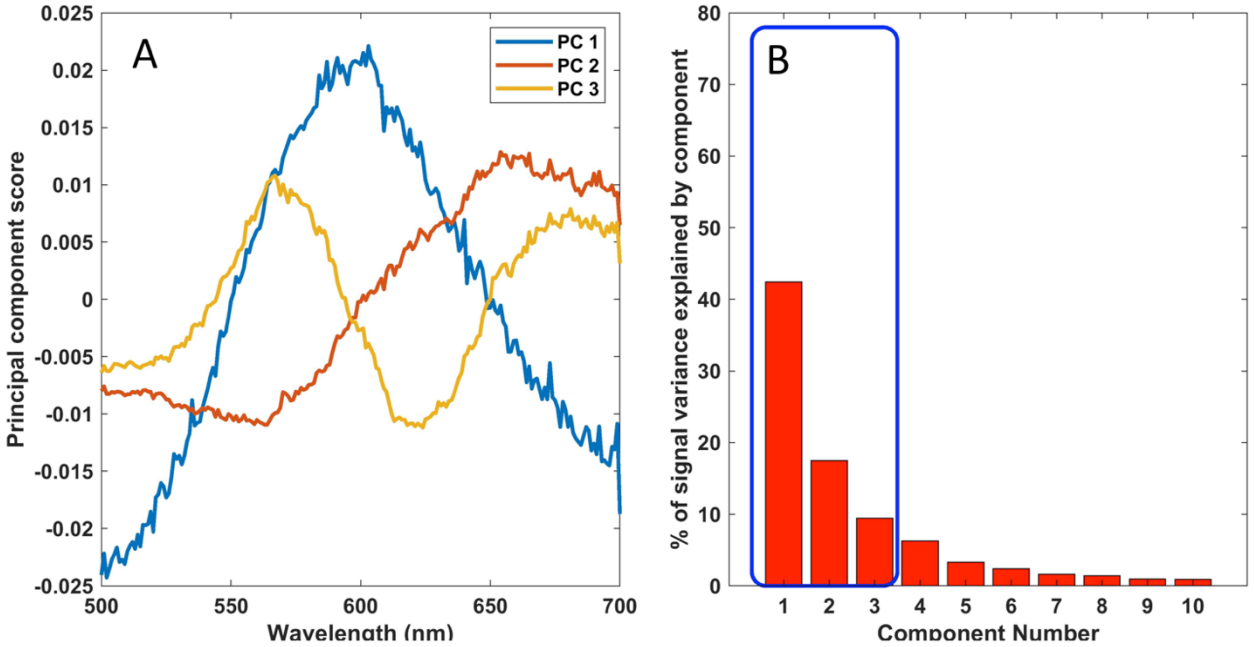

Figure 6.6. Principal component analysis characterizes GNP scattering spectra. Principal component spectra for the first 3 principal components of GNP scattering spectra (A). GNP scattering spectral signal explained well by the first 3 principal components, after which subsequent components each contribute less than 7% to the total spectral shape (B).

When overlaying the scaling factor for the first principal component in color over respective GNPs in the PWS image, it can be seen in Figure 6.7 that internalized GNPs show a much higher variation in this component scaling when compared to GNPs on glass.

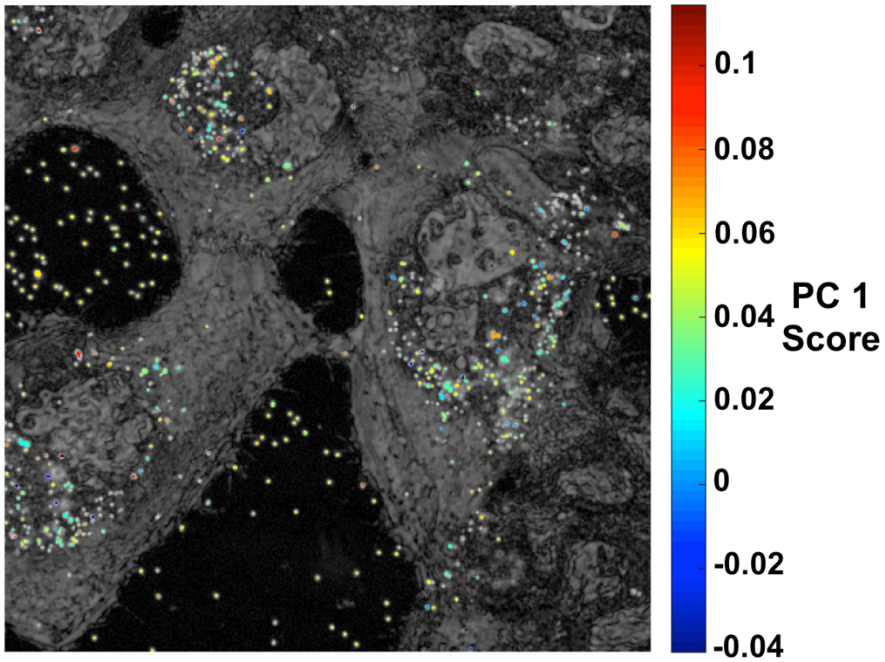

Figure 6.7. Image of HeLa cells incubated with GNPs (bright specks). GNPs color-coded by score of the first spectral principal component (PC 1).

To further show this effect, we show a plot of the first 3 principal components in figure 6.8, together which account for 69.4% of the spectral scattering shape measured from GNPs in this experiment.

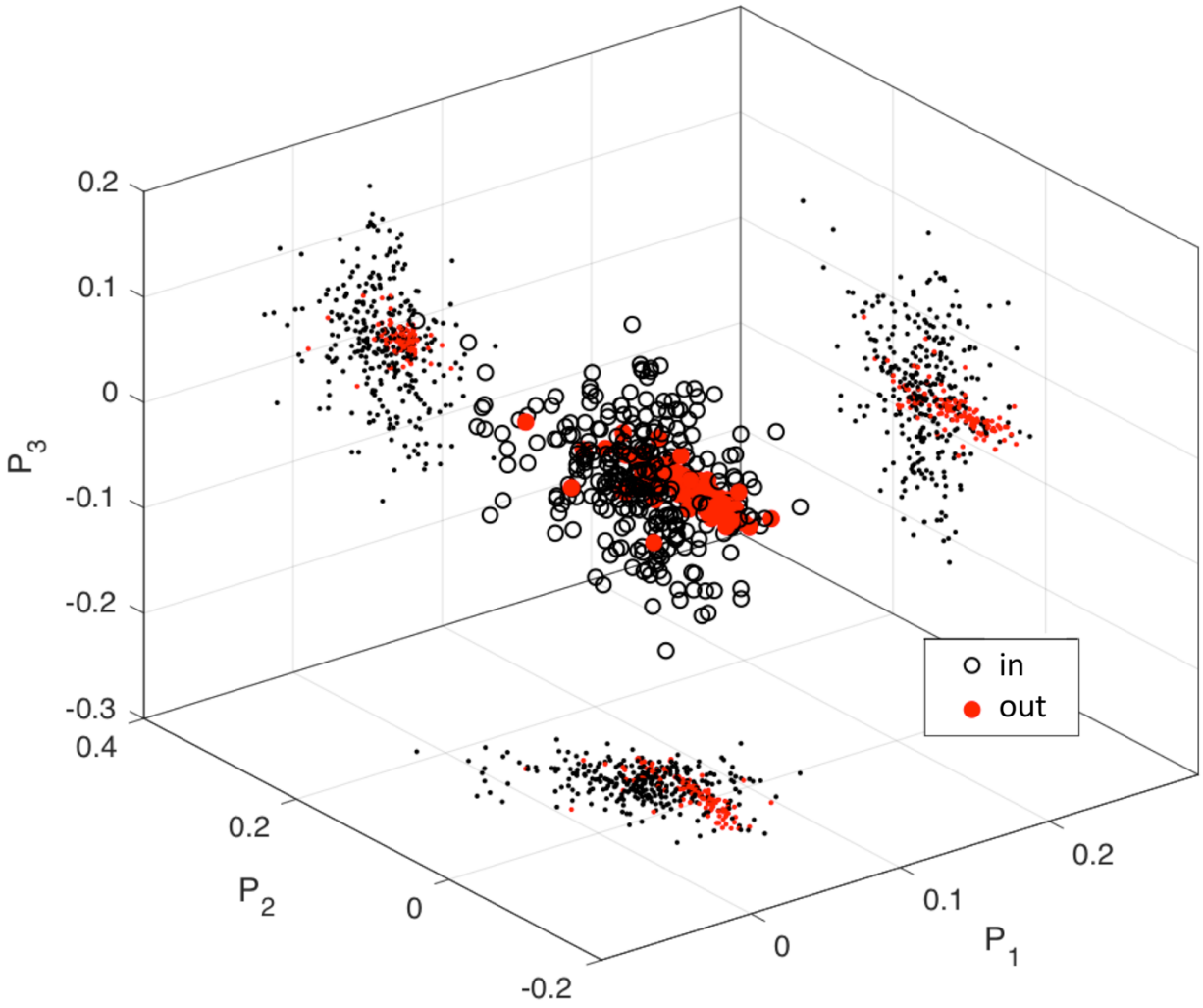

Figure 6.8. 3D scatter plot of principal component scores (P_1, P_2, and P_3, respectively) for each GNP location. GNPs inside cells show tighter clustering of principal component scores than GNPs outside of cells.

Clustering of spectral character is noticeably tighter for GNPs outside of cells (scatterplot occupancy volume of 0.00049 compared to 0.0039 for internalized cells)[212] when compared to those located within cell margins, which display a very wide variation in principal component scores. These variances are potentially in concordance with the larger variety of different proteins that the nanoparticle interact intracellularly comparing with those extracellularly.

6.5. Discussion

Here, we have demonstrated the use of live-cell PWS for imaging of GNP agglomerates in live cells. When compared to a bright field reflected image (BFRI) collected by averaging backscatter image intensity across wavelength, the PWS analysis used here to obtain RMS images yields a much higher contrast of GNPs compared to the field background. This enhanced sensitivity to GNPs lends this analysis for improved imaging and segmentation of GNPs from the hyperspectral image. Furthermore, RMS has been used for quantification of cellular structure in previous work[206,213,214], and we foresee its parallel implementation for localization and study of interactions between GNPs and live cells.

As mentioned above, live-cell PWS enables imaging of nanoparticle clusters by means of measuring the spectral signature of objects throughout the field of view. Harnessing this capability, we measured how mean scattering spectra from GNP clusters inside live HeLa cells have a higher peak wavelength than clusters outside of the cell margins. One of the most common routes for GNP internalization involves binding to the plasma membrane by specific and/or non-specific binding, followed by agglomeration via membrane trafficking, and then intracellular transport through endocytic (vesicular) trafficking. Before or possibly during this process, the GNPs aggregate and begin to travel toward their intracellular target.

It is known that gold nanoparticles can induce stress to cells in culture through production of reactive oxygen species, which have the potential to lead to apoptotic signaling[215–217]. Here we make the observation that addition of unconjugated gold nanoparticles to an *in vitro* culture of HeLa cells creates a direct response in nuclear chromatin structure, manifested in a decrease in nuclear fractal dimension indicating a less compact or heterogeneous chromatin architecture. Further study of the time-dependent variance in the distribution of nuclear RMS revealed a significantly slowed distribution of nuclear chromatin dynamics accompanying this less-compact

structure. These interesting findings warrant further study to clarify the mechanisms of GNP-induced nuclear restructuring and whether this approach might be of interest in future approaches toward engineering of chromatin structure for various applications such as in chemotherapeutic adjuvant therapy.

To help understand the specific scattering spectra characteristics than might change as a consequence from this process, we performed principal component analysis on an array of all GNP cluster spectra, decomposing each into a linear sum of the characteristic component spectra. While it is unclear which biological and plasmonic modifications are directly responsible for the specific spectral features each component represents, further studies integrating controlled physicochemical changes to GNP structure and aggregation would help to clarify the individual contributions to bulk differences in spectra observed here.

An interesting observation, however, is the much larger variation in principal component scores for internalized GNPs when compared to GNPs outside the cell on the bare glass coverslip. The GNPs can clearly be identified in the cytoplasm of the HeLa cells, in agreement with the general characterization of how GNPs localize in the cytoplasm rather than the nucleus[207]. Intracellular movement of GNPs in the cytoplasm is much higher than GNPs outside of the cell, which largely remain motionless on the coverslip, as can be observed in Supplementary video 3. It is possible that motion of GNPs during acquisition could affect the observed scattered spectra, depending on the displacement achieved during the integration time of the microscope, which could potentially explain the wide variation in spectral component scores from internalized GNPs shown in Figure 6.8.

Measuring the spectral properties of GNPs in the cell environment will also prove valuable for photothermal applications where the light used should match the GNP plasmon, which could have changed due to aggregation or interaction with plasma proteins. By modifying the incubation

protocol, different GNP populations can be imaged. For example, by incubating cells under low temperature or by inhibiting endocytosis, it will be possible to image GNP clusters on the plasma membrane. This information will allow deeper understanding of GNP-plasma membrane interactions.

In conclusion, we have presented and tested the novel application of a hyperspectral microscopy technique, live-cell PWS, for the imaging and spectral characterization of aggregated GNPs live cancer cells. This technique provides important information about the localization of the GNP clusters as well as their plasmonic properties in the cellular environment. An interesting observation was made that suggests GNP treatment affects nuclear structure and activity in cancer cells which warrants further investigation. Continued study of GNP spectra and intracellular interactions with this microscopy technique will help current research projects focused on intracellular localization and the interactions between GNPs and the plasma membrane during intracellular uptake. We expect that this easy-to-use microscopy technique will become a useful tool in research projects pertaining to GNPs in cancer cell models.

6.6. Supplementary Figures

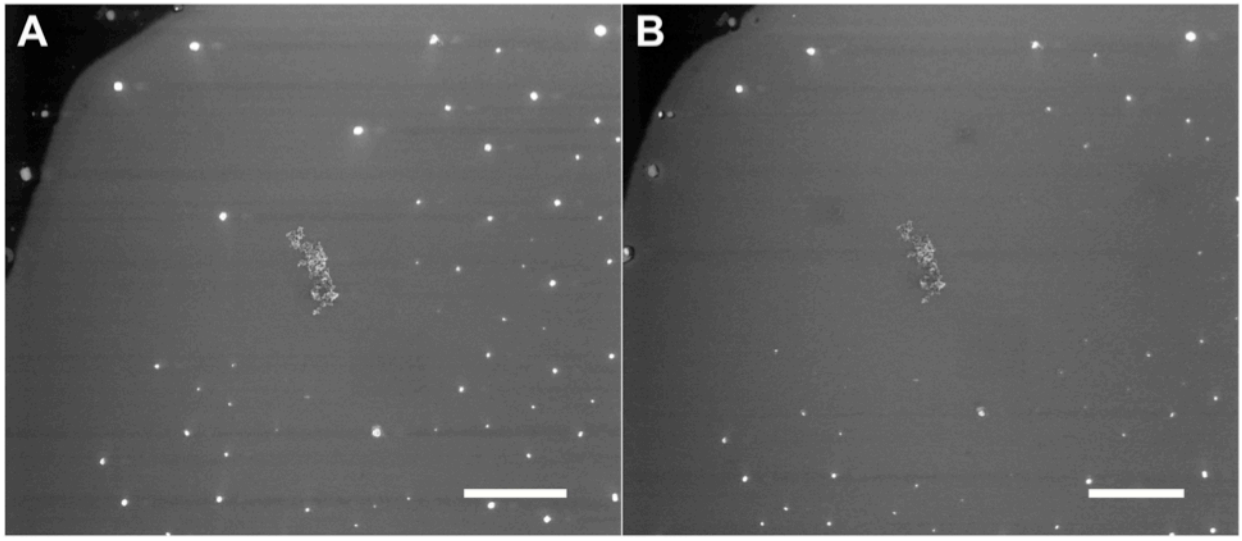

Figure 6.9. Confirmation of structures in ESEM images. ESEM images of GNP cluster surrounded by salt crystals (A) before and (B) after electron beam bombardment confirms distinct composition of bright structures in the image. Salt crystals bombarded by the electron beam quickly disappear whereas GNPs remain on the glass slide.

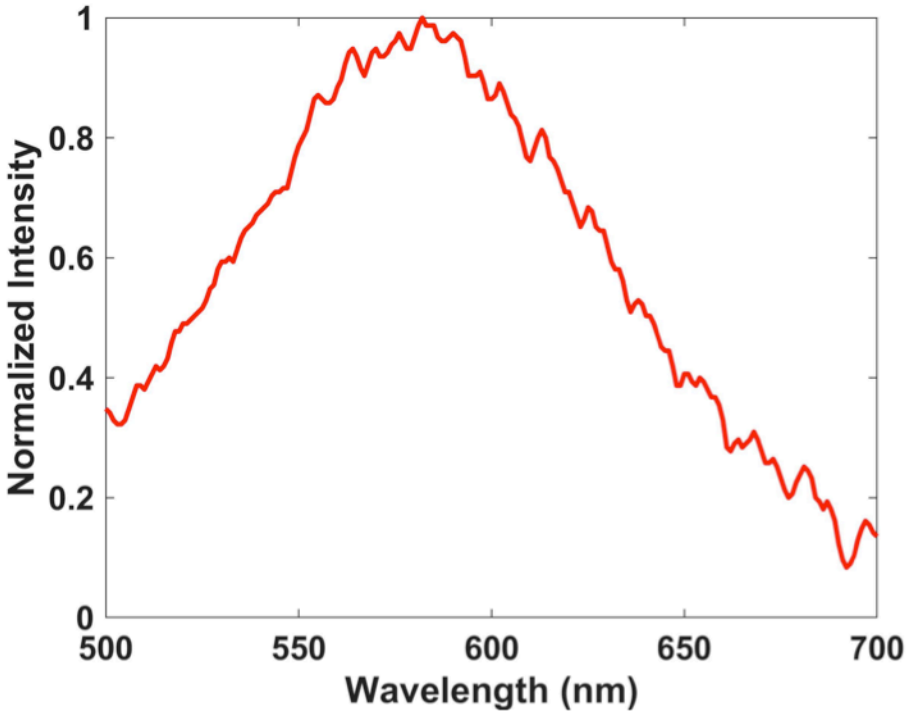

Figure 6.10. UV-Vis absorption spectrum of stock GNP suspension used for these studies.

Chapter 7:

Measuring light scattering and absorption properties of coral tissue and skeleton with Inverse Spectroscopic Optical Coherence Tomography (ISOCT)

Authors: Graham Spicer, Aya Eid, Daniel Wangpraseurt, Timothy Swain, Jimmy Winkelmann, Ji Yi, Michael Kühl, Luisa Marcelino, and Vadim Backman

7.1. Abstract

The success of reef-building corals for >200 million years has been dependent on the mutualistic interaction between the coral host and its photosynthetic endosymbiont dinoflagellates (family Symbiodiniaceae) that supply the coral host with nutrients and energy for growth and calcification. While multiple light scattering in coral tissue and skeleton significantly enhance the light microenvironment for Symbiodiniaceae, the mechanisms of light propagation in tissue and skeleton remain largely unknown due to a lack of technologies to measure the intrinsic optical properties of both compartments in live corals. Here we introduce ISOCT (inverse spectroscopic optical coherence tomography), a non-invasive approach to measure optical properties and three-dimensional morphology of living corals at micron- and nano-length scales, respectively, which are involved in the control of light propagation. ISOCT enables measurements of optical properties in the visible range and thus allows for characterization of the density of light harvesting pigments in coral. We used ISOCT to characterize the optical scattering coefficient (μ_s) of the coral skeleton and chlorophyll *a* concentration of live coral tissue. ISOCT further characterized the overall micro- and nano-morphology of live tissue by measuring differences in the sub-micron spatial mass density distribution (D) that vary throughout the tissue and skeleton and give rise to light scattering, and this enabled estimates of the spatial directionality of light scattering, i.e., the anisotropy coefficient, g. Thus, ISOCT enables non-invasive imaging of nanoscale structure and light scattering dynamics in live corals and other optically dense biological systems and could provide important insights into coral growth and photophysiology.

7.2. Introduction

Reef-building corals provide critical habitat for as many as 1.3 million species [218], which in turn directly support the lives of more than 500 million people [219]. The establishment, succession and maintenance of such coral reef ecosystems rely on a mutualistic endosymbiosis between a calcifying cnidarian animal and photosynthetic dinoflagellates of the family Symbiodiniaceae, which live within the coral tissue and provide the host with most of its energy demand through excretion of photosynthetically-fixed carbon [220]. Reef-building corals consist of thin tissue that deposits and covers a calcium carbonate skeleton, and such a configuration has evolved a variety of strategies to increase light availability to Symbiodiniaceae for greater photosynthate output, while minimizing light stress, which can typically occur in shallow waters especially when associated with high temperature [221,222]. Anomalously high temperatures and irradiances can impair photosynthetic efficiency leading to photodamage and production of reactive oxygen species (ROS) which may lead to the expulsion of the symbionts (coral bleaching) and result in death of the colony [222–226]. The trajectory of climate change is increasing the frequency and severity of coral bleaching events creating an urgent need to understand the mechanisms of light collection in corals [219,227,228].

Different strategies to maximize light availability to Symbiodiniaceae have been described. Downwelling light that is not absorbed by the symbionts in the first pass can be scattered back into the tissue by the calcium carbonate skeleton and thus increase the light availability [87,229–233]. Within tissue, light scattering together with dynamic light redistribution due to tissue contraction and expansion can significantly increase light availability to symbionts [234–236]. Light-scattering or absorption by fluorescent host pigments can further modulate the light microenvironment of the Symbiodiniaceae, while also filtering out damaging short-wavelength radiation [225,237–239] and

affecting radiative heating of the coral tissue [240,241]. Corals can also actively regulate symbiont cell densities and thereby adjust microalgal self-shading within their tissues [242].

Coral photophysiology is strongly affected by the light transport and absorption properties of coral tissue components and skeleton [234–236]. In coral tissue and skeleton, downwelling light undergoes both scattering and absorption, where spatial variations in refractive index lead to light scattering [3,235,243,244]. In tissue, refractive index variations are primarily due to intracellular structures, ranging from macromolecular complexes to organelles, and intercellular boundaries [245]. In the skeleton, light scattering is affected by variations in density of structures ranging from tens of nanometers in size (e.g., calcium carbonate nanograins, orientation and subsequent birefringence of the constitutive skeletal nanograins, organic matrix-skeleton boundaries) to micrometers (septa, corallites) [230,232,246]. The overall organization of these structures which are assembled hierarchically as a fractal [232,247,248], can be characterized by their spatial autocorrelation function $B_n(r)$, with its functional shape parameterized by D, a fractal dimension [3,249]. Measuring D from the skeletons of 88 coral species revealed their overall skeletal organization to be a 'mass-fractal' structure (i.e., average $D<3$), which correlated with their growth rates, light-scattering properties and bleaching susceptibility. This emerging picture suggests that corals that grow at faster rates are more likely to have lower skeletal fractal-dimensions, denser skeletons, lower light-scattering properties, and higher bleaching susceptibility [230,232,246–248]. Coral tissue and skeleton differ in their respective absorption properties. Photosynthetic pigments within Symbiodiniaceae are the dominant light absorbers in tissue, where absorption spectra exhibit characteristic peaks corresponding to symbiont pigment composition [234,238,244,250,251]. Coral skeletons, on the other hand, are weakly absorbing with light transport dominated by scattering processes [230–232,252]. An ideal technology would allow non-invasive, three-dimensional, real-time imaging of the key

optical (absorption and scattering) and architectural (mass-fractal dimension *D*) properties in tissue and skeleton of live coral specimens.

Here we apply a variant of optical coherence tomography (OCT) to the study of coral optical properties. OCT is a non-invasive 3-D optical imaging technique that uses focused light typically in the near-infrared to probe and collect cross-sectional images from a sample that scatters light. First introduced in 1991, OCT has found widespread use in ophthalmology for clinical retinal imaging and a wide array of other biomedical applications including cardiology and dentistry [65,253]. OCT is a label-free technique that requires no sample preparation, relying on intrinsic differences in optical backscattering intensity within a sample to provide contrast. The transverse resolution is provided by scanning a focused beam across a sample and is determined by the numerical aperture of the focusing objective. The axial resolution is dependent on the center wavelength and bandwidth of illumination, and axial spatial resolution on the order of one micron can be achieved [163]. The depth of penetration depends on the scattering and absorption properties of the imaged object and in most biological tissues ranges from a few hundred microns to a millimeter. Recently, OCT has been used to image tissue and skeletons of live corals, providing complete 3-D structural images of tissue, skeleton, and chromatophore distribution not previously obtainable in a living coral [87]. In addition, the rapid imaging capability of OCT enabled live microscale study of coral polyp movement in response to high light illumination.

While OCT holds a significant potential for coral imaging, its capabilities can be significantly enhanced to enable a comprehensive and quantitative imaging of coral optical properties. For a given resolution voxel, traditional OCT image intensity is proportional to the amount of backscattered light, making it impossible to decouple the effects of absorption and scattering, which would be required to measure pigment concentration and composition and the scattering properties of coral tissue [254]. A complete characterization of light scattering involves the

scattering coefficient, μ_s, which quantifies the total amount of light scattered in all directions, the angular distribution of scattered light, $p(\theta)$, also known as the phase function, and the absorption coefficient, μ_a. Another metric frequently employed in characterizing light transport properties of corals is the reduced scattering coefficient, $\boldsymbol{\mu_S' = \mu_s(1 - g)}$, where the anisotropy factor (g) is equal to the average cosine of the phase function $p(\theta)$ and $\boldsymbol{\mu_S'}$ represents the inverse of the transport mean free path, the distance at which the trajectory of a photon in a medium becomes random.

Approaches to decouple these parameters included an OCT modality that, in addition to the backscattering coefficient, μ_b, calculates the attenuation of the OCT signal in the longitudinal direction [255]. The latter is proportional to $\mu_a + \mu_s$, integrated over the bandwidth and over several resolution voxels (typically ~50-100 μm). The phase function is then assumed to have a specific Henyey-Greenstein form, which was first developed to describe light scattering by interstellar dust and was later adopted to biomedical optics applications, and is parameterized by the single parameter $\boldsymbol{g}$ [256]. This links coefficients μ_s and μ_b and allows estimation of μ_s and g. This model assumes absorption is negligible, so it cannot be measured under this approximation. Furthermore, this functional form is only applicable in the very limiting case of a refractive index correlation function $B_n(r)$ with D=3, which is not appropriate for coral light scattering since skeletal organization shows on average D<3 [232].

Here we adopt a recently developed extension of OCT, inverse spectroscopic OCT (ISOCT), to obtain a comprehensive characterization of tissue and skeletal scattering, absorption, and architectural properties, which is independent of Henyey-Greenstein functional formalism and thus allows for evaluation of scattering properties rising from mass-fractal structures with D=<3 and D>3. ISOCT measures the optical spectra of the OCT signal for any given 3-D voxel returning a 4-D data cube as a function of the voxel coordinates x, y, z, and wavelength λ [54,75–77]. The absorption spectra of prevalent pigments are measured *a priori*. We reasoned that because the

narrow-band absorption spectra of pigments are drastically different from the broad-band, slowly varying spectra of backscattered light, $\mu_s(\lambda)$, the pigment concentration and composition could be extracted from $\mu_s(\lambda) + \mu_a(\lambda)$. Then $\mu_s(\lambda)$ and $\mu_a(\lambda)$ can be decoupled. Because the spectrum of $\mu_b(\lambda)$ is functionally related to $p(\theta)$ through a Fourier transform, the combination of μ_s and μ_b can be used to extract $p(\theta)$ without making an approximation that $p(\theta)$ can be completely characterized by a single parameter $\boldsymbol{g}$. In turn, the scattering properties can be used to estimate subdiffractional structural properties of the tissue and the skeleton, which provide further information on the growth pattern of a coral. In the present study, we use ISOCT to image the concentration and composition of tissue pigments, the scattering coefficient and the angular distribution of scattered light of both the tissue and the skeleton *in vivo*. These measures fully characterize light interaction and transport within a coral.

7.3. Materials and methods

7.3.1. Inverse Spectroscopic Optical Coherence Tomography (ISOCT) instrument

The instrument used for ISOCT imaging has been described elsewhere [2,76]. For these studies, a visible (520-720 nm) spectral domain OCT system was used with a home-built spectrometer. The spectrometer camera frame rate was 45,000 frames per second, allowing for collection of a 512x512 pixel lateral scan in 5.8 seconds. Laser power at the sample did not exceed 10 mW during imaging, which in combination with the short scan time limited light exposure and potential phototoxicity to the coral. The visible spectrometer utilized a 4,096 pixel line-scan camera to obtain the spectrum of the OCT interferogram at each acquisition location across the sample. The spectral resolution of the spectrometer provided an axial imaging range of ~1.5 mm, allowing for sufficient imaging depth in the spatial domain to image through weakly scattering coral tissue in the visible band. A detailed description of methods for OCT spatial resolution

measurement is included in the following section. The lateral resolution was calculated to be 8.8 μm, and axial resolution was measured to be 1.22 μm in air (Supplementary Figure 1B).

7.3.2. OCT system resolution

To determine the lateral spatial resolution of the OCT system shown in supplementary figure 1(A), a razor edge was scanned at the objective focal plane with high sampling density (512 A lines collected in a 100 μm scan length) to create a resolution-limited OCT image of the razor edge intensity step function. OCT intensity along the axial dimension was summed over a 50 μm depth range to isolate the razor reflection signal from background noise, creating an *en face* projection image. This 2D *en face* image was summed along the edge dimension to average the edge step function for analysis. A Savitzky-Golay filter was applied to this edge response function to gently smooth the signal and calculate the first spatial derivative of intensity as a function of distance. The width of this first derivative peak characterizes the sharpness of the edge response function, quantifying lateral resolution of the OCT system assuming a sharp cutoff of true sample, high enough sampling density relative to system resolution, and an acceptably small filter kernel relative to resolution. The full width at half-maximum (FWHM) of the first spatial derivative peak is given as the lateral resolution of the OCT system.

Axial resolution of the OCT system shown in supplementary figure 1(B) was measured by scanning a mirror placed at the objective focal point with a neutral-density (ND) filter placed in the sample arm to attenuate signal, avoiding spectrometer detector saturation. The peak corresponding to mirror signal in a single OCT A-line signal was analyzed, the FWHM of which characterized the axial resolution of the system. All analysis was performed using Matlab software.

7.3.3. Live coral imaging

Live *Diploastrea heliopora* and *Merulina ampliata* reef-building corals were obtained from the aquarium trade and from the Shedd Aquarium, Chicago, IL who approved the coral species used in this study for research by their institutional review board, i.e., no endangered or threatened species as listed by the US Endangered Species was used in this study. Corals were kept in a saltwater tank (JBJ Nano Cube 28 gallon) with two Acela pumps rated at 1000 L per hour and a 105 W quad compact fluorescent lamp (10,000 K, 3.75 W/gallon), maintained at a temperature of 26.5±0.5°C. ISOCT images were acquired by placing the coral in a shallow dish, removing the majority of water covering the coral tissue and immediately scanning the focused sample laser beam over the region of interest, a process that lasted less than 10 seconds.

To determine the location of the skeleton in the OCT images, a preliminary scan of a selected region of coenosarc tissue was acquired. Then, while covering the OCT objective, a Waterpik system was used to wash away all of the coral tissue within the previously scanned region. Care was taken to prevent the coral frag from moving during this process, and a follow-up scan of the same region with the same instrument settings was acquired. For both scans, water covering the sample was kept to a minimal depth ~1 mm to ensure accurate vertical colocalization between the scans before and after tissue removal.

7.3.4. Light scattering model for ISOCT signal analysis

Light propagation through a turbid medium, including a biological tissue, is fully determined by the spatial distribution of the complex optical refractive index $n(x,y,z,\lambda)$ [3,257]. Spatial variations in the absolute value of refractive index give rise to light scattering, while the imaginary part gives rise to light absorption. The respective fundamental optical properties are the differential scattering cross section function $\sigma_s(\theta,\lambda,x,y,x)$ [cm^2], which describes the amplitude of

light scattering as a function of scattering angle θ, and the absorption coefficient μ_a(x,y,z,λ) [cm^{-1}], described as the probability of light absorption per infinitesimal path length. Under the first-order Born approximation, which generally describes a medium with relatively weak scattering potential and is broadly applicable to most biological tissues, σ_s is related to the autocorrelation function of n(x,y,z) via a Fourier transform [258]. For a given (x,y,z) position within a turbid medium, scattering properties are described via the scattering coefficient, μ_s [cm^{-1}], which is the integral of σ_s per unit volume over all directions, and the angular (phase) function of scattering $p(\theta)$ [259]. Other properties, such as the backscattering coefficient μ_b, which describes the likelihood of an incident photon scattering in the direction of origin, can also be derived from σ_s. The ISOCT signal is scaled by μ_b, and in order to relate the ISOCT signal to the optical properties of the medium, we model the autocorrelation of the refractive index distribution B_n using the three-parameter Whittle-Matérn model,

$$B_n(r) = A_n \left(\frac{r}{L_n}\right)^{(D-3)/2} K_{(D-3)/2}\left(\frac{r}{L_n}\right), \quad (1)$$

where r is the spatial separation between any two points, A_n is proportional to the variance of the refractive index σ_n, L_n represents a correlation distance, D describes the shape of the correlation function, and $K_x()$ denotes the modified Bessel function of the second [3]. Because the exact form of B_n cannot be known *a priori* and may vary not only across different types of biological tissue but even within the same tissue type, an advantage of this model is its versatility. Parameterized by D, the majority of the realistic functional forms of the autocorrelation function are well represented by the model and can be ascertained experimentally, thus eliminating the need to assume a specific form *a priori*. For D<3, the autocorrelation function has an inverse power-law form typical of a fractal tissue organization with the fractal dimension D. For 3<D<4, the autocorrelation function is a stretched exponential function. It is an exponential function with attenuation length L_n for D=4

and a Gaussian for D approaching infinity. Physically, D is a fractal dimension, characterizing the degree of self-similarity of structures at different length scales, and can alternatively be thought to characterize the degree of clumpiness in a continuous random medium. Enhanced backscattering spectroscopy measurement of D from various hard and soft scattering structures is reported in figure 6 from a prior publication[232], with mean D values from samples ranging from ~2 for to >3. Earlier techniques attempting to measure μ_s and g frequently relied on the approximation of $p(\theta)$ as the Henyey-Greenstein function, which corresponds to a special case of the Whittle-Matérn model for D=3 [231,252,259,260]. However, the shape of $p(\theta)$ varies considerably with changes in D, as can be appreciated from Figure 7.1(A) which shows an example of $p(\theta)$ behavior for D ranging from 1 to 5. Scattering behavior is also strongly influenced by changes in both D and g, as can be observed in Figure 7.1(B) which shows the behavior of μ_s as a function of D and g.

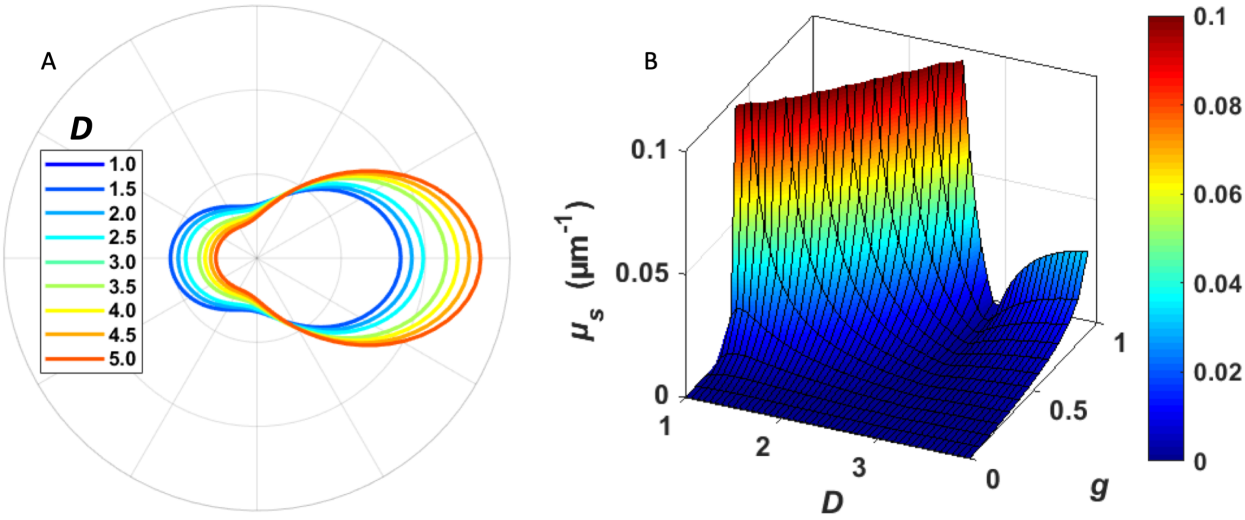

Figure 7.1. Changes in *D* affect light scattering behavior. (A) Shape of scattering phase function, $p(\theta)$, for D values ranging from 1-5. Simulated phase function incorporates correlation length l_c of 50 nm and wavelength of 600 nm in the absence of absorption. (B) Surface plot shows behavior of scattering coefficient with respect to changes in D and g in the Born approximation as characterized theoretically in a previously reported derivation[3].

Applied to the imaging of coral tissue, ISOCT measures the optical backscattering intensity, $I_b(\lambda,x,y,z)$, the square of which is proportional to the product of $\mu_b(\lambda,x,y,z)$ of the sample and the attenuation term integrated over the depth above the voxel of interest, which depends on the sum of the scattering and absorption coefficients of the medium, $\mu_t = \mu_s(\lambda) + \mu_a(\lambda)$, for a given voxel. These relative contributions of scattering and absorption were fit using a Matlab code implementing the Nelder-Mead algorithm [261] to iteratively minimize the sum of square differences as mathematically described by the following cost function:

$$cost(c_a, c_s, D, Lc) = \sum_{\lambda_{i=1}}^{\lambda_{i=N}} |\mu_t^*(\lambda_i) - f(c_a, c_s, D, Lc, \lambda_i)|^2 \quad (2)$$

where $f(c_a, c_s, D, Lc) = c_a\ \mu_a^*(\lambda_i) + c_s\ \mu_S^*(\lambda_i, D, Lc)$; $c_a,\ c_s \in [0, \frac{1}{2}]$. For simplicity, we introduce * to denote where a metric was normalized by its maximum along wavelength. Thus, the absolute coefficients are defined as:

$$\mu_a(\lambda) = c_a\ \mu_a^*(\lambda)\ \max\{\mu_t(\lambda_i)\} \quad (3)$$

$$\mu_s(\lambda) = c_S\ \mu_s^*(\lambda, D, Lc)\ \max\{\mu_t(\lambda_i)\} \quad (4)$$

Using equation (2), the effect of absorption is estimated from the attenuation coefficient spectrum based on the characteristic absorption spectrum that is distinct from the scattering spectrum, which decouples $\mu_s(\lambda)$ and $\mu_a(\lambda)$. (see 'ISOCT analysis' section in Results for details on the estimated absorption spectra). The next step is to determine D within a given resolution voxel (approximately 9x9x1.2 μm) of the sample by fitting $\mu_b(\lambda)$ using the Whittle-Matérn model: $\mu_b(\lambda) \propto \lambda^{\frac{D}{2}-2}$ [76]. As a result, ISOCT measures the set of three parameters (optical parameters μ_s and μ_b and the ultrastructural parameter D) in 3-D. The Whittle-Matérn model is then used to calculate g and μ_S' using equation (6) from a previous publication[3]. Furthermore, one can fully characterize all three ultrastructural parameters (A_n, L_n, D from equation 1) from the measured optical properties (μ_s, μ_b) for a more thorough characterization of the structure of the medium[3]. The analysis of ISOCT in

coral skeletons is similar with the exception that in coral skeletons, as opposed to coral tissue, $\mu_s(\lambda) >> \mu_a(\lambda)$ [232] and the skeletal light absorption is neglected.

7.3.5. ISOCT signal analysis

A full description of the steps for processing ISOCT data is given in Results, along with a processing flowchart in Figure 1. Briefly, the spectral domain OCT data collected at wavelengths between 520 and 720 nm were converted to spectrally-dependent OCT images through a short-time Fourier transform (STFT) with 22 separate Gaussian windows, each with full width at half-maximum (FWHM) of 20 nm. System spectral response was accounted for by calibration with scans of a reference solution of 80 nm polystyrene beads in water, approximating a medium with Rayleigh scattering behavior. Next, surfaces of either coral tissue or skeleton were detected with either an edge detection algorithm or manual segmentation. The surface edge detection algorithm was implemented through a custom Matlab script and operated on each OCT B-scan in the image cube by first filtering and adjusting intensity values to optimize image contrast. Then, an extended-maxima transform was applied to binarize the image, delineating the B-scan region containing scattering sample. Binary morphological operations then detected the top surface of this sample region, which when combined with all B-scans provided a 2-D sample surface profile image for the 3-D OCT scan. The signal intensity decay as a function of depth below the detected edge was fit with an exponential function over a 90 μm depth to quantify the total attenuation coefficient, μ_t, for each OCT A-line for each wavelength. This method for measuring μ_t was verified by applying it to samples of polystyrene spheres with known magnitude of μ_t across a μ_t range relevant for tissue described in Materials and Methods subsection “Validation of μ_t measurement”. The full spectrum of μ_t was then decomposed into a linear combination of scattering and absorption coefficients assuming an absorption dominated by chlorophyll *a* (see ISOCT analysis section in

results regarding how the shape of μ_t spectra showed a characteristic peak of chlorophyll *a* absorption, which was the predominant peak for the corals measured). The true backscattering spectrum from each voxel was measured by dividing the OCT spectrum by the spectrally-dependent μ_t attenuation term above the voxel. This corrected spectrum was then fit to the power-law relation with wavelength shown above to determine *D*.

For calculation of chlorophyll *a* density, the linearly decomposed spectrum of μ_t, consisting of the respective fractional contributions of μ_s and μ_a was taken with the full spectral shape of μ_a assumed to be that of chlorophyll *a* in methanol. This absorption spectrum was taken from values collected by J. Li and provided on the Oregon Medical Laser Center webpage [262], and shows a characteristic peak in the visible around 660 nm. The spectroscopic resampling of OCT data was performed with STFT window FWHM of 20 nm, meaning that absorption peaks from other pigments that fall outside this width from the peak at 660 nm would have negligible contribution to the linear regression used to compute μ_a contribution and would not contribute to the calculation of chlorophyll *a* concentration. Chlorophyll *a* concentration was then calculated by dividing the measured absorption coefficient by the molar extinction coefficient provided, scaled by the peak intensity at 660 nm. This molar concentration was converted to areal density [mg/cm^2] by molar conversion of chlorophyll *a* and integrating the volumetric concentration over the 90 μm thickness of tissue used for μ_t measurement.

7.3.6. Validation of μ_t measurement

Validation of μ_t measurement technique was performed by scanning aqueous suspensions of 200 μm diameter polystyrene latex beads with concentrations ranging from 0.1-1.0 wt%. A 50 μL droplet of the suspension of interest was pipetted onto a quartz plate and a 2 x 2 mm area was scanned with 256 x 256 pixels. The surface of the droplet was angled slightly and manual lateral

segmentation of the *en face* image was later performed to ensure only clean signal that was free from specular reflection was included in μ_t analysis. The same code applied to coral image processing was used to calculate mean μ_t from beads samples. For each concentration the mean μ_t from 3 sample regions were averaged and standard error on the mean (SEM) was plotted as error bars in Supplementary figure 7.9. Theoretical μ_t values for each concentration were calculated from Mie Theory and used as the ordinate axis for parity comparison.

7.3.7. Analysis of microvariability of *D*

To confirm the true spatial variability of *D* values in the tissue of living coral, we performed an averaging box analysis on two-dimensional *D* maps of *Merulina ampliata* tissue and an aqueous suspension of 80 nm beads (2 wt%). For this analysis, a square box with given edge length was placed randomly within the 2D *D* map and an average *D* was calculated from all pixels contained within. This random sampling was repeated 1000 times for each edge length tested, and the standard deviation over these 1000 samples was interpreted as the square root of the local spatial variance in *D*. For the sample of 80 nm polystyrene beads, the expected number of beads contained within a resolution voxel of the OCT system is on the order of 10^4 so this medium is considered to be spatially homogeneous with constant *D*. Therefore, the spatial variance in *D* due to instrument noise and subsequent propagation through processing is fully characterized by this measurement of 80 nm beads shown in Figure 7.8(C). The higher spatial variance in *D* seen from the same analysis applied to the *Merulina ampliata D* map is due to an additional spatial variance in sample structure quantified by *D*.

7.4. Results

7.4.1. ISOCT analysis

Here we describe a novel OCT data processing method employed to extract structural and optical properties from OCT data (Figure 7.2). A short-time Fourier Transform was applied to the raw OCT data using Gaussian windows (FWHM of 20 nm) to compute a spectral cube consisting of OCT intensity as a function of 3-D position and wavelength. This data cube is collected by raster scanning the OCT sample laser beam across the sample surface, collecting an OCT A-line, or the backscatter intensity function versus depth, from each transverse position. The series of A-lines from a single scan across the sample form an OCT B-scan image, which displays a depth-slice of backscattering intensity from the sample in question. From OCT B-scan images the surface of the coral tissue and skeleton were detected, and the wavelength dependent attenuation coefficient μ_t was computed from the spectral cube by fitting an exponential fit in depth at a fixed thickness of 90 μm below each surface for every lateral position according to the Beer-Lambert law. This thickness was selected in order to provide sufficient depth information within the constraints of axial resolution of the spectrally resolved OCT images and optical penetration through the coral tissue and skeleton under study. This technique for calculating μ_t was validated for by measuring standard aqueous suspensions of 200 nm polystyrene spheres with known μ_t from Mie theory (see section 7.3.6. Validation of μ_t measurement). The backscattering coefficient μ_b was calculated for the tissue by averaging signal intensity from the first 90 μm of tissue from the surface. Using the thickness of the tissue layer and calculated attenuation coefficient, the decaying signal intensity in the cube was compensated by the spectrally dependent attenuation in order to yield an accurate backscattering spectral shape. From this modified spectral cube, the backscattering coefficient of the skeleton was computed by averaging the upper 90 μm of the

skeletal layer.

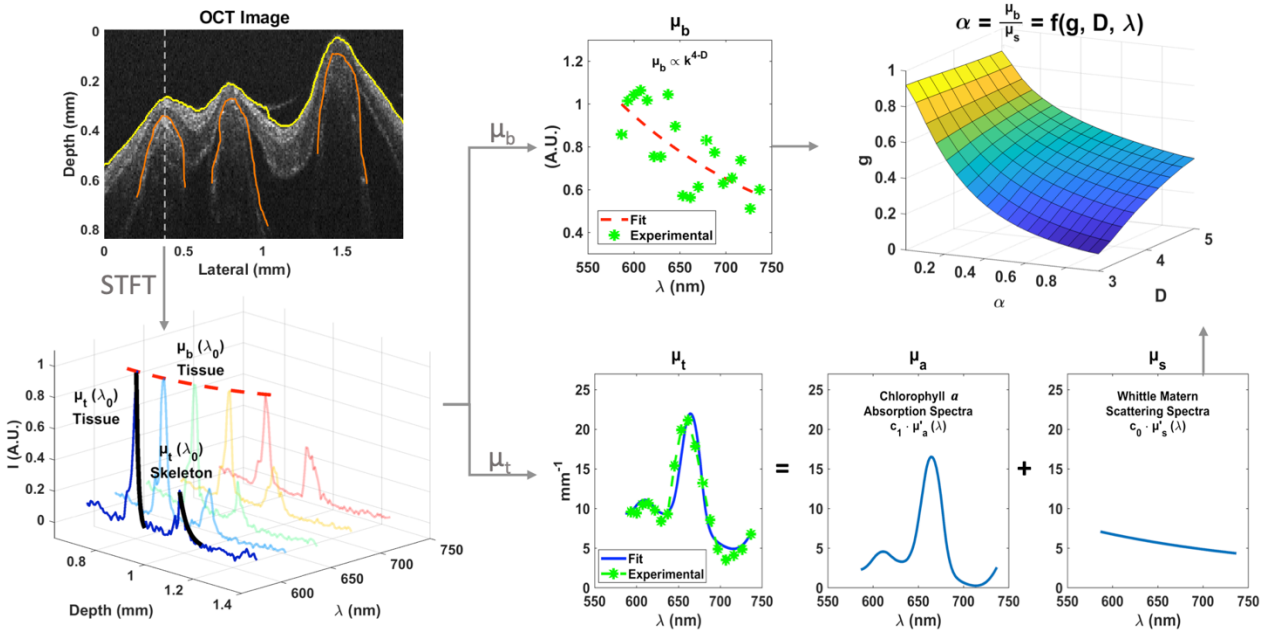

Figure 7.2. Flowchart for ISOCT data processing. Processing starts with the acquisition of the OCT volume and detection of surfaces of tissue and skeleton. From a short-time Fourier transform, the spectral cube is generated and wavelength-dependent backscattering and attenuation coefficients are computed. Fractal dimension D is fit from μ_b, and the μ_s spectral shape and scaling factors for μ_a and μ_s are also fit. Finally, the wavelength-dependent (g) is computed from the albedo (α) and D.

Next, from the backscattering coefficient of the tissue and skeleton, the first-order Born approximation was employed, reducing the spectral dependence to a simple power law fit with fractal dimension D (Figure 1C). D was fit for every lateral position of the tissue and skeleton where the surface edge was available from an extended-maxima transform based algorithm for the tissue surface or manual segmentation for the skeleton surface, specular reflection was absent, and

topography was within the roll-off sensitivity range of the OCT instrument, which is due primarily to spectral resolution of the spectrometer and is on the order of -10 dB/mm in air for the visible spectrometer used in this study.

From $\mu_t(\lambda)$ of the tissue layer and the skeleton layer, the μ_s spectral shape was fit by assuming that the Whittle-Matérn functional form can parameterize the statistics of the local refractive index variations using three structurally relevant parameters, σ_n, D, and L_n [3], see methods. Additionally, we observed that the shape of μ_t spectra showed a characteristic peak of chlorophyll *a* absorption. For the corals measured, this was the predominant absorption feature observed and so for this model, the predominant absorbing pigment of chlorophyll *a* was assumed to be responsible for all absorption within the coral tissue. Using this assumption, the relative contributions of μ_a and μ_s to the total μ_t spectrum were fit using the Nelder-Mead algorithm described in "Light scattering model for ISOCT signal analysis" in Materials and methods in order to minimize the cost function of deviation from the experimentally measured total attenuation spectrum. To scale measured μ_b intensity, a standard sample of 80 nm polystyrene sphere suspension with known scattering properties was measured for calibration. Finally, the ratio of μ_b to μ_s, known as the reflection albedo α, is related to the structural parameters D and g within the Born approximation and is described in a prior publication [3]. Using this relationship, a lookup table was computed to determine g for given α and D.

7.4.2. Mapping structural and optical properties and chlorophyll *a* surface density measurement

To measure structural and optical properties from the tissue and skeleton of live corals, we scanned specific regions on specimen fragments of *Merulina ampliata* and *Diploastrea heliopora* with our visible OCT system. The 3-D nature and micron-scale resolution of visible OCT imaging

can be appreciated in Supplementary video 4, which shows a flythrough of OCT B-scans of a *Diploastrea heliopora* polyp mouth. The spectrally enabled ability of ISOCT to quantify tissue structure through its fractal dimension *D* is also demonstrated in Figure 7.3 (see Supplementary video 5 for a rendered scan volume of the coenosarc region of *Merulina ampliata*). In this rendering, the traditional OCT intensity is depicted as a grayscale image and *D* values are represented by color hue. It is apparent that in coral tissue, *D* has a heterogeneous spatial distribution with certain tissue regions showing *D* as low as 1.5 while others show *D* values as high as 5. Furthermore, it is seen that for many regions in the tissue, *D* does not reflect a value sufficiently close to 3 to make the assumption of a Henyey-Greenstein scattering phase function appropriate.

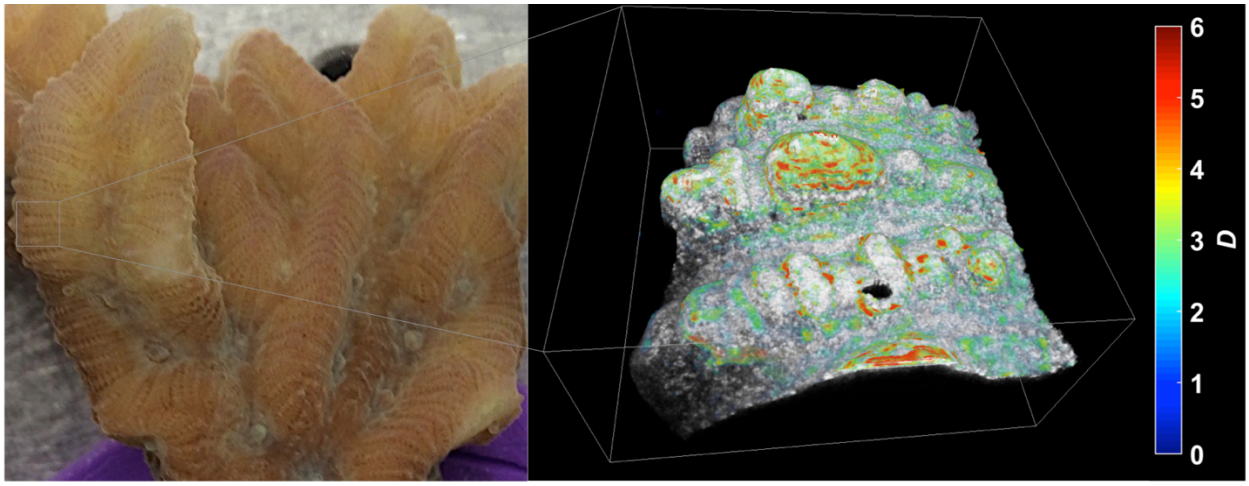

Figure 7.3. Example rendering of ISOCT data from *Merulina ampliata*. Photograph of live coral measured shown on left, with box demarcating region scanned. 3-D volumetric rendering of OCT scan volume shown on right, with traditional OCT image intensity shown in grayscale with 3-D overlay of local *D* value in color. Rendering box is 2.56x2.56x1.5 mm.

Linking the ultrastructural characteristics and corresponding optical properties of corals is fundamental for mechanistic understanding of light transport in these ecologically important organisms. ISOCT provides an unparalleled method for mapping the spatial distribution of these properties with high spatial resolution. Maps of some of these properties, namely the total attenuation coefficient μ_t, areal density of chlorophyll *a*, which is directly related to μ_a, and *D* from representative regions of coenosarc tissue in *Merulina ampliata* and *Diploastrea heliopora* are shown in Figure 7.4. An example projection map of scattering anisotropy, *g*, calculated from the measured scattering albedo and *D*, is shown in Figure 7.5. Accompanying histograms of calculated *g* distributions from tissue and skeleton of *Merulina ampliata* and *Diploastrea heliopora* show that both compartments have *g* close to 1 indicating high forward scattering from these structures.

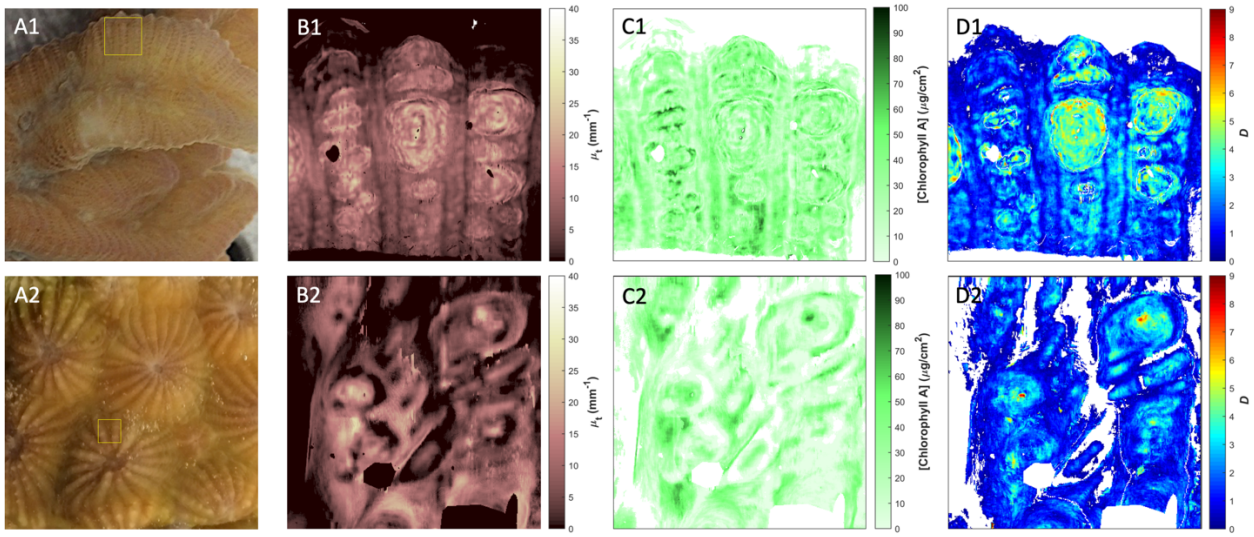

Figure 7.4. Top-down projection maps of optical and structural properties. Photographs of *Merulina ampliata* (A1) and *Diploastrea heliopora* (A2) with box demarcating region scanned with ISOCT. *En face* projection maps of total attenuation coefficient μ_t (B1, B2), chlorophyll *a* concentration (C1, C2), and *D* value (D1, D2) for *Merulina* and *Diploastrea*, respectively. Maps B1, C1, and D1 are 2.56 x 2.56 mm; maps B2, C2, and D2 are 1.85 x 1.85 mm.

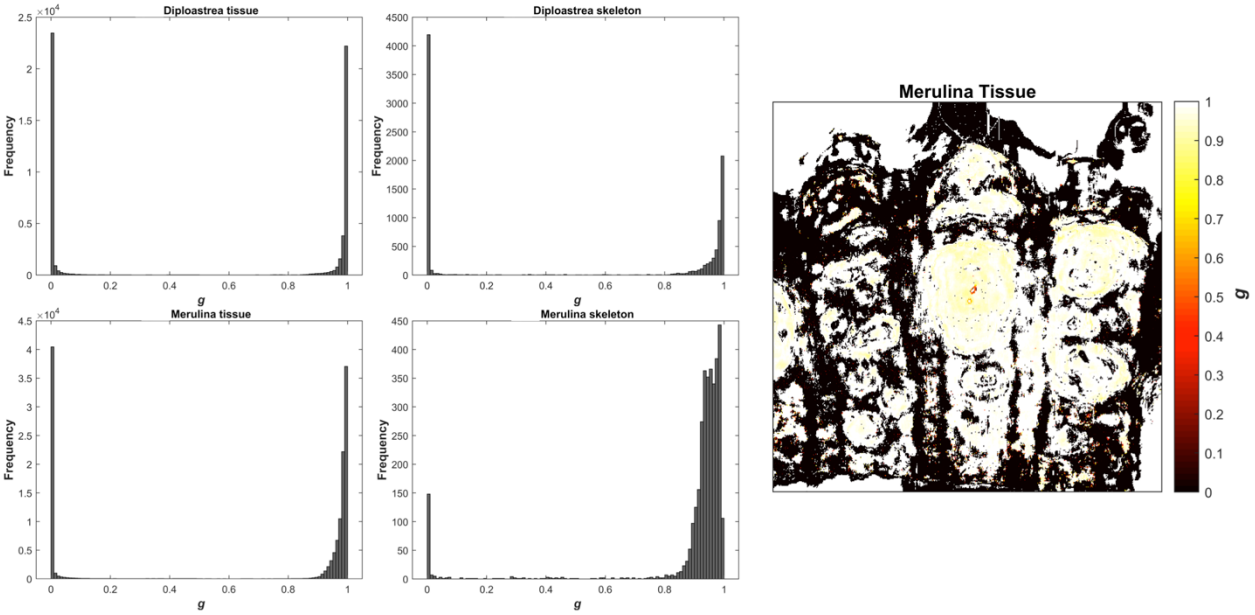

Figure 7.5. Quantifying scattering anisotropy in coral. Histograms of scattering anisotropy *g* from tissue and skeleton of *Merulina ampliata* and *Diploastrea heliopora*. Projection map of *g* from tissue layer of *Merulina ampliata* (right).

While the penetration of visible OCT is somewhat limited through the highly absorbing and scattering tissues of many corals, variability in tissue thickness and skeletal topography allows for imaging directly through living tissue and quantifying optical and structural properties from certain areas of the coral coenosteum, i.e. the skeletal material formed below the connective tissue between polyps. To confirm the location of the skeleton in these regions, we captured OCT scans from a specific region of coenosarc in *Diploastrea heliopora* before and after tissue removal (see peaks of skeletal plates easily resolved through tissue in Supplementary video 6). Maps of total attenuation coefficient μ_t, chlorophyll *a* concentration, and *D* of *Merulina ampliata* and *Diploastrea heliopora* skeletons are shown in Figure 7.6.

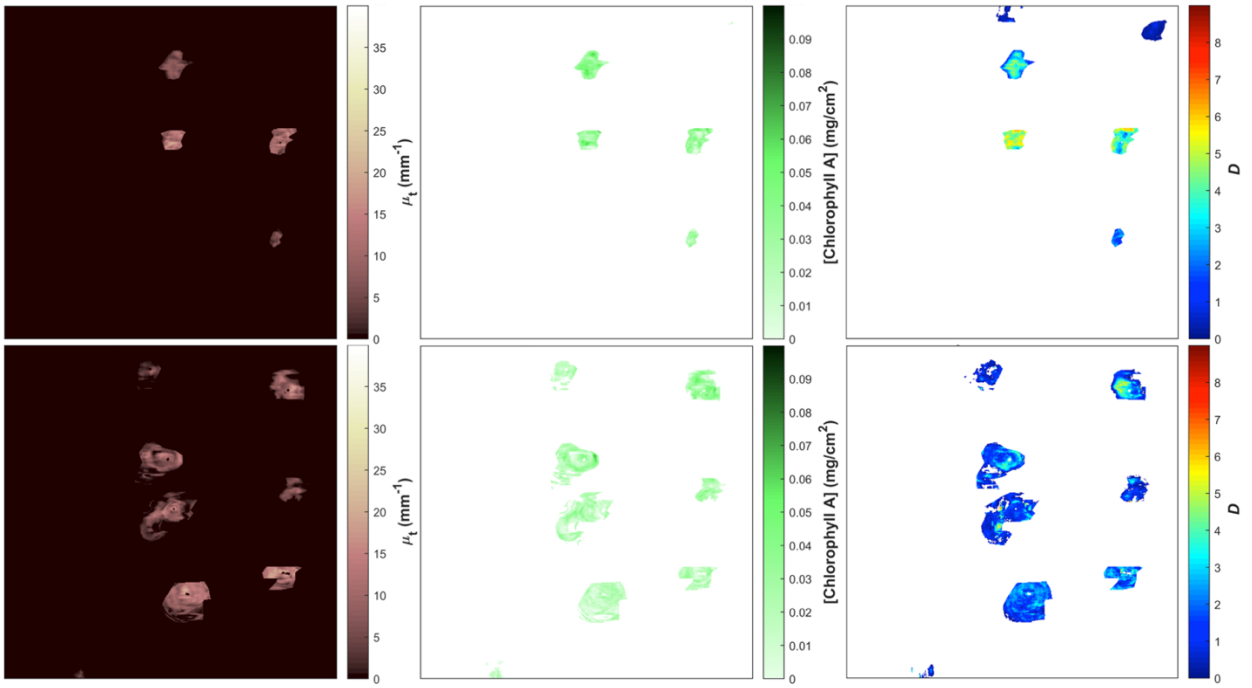

Figure 7.6. Optical and structural property maps from coral skeletons. *En face* projection maps of μ_t, Chlorophyll A density, and *D* for visible skeletal ridges from *Merulina ampliata* (top row) and *Diploastrea heliopora* (bottom row).

Chlorophyll *a* areal density was determined by ISOCT for the first 90 µm of tissue thickness for surface areas over skeletal ridges and valleys (Figure 7.4(C1) and (C2), respectively, see inset in Figure 7.4(A1) and (A2)). While considerable spatial variability was observed across skeletal ridges and valleys (from 0.05 – 0.1 mg/cm^2), the average chlorophyll *a* density was 29.5 ± 14.4 µg/cm^2 for *Merulina ampliata* and 17.9 ± 15.8 µg/cm^2 for *Diploastrea heliopora.*

Spatial variability of all three of these properties in the projected view is apparent and of consequence when modeling light transport within the whole colony. A large variability in the structural parameter *D* was observed for the tissue and skeletal compartments of *Merulina ampliata* and *Diploastrea heliopora*, as can be observed from histograms of these values in Figure 7.7.

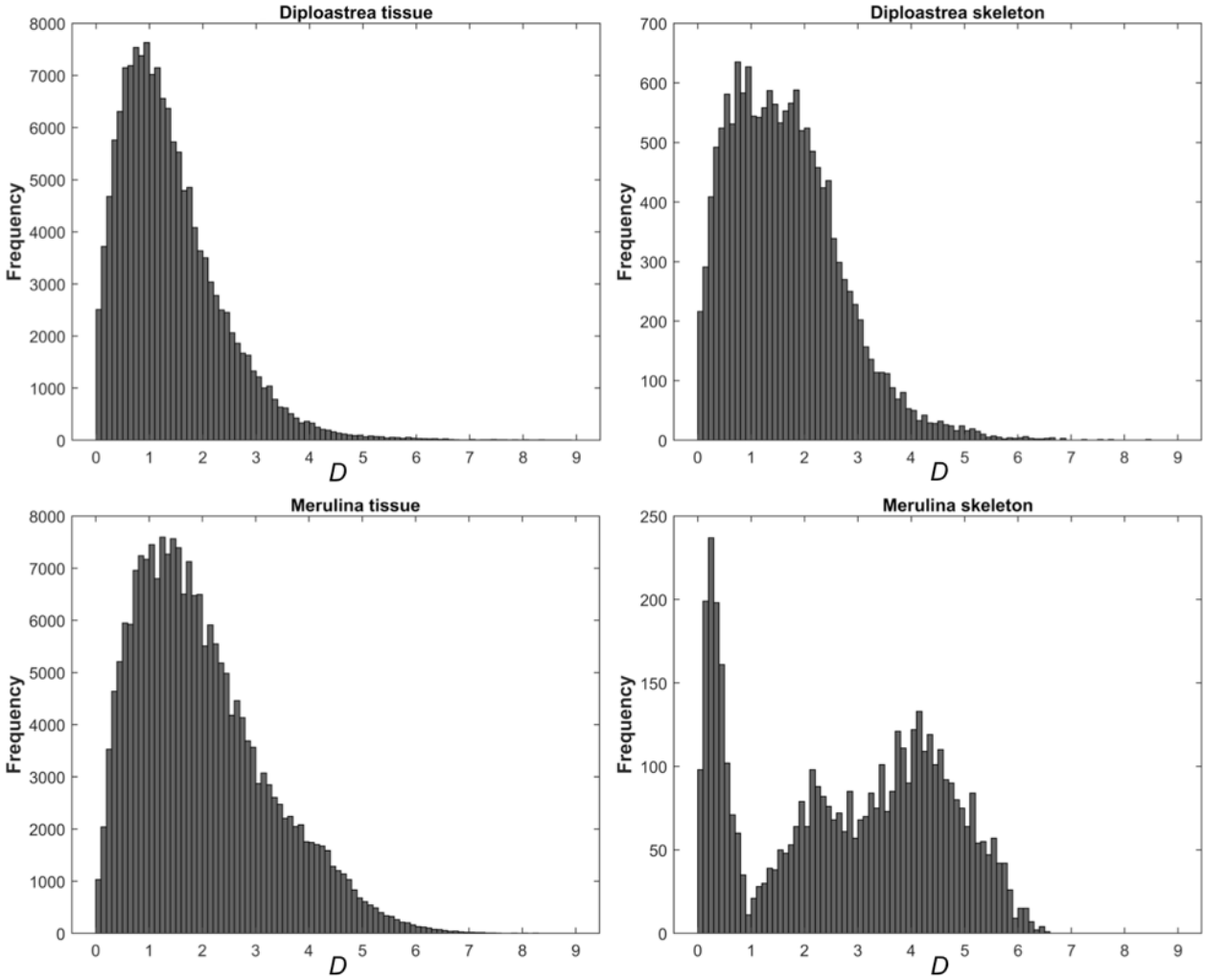

Figure 7.7. Histograms of *D* values from tissue and skeletal compartments of *Merulina ampliata* and *Diploastrea heliopora*. Frequency plotted reflects likelihood of a 5 x 5 μm pixel having a given *D* value.

Measured spatial variance can be considered as the sum of true spatial variance and instrumental variance. Instrument variance can be assessed when measuring the spatial variability of a truly homogenous sample. To determine instrument variance, we measured an aqueous suspension of 80 nm polystyrene beads at a concentration of 2 wt%, a medium reasonably homogenous considering each OCT resolution voxel contains on the order of 10^4 particles. We

applied the same ISOCT analysis algorithm to a scan of these beads as was applied to the data acquired from coral tissues, and used a randomized square averaging box to randomly sample *D* values at various locations on a projected *D* map. By plotting the standard deviation of *D* values from this random sampling with respect to the edge length of the averaging box, the degree of spatial variance is expressed (Figure 7.8). Results from an example scan of *Merulina* tissue thus yielded a significantly higher spatial variance than the intrinsic variance of the ISOCT instrument.

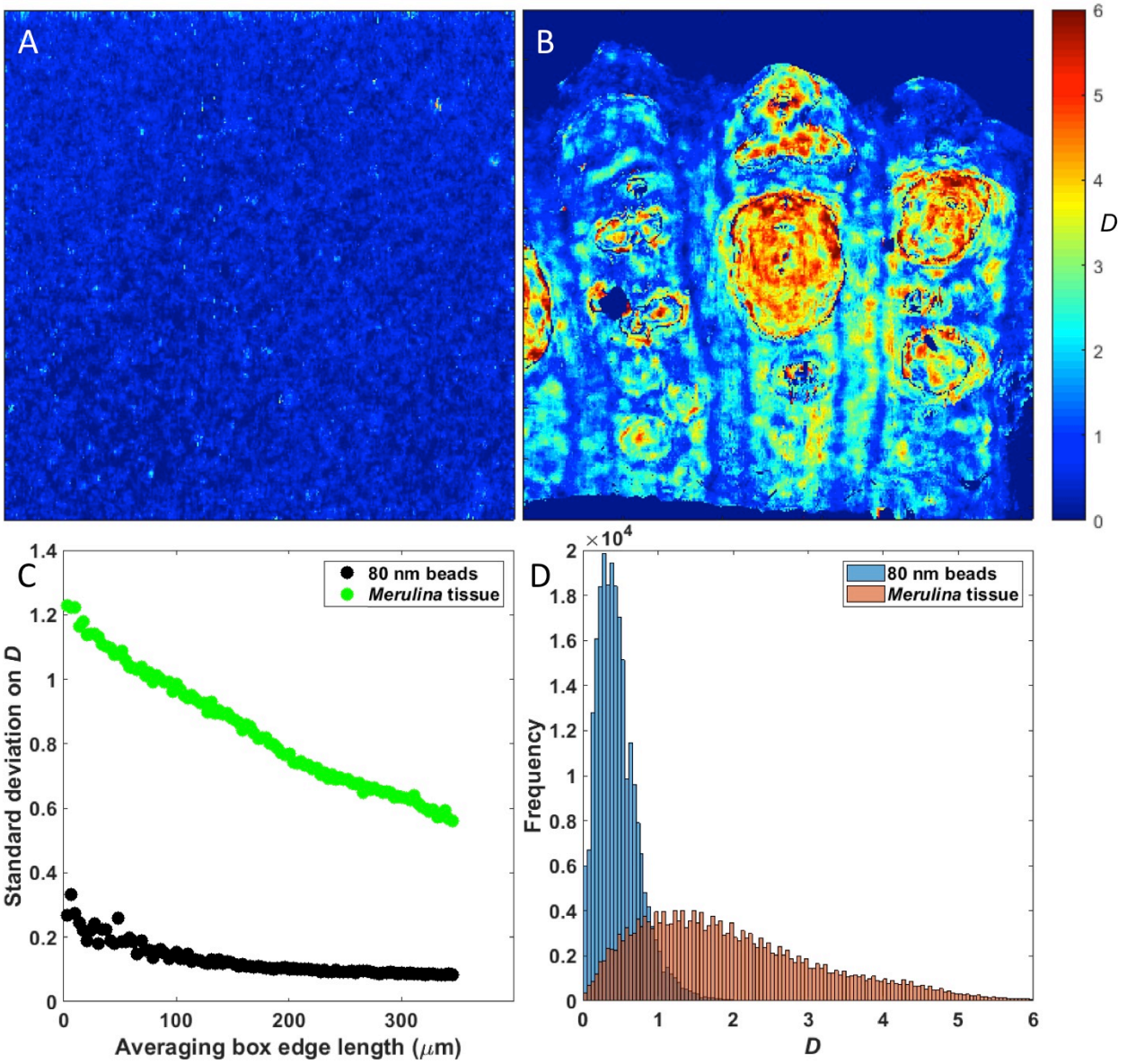

Figure 7.8. Spatial microvariability of *D* in coral far exceeds the noise floor. 2D maps of *D* from (A) 80 nm polystyrene beads suspension and (B) *Merulina ampliata* tissue. (C) Spatial variance comparison between *D* value maps from a homogenous sample of 80 nm polystyrene beads and *Merulina ampliata* tissue. (D) Histogram of *D* values from maps in (A) and (B).

7.5. Discussion

In this proof-of-concept study, we demonstrate that visible light ISOCT, which combines the structural and chemical analytic capabilities of spectroscopy with the high-resolution 3-D imaging of OCT, enables the non-invasive mapping of fundamental optical properties of coral tissue including chlorophyll *a* concentration, the absorption coefficient, the scattering and the reduced scattering coefficients, and the critical parameters governing the angular distribution of scattered light (*g* and *D*). In addition, ultrastructural properties such as the variance of the refractive index within tissue and the correlation length scale of the refractive index variations can also be estimated. This ability to non-invasively extract and 3-D map fundamental optical and structural properties in living corals is a breakthrough in coral biology, which now allows the quantification of optical parameters needed for rigorous simulations of light transport in corals.

The spectral decomposition in ISOCT enables more accurate and more complete characterization of light scattering in coral tissue. Previous studies of optical transport in corals have focused on coral controls of Symbiodiniaceae light exposure due to tissue scattering and lateral light transport [235,252] and skeletal scattering [230,232,263]. Hitherto, simulations of light propagation in corals have largely relied on the assumption that light scattering direction in coral tissue is dictated by the Henyey-Greenstein phase function, which is a special case of the Whittle-Matérn phase function when *D* is equal to 3 [75,252]. ISOCT spectral decomposition now enables the actual measurement of *D* in living coral tissue, thus removing the need for the Henyey-Greenstein approximation. Indeed, as seen in Figure 2, coral tissue *D* values vary significantly with location. This variability is an inherent property of coral tissue and is significantly greater than the technical variability of measuring *D*. By precisely measuring *D* and *g*, accurate information regarding the scattering phase function can now be implemented in more refined models of light propagation in the coral tissue. With the capability of ISOCT to measure spatially resolved ultrastructure and

optical properties, we foresee this technique to significantly enhance current understanding of light propagation throughout the coral holobiont. Beyond photophysiology, *D* is a key descriptor of coral tissue and skeletal ultrastructure and growth pattern, which can be used e.g. as a proxy for the rate of coral calcification [232,246], and in tissue, *D* of cell nuclei has been shown to be a critical regulator of transcriptional plasticity [214].

There are, however, limitations of ISOCT measurement of optical and structural properties that must be considered for corals. First, the limited penetration depth of OCT imaging in the visible spectral range is restricted to superficial regions of tissue and skeleton. In fact, where coral tissue was thick in regions between skeletal plates or protrusions, the coral skeleton was not visible with our OCT system. The difficulty in imaging through thick coral tissue is compounded by the limitations in effective working range, as all Fourier domain OCT systems have a roll-off in image intensity with depth [264]. While the limitation of roll-off can be somewhat alleviated through motorized stage control and application of automated surface detection and stitching algorithms, the limited optical penetration in the visible range required for analysis of chlorophyll *a* concentration restricts application of this technique to the soft tissue compartment and superficial skeleton only in regions where tissue is thin. Implementation of dual-band ISOCT incorporating both visible and infrared channels to provide complementary structural information has shown great promise in resolving deeper structural features in tissue and skeleton of *Diploastrea heliopora*, as can be observed in Supplementary figure 7.11.

Additionally, the analysis method presented here relies on several assumptions regarding the coral tissue structure in order to determine the optical and structural properties presented. In the calculation of μ_t from each compartment, it was thus assumed that the medium was randomly homogeneous in keeping with Beer-Lambert law along the 90 μm depth of fitting. While this is a fair assumption for many tissue regions, the region of averaging, in some cases, might include

distinct layers of epidermis, mesoglea, and gastrodermis, which may have different attenuation properties. For a coarse modeling of optical transport, such bulk properties may still be of use, but a strength of OCT in this application is its measurement of optical properties with high spatial resolution that will allow for a more detailed analysis of photon propagation in these specific tissue compartments in future study. For instance, transmission electron microscopy (TEM) has been used to image the nanoscale structure of tissue as an independent metric of the statistical mass-density autocorrelation function characterized with ISOCT[78,265]. These complementary techniques can be applied to each compartment of the tissue to fully characterize the structural properties and scattering therein. The coral skeleton presents a separate challenge with topographic roughness, and optical properties in this study were only measured from the top of septal plates where structure within the skeleton appeared homogeneous in OCT B-scans. While the interpretation of anatomical features in OCT scans of living corals remains unclear for certain species, the tissue stripping presented in Supplementary video 6 confirms septal plates are clearly discernable through the tissue with visible OCT.

The linear fitting used to separate scattering and absorption coefficients from μ_t relied on the assumption that chlorophyll *a* was the predominant absorber present in the coral tissue, simplifying this fitting procedure. A more detailed analysis taking into account additional absorbing pigments in the coral tissue such as endogenous fluorophores, fluorescent and non-fluorescent host pigments, in pigment granules [238,240] is feasible, provided the pigment absorption spectrum is known *a priori* and it contains a distinctive feature within the visible wavelength band analyzed. Fitting the measured backscattering spectrum to calculate fractal dimension, *D*, relies on the assumption that the autocorrelation function of the medium can be modeled as a Whittle-Matérn function and that the first-order Born approximation applies. These approximations have been applied to the analysis of mammalian tissues previously [3,75,76,243], and when the influence of

absorbing pigments is properly compensated should also be applicable to media such as coral tissue. The average chlorophyll *a* areal density mapped in Figure 3 is 29.5 ± 14.4 μg/cm^2 for *Merulina ampliata* and 17.9 ± 15.8 μg/cm^2 for *Diploastrea heliopora*. These values are comparable to chlorophyll *a* concentrations measured in tissues of several species of healthy corals, which can range between 3 and 50 μg/cm^2 [266–271].

ISOCT allows for direct measurement of optical properties and three-dimensional micro-morphology in living corals, which will facilitate the understanding of light propagation and radiative energy budgets in corals. This is key to a better mechanistic understanding of coral photophysiology and thermal resilience in a changing climate. The emerging picture is that of a tissue-skeletal system that modulates optical and thermal properties of corals through a variety of strategies to optimize light regimes and heating for the photosynthetic algal symbionts harbored in their tissues. The strategies uncovered range from skeletal- and tissue- light scattering that increase symbiont light exposure [230,232–234,244,252,272] to fluorescent pigments in the tissue that modulate light absorption, light scattering and heating in the tissue [238,240,241,273] to dynamic light redistribution resulting from tissue contraction and expansion [234–236]. Skeletal light scattering has been implicated in the acceleration of light stress of *in hospite* Symbiodiniacea under increased temperature by a positive feedback-loop between photodamage and symbiont loss that results in coral bleaching[230,232,233,272] and can affect coral recovery from bleaching events [274]. Green fluorescent protein-like host pigments have been shown to reduce coral tissue heating and light absorption by increased light scattering at high concentrations of pigment, which enhances reflectivity and thus diminishes light penetration further into the tissue leading to reduced tissue heating [240]. These different properties vary significantly among coral species resulting in unique light microenvironments for the symbiont algae and distinct stress-mitigating strategies [232–235,275].

Imaging both skeletal and tissue compartments in living corals as one system will help to further elucidate different photophysiology responses to thermal stress.

In conclusion, we introduce in this work the novel application of ISOCT to study the microscale structure and optical properties of live corals. We believe this technique to be unique for this application in its ease of use, imaging speed, spectral information, high working distance, and micron-scale resolution. The rapid imaging speed and low phototoxicity of ISOCT could be used in future studies to monitor real-time responses to stressors or other stimuli. Furthermore, spectroscopic analysis of the ISOCT signal could be used to infer nanoscale changes in cellular structure, such as dysregulated nuclear chromatin condensation, or altered absorption profiles from changes in pigment expression and Symbiodiniaceae distribution. The inherent quantitative and spatially-resolved nature of ISOCT will also prove useful in future study of photonic transport within the whole holobiont, an effect heretofore studied separately in coral skeletons and tissues.

7.6. Supplementary Figures

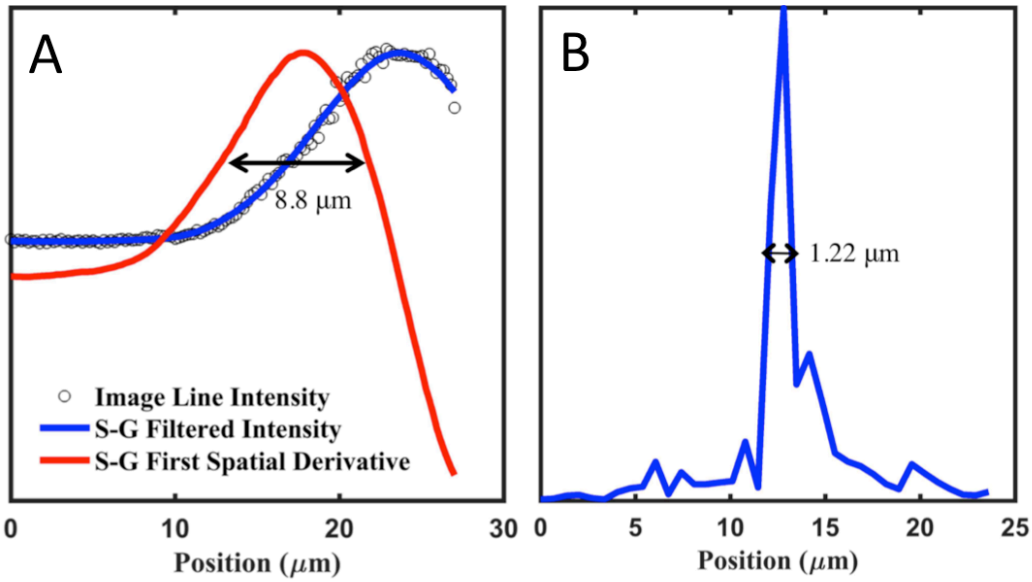

Figure 7.9. Spatial resolution of OCT system. Quantification of spatial resolution of visible OCT system used in lateral (A) and axial (B) directions.

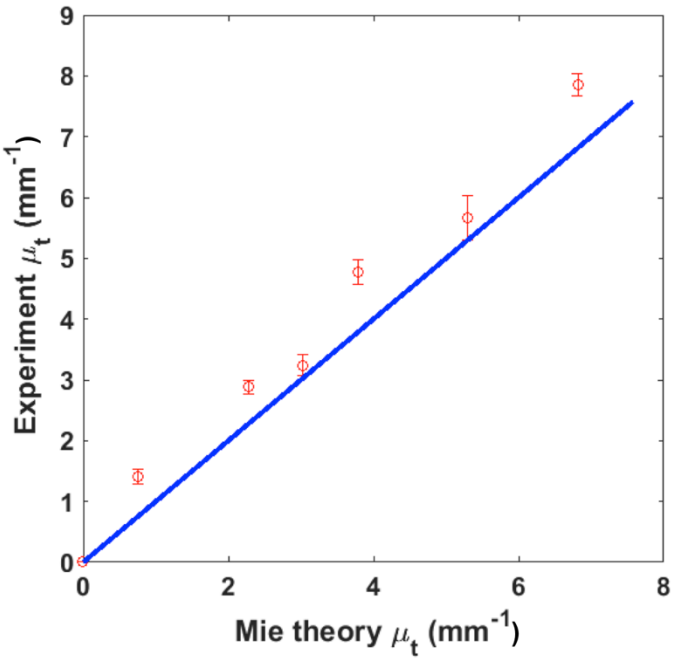

Figure 7.10. Validation of total attenuation coefficient measurement. Experimental (red series) comparison with Mie theory (blue line) for samples of 200 nm polystyrene spheres of varying

concentrations (0.1-1.0 wt%).

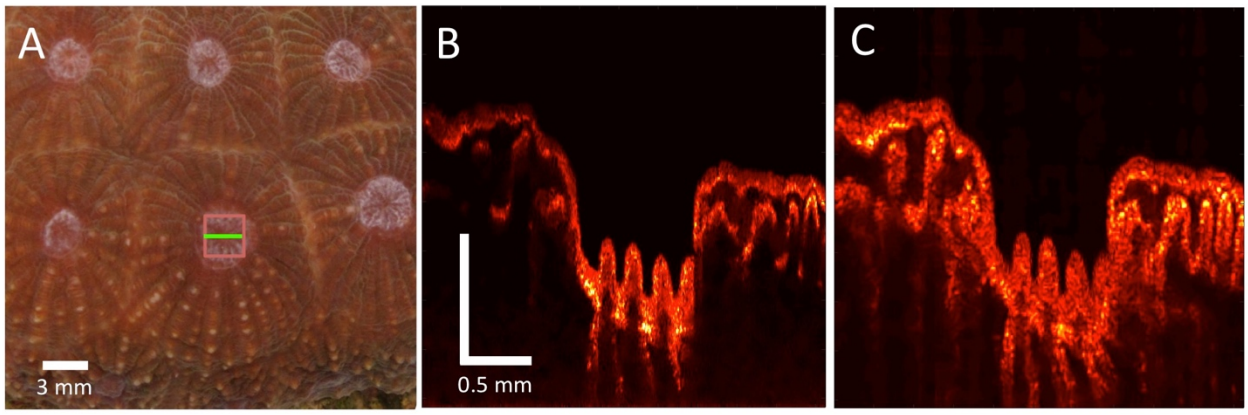

Figure 7.11. *Diploastrea heliopora* imaged with dual-band ISOCT. (A) Photograph of live coral with 2.8x2.8 mm OCT scan region demarcated by salmon box. OCT B-scans show depth section through tissue layer down to underlying skeleton. Complementary strengths of high spatial resolution of visible channel (B) and penetration depth of infrared channel (C) shown in side-by-side B-scans taken from cross-section shown by green line in (A).

7.7. Supplementary video captions

Supplementary video 4. Flythrough of OCT B-scans collected from a live *Diploastrea heliopora* polyp mouth. B-scan image shown on left, *en face* projection with B-scan slice location demarcated with line shown on right. Frame width 2.56 mm, frame depth 1.5 mm.

Supplementary video 5. 3D rendering of ISOCT scan of *Merulina ampliata* coenosarc. Traditional OCT image shown in grayscale, with color overlay corresponding to local *D* value.

Supplementary video 6. Coral skeleton identified by tissue removal. A side-by-side video of a flythrough of corresponding OCT B-scans showing the intact coral (left side) and stripped skeleton (right side). Image cube size is 2.56x2.56x2.56 mm.

Chapter 8:

Conclusions and Future Directions

8.1. Summary

The work presented in this dissertation advances a transformative, multidisciplinary approach to the early detection of metastasis, integrating the fields of cancer biology, biomaterials, and biophotonics, with the potential to answer a variety of scientific questions that extend beyond the scope of this application. By engineering a biomaterial implant to attract circulating tumor cells and metastasis-associated immune cells, a "metastasis magnet" that can be used as a sentinel site for early metastatic surveillance has been developed. Metastasis-associated changes in the structure of the integrated implant were detected with a newly-developed extension of an emerging 3D optical imaging modality, inverse spectroscopic optical coherence tomography (ISOCT), in a mouse model of metastatic breast cancer. Scaffold structures that were altered in the presence of metastasis included extracellular collagen density and arrangement, vascular size and endothelial density, and the averaged mass fractal dimension of scaffold-resident cells, which are determined to all contribute to a difference in signal measured with ISOCT. Development of a dual band ISOCT instrument and ISOCT needle probe were pursued with the goal of adaptation of the current lab benchtop instrument to a clinically viable device for *in vivo* measurements. Development of spectral analysis techniques for nanoparticle characterization and tracking in cancer cell cultures and ISOCT development for imaging measurement of optical and structural properties in live corals were separately presented, pertaining to a central theme of the diverse applications of OCT and hyperspectral imaging techniques. From a scientific perspective, the identification of distinct metastasis-associated changes in stromal compartments of the scaffold as well as a separate structural phenotype of scaffold-resident cells advances the understanding of the structural preconditioning of the pre-metastatic niche. From a technological perspective, the advancement of optical coherence tomography in the dual-band benchtop and visible needle-probe configurations presented here will be of interest for various clinical and laboratory applications and for continued

development of optical coherence tomography-based imaging modalities. From a utilization perspective, the application of the developed imaging techniques to the fields of cancer biology, nanomaterials, and marine biology presented here has provided new insight into the structural characteristics and remodeling of these systems through label-free non-perturbative imaging.

8.2. Future directions

The following section will describe future studies and developments to the work presented in the dissertation to further its significance and impact.

8.2.1. Elucidate mechanisms of ECM-induced cellular restructuring

In **Chapter 3**, we presented findings that indicate the fractal dimension of cellular colonies is directly influenced by the degree of crosslinking of the collagen substrate they are grown on. This increase in fractal dimension is accompanied by the adoption of a more proliferative phenotype, as is shown in figures 3.3 and 3.4. The mechanisms linking these bulk phenotype and structural responses are still poorly understood, yet in many cells the nucleus is one of the most highly scattering structures in the visible bandwidth[276]. We hypothesize that cancer cells respond to matrix stiffness and structure through mechanotransduction that affects gene transcription in the nucleus in part by affecting packing of chromatin in the nucleus. This packing is directly measurable at the sub-cellular level through partial-wave spectroscopic (PWS) microscopy and the bulk cellular level with ISOCT at different levels of spatial resolution. PWS microscopy can be used to test the hypothesis that culture on a stiffer matrix results in a more condensed chromatin topology, manifesting in the measurement of a higher nuclear fractal dimension. Alternative techniques to measure chromatin topology include ChromEM labeling paired with transmission electron microtomography[277], labeled or intrinsic contrast superresolution microscopy[278–280], or Hi-C for contact probability and chromatin fractal dimension analysis[214]. A concomitant response

in gene expression profiles from cells in this system can be profiled using RNA sequencing analysis, and matrix-associated changes in cancer cell stemness can be investigated through cell sorting and immunofluorescent labeling of cells with CD144 differentiation marker. In addition to providing new methodology for study of cellular-extracellular matrix interactions in carcinogenesis and early metastasis, this study could provide new insight into the interplay between a cancer cell's environment and nuclear structure as it relates to functional gene expression, with potential for direct translation to more relevant model systems for screening of chemotherapeutic adjuvants *in vitro*. Furthermore, the potential connection of bulk cellular fractal dimension to a direct measure of nuclear structure will help to clarify the link between other ISOCT measurements of cell suspensions such as those presented in figure 5.5 and a previous work[116] and intracellular structures of interest with implications for determining a potential link between global structure and behavioral phenotype in cancer cells.

Although this study explored ISOCT sensitivity to collagen crosslinking, a biological process commonly implicated in cancer progression, it would be interesting to conduct additional studies on other aspects of ECM remodeling. In addition to ECM deposition and crosslinking, degradation with a suite of proteolytic enzymes such as matrix metalloproteinases is an important effect in tumor microenvironment remodeling which is in part responsible for tumor cell migration across the basement membrane, the first of several steps in the biological paradigm of metastatic dissemination. Further study of ISOCT sensitivity to ECM degradation and cellular response would be of potential interest broadly in the cancer research community.

8.2.2. Further development of ISOCT imaging modalities for scaffold-based screening

In **Chapter 4,** the development of two separate instrumentation schemes for ISOCT was presented: (1) a dual-bandwidth benchtop system operating in the visible and infrared ranges, and

(2) a visible band needle probe. While the general motivation for development of these techniques is the measurement of a subcutaneous scaffold for metastasis screening, these techniques have great potential in other applications, and the dual-bandwidth OCT system has shown utility in study of wound healing processes[2]. Focus was given to the complementary imaging information provided by dual-band OCT, namely the high-spatial resolution visible channel complementing the superior penetration imaging provided by the infrared channel, but there is great potential value in the development of ISOCT processing analysis across the whole k-range given by these two channels. Currently, ISOCT D is calculated by fitting of the linearized spectrally-resolved backscattering signal that is produced by a short-time Fourier transform of the raw OCT signal, which covers a limited k-range in the visible channel. Independently calculating D from the visible and infrared channels was not practicable because the very narrow k-range provided in the infrared lead to very noisy fitting for D across the narrow spectrum. However, a much more robust calculation of D is possible in principle by cross-channel calibration and fitting at a fewer number of sampling spectral points, for instance 2 bands in the visible and 1 in the infrared. The calibration could be achieved by measurement of a polystyrene sphere scattering standard, which is currently employed for μ_b normalization in our algorithm developed for coral imaging. In principle, this cross-band fitting approach for D would improve the robustness of the D values calculated, but also broaden the theoretical and experimental length scale sensitivity of D, which was previously reported to be from 30-450 nm for an imaging bandwidth from 650-800 nm[75].

The design and development of the visible ISOCT needle probe presented focused on the fabrication processes involved and design considerations, since these are not widely reported in the literature for this instrumentation scheme. The development of this needle probe is ongoing, with the current challenge of insufficient reference signal from the internal gold layer interface being addressed by a custom optics company (LaseOptics Corporation) that possesses the CO_2

laser-based fiber splicer that is required for this step. While an external reference arm configuration would also address this challenge and allow for imaging with the current probe, it would not be viable for robust measurement in the clinic due to severe fiber-strain induced polarization differences and dispersion differences which degrade image quality; such a system would not be feasible for clinical use. Additional improvements to be made include the stability of the custom visible-band optical rotary joint, which is being re-built incorporating a custom pre-aligned achromatic doublet configuration (Princetel, Inc) to replace the rotating visible collimators previously used. The closer tolerances and smaller working distances of the modified rotary joint will reduce the eccentricity in optical throughput, leading to enhanced stability of probe signal during radial scanning. When assembled, imaging proof of concept and spectral performance characterization would allow for design refinement and pilot studies in a mouse model.

Finally, the findings of increased metastasis-associated fibrosis of the scaffold in the mouse model presented in Chapter 5 suggest that a large contributor to potentially diagnostic ISOCT signal is collagen distribution, density, and/or alignment. While ISOCT is sensitive to these effects, a more direct method of imaging collagen and other fibrous tissue structures is polarization-sensitive methods that utilize intrinsic tissue birefringence as a contrast mechanism. Polarization-sensitive OCT[281] is one such method, which has been improved in recent years through full characterization of the Jones matrix of a sample[282], allowing for accurate imaging of local birefringence, vasculature[187], and more recently mechanical stiffness[283,284] in biological samples. By probing a sample with 4 independent polarization states, this approach avoids the need for polarization-maintaining fibers that are not compatible with rotational scanning for *in vivo* probe configurations[285] and has recently been introduced in a birefringence imaging needle probe for breast tumor margin detection[286]. While this introduced needle probe incorporated a GRIN focusing lens which is not compatible with ISOCT due to chromatic aberrations, future

development of a dual-modality polarization-sensitive probe capable of ISOCT analysis is feasible in principle. In conjunction with recently introduced spectral-contrast OCT angiography analysis[163], this multi-contrast OCT approach has the potential to provide valuable independent measurement of tissue birefringence, vascularity, and fractal dimension for a more powerful suite of diagnostic parameters.

8.2.3. Building a clinically-relevant model of detection

The results of an investigation into structural changes occurring at the scaffold that are related to metastatic cancer and may be useful biomarkers for imaging-based screening at the scaffold presented in **Chapter 5** are limited in several regards, which warrant some further study. The mouse model in these studies used a proactive scaffold implantation timeline, whereby the scaffold was implanted 28 days prior to tumor inoculation on order to allow the scaffold site to heal, the foreign body response to normalize, and tissue to fully incorporate into the implant before the groups were differentiated by inoculation with tumor cells or PBS control. This timeline differs from the timeline that would occur in a clinical study, where the scaffold would only be implanted in patients after cancer had been diagnosed and treated. While a variety of spontaneous and tumor-resection models incorporating the scaffold are currently being explored, until now imaging-based detection of scaffold changes for cancer detection has been limited to the simpler model described above. Extension of non-invasive imaging to tumor resection models of metastatic cancer would be directly relevant and indicate whether previously detected changes to the scaffold remain after removal of the primary tumor.

Further studies would also be required to determine whether these imaging techniques can be sensitive to the arrival of tumor cells at the scaffold in order to discern circulating metastasis from systemic effects of primary *in situ* carcinoma. The currently presented study suggests that

the detectable changes in scaffold structure are due to systemic effects associated with presence of cancer in the body; collagen deposition is mediated by activated fibroblasts at the scaffold site, and delivery of tumor-secreted exosomes to the scaffold site affect local restructuring, activation, and recruitment of immune cells. A separate study using spectral ultrasound imaging found that the predominant structural signature arises due to differences in scaffold resident cell populations[118]; this finding is supported by recent preliminary data [courtesy of Sophia Orbach] indicating higher relative populations of macrophages and granulocytes in the scaffolds of diseased mice. A similar study design pursued with ISOCT imaging and analysis of cellular *D* mirrored this result, indicating that both acoustic and optical scattering signatures are affected by differences in resident cell populations. These findings warrant further study to determine significance and stability of difference in cell populations in more translatable models of cancer treatment such as the resection model mentioned above. The spatial resolution of ultrasound imaging on the order of 50 micrometers limits it to bulk measurements of tissue, but optical techniques such as OCT have the potential for high-resolution segmentation and "optical biopsy"[287] which may discern differences in scaffold resident cells. Alternatively, a pilot study utilizing intravital microscopy through a dorsal skinfold window chamber could be used to observe scaffold micro-vascularization longitudinally to provide better insight into how differentially-regulated angiogenesis in diseased mice potentiates delivery of fluorescent tumor cells and other immune cells to the scaffold[288].

A major observation from the presented study was that collagen deposition and fibrosis at the scaffold may be differentially regulated in healthy mice and in mice with cancer. During initial integration of the scaffold when groups are identical in our study design, the foreign body response to the scaffold mediates tissue ingrowth and formation of a fibrous capsule around the scaffold, which is readily observed in histology (figure 5.11) and OCT scans (figure 4.3). In histology

sections through the center of the scaffold, tissue ingrowth and angiogenesis in the middle is noticeably less than at the edges despite allowing more than adequate time for the scaffold to fully integrate. The scaffolds used for these studies were individually pressed in a steel die which produces surfaces with a burnished sheen. In other studies utilizing scaffolds that had the same dimensions but were punched from a large sheet, histology showed a much higher degree of tissue ingrowth throughout the full thickness of the scaffold. This difference might be attributed to more ragged edges produced by the punching process and greater pore interconnectivity allowing for faster and more complete integration into the host tissues. These observations between different scaffold fabrication techniques warrant further study, in particular for pending FDA approval of scaffolds as a medical device for future clinical studies. Differences in the degree of scaffold integration would affect the signal and potential applicability of imaging-based cancer screening at the scaffold.

A vision for clinical implementation of scaffold technology for early detection of metastasis requires the development of a feasible screening paradigm that is both acceptable to patients and sensitive to disease progression. In the example of a patient with diagnosis of ductal carcinoma in situ, the current recommended treatment is either mastectomy or breast-conserving surgery but there are no clear recommendations for follow-up procedures[289]. During the initial removal of the primary tumor and margins, a scaffold(s) would be implanted in the resection wound and/or at a subcutaneous site proximal to the tumor site, potentially near an axillary lymph node. Often this primary resection is accompanied by radiation treatment which would influence placement of the scaffolds. After the implantation site(s) had healed, a non- or minimally-invasive monitoring regimen would be initiated for regular (weekly/monthly) check-ups at the doctor's office. These would consist of routine physical examination in addition to a developed screening protocol for scaffold monitoring utilizing an individually superior imaging technique or some

combination thereof. For this imaging, spectral ultrasound imaging through the skin[118] or ISOCT imaging delivered through a needle probe with additional multimodal functionality described in the above section for quantitative measurement of collagen and vasculature in addition to established spectroscopic analysis would be implemented. The results of such an imaging procedure would be morphology interpreted by a trained physician and a composite score predictive of cancer progression risk. This score would be developed through training and validation of datasets from clinical studies, similar to the bagged decision tree analysis implemented in a prior study using spectral ultrasound for multiparameter cancer detection in a mouse model[118]. If the risk score from imaging measurement exceeded a threshold, a biopsy would be taken of the scaffold for analysis of gene expression[119] or other biological metric determined for more robust determination of metastatic progression. The implementation of such a strategy has great potential to transform the clinical paradigm of patient follow-up after treatment of a primary tumor, increasing rates of early detection and efficacy of treatment, thereby improving human health.

8.2.4. Extension to other applications of ISOCT

Chapter 6 reports the application of partial wave spectroscopic microscopy for enhanced contrast imaging and spectroscopic analysis of scattering signal from gold nanoparticles in cancer cells. This technique can be considered as a sister technique to ISOCT, as both utilize spectroscopic analysis of interference signal to obtain information about the nanoscale macromolecular arrangement of biological samples. While the respective spatial resolutions and working depths of PWS and ISOCT limit them to high and low resolution imaging of thin and thick samples, respectively, there is an overlap in application of these techniques that has been used to study effects of chromatin decompaction through measurement of D with ISOCT and RMS with PWS,

which are related parameters and report the fractal dimension of mass density in the sample[78,115]. The use of PWS presented here for spectroscopy-based classification of gold nanoparticles has potential for adaptation into the use of gold nanoparticles as spectral contrast agents in ISOCT imaging. Previously, gold nanoparticles have been studied as contrast agents in traditional optical coherence tomography to aid in deep contrast imaging of skin and hair follicles in rabbits[290] and humans[291]. The tunable plasmonic properties of gold nanoparticles were also demonstrated in true color spectroscopic OCT measurements of tissue phantoms[292] and we anticipate the analysis techniques developed for PWS would be generalizable to ISOCT for analysis of plasmonic nanoparticles. The molecular environment *in vivo* is very complex with an innumerable variety of intra- and extra-cellular proteins and fouling agents that potentially affect plasmonic properties, but it is conceivable that high throughput volumetric imaging of large nanoparticle populations enabled by ISOCT could provide interesting spectrally-resolved information regarding different tissue microenvironments.

Another finding from this study shown in figure 6.4 indicates that in cancer cell culture, gold nanoparticle treatment affects nuclear structure and dynamics, leading to a lower degree of chromatin compaction and less motion in the nucleus. While this finding is novel and interesting, it raises several questions about the mechanisms involved in the observed nuclear changes and potential implications for nanoparticle-based cancer therapies. The changes in nuclear structure were observed in the case that the nanoparticles were localized in the cytoplasm and perinuclear regions of the cell; in general nanoparticles do not end up in the nucleus of the cell, yet still affect its structure and function. Additional studies warranted to clarify the causality and mechanisms of this effect include time course measurements of cellular structure and dynamics to measure longitudinal response to treatment over 24 hours, determination of dose-response effect of nanoparticle concentration on nuclear structure, and cellular metabolism assays such as WST or

MTT for correlation with nuclear dynamic imaging. A main hypothesis for the observed nuclear changes is the production of reactive oxygen species (ROS) due to a cellular stress response, which has been previously implicated in the biological response to gold and other metallic nanoparticles in cells[215–217,293]. This hypothesis can be tested through ROS-specific assays on nanoparticle-treated cells, fluorescent dye indicator imaging of produced ROS in the cell, and introduction of ROS scavengers to test the potential abrogation of nanoparticle-induced nuclear response. The imaging of these effects enabled by PWS microscopy would be of potential scientific interest in the fields of nanoparticle-based therapeutics and nanobiotechnology.

Chapter 7 introduces the application and development of ISOCT imaging and analysis for comprehensive study of coral structure and light transport. This work was introduced as a proof-of-concept study showing the technique to be valuable for quantification of light scattering parameters that were previously unobtainable with existing techniques and were assumed for previous simulations of optical transport in corals. Further development of this technique would allow for generalized application to a wider array of model systems. The first development to be made would be the inclusion of multiple absorbing pigments in the spectral fitting model used to decouple scattering and absorption in coral tissue. The presented work operated on the assumption that chlorophyll *a* is the dominant absorber in coral tissue, and that all measured absorption in coral tissue can be characterized by the measured absorption spectrum of chlorophyll *a* in solution.

While this assumption may be a valid first-order approximation for the coral specimens studied which did not display a noticeable degree of fluorescence and did not contain noticeable pigment granules in their tissues, may corals display vivid fluorescence and can contain a wide array of strongly absorbing endogenous pigments. For example, in a separate study of different coral species from Shedd Aquarium representing the genera *Acropora*, *Favia*, *Favites*, *Montipora*, *Paragoniastrea*, *Pavona*, and *Pocillopora*, several species, notably *Paragoniastrea australensis*

and *Pocillopora damicornis* displayed dense distributions of strongly scattering pigment granules within the host tissues which are visible in OCT images. These pigments have distinct absorption spectra from chlorophyll *a* and must be considered in the light scattering and absorption model if applied to determine the scattering spectra of host tissues in similar specimens. The spectral fitting presented requires knowledge of pigment absorption spectra *a priori*.

Spatial segmentation and fitting of integrated attenuation coefficient from OCT measurements of these pigment granules *in situ* may be used to determine their relative absorption spectra in OCT scans, but this approach suffers from limited spatial and spectral resolution inherent in spectroscopic OCT. To address this, independent measurement of pigment absorption spectra through diffuse or enhanced backscattering spectroscopy or destructive extraction and measurement with spectrophotometry would be helpful in future incorporation of multiple absorbing pigments in the ISOCT analysis of coral. The aforementioned trade-off between spatial and spectral resolution from the short-time Fourier transform limits the number of distinct pigments that can be incorporated into this analysis due to the possibility of spectral overfitting. Future studies of multiple pigments would select a coral species demonstrating appreciably high expression of pigments with distinct absorption spectral features within the wavelength range of the visible OCT spectrometer. Increasing spectrometer bandwidth to the full visible range would help to capture a wide range of pigment features while maintaining adequate roll off-limited imaging depth which, due to penetration depth in corals being typically limited by scattering, is not limiting in the application of flat coral imaging. For samples with large differences in topography, an integrated multi-depth scanning protocol can be implemented through the use of a motorized stage (Zaber).

All OCT studies of coral we have conducted require removal of most of the water covering the live coral sample to address issues with dispersion and focusing that occur through variable

thicknesses of water. This procedure induces stress to the coral and may cause a degree of tissue contraction which affects morphology and potential measurements of optical and structural properties. Other studies of coral utilize flow-through chambers to maintain water conditions and coral homeostasis during measurement. Adapting this approach for OCT imaging requires the use of water immersion optics in the focusing sample arm. In lieu of a water-immersion OCT scan objective which is not commercially available, we developed a custom lens cap with microscope cover glass imaging window for water immersion imaging, which allows for focusing in the sample arm through a fixed thickness of water that was readily compensated through placement of a water cuvette in the reference arm or digital dispersion compensation[264]. This controlled environment could allow for dynamic measurement of coral stress response to changes in temperature or lighting and has the potential to elucidate complex mechanisms underlying the effects of light transport in the coral bleaching response.

The results presented in Chapter 7 provide only a snapshot of the optical and structural properties of two example corals as a proof of concept. Several conclusions can be drawn from this small amount of data, including the observation that *D* in coral tissues varies widely based on spatial location and does not suit Henyey-Greenstein phase function formalism. These results can be further strengthened by extension of the technique for measurement of tissues and skeleton in living corals of a wider range of species for which some data has already been acquired. Other considerations to address are more precise segmentation of the different layers of coral tissue and skeleton. While this study determined that the coral skeleton is clearly visible through areas of thinned tissue, particularly over the ridges of septal plates in the coenosteum, the accurate segmentation of specific layers of gastrodermis and mesoglea from OCT scans in different regions of different coral species requires anatomical knowledge that has not yet been firmly established. By establishing a broader survey of optical and structural properties in each tissue compartment in

coenosarc and polyp regions, photon propagation simulations will be more well-informed and allow for greater understanding of how corals harvest light.

References

1. Rao, S. S. *et al.* Enhanced survival with implantable scaffolds that capture metastatic breast cancer cells in vivo. *Cancer Res.* **76,** 5209–5218 (2016).
2. Liu, R. *et al.* Single capillary oximetry and tissue ultrastructural sensing by dual-band dual-scan inverse spectroscopic optical coherence tomography. *Light Sci. Appl.* **7,** 57 (2018).
3. Rogers, J. D., Capoğlu, I. R. & Backman, V. Nonscalar elastic light scattering from continuous random media in the Born approximation. *Opt. Lett.* **34,** 1891–3 (2009).
4. American Cancer Society. *Cancer Facts and Figures 2015*. (2015). doi:10.3322/caac.21254
5. Gupta, G. P. & Massagué, J. Cancer Metastasis: Building a Framework. *Cell* **127,** 679–695 (2006).
6. Weigelt, B., Peterse, J. L. & van't Veer, L. J. Breast cancer metastasis: markers and models. *Nat. Rev. Cancer* **5,** 591–602 (2005).
7. The American Cancer Society. American Cancer Society Guidelines for the Early Detection of Cancer. *Www.Cancer.Org* (2014). at <http://www.cancer.org/healthy/findcancerearly/cancerscreeningguidelines/american-cancer-society-guidelines-for-the-early-detection-of-cancer>
8. Cardoso, F., Harbeck, N., Fallowfield, L., Kyriakides, S. & Senkus, E. Locally recurrent or metastatic breast cancer: ESMO Clinical Practice Guidelines for diagnosis, treatment and follow-up. *Ann. Oncol.* **23,** vii11-vii19 (2012).
9. Lam, D. L., Houssami, N. & Lee, J. M. Imaging surveillance after primary breast cancer treatment. *Am. J. Roentgenol.* **208,** 676–686 (2017).
10. Del Turco, M. R. Intensive Diagnostic Follow-up After Treatment of Primary Breast Cancer. *Jama* **271,** 1593 (2011).
11. GIVIO. Impact of Follow-up Testing on Survival and Health-Related Quality of Life in Breast Cancer Patients. *Jama* **271,** 1587–1592 (1994).
12. Palli, D. *et al.* Intensive vs Clinical Follow-up After Treatment of Primary Breast Cancer: 10-Year Update of a Randomized Trial. *Jama* **281,** 1586 (1999).
13. Houssami, N. *et al.* Accuracy and outcomes of screening mammography in women with a personal history of early-stage breast cancer. *JAMA - J. Am. Med. Assoc.* **305,** 790–799 (2011).
14. Del Turco, M. R., Cariddi, P. D., Ciatto, S., Pacini, P. & Distante, V. The efficacy of intensive follow-up testing in breast cancer cases. *Ann. Oncol.* **6,** 37–39 (1995).
15. Rusch, P. *et al.* Distant metastasis detected by routine staging in breast cancer patients participating in the national German screening programme: consequences for clinical practice. *Springerplus* **5,** (2016).
16. Bernardi, D. *et al.* Breast cancer screening with tomosynthesis (3D mammography) with acquired or synthetic 2D mammography compared with 2D mammography alone (STORM-2): a population-based prospective study. *Lancet Oncol.* **17,** 1105–1113 (2016).
17. Rocha García, A. M. & Mera Fernández, D. Breast tomosynthesis: state of the art. *Radiologia* **277,** 663–684 (2019).
18. McDonald, E. S. *et al.* Effectiveness of digital breast tomosynthesis compared with digital mammography: Outcomes analysis from 3 years of breast cancer screening. *JAMA Oncol.* **2,** 737–743 (2016).
19. Hodara, E. *et al.* Multiparametric liquid biopsy analysis in metastatic prostate cancer. *JCI*

Insight **4,** 1–10 (2019).
20. Palmirotta, R. *et al.* Liquid biopsy of cancer: a multimodal diagnostic tool in clinical oncology. *Ther. Adv. Med. Oncol.* **23,** 153 –156 (2017).
21. Riethdorf, S. *et al.* Detection of circulating tumor cells in peripheral blood of patients with metastatic breast cancer: A validation study of the cell search system. *Clin. Cancer Res.* **13,** 920–928 (2007).
22. Kalluri, R. The biology and function of exosomes in cancer. *J Clin Invest* **126,** 1208–1215 (2016).
23. Azmi, A. S., Bao, B. & Sarkar, F. H. Exosomes in cancer development, metastasis, and drug resistance: A comprehensive review. *Cancer Metastasis Rev.* **32,** 623–642 (2013).
24. Cristofanilli, M. *et al.* Circulating tumor cells, disease progression, and survival in metastatic breast cancer. *N. Engl. J. Med.* **351,** 781–791 (2004).
25. Hyunh, K. & Hoon, D. S. B. Liquid Biopsies for Assessing Metastatic Melanoma Progression. *Crit Rev Oncog* **21,** 141–154 (2016).
26. Woo, D. & Yu, M. Circulating tumor cells as "liquid biopsies" to understand cancer metastasis. *Transl. Res.* **201,** 128–135 (2018).
27. Kerbel, R. S., Man, M. S. & Dexter, D. A model of human cancer metastasis: Extensive spontaneous and artificial metastasis of a human pigmented melanoma and derived variant sublines in nude mice. *J. Natl. Cancer Inst.* **72,** 93–108 (1984).
28. Fidler, I. J., Gruys, E., Cifone, M. A., Barnes, Z. & Bucana, C. Demonstration of multiple phenotypic diversity in a murine melanoma of recent origin1, 2, 3, 4. *J. Natl. Cancer Inst.* **67,** 947–956 (1981).
29. Fidler, I. J. Metastasis: Quantitative Analysis of Distribution and Fate of Tumor Emboli Labeled With 125I-5-Iodo-2′ -deoxyuridine. *J. Natl. Cancer Inst.* **45,** 773–782 (1970).
30. Tauro, B. J. *et al.* Two Distinct Populations of Exosomes Are Released from LIM1863 Colon Carcinoma Cell-derived Organoids. *Mol. Cell. Proteomics* **12,** 587–598 (2012).
31. Wang, Y. & Zhou, B. P. Epithelial-mesenchymal transition in breast cancer progression and metastasis. *Chin. J. Cancer* **30,** 603–611 (2011).
32. Chambers, A. F., Groom, A. C. & MacDonald, I. C. Metastasis: Dissemination and growth of cancer cells in metastatic sites. *Nat. Rev. Cancer* **2,** 563–572 (2002).
33. Fidler, I. J. The pathogenesis of cancer metastasis: the 'seed and soil' hypothesis revisited. *Nat. Rev. Cancer* **3,** 1–6 (2003).
34. Riggi, N., Aguet, M. & Stamenkovic, I. Cancer Metastasis: A Reappraisal of Its Underlying Mechanisms and Their Relevance to Treatment. *Annu. Rev. Pathol. Mech. Dis.* **13,** 117–140 (2017).
35. Paget, S. The Distribution of Secondary Growths in Cancer of the Breast. *Lancet* **133,** 571–573 (1889).
36. Kaplan, R. N. *et al.* VEGFR1-positive haematopoietic bone marrow progenitors initiate the pre-metastatic niche. *Nature* **438,** 820–7 (2005).
37. Kaplan, R. N., Psaila, B. & Lyden, D. Bone marrow cells in the 'pre-metastatic niche': within bone and beyond. *Cancer Metastasis Rev.* **25,** 521–529 (2007).
38. Steeg, P. S. Tumor metastasis: mechanistic insights and clinical challenges. *Nat Med* **12,** 895–904 (2006).
39. Guo, Y. *et al.* Effects of exosomes on pre-metastatic niche formation in tumors. *Mol. Cancer* **18,** 1–11 (2019).
40. Liu, Y. & Cao, X. Characteristics and Significance of the Pre-metastatic Niche. *Cancer Cell* **30,** 668–681 (2016).

41. Minciacchi, V. R., Freeman, M. R. & Di Vizio, D. Extracellular Vesicles in Cancer: Exosomes, Microvesicles and the Emerging Role of Large Oncosomes. *Semin. Cell Dev. Biol.* **40,** 41–51 (2015).
42. Hiratsuka, S. *et al.* Hepato-entrained B220 + CD11c + NK1.1 + cells regulate pre-metastatic niche formation in the lung . *EMBO Mol. Med.* **10,** e8643 (2018).
43. Hiratsuka, S., Watanabe, A., Aburatani, H. & Maru, Y. Tumour-mediated upregulation of chemoattractants and recruitment of myeloid cells predetermines lung metastasis. *Nat. Cell Biol.* **8,** 1369–1375 (2006).
44. Seubert, B. *et al.* Tissue inhibitor of metalloproteinases (TIMP)-1 creates a premetastatic niche in the liver through SDF-1/CXCR4-dependent neutrophil recruitment in mice. *Hepatology* **61,** 238–248 (2015).
45. Costa-Silva, B. *et al.* Pancreatic cancer exosomes initiate pre-metastatic niche formation in the liver. *Nat. Cell Biol.* **17,** 816–826 (2015).
46. Kim, S. *et al.* Carcinoma Produced Factors Activate Myeloid Cells via TLR2 to Stimulate Metastasis. *Nature* **457,** 102–106 (2009).
47. Hiratsuka, S. *et al.* The S100A8-serum amyloid A3-TLR4 paracrine cascade establishes a pre-metastatic phase. *Nat. Cell Biol.* **10,** 1349–1355 (2008).
48. Erler, J. T. *et al.* Lysyl oxidase is essential for hypoxia-induced metastasis. *Nature* **440,** 1222–1226 (2006).
49. Erler, J. T. *et al.* Hypoxia-Induced Lysyl Oxidase Is a Critical Mediator of Bone Marrow Cell Recruitment to Form the Premetastatic Niche. *Cancer Cell* **15,** 35–44 (2009).
50. Psaila, B. & Lyden, D. The metastatic niche: adapting the foreign soil. *Nat. Rev. Cancer* **9,** 285–293 (2009).
51. Gao, D. *et al.* Endothelial progenitor cells control the angiogenic switch in mouse lung metastasis. *Science (80-.).* **319,** 195–198 (2008).
52. Criscuolo, G. R., Lelkes, P. I., Rotrosen, D. & Oldfield, E. H. Cytosolic calcium changes in endothelial cells induced by a protein product of human gliomas containing vascular permeability factor activity. *J. Neurosurg.* **71,** 884–891 (1989).
53. Martin, R. M., Görisch, S. M., Leonhardt, H. & Cardoso, M. C. An unexpected link between energy metabolism, calcium, chromatin condensation and cell cycle. *Cell Cycle* **6,** 2422–2424 (2007).
54. Spicer, G. L. C. *et al.* Detection of Extracellular Matrix Modification in Cancer Models with Inverse Spectroscopic Optical Coherence Tomography. *Phys. Med. Biol.* **61,** 6892–6904 (2016).
55. Aguado, B. A., Bushnell, G. G., Rao, S. S., Jeruss, J. S. & Shea, L. D. Engineering the pre-metastatic niche. *Nat. Publ. Gr.* **1,** 1–12 (2017).
56. Anderson, J. M., Rodriguez, A. & Chang, D. T. Foreign body reaction to biometarials. *Semin Immunol.* **20,** 86–100 (2008).
57. Ward, W. K. A Review of the Foreign-body Response to Subcutaneously-implanted Devices: The Role of Macrophages and Cytokines in Biofouling and Fibrosis. *J. Diabetes Sci. Technol.* **6,** 226–228 (2012).
58. Aguado, B. A. *et al.* Biomaterial Scaffolds as Pre-metastatic Niche Mimics Systemically Alter the Primary Tumor and Tumor Microenvironment. *Adv. Healthc. Mater.* **1700903,** 1–11 (2018).
59. Aguado, B. A. *et al.* Extracellular matrix mediators of metastatic cell colonization characterized using scaffold mimics of the pre-metastatic niche. *Acta Biomater.* **33,** 13–24 (2016).

60. Azarin, S. M. *et al.* In vivo capture and label-free detection of early metastatic cells. *Nat Commun* **6,** (2015).
61. Bushnell, G. G. *et al.* Biomaterial scaffolds recruit an aggressive population of metastatic tumor cells in vivo. *Cancer Res.* canres.2502.2018 (2019). doi:10.1158/0008-5472.CAN-18-2502
62. Yu, M. *et al.* Ex vivo culture of circulating breast tumor cells for individualized testing of Drug Susceptibility. *Science (80-.).* **345,** 216–220 (2014).
63. Lee, J., Kohl, N., Shanbhang, S. & Parekkadan, B. Scaffold-integrated microchips for end-to-end in vitro tumor cell attachment and xenograft formation. *Technol. (Singap World Sci)* **3,** 179–188 (2015).
64. Bichsel, C. A. *et al.* Diagnostic microchip to assay 3D colony-growth potential of captured circulating tumor cells. *Lab Chip* **12,** 2313–2316 (2012).
65. Huang, D. *et al.* Optical coherence tomography. *Science* **254,** 1178–1181 (1991).
66. Duker, J. S. & Adhi, M. Optical coherence tomography - current and future applications. *Curr Opin Ophthalmol.* **24,** 213–221 (2013).
67. Yasuno, Y. *Tutorial on Optical Coherence Tomography: Principles, Implementation, and Applications in Ophthalmology*. (2014).
68. Leitgeb, R., Hitzenberger, C. K. & Fercher, A. F. Performance of fourier domain vs. time domain optical coherence tomography. *Opt. Express* **11,** 889–894 (2003).
69. Huber, R., Adler, D. C., Srinivasan, V. J. & Fujimoto, J. G. Fourier domain mode locking at 1050 nm for ultra-high-speed optical coherence tomography of the human retina at 236,000 axial scans per second. *Opt. Lett.* **32,** 2049 (2007).
70. Potsaid, B. *et al.* Ultrahigh speed Spectral / Fourier domain OCT ophthalmic imaging at 70,000 to 312,500 axial scans per second. *Opt. Express* **61,** 15149–15169 (2008).
71. Born, M. & Wolf, E. *Principles of Optics*. (Cambridge University Press, 1997).
72. Izatt, J. A. & Choma, M. A. Theory of Optical Coherence Tomography. *Opt. Coherence Tomogr.* 47–72 (2008). doi:10.1007/978-3-540-77550-8_2
73. Fercher, A. F., Drexler, W., Hitzenberger, C. K. & Lasser, T. Optical coherence tomography – development, principles, applications. *Z. Med. Phys.* **20,** 251–276 (2010).
74. Backman, V. Chapter 4: Fundamental light-tissue interactions: light scattering and absorption 4.1. 1–31
75. Yi, J. *et al.* Can OCT be sensitive to nanoscale structural alterations in biological tissue? *Opt. Express* **21,** 1642–1645 (2013).
76. Yi, J. & Backman, V. Imaging a full set of optical scattering properties of biological tissue by inverse spectroscopic optical coherence tomography. *Opt. Lett.* **37,** 4443–5 (2012).
77. Yi, J. *et al.* Spatially resolved optical and ultrastructural properties of colorectal and pancreatic field carcinogenesis observed by inverse spectroscopic optical coherence tomography. *J. Biomed. Opt.* **19,** 36013 (2014).
78. Yi, J., Stypula-Cyrus, Y., Blaha, C., Roy, H. K. & Backman, V. Fractal characterization of chromatin decompaction in live cells. *Biophys. J.* **109,** 1–9 (2015).
79. Cherkezyan L *et al.* Nanoscale changes in chromatin organization represent the initial steps of tumorigenesis: a transmission electron microscopy study. *BMC Cancer* **14,** 189 (2014).
80. Arifler, D., Pavlova, I., Gillenwater, A. & Richards-Kortum, R. Light scattering from collagen fiber networks: micro-optical properties of normal and neoplastic stroma. *Biophys. J.* **92,** 3260–74 (2007).
81. Müller, M. G. *et al.* Spectroscopic detection and evaluation of morphologic and

biochemical changes in early human oral carcinoma. *Cancer* **97,** 1681–92 (2003).
82. Arseni, L., Lombardi, A. & Orioli, D. From structure to phenotype: Impact of collagen alterations on human health. *Int. J. Mol. Sci.* **19,** (2018).
83. Yabushita, H. *et al.* Characterization of human atherosclerosis by optical coherence tomography. *Circulation* **106,** 1640–1645 (2002).
84. Lee, M. W. *et al.* Comprehensive intravascular imaging of atherosclerotic plaque in vivo using optical coherence tomography and fluorescence lifetime imaging. *Sci. Rep.* **8,** 1–12 (2018).
85. Van Soest, G. *et al.* Imaging atherosclerotic plaque composition with intracoronary optical coherence tomography. *Netherlands Hear. J.* **17,** 448–450 (2009).
86. Ovchinnikova, O. A. *et al.* The collagen cross-linking enzyme lysyl oxidase is associated with the healing of human atherosclerotic lesions. *J. Intern. Med.* n/a-n/a (2014). doi:10.1111/joim.12228
87. Wangpraseurt, D., Wentzel, C., Jacques, S. L., Wagner, M. & Ku, M. In vivo imaging of coral tissue and skeleton with optical coherence tomography. *J. R. Soc. Interface* **14,** (2017).
88. Spicer, G. *et al.* Measuring light scattering and absorption properties of coral tissue and skeleton with Inverse Spectroscopic Optical Coherence Tomography (ISOCT). *Sci. Rep.* **Submitted,** (2019).
89. Lu, P., Weaver, V. M. & Werb, Z. The extracellular matrix: A dynamic niche in cancer progression. *J. Cell Biol.* **196,** 395–406 (2012).
90. Nelson, C. M. & Bissell, M. J. Of Extracellular Matrix, Scaffolds, and Signaling: Tissue Architecture Regulates Development, Homeostasis, and Cancer. *Annu Rev Cell Dev Biol* **22,** 287–309 (2006).
91. Dvorak, H. F., Weaver, V. M., Tlsty, T. D. & Bergers, G. Tumor microenvironment and progression. *J. Surg. Oncol.* **103,** 468–474 (2011).
92. Chaudhuri, O. *et al.* Extracellular matrix stiffness and composition jointly regulate the induction of malignant phenotypes in mammary epithelium. *Nat. Mater.* **10,** 1–9 (2014).
93. Peddareddigari, V. G., Wang, D. & Dubois, R. N. The tumor microenvironment in colorectal carcinogenesis. *Cancer Microenviron.* **3,** 149–166 (2010).
94. Cox, T. R. & Erler, J. T. Remodeling and homeostasis of the extracellular matrix: implications for fibrotic diseases and cancer. *Dis. Model. Mech.* **4,** 165–178 (2011).
95. Barcus, C. E., Keely, P. J., Eliceiri, K. W. & Schuler, L. a. Stiff collagen matrices increase tumorigenic prolactin signaling in breast cancer cells. *J. Biol. Chem.* **288,** 12722–12732 (2013).
96. Pickup, M. W., Mouw, J. K. & Weaver, V. M. The extracellular matrix modulates the hallmarks of cancer. *EMBO Rep* **15,** 1243–1253 (2014).
97. Zou, X. *et al.* Up-regulation of type I collagen during tumorigenesis of colorectal cancer revealed by quantitative proteomic analysis. *J. Proteomics* **94,** 473–485 (2013).
98. Fraley, S. I. *et al.* Three-dimensional matrix fiber alignment modulates cell migration and MT1-MMP utility by spatially and temporally directing protrusions. *Sci. Rep.* **5,** 14580 (2015).
99. Levental, K. R. *et al.* Matrix Crosslinking Forces Tumor Progression by Enhancing Integrin Signaling. *Cell* **139,** 891–906 (2009).
100. Naba, A. *et al.* Extracellular matrix signatures of human primary metastatic colon cancers and their metastases to liver. *BMC Cancer* **14,** 518 (2014).
101. Chen, X., Nadiarynkh, O., Plotnikov, S. & Campagnola, P. J. Second harmonic generation

microscopy for quantitative analysis of collagen fibrillar structure. *Nat. Protoc.* **7,** 654–669 (2012).
102. Nadiarnykh, O., LaComb, R. B., Brewer, M. a & Campagnola, P. J. Alterations of the extracellular matrix in ovarian cancer studied by Second Harmonic Generation imaging microscopy. *BMC Cancer* **10,** 94 (2010).
103. Zhuo, S., Chen, J., Xie, S., Hong, Z. & Jiang, X. Extracting diagnostic stromal organization features based on intrinsic two-photon excited fluorescence and second-harmonic generation signals. *J. Biomed. Opt.* **14,** 020503 (2009).
104. Butler, E., Hardin, J. & Benson, S. The role of lysyl oxidase and collagen crosslinking during sea urchin development. *Exp. Cell Res.* **173,** 174–182 (1987).
105. Cox, T. R. *et al.* LOX-Mediated Collagen Crosslinking Is Responsible for Fibrosis-Enhanced Metastasis. *Cancer Res.* **73,** 1721–1732 (2013).
106. Kirschmann, D. A. *et al.* A Molecular Role for Lysyl Oxidase in Breast Cancer Invasion. *Cancer Res.* **62,** 4478–4483 (2002).
107. Baker, A.-M. *et al.* The role of lysyl oxidase in SRC-dependent proliferation and metastasis of colorectal cancer. *J. Natl. Cancer Inst.* **103,** 407–424 (2011).
108. Kim, Y. *et al.* Differential expression of the LOX family genes in human colorectal adenocarcinomas. *Oncol. Rep.* **22,** 799–804 (2009).
109. Baker, A.-M., Bird, D., Lang, G., Cox, T. R. & Erler, J. T. Lysyl oxidase enzymatic function increases stiffness to drive colorectal cancer progression through FAK. *Oncogene* **32,** 1863–8 (2012).
110. Tse, J. M. *et al.* Mechanical compression drives cancer cells toward invasive phenotype. *Proc. Natl. Acad. Sci. U. S. A.* **109,** 911–6 (2012).
111. Conklin, M. W. *et al.* Aligned Collagen Is a Prognostic Signature for Survival in Human Breast Carcinoma. *AJPA* **178,** 1221–1232 (2011).
112. Slaughter, P., Southwick, W. & Smejkal, W. "Field cancerization" in oral stratified squamous epithelium. *Cancer* **6,** 963–968 (1953).
113. Rucker, R. B. *et al.* Copper , lysyl oxidase , and extracellular matrix protein cross-linking. *Am J Clin Nutr* **67,** 996–1002 (1998).
114. Stoller, P., Reiser, K. M., Celliers, P. M. & Rubenchik, A. M. Polarization-Modulated Second Harmonic Generation in Collagen. *Biophys. J.* **82,** 3330–3342 (2002).
115. Stypula-Cyrus, Y. *et al.* HDAC up-regulation in early colon field carcinogenesis is involved in cell tumorigenicity through regulation of chromatin structure. *PLoS One* **8,** e64600 (2013).
116. Yi, J., Stypula-Cyrus, Y., Blaha, C., Roy, H. K. & Backman, V. Fractal characterization of chromatin decompaction in live cells. *Biophys. J.* **109,** 2218–2226 (2015).
117. Mutyal, N. N. *et al.* Biological Mechanisms Underlying Structural Changes Induced by Colorectal Field Carcinogenesis Measured with Low-Coherence Enhanced Backscattering (LEBS) Spectroscopy. *PLoS One* **8,** e57206 (2013).
118. Bushnell, G. G. *et al.* Biomaterial scaffolds and high frequency spectral ultrasound to non-invasively detect metastasis in vivo. *Prep.* (2019).
119. Oakes, R. S. *et al.* Synthetic diagnostic sites reflect disease progression and predict therapeutic response. *Submitted* (2019).
120. Lee, S.-W. *et al.* Optimization for Axial Resolution, Depth Range, and Sensitivity of Spectral Domain Optical Coherence Tomography at 1.3 μm. *J Korean Phys Soc* **55,** 2354–2360 (2009).
121. Kodach, V. M., Kalkman, J., Faber, D. J. & van Leeuwen, T. G. Quantitative comparison

of the OCT imaging depth at 1300 nm and 1600 nm. *Biomed. Opt. Express* **1,** 176 (2010).
122. Zhang, X. *et al.* Dual-band spectral-domain optical coherence tomography for in vivo imaging the spectral contrasts of the retinal nerve fiber layer. *Opt. Express* **19,** 19653 (2011).
123. Quirk, B. C. *et al.* In situ imaging of lung alveoli with an optical coherence tomography needle probe. *J. Biomed. Opt.* **16,** 036009 (2011).
124. Phipps, J. E. *et al.* Macrophages and intravascular OCT bright spots: A quantitative study. *JACC Cardiovasc. Imaging* **8,** 63–72 (2015).
125. Han, S., Sarunic, M. V., Wu, J., Humayun, M. & Yang, C. Handheld forward-imaging needle endoscope for ophthalmic optical coherence tomography inspection. *J. Biomed. Opt.* **13,** 020505 (2008).
126. Lorenser, D., Mclaughlin, R. A. & Sampson, D. D. *Optical Coherence Tomography in a Needle Format*. *Optical Coherence Tomography* (Springer, 2015). doi:10.1007/978-3-319-06419-2
127. Lorenser, D., Yang, X. & Sampson, D. D. Accurate modeling and design of graded-index fiber probes for optical coherence tomography using the beam propagation method. *IEEE Photonics J.* **5,** 3900015 (2013).
128. Han, S., Sarunic, M. V., Wu, J., Humayun, M. & Yang, C. Handheld forward-imaging needle endoscope for ophthalmic optical coherence tomography inspection. *J. Biomed. Opt.* **13,** 020505 (2008).
129. Liang, C. *et al.* A forward-imaging needle-type OCT probe for image guided stereotactic procedures. *Opt. Express* **19,** 26283–26294 (2011).
130. Xi, J. *et al.* Diffractive catheter for ultrahigh-resolution spectral-domain volumetric OCT imaging. *Opt. Lett.* **39,** 2016–9 (2014).
131. Mavadia-Shukla, J. *et al.* High-speed, ultrahigh-resolution distal scanning OCT endoscopy at 800 nm for in vivo imaging of colon tumorigenesis on murine models. *Biomed. Opt. Express* **9,** 3731 (2018).
132. Yuan, W., Brown, R., Mitzner, W., Yarmus, L. & Li, X. Super-achromatic monolithic microprobe for ultrahigh-resolution endoscopic optical coherence tomography at 800 nm. *Nat. Commun.* **8,** 1–8 (2017).
133. Singh, K., Gardecki, J. A. & Tearney, G. J. Common path endoscopic probes for optical coherence tomography (Conference Presentation). in (eds. Tearney, G. J. & Wang, T. D.) **10040,** 100400U (International Society for Optics and Photonics, 2017).
134. Singh, K. *et al.* In-line optical fiber metallic mirror reflector for monolithic common path optical coherence tomography probes. *Lasers Surg. Med.* **50,** 230–235 (2018).
135. Neumann, M. H. D., Bender, S., Krahn, T. & Schlange, T. ctDNA and CTCs in Liquid Biopsy – Current Status and Where We Need to Progress. *Comput. Struct. Biotechnol. J.* **16,** 190–195 (2018).
136. Alix-Panabières, C. & Pantel, K. Clinical applications of circulating tumor cells and circulating tumor DNA as liquid biopsy. *Cancer Discov.* **6,** 479–491 (2016).
137. Wong, C. C.-L. *et al.* Hypoxia-inducible factor 1 is a master regulator of breast cancer metastatic niche formation. *Proc. Natl. Acad. Sci.* **108,** 16369–16374 (2011).
138. Sceneay, J., Smyth, M. J. & Möller, A. The pre-metastatic niche: finding common ground. *Cancer Metastasis Rev.* **32,** 449–464 (2013).
139. Sleeman, J. P. The metastatic niche and stromal progression. *Cancer Metastasis Rev.* **31,** 429–440 (2012).
140. Cross, V. L. *et al.* Dense type I collagen matrices that support cellular remodeling and

microfabrication for studies of tumor angiogenesis and vasculogenesis in vitro. *Biomaterials* **31,** 8596–8607 (2010).
141. Hall, M. S. *et al.* Fibrous nonlinear elasticity enables positive mechanical feedback between cells and ECMs. *Proc. Natl. Acad. Sci.* **113,** 14043–14048 (2016).
142. Schmittgen, T. D. & Livak, K. J. Analyzing real-time PCR data by the comparative CTmethod. *Nat. Protoc.* **3,** 1101–1108 (2008).
143. JUNQUEIRA, L. C. U., BIGNOLAS, G. & BRENTANI, R. R. Picrosirius staining plus polarization microscopy, a specific method for collagen detection in tissue sections. *Histochem. J.* **11,** 447–455 (1979).
144. Radosevich, A. J. *et al.* Rectal Optical Markers for in Vivo Risk Stratification of Premalignant Colorectal Lesions. *Clin. Cancer Res.* **21,** 4347–4355 (2015).
145. Radosevich, A. J. *et al.* Ultrastructural alterations in field carcinogenesis measured by enhanced backscattering spectroscopy. *J. Biomed. Opt.* **18,** 097002 (2013).
146. Radosevich, A. J. *et al.* Buccal Spectral Markers for Lung Cancer Risk Stratification. *PLoS One* **9,** e110157 (2014).
147. Lu, P., Takai, K., Weaver, V. M. & Werb, Z. Extracellular Matrix degradation and remodeling in development and disease. *Cold Spring Harb. Perspect. Biol.* **3,** 1–24 (2011).
148. Ireland, L. V. & Mielgo, A. Macrophages and Fibroblasts, Key Players in Cancer Chemoresistance. *Front. Cell Dev. Biol.* **6,** 1–14 (2018).
149. Springer, N. L. & Fischbach, C. Biomaterials approaches to modeling macrophage–extracellular matrix interactions in the tumor microenvironment. *Curr Opin Biotechnol* **40,** 16–23 (2016).
150. Mescher, A. L. Macrophages and fibroblasts during inflammation and tissue repair in models of organ regeneration. *Regeneration* **4,** 39–53 (2017).
151. Conklin, M. W. *et al.* Aligned collagen is a prognostic signature for survival in human breast carcinoma. *Am. J. Pathol.* **178,** 1221–32 (2011).
152. Georgakoudi, I. *et al.* Trimodal spectroscopy for the detection and characterization of cervical precancers in vivo. *Am. J. Obstet. Gynecol.* **186,** 374–382 (2002).
153. Qu, J., MacAulay, C., Lam, S. & Palcic, B. Optical properties of normal and carcinomatous bronchial tissue. *Appl. Opt.* **33,** 7397–7405 (1994).
154. Neuman, R. E. & Logan, M. A. The determination of hydroxyproline. *J. Biol. Chem.* **184,** 299–306 (1950).
155. Bartoli, C. R. Capsule Thickness Correlates With Vascular Density and Blood Flow Within Foreign-Body Capsules Surrounding Surgically Implanted Subcutaneous Devices. *Artif. Organs* **34,** 857–861 (2010).
156. Kaplan, R. N., Rafii, S. & Lyden, D. Preparing the "soil": the premetastatic niche. *Cancer Res.* **66,** 11089–93 (2006).
157. Li, B. *et al.* VEGF and PlGF promote adult vasculogenesis by enhancing EPC recruitment and vessel formation at the site of tumor neovascularization. *FASEB J.* **20,** 1495–1497 (2006).
158. Thompson, C. A., Purushothaman, A., Ramani, V. C., Vlodavsky, I. & Sanderson, R. D. Heparanase regulates secretion, composition, and function of tumor cell-derived exosomes. *J. Biol. Chem.* **288,** 10093–10099 (2013).
159. Maia, J., Caja, S., Strano Moraes, M. C., Couto, N. & Costa-Silva, B. Exosome-Based Cell-Cell Communication in the Tumor Microenvironment. *Front. Cell Dev. Biol.* **6,** 1–19 (2018).

160. Pradeep, C. R., Sunila, E. S. & Kuttan, G. Expression of vascular endothelial growth factor (VEGF) and VEGF receptors in tumor angiogenesis and malignancies. *Integr. Cancer Ther.* **4,** 315–321 (2005).
161. Liu, S. *et al.* Vascular endothelial growth factor plays a critical role in the formation of the pre-metastatic niche via prostaglandin E2. *Oncol. Rep.* **32,** 2477–2484 (2014).
162. Ronneberger, O., Fischer, P. & Brox, T. U-net: Convolutional networks for biomedical image segmentation. *arXiv* **9351,** 1–8 (2015).
163. Winkelmann, J. A. *et al.* Spectral contrast optical coherence tomography angiography enables single-scan vessel imaging. *Light Sci. Appl.* **8,** (2019).
164. Di Vito, L. *et al.* Identification and quantification ofmacrophage presence in coronary atherosclerotic plaques by optical coherence tomography. *Eur. Heart J. Cardiovasc. Imaging* **16,** 807–813 (2015).
165. Tearney, G. J. *et al.* Quantification of macrophage content in atherosclerotic plaques by optical coherence tomography. *Circulation* **107,** 113–119 (2003).
166. Sheikh, Z., Brooks, P. J., Barzilay, O., Fine, N. & Glogauer, M. Macrophages, foreign body giant cells and their response to implantable biomaterials. *Materials (Basel).* **8,** 5671–5701 (2015).
167. Woodruff, M. A. & Hutmacher, D. W. The return of a forgotten polymer - Polycaprolactone in the 21st century. *Prog. Polym. Sci.* **35,** 1217–1256 (2010).
168. Sun, H., Mei, L., Ã, C. S., Cui, X. & Wang, P. The in vivo degradation , absorption and excretion of PCL-based implant. **27,** 1735–1740 (2006).
169. Pitt, G. G., Gratzl, M. M., Kimmel, G. L., Surles, J. & Sohindler, A. Aliphatic polyesters II. The degradation of poly (DL-lactide), poly (ε-caprolactone), and their copolymers in vivo. *Biomaterials* **2,** 215–220 (1981).
170. Woodward, S. C., Brewer, P. S., Moatamed, F., Schindler, A. & Pitt, C. G. The intracellular degradation of poly(episolon-caprolactone). *J. Biomed. Mater. Res.* **19,** 437–444 (1985).
171. Ferreira, J., Gloria, A., Cometa, S., Coelho, J. F. J. & Domingos, M. Effect of in vitro enzymatic degradation on 3D printed poly(ε-caprolactone) scaffolds: morphological, chemical and mechanical properties. *J. Appl. Biomater. Funct. Mater.* **15,** 0–0 (2017).
172. Ramírez Hernández, A., Contreras, O. C., Acevedo, J. C., Guadalupe, L. & Moreno, N. Poly(ε-caprolactone) Degradation Under Acidic and Alkaline Conditions. *Am. J. Polym. Sci.* **3,** 70–75 (2013).
173. Lam, C. X. F., Teoh, S. H. & Hutmacher, D. W. Comparison of the degradation of polycaprolactone and polycaprolactone – (β -tricalcium phosphate) scaffolds in alkaline medium. *Polym. Int.* **728,** 718–728 (2007).
174. Mukerjee, A., Pruthi, V. & Sinha, V. R. Preparation and characterization of poly-ε-caprolactone carrier particles for controlled insulin delivery. *ICBPE 2006 - Proc. 2006 Int. Conf. Biomed. Pharm. Eng.* 276–279 (2006). doi:10.1109/ICBPE.2006.348599
175. Høye, A. M. & Erler, J. T. Structural ECM components in the premetastatic and metastatic niche. *Am. J. Physiol. Physiol.* **310,** C955–C967 (2016).
176. Ruvolo, P. P. Galectin 3 as a guardian of the tumor microenvironment. *Biochim. Biophys. Acta - Mol. Cell Res.* **1863,** 427–437 (2016).
177. Peinado, H., Lavotshkin, S. & Lyden, D. The secreted factors responsible for pre-metastatic niche formation: old sayings and new thoughts. *Semin. Cancer Biol.* **21,** 139–46 (2011).
178. Choi, S. K., Kim, H. S., Jin, T. & Moon, W. K. LOXL4 knockdown enhances tumor

growth and lung metastasis through collagen-dependent extracellular matrix changes in triple-negative breast cancer. *Oncotarget* **8,** 11977–11989 (2017).
179. Song, G. *et al.* TIMP1 is a prognostic marker for the progression and metastasis of colon cancer through FAK-PI3K/AKT and MAPK pathway. *J. Exp. Clin. Cancer Res.* **35,** 1–12 (2016).
180. Gong, Y. *et al.* TIMP-1 Promotes Accumulation of Cancer Associated Fibroblasts and Cancer Progression. *PLoS One* **8,** 19–22 (2013).
181. Hiratsuka, S. *et al.* MMP9 induction by vascular endothelial growth factor receptor-1 is involved in lung-specific metastasis. *Cancer Cell* **2,** 289–300 (2002).
182. Jacobson, A. & Cunningham, J. L. Connective tissue growth factor in tumor pathogenesis. *Fibrogenes. Tissue Repair* **5,** S8 (2012).
183. Braig, S., Wallner, S., Junglas, B., Fuchshofer, R. & Bosserhoff, A. K. CTGF is overexpressed in malignant melanoma and promotes cell invasion and migration. *Br. J. Cancer* **105,** 231–238 (2011).
184. Lipson, K. E., Wong, C., Teng, Y. & Spong, S. CTGF is a central mediator of tissue remodeling and fibrosis and its inhibition can reverse the process of fibrosis. *Fibrogenesis Tissue Repair* **5,** S24 (2012).
185. Wells, J. E., Howlett, M., Cole, C. H. & Kees, U. R. Deregulated expression of connective tissue growth factor (CTGF/CCN2) is linked to poor outcome in human cancer. *Int. J. Cancer* **137,** 504–511 (2015).
186. Barker, H. E., Cox, T. R. & Erler, J. T. The rationale for targeting the LOX family in cancer. *Nat. Rev. Cancer* **12,** 540–552 (2012).
187. Li, E., Hong, Y.-J., Yasuno, Y., Kasaragod, D. & Makita, S. Three-dimensional multi-contrast imaging of in vivo human skin by Jones matrix optical coherence tomography. *Biomed. Opt. Express* **8,** 1290 (2017).
188. Kang, J. H. *et al.* Gold nanoparticle-based colorimetric assay for cancer diagnosis. *Biosens. Bioelectron.* **25,** 1869–1874 (2010).
189. Jain, S., Hirst, D. G. & O'Sullivan, J. M. Gold nanoparticles as novel agents for cancer therapy. *Br. J. Radiol.* **85,** 101–113 (2012).
190. Song, L. *et al.* Efficient, pH-Triggered Drug Delivery Using a pH-Responsive DNA-Conjugated Gold Nanoparticle. *Adv. Healthc. Mater.* **2,** 275–280 (2013).
191. de la Rica, R. & Stevens, M. M. Plasmonic ELISA for the ultrasensitive detection of disease biomarkers with the naked eye. *Nat. Nanotechnol.* **8,** 1759–1764 (2012).
192. R. de La Rica and A. H. Verders. No Title. *J. Am. Chem. Soc.* **133,** 2875–7 (2011).
193. Seekell, K. *et al.* Feasibility study of brain tumor delineation using immunolabeled gold nanorods. *Biomed. Opt. Express* **4,** 2284–2295 (2013).
194. Alanazi, F. K., Radwan, A. A. & Alsarra, I. A. Biopharmaceutical applications of nanogold. *Saudi Pharm. J.* **18,** 179–193 (2010).
195. Jiang, H. & Sun, S. X. Cellular Pressure and Volume Regulation and Implications for Cell Mechanics. *Biophys. J.* **105,** 609–619 (2013).
196. Wang, H. *et al.* In vitro and in vivo two-photon luminescence imaging of single gold nanorods. *Proc. Natl. Acad. Sci.* **102,** 15752–15756 (2005).
197. Hu, M. *et al.* Dark-field microscopy studies of single metal nanoparticles: understanding the factors that influence the linewidth of the localized surface plasmon resonance. *J. Mater. Chem.* **18,** 1949–1960 (2008).
198. Zagaynova, E. V *et al.* Contrasting properties of gold nanoparticles for optical coherence tomography: phantom, in vivo studies and Monte Carlo simulation. *Phys. Med. Biol.* **53,**

4995–5009 (2008).
199. Debouttière, P.-J. *et al.* Design of Gold Nanoparticles for Magnetic Resonance Imaging. *Adv. Funct. Mater.* **16,** 2330–2339 (2006).
200. Lahr, R. & Vikesland, P. Surface-enhanced Raman spectroscopy (SERS) cellular imaging of intracellularly biosynthesized gold nanoparticles. *ACS Sustain. Chem. …* A-J (2014).
201. Patskovsky, S., Bergeron, E., Rioux, D. & Meunier, M. Wide-field hyperspectral 3D imaging of functionalized gold nanoparticles targeting cancer cells by reflected light microscopy. *J. Biophotonics* **7,** 1–7 (2014).
202. Liba, O., Sorelle, E. D., Sen, D. & De La Zerda, A. Contrast-enhanced optical coherence tomography with picomolar sensitivity for functional in vivo imaging. *Sci. Rep.* **6,** 1–12 (2016).
203. Tucker-Schwartz, J. & Skala, M. Contrast enhancement in optical coherence tomography. *SPIE Newsroom* 2–4 (2012). doi:10.1117/2.1201212.004626
204. Li, W. & Chen, X. Gold nanoparticles for photoacoustic imaging. *Nanomedicine (London, United Kingdom)* **10,** 299–320 (2015).
205. Fairbairn, N., Christofidou, a., Kanaras, A. G., Newman, T. a. & Muskens, O. L. Hyperspectral darkfield microscopy of single hollow gold nanoparticles for biomedical applications. 4163–4168 (2012). doi:10.1039/c2cp43162a
206. Almassalha, L. M. *et al.* Label-free imaging of the native , living cellular nanoarchitecture using partial-wave spectroscopic microscopy. *Proc. Natl. Acad. Sci.* **113,** E6372–E6381 (2016).
207. Jeynes, J. C. G., Jeynes, C., Merchant, M. J. & Kirkby, K. J. Measuring and modelling cell-to-cell variation in uptake of gold nanoparticles. *Analyst* **138,** 7070–7074 (2013).
208. Chandler, J. E., Maneval, C. D., White, C. A. & Levenson, R. M. High-speed spectral nanocytology for early cancer screening screening. *J. Biomed. Opt.* **18,** 17002-1–9 (2013).
209. Cherkezyan, L. *et al.* Interferometric spectroscopy of scattered light can quantify the statistics of subdiffractional refractive-index fluctuations. *Phys. Rev. Lett.* **111,** (2013).
210. Subramanian, H. *et al.* Partial-wave microscopic spectroscopy detects subwavelength refractive index fluctuations: an application to cancer diagnosis. *Opt. Lett.* **34,** 518–20 (2009).
211. Almassalha, L. M. *et al.* The global relationship between chromatin physical topology, fractal structure, and gene expression. *Sci. Rep.* **7,** 1–13 (2017).
212. Preparata, F. P. & Hong, S. J. Convex hulls of finite sets of points in two and three dimensions. *Commun. ACM* **20,** 87–93 (1977).
213. Bauer, G. M. *et al.* The transformation of the nuclear nanoarchitecture in human field carcinogenesis. *Futur. Sci. OA* **3,** FSO206 (2017).
214. Almassalha, L. M. *et al.* Macrogenomic engineering via modulation of the scaling of chromatin packing density. *Nat. Biomed. Eng.* **1,** 902–913 (2017).
215. Lee, H. & Lee, D. G. Gold nanoparticles induce a reactive oxygen species-independent apoptotic pathway in Escherichia coli. *Colloids Surfaces B Biointerfaces* **167,** 1–7 (2018).
216. Minai, L., Yeheskely-Hayon, D. & Yelin, D. High levels of reactive oxygen species in gold nanoparticle-targeted cancer cells following femtosecond pulse irradiation. *Sci. Rep.* **3,** 1–7 (2013).
217. Brenneisen, P. & Reichert, A. Nanotherapy and Reactive Oxygen Species (ROS) in Cancer: A Novel Perspective. *Antioxidants* **7,** 31 (2018).
218. Fisher, R. *et al.* Species richness on coral reefs and the pursuit of convergent global estimates. *Curr. Biol.* **25,** 500–505 (2015).

219. Wilkinson, C. *Status of Coral Reefs of the World: 2008*. *Status of Coral Reefs of the World: 2008* (2008).
220. Muscatine, L. in *Ecosystems of the World* (ed. Zubinsky, Z.) 75–87 (Elsevier Science Publishing Company, Inc., 1990).
221. Falkowsky, P., Jokiel, P. & Kinzie, R. in *Ecosystems of the World 25: Coral Reefs* (ed. Dubinsky, Z.) 89–107 (Elsevier, 1990).
222. Suggett, D. J., Warner, M. E. & Leggat, W. Symbiotic Dinoflagellate Functional Diversity Mediates Coral Survival under Ecological Crisis. *Trends Ecol. Evol.* **32,** 735–745 (2017).
223. Warner, M. E., Fitt, W. K. & Schmidt, G. W. Damage to photosystem II in symbiotic dinoflagellates: A determinant of coral bleaching. *Proc. Natl. Acad. Sci.* **96,** 8007–8012 (1999).
224. Bhagooli, R. & Hidaka, M. Photoinhibition , bleaching susceptibility and mortality in two scleractinian corals , Platygyra ryukyuensis and Stylophora pistillata , in response to thermal and light stresses. *Comp. Biochem. Physiol. Part A* **137,** 547–555 (2004).
225. Lesser, M. & Farrell, J. Exposure to solar radiation increases damage to both host tissues and algal symbionts of corals during thermal stress. *Coral Reefs* **23,** 367–377 (2004).
226. Downs, C. A. *et al.* Heat-Stress and Light-Stress Induce Different Cellular Pathologies in the Symbiotic Dinoflagellate during Coral Bleaching. *PLoS One* **8,** 1–16 (2013).
227. Hoegh-Guldberg, O. *et al.* Coral Reefs Under Rapid Climate Change and Ocean Acidification. *Science (80-.).* **318,** 1737–1743 (2008).
228. Baker, A. C., Glynn, P. W. & Riegl, B. Climate change and coral reef bleaching : An ecological assessment of long-term impacts , recovery trends and future outlook. *Estuar. Coast. Shelf Sci.* **80,** 435–471 (2008).
229. Kühl, M., Cohen, Y., Dalsgaard, T., Jorgensen, B. B. & Revsbech, N. P. Microenvironment and photosynthesis of zooxanthellae in scleractinian corals studied with microsensors for O2, pH and light. *Mar. Ecol. Prog. Ser.* **117,** 159–177 (1995).
230. Enriquez, S., Mendez, E. R. & Iglesias-Prieto, R. Multiple scattering on coral skeletons enhances light absorption by symbiotic algae. *Limnol. Oceanogr.* **50,** 1025–1032 (2005).
231. Terán, E., Méndez, E. R., Enríquez, S. & Iglesias-Prieto, R. Multiple light scattering and absorption in reef-building corals. *Appl. Opt.* **49,** 5032 (2010).
232. Marcelino, L. A. *et al.* Modulation of Light-Enhancement to Symbiotic Algae by Light-Scattering in Corals and Evolutionary Trends in Bleaching. *PLoS One* **8,** (2013).
233. Swain, T. D. *et al.* Skeletal light-scattering accelerates bleaching response in reef-building corals. *BMC Ecol.* **16,** 10 (2016).
234. Wangpraseurt, D., Larkum, A. W. D., Ralph, P. J., Kühl, M. & Michelou, V. K. Light gradients and optical microniches in coral tissues. *Front. Microbiol.* **3,** 1–9 (2012).
235. Wangpraseurt, D., Larkum, A. W. D., Franklin, J., Szabó, M. & Ralph, P. J. Lateral light transfer ensures efficient resource distribution in symbiont-bearing corals. 489–498 (2014). doi:10.1242/jeb.091116
236. Lichtenberg, M., Larkum, A. W. D. & Kühl, M. Photosynthetic acclimation of Symbiodinium in hospite depends on vertical position in the tissue of the scleractinian coral Montastrea curta. *Front. Microbiol.* **7,** 1–13 (2016).
237. Schlichter, D., Fricke, H. W. & Weber, W. Light harvesting by wavelength transformation in a symbiotic coral of the Red Sea twilight zone. *Mar. Biol.* **91,** 403–407 (1986).
238. Salih, A., Larkum, A., Cox, G., Kühl, M. & Hoegh-Guldberg, O. Fluorescent pigments in corals are photoprotective. *Nature* **408,** 850–853 (2000).
239. Smith, E. G., D'Angelo, C., Salih, A. & Wiedenmann, J. Screening by coral green

fluorescent protein (GFP)-like chromoproteins supports a role in photoprotection of zooxanthellae. *Coral Reefs* **32,** 463–474 (2013).
240. Lyndby, N. H., Kühl, M. & Wangpraseurt, D. Heat generation and light scattering of green fluorescent protein-like pigments in coral tissue. *Sci. Rep.* **6,** 26599 (2016).
241. Jimenez, I. M., Larkum, A. W. D., Ralph, P. J. & Kühl, M. Thermal effects of tissue optics in symbiont-bearing reef-building corals. *Limnol. Oceanogr.* **57,** 1816–1825 (2012).
242. Stimson, J. The annual cycle of density of zooxanthellae in the tissues of field and laboratory-held Pocillopora damicornis (Linnaeus). *J. Exp. Mar. Bio. Ecol.* **214,** 35–48 (1997).
243. Capoğlu, I. R., Rogers, J. D., Taflove, A. & Backman, V. Accuracy of the Born approximation in calculating the scattering coefficient of biological continuous random media. *Opt. Lett.* **34,** 2679–2681 (2009).
244. Wangpraseurt, D. *et al.* The in situ light microenvironment of corals. *Limnol. Oceanogr.* **59,** 917–926 (2014).
245. Backman, V., Wax, A. & Zhang, H. F. *A Laboratory Manual in Biophotonics*. (CRC Press, 2018).
246. Swain, T. D. *et al.* Relating Coral Skeletal Structures at Different Length Scales to Growth, Light Availability to Symbiodinium, and Thermal Bleaching. *Front. Mar. Sci.* **5,** (2018).
247. Von Euw, S. *et al.* Biological control of aragonite formation in stony corals. *Science (80-.).* **356,** 933–938 (2017).
248. Cuif, J. P. & Dauphin, Y. The environment Recording Unit in coral skeletons - a synethesis of strucural and chemical evdinces for a biochemically driven, stepping-growth process in fibres. *Biogeosciences, Eur. Geosci. Union* **2,** 61–73 (2005).
249. Rogers, J. D., Radosevich, A. J., Ji Yi & Backman, V. Modeling Light Scattering in Tissue as Continuous Random Media Using a Versatile Refractive Index Correlation Function. *IEEE J. Sel. Top. Quantum Electron.* **20,** 173–186 (2014).
250. Levy, O., Achituv, Y., Yacobi, Y. Z., Dubinsky, Z. & Stambler, N. Diel `tuning' of coral metabolism: physiological responses to light cues. *J. Exp. Biol.* **209,** 273–283 (2006).
251. Venn, A. A., Wilson, M. A., Trapido-Rosenthal, H. G., Keely, B. J. & Douglas, A. E. The impact of coral bleaching on the pigment profile of the symbiotic alga, Symbiodinium. *Plant, Cell Environ.* **29,** 2133–2142 (2006).
252. Wangpraseurt, D., Jacques, S. L., Petrie, T., Kühl, M. & Hochberg, E. J. Monte Carlo Modeling of Photon Propagation Reveals Highly Scattering Coral Tissue. *Front. Plant Sci.* **7,** 1–10 (2016).
253. Shimada, Y., Sadr, A., Sumi, Y. & Tagami, J. Application of Optical Coherence Tomography (OCT) for Diagnosis of Caries, Cracks, and Defects of Restorations. *Curr. Oral Heal. Reports* **2,** 73–80 (2015).
254. Xu, C., Marks, D. L., Do, M. N. & Boppart, S. A. Separation of absorption and scattering profiles in spectroscopic optical coherence tomography using a least-squares algorithm. *Opt. Express* **12,** 4790 (2004).
255. Levitz, D. *et al.* Determination of optical scattering properties of highly-scattering media in optical coherence tomography images. *Opt. Express* **12,** 543–545 (2004).
256. Henyey, L. G. & Greenstein, J. L. Diffuse radiation in the Galaxy. *Astrophys. J.* **93,** 70–83 (1941).
257. Xu, M. & Alfano, R. R. Fractal mechanisms of light scattering in biological tissue and cells. *Opt. Lett.* **30,** 3051–3053 (2005).

258. Akira Ishimaru. *Wave Propagation and Scattering in Random Media*. (IEEE Publications, 1997).
259. Jacques, S. L. Optical properties of biological tissues: a review. *Phys. Med. Biol.* **58,** R37–R61 (2013).
260. Binzoni, T., Leung, T. S., Gandjbakhche, A. H., Rüfenacht, D. & Delpy, D. T. The use of the Henyey–Greenstein phase function in Monte Carlo simulations in biomedical optics. *Phys. Med. Biol.* **51,** N313 (2006).
261. Lagarias, Jeffrey, C., Reeds, James, A., Wright, Margaret, H. & Wright, Paul, E. Convergence properties of the nelder–mead simplex method in low dimensions. *SIAM J. Optim.* **9,** 112–147 (1998).
262. Jacques, S. L. & Prahl, S. Chlorophyll A. *PhotochemCAD package* (1997). at <https://omlc.org/spectra/PhotochemCAD/html/122.html>
263. Stambler, N. & Dubinsky, Z. Corals as light collectors: an integrating sphere approach. *Coral Reefs* **24,** 2–9 (2005).
264. Wojtkowski, M. *et al.* Ultrahigh-resolution, high-speed, Fourier domain optical coherence tomography and methods for dispersion compensation. *Opt. Express* **12,** 707–709 (2004).
265. Li, Y. *et al.* Measuring the Autocorrelation Function of Nanoscale Three- Dimensional Density Distribution in Individual Cells Using Scanning Transmission Electron Microscopy, Atomic Force Microscopy, and a New Deconvolution Algorithm. *Microsc Microanal* **23,** 661–667 (2017).
266. Winters, G., Holzman, R., Blekhman, A., Beer, S. & Loya, Y. Photographic assessment of coral chlorophyll contents: Implications for ecophysiological studies and coral monitoring. *J. Exp. Mar. Bio. Ecol.* **380,** 25–35 (2009).
267. Apprill, A. M., Bidigare, R. R. & Gates, R. D. Visibly healthy corals exhibit variable pigment concentrations and symbiont phenotypes. *Coral Reefs* **26,** 387–397 (2007).
268. Bellworthy, J. & Fine, M. Beyond peak summer temperatures, branching corals in the Gulf of Aqaba are resilient to thermal stress but sensitive to high light. *Coral Reefs* **36,** 1071–1082 (2017).
269. Brown, B. E., Dunne, R. P., Goodson, M. S. & Douglas, a E. Experience shapes the susceptibility of a reef coral to bleaching. *Coral Reefs* **21,** 119–126 (2002).
270. Siebeck, U. E., Marshall, N. J., Klüter, A. & Hoegh-Guldberg, O. Monitoring coral bleaching using a colour reference card. *Coral Reefs* **25,** 453–460 (2006).
271. Anthony, K. R. N. & Hoegh-Guldberg, O. Variation in coral photosynthesis, respiration and growth characteristics in contrasting light microhabitats: an analogue to plants in forest gaps and understoreys? *Funct. Ecol.* **17,** 246–259 (2003).
272. Wangpraseurt, D. *et al.* In vivo microscale measurements of light and photosynthesis during coral bleaching: Evidence for the optical feedback loop? *Front. Microbiol.* **8,** 1–12 (2017).
273. Dove, S. G. & Ranganathan, O. H. S. Major colour patterns of reef-building corals are due to a family of GFP-like proteins. *Coral Reefs* 197–204 (2006). doi:10.1007/PL00006956
274. Rodriguez-Roman, A., Hernandez-Pech, X., Thome, P. E., Enriquez, S. & Iglesias-Prieto, R. Photosynthesis and light utilization in the Caribbean coral Montastrea faveolata recovering from a bleaching event. *Light Sci. Appl.* **51,** 2702–2710 (2006).
275. Gittins, J. R., D'Angelo, C., Oswald, F., Edwards, R. J. & Wiedenmann, J. Fluorescent protein-mediated colour polymorphism in reef corals: Multicopy genes extend the adaptation/acclimatization potential to variable light environments. *Mol. Ecol.* **24,** 453–465 (2015).

276. Marina, O. C., Sanders, C. K. & Mourant, J. R. Correlating light scattering with internal cellular structures. *Biomed. Opt. Express* **3,** 296 (2012).
277. Ou, H. D. *et al.* ChromEMT: Visualizing 3D chromatin structure and compaction in interphase and mitotic cells. *Science (80-.).* **357,** (2017).
278. Rust, M. J., Bates, M. & Zhuang, X. Stochastic optical reconstruction microscopy (STORM) provides sub-diffraction-limit image resolution. *Nat. Methods* **3,** 793–795 (2009).
279. Dong, B. *et al.* Super-resolution spectroscopic microscopy via photon localization. *Nat. Commun.* **7,** 1–8 (2016).
280. Eshein, A. *et al.* Sub-10-nm imaging of nucleic acids using spectroscopic intrinsic-contrast photon-localization optical nanoscopy (SICLON). *Opt. Lett.* **43,** 5817 (2018).
281. Hee, M. R., Huang, D., Swanson, E. A. & Fujimoto, J. G. Polarization-sensitive low-coherence reflectometer for birefringence characterization and ranging. *J. Opt. Soc. Am. B* **9,** 1992 (2008).
282. Makita, S., Yamanari, M. & Yasuno, Y. Generalized Jones matrix optical coherence tomography: performance and local birefringence imaging. *Opt. Express* **18,** 854 (2010).
283. Li, E., Makita, S., Azuma, S., Miyazawa, A. & Yasuno, Y. Compression optical coherence elastography with two-dimensional displacement measurement and local deformation visualization. *Opt. Lett.* **44,** 787 (2019).
284. Schmitt, J. M. OCT elastography: imaging microscopic deformation and strain of tissue. *Opt. Express* **3,** 199 (1998).
285. de Boer, J. F., Hitzenberger, C. K. & Yasuno, Y. Polarization Sensitive Optical Coherence Tomography: A Review. *Biomed. Opt. Express* **8,** 1838–1873 (2017).
286. Villiger, M. *et al.* Deep tissue volume imaging of birefringence through fibre-optic needle probes for the delineation of breast tumour. *Sci. Rep.* **6,** 1–11 (2016).
287. Tearney, G. J. *et al.* In Vivo Endoscopic Optical Biopsy with Optical Coherence Tomography. *Science (80-.).* **276,** 2037–2039 (1997).
288. Schreiter, J., Meyer, S., Schmidt, C., Schulz, R. M. & Langer, S. Dorsal skinfold chamber models in mice. *GMS Interdiscip. Plast. Reconstr. Surg. DGPW* **6,** Doc10 (2017).
289. López, M. E. *et al.* Ductal carcinoma in situ (DCIS): Posttreatment follow-up care among Latina and non-Latina White women. *J. Cancer Surviv.* **7,** 219–226 (2013).
290. Zagaynova, E. V. *et al.* Contrasting properties of gold nanoparticles for optical coherence tomography: Phantom, in vivo studies and Monte Carlo simulation. *Phys. Med. Biol.* **53,** 4995–5009 (2008).
291. Mogensen, M. *et al.* Two optical coherence tomography systems detect topical gold nanoshells in hair follicles, sweat ducts and measure epidermis. *J. Biophotonics* **11,** e201700348 (2018).
292. Li, Y. L., Seekell, K., Yuan, H., Robles, F. E. & Wax, A. Multispectral nanoparticle contrast agents for true-color spectroscopic optical coherence tomography. *Biomed. Opt. Express* **3,** 1914–23 (2012).
293. Dayem, A. A. *et al.* The role of reactive oxygen species (ROS) in the biological activities of metallic nanoparticles. *Int. J. Mol. Sci.* **18,** 1–21 (2017).
294. Liu, R. *et al.* A theoretical model for optical oximetry at the single-cell level : Exploring hemoglobin oxygen saturation through backscattering of single red blood cells. *Phys. Rev. Lett.* **submitted,** (2016).
295. Winkelmann, J. A., Spicer, G., Yi, J. & Backman, V. Visible Inverse Spectroscopic Optical Coherence Tomography Probe for Spatially Resolved Nanoscale Characterization.

in *Biomedical Optics and 3-D Imaging* (2016).

Vita

Graham Lorne Cameron Spicer was born on August 30th, 1991 in Columbia, Maryland. He received the degrees of Bachelor of Science in Physics and Bachelor of Science in Chemical Engineering from Carnegie Mellon University in 2013. A degree of Doctor of Philosophy in Chemical Engineering from Northwestern University is anticipated in 2019. This manuscript was typed by the author.

Publications:

1. **Spicer, G**., Efeyan, A., Adam, A., Thompson, S. Universal guidelines for the conversion of proteins and dyes into functional nanothermometers. Journal of Biophotonics. e2141 (2019).

2. Winkelmann, J., Eid, A., **Spicer, G.**, Almassalha, L., Nyguen, T. Q., Backman, V. Spectral Contrast Optical Coherence Tomography Angiography Enables Single-Scan Vessel Imaging. Light: Science and Applications. 8, 7 (2019).

3. **Spicer, G.,** Almassalha, L., Martinez, I., ...Backman, V. Label free localization of nanoparticles in live cancer cells using spectroscopic microscopy. Nanoscale. 10, 19125-19130 (2018).

4. Liu, R., Winkelmann, J., **Spicer, G.**, Zhu, Y., Eid, A., Ameer, G., Yi, J., Backman, V. Single capillary oximetry and tissue ultrastructural sensing by dual-band dual-scan inverse spectroscopic optical coherence tomography. Light: Science and Applications. 7, 57 (2018).

5. Liu, R., **Spicer, G.**, Chen, S., Zhang, H. F., Yi, J., Backman, V. A theoretical model for optical oximetry at the single-cell level: Exploring hemoglobin oxygen saturation through backscattering of single red blood cells. J Biomed Opt. 22, 025002 (2017).

6. Rao, S., Azarin, S., Bushnell, G., **Spicer, G.**, Aguado, B., Stoehr, J., Jiang, E., Backman, V., Shea, L. , Jeruss, J. Enhanced Survival with Implantable Scaffolds that Capture Metastatic Breast Cancer Cells *In Vivo*. Cancer Res. 76, 5209-5218 (2016).

7. **Spicer, G.**, Azarin, S., Yi, J., Young, S., Ellis, R., Bauer, G. M., Shea, L. D., Backman, V. Detection of Extracellular Matrix Modification in Cancer Models with Inverse Spectroscopic Optical Coherence Tomography. Phys. Med. Biol. 61, 6892-6904 (2016).

8. Winkelmann, J., **Spicer, G.**, Yi, J., Backman, V. Visible Inverse Spectroscopic Optical Coherence Tomography Probe for Spatially Resolved Nanoscale Characterization. Clinical and Translational Biophotonics in *Biomedical Optics and 3-D Imaging* (2016). Fort Lauderdale, Florida United States, 25–28 April 2016, ISBN: 978-1-943580-10-1.

9. Zhang, D., Capoglu, I., Li, Y., Cherkezyan, L., Chandler, J., **Spicer, G.**, ... Backman, V. FDTD-Based Optical Microscopy Simulation of Dispersive Media Facilitates the Development of Optical Imaging Techniques. J. Biomed. Opt. 21, 065004 (2016).

10. Cheng, J., Xian, B. C., Hauser, B., Nandakumar, N., Smongeski, E., **Spicer, G.**, …Grossmann, I. E. Conceptual Design of an Aromatics Plant from Shale Gas. *CACHE Process Design Case Studies*, Vol. 11. (2013).

11. Youngblood, R. L., Sampson, J. P., Lebioda, K. L., **Spicer, G.**, Shea, L. D. Microporous Scaffolds Drive Assembly and Maturation of Progenitors into Beta Cell Clusters. Acta Biomateriala. Submitted (2019).

12. **Spicer, G.**, Eid, A., Wangpraseurt, D., Swain, T., Winkelmann, J., Yi, J., Kühl, M., Marcelino, L., Backman, V. Measuring light scattering and absorption properties of coral tissue and skeleton with Inverse Spectroscopic Optical Coherence Tomography (ISOCT). Scientific Reports. Submitted (2019).

13. **Spicer, G.**, Bushnell, G., Eid, A., Winkelmann, J., Ellis, R., Orbach, S., Yi, J., Backman, V., Shea, L. D. Identification of structural changes at a synthetic pre-metastatic niche for label-free screening of early metastasis. In preparation (2019).

Presentations:

1. Eid, A., Winkelmann, J. A., **Spicer, G.**, Almassalha, L. M., Backman, V. Spectral based tissue classification and ultrastructural characterization using ISOCT. Oral presentation at SPIE BiOS, San Francisco, California, February 2, 2019.

2. Winkelmann, J. A., **Spicer, G.**, Eid, A., Nguyen, T. Q., Backman, V. Detection of ultrastructural modification in a synthetic pre-metastatic niche with inverse spectroscopic optical coherence tomography (ISOCT). Oral presentation at SPIE BiOS, San Francisco, California, February 5, 2019.

3. **Spicer, G.**, Bushnell, G. G., Eid, A., Winkelmann, J. A., Liu, R., Yi, J., Azarin, S. M., Shea, L. D., Backman, V. Detection of ultrastructural modification in a synthetic pre-metastatic niche with inverse spectroscopic optical coherence tomography (ISOCT). Oral presentation at SPIE BiOS, San Francisco, California, January 31, 2018.

4. Eshein, A., Zhou, X., Almassalha, L. M., Gladstein, S., Li, Y., Nguyen, T. Q., Chandler, J. E., **Spicer, G.**, Sun, C., Zhang, H. F., Backman, V. Multimodal nanoscale imaging of chromatin with super resolution microscopy and partial wave spectroscopy. Oral presentation at SPIE BiOS, San Francisco, California, January 30, 2018.

5. Liu, R., Winkelmann, J. A., **Spicer, G.**, Eid, A., Zhu, Y., Nguyen, T. Q., Ameer, G. A., Yi, J., Backman, V. *In vivo* functional microangiography with sensitivity down to the capillary level by dual band dual scan inverse spectroscopic optical coherence tomography (D2-ISOCT). Oral presentation at SPIE BiOS, San Francisco, California, January 29, 2018.

6. Li, Y., Dong, B., Eshein, A., **Spicer, G.**, Wu, W., Almassalha, L. M., Liu, R., Nguyen, T. Q., Chandler, J. E., Sun, C., Zhang, H. F., Backman, V. Chromatin structure quantification from super-resolution intrinsic fluorescence imaging. Oral presentation at SPIE BiOS, San Francisco, California, January 28, 2018.

7. Liu, R., **Spicer, G.**, Chen, S., Zhang, H. F., Yi, J., Backman, V. A theoretical model for optical oximetry at the capillary-level by optical coherence tomography. Oral presentation at SPIE BiOS, San Francisco, California, January 31, 2017.

8. **Spicer, G.**, Young, S., Yi, J., Shea, L. D., Backman, V. ISOCT study of effects of enzymatic crosslinking of collagen in field carcinogenesis. Oral presentation at SPIE BiOS, San Francisco, California, February 14, 2016.

9. Rao, S. S., Azarin, S. M., **Spicer, G.**, Bushnell, G. G., Aguado, B. A., Stoehr, J., Backman, V., Jeruss, J. S., Shea, L. D. Implantable micro-porous poly(ε-caprolactone) scaffolds for early detection of breast cancer metastasis. Poster presentation at BMES Annual Meeting, October 7-10, 2015.

10. **Spicer, G.**, Yi, J., Azarin, S. M., Young, S., Winkelmann, J., Eid, A., Liu, R., Shea, L. D., Backman, V. Inverse Spectroscopic Optical Coherence Tomography Study of ECM Interactions in Cancer. Poster presentation at BMES Annual Meeting, October 7-10, 2015.

11. Wu, W., Radosevich, A. J., Nguyen, Q., Young S., Li, Y., Eshein, A., **Spicer, G.**, Roy, H., Backman, V. Calculating optical properties of specific structure inside tissue using transmission electron microscopy (TEM). Oral presentation at SPIE BiOS, San Francisco, California, February 10, 2015.